The systematic assembly of prostate specific antigen electrochemical sensors based on asymmetric Co(II) phthalocyanines, graphitic quantum dots and an aptamer

A thesis submitted in fulfilment of the requirements for the degree

of

Doctor of Philosophy (PhD)

in

Chemistry

Of

Rhodes University

By

Siphesihle Robin Nxele

Supervisor

Distinguished Professor Tebello Nyokong

August 2021

Dedications

To the village that raised me and got me this far, to my parents Israel and Sharon Nxele, and to the researchers that will come after me and be inspired by this work.

"Here's to the end of this chapter. To all the late nights, early mornings, learnings gained, and experiences shared. Here's to the hardships that became our teachers, to the heaviness that taught us how to rise again and to the people who would stop their world to sit and celebrate our presence. Here's to the times we chose feeling over disconnection, freedom over perfection, courage over what's known and certain, and doing the work. Here's to releasing what wasn't ours to keep. Here's to holding our palms wide open to our blessings. And here's to taking one step forward into the hope and possibility of tomorrow."

- Danielle Doby

Acknowledgements

To my supervisor and the powerhouse who made this PhD dream a reality for me, distinguished Professor Tebello Nyokong, I cannot thank you enough Prof. I am forever grateful.

Thank you to Dr Fethi Bedioui as well as my supervisors at Chimie Paristech, Prof. Anne Varenne, Dr Fanny d'Orlye, Dr Laura Trapiella-Alfonso and my research group in France for hosting me and being a part of this PhD journey.

Thank you to Professor Philani Mashazi and Professor Janice Limson for helping me at the very beginning of this journey with bringing this project to life.

I also express my sincere gratitude to Miss Gail Cobus, Dr Jonathan Britton, Professor John Mack and Mr Francis Chindeka for their support and help during the course of this research. Thank you to Dr David Oluwole, who mentored me at that start of this PhD journey. Thank you to my lab S22 colleagues who have always been so helpful.

A special thank you goes to Mr Tendai Chonzi, Dr Allan Sanyanga, Miss Reitumetse Nkhahle, Miss Sivu Mapukata and Mr Nnamdi Nwahara for being my support structure in and out of this academic space.

Thank you to my friends and family for your love, kindness and patience throughout this journey.

Thank you to Rhodes University (South Africa) and Chimie Paristech (France).

Financial support from the French government (campus France) and the National Research Foundation (NRF) of South Africa through DST/NRF South African Research Chairs Initiative for Professor of Medicinal Chemistry and Nanotechnology (UID 62620) is gratefully acknowledged.

Preface

The need for low-cost, efficient and simple diagnostic tools has led to more research going into this subject, with the aim of making such medical devices more accessible where they are needed. This has led to more researchers developing point-of-care devices for this purpose worldwide, by sensor fabrication. This thesis focuses on electrochemical sensor development for the early diagnosis of prostate cancer. It is common knowledge that prostate cancer is one of the most prevalent carcinomas that have claimed lives due to late diagnosis where even the most invasive treatments have failed. For this reason, development of early detection devices that can even be used in the comfort of home is necessary and quite crucial. Electrochemical sensors have gained much attention due to their ease of fabrication, cost effectiveness, simplicity, ease of use and high efficiency. Using nanocomposites as modifiers has also become popular as they provide greater stability and improve detection limits when used together with biomolecules. With that said, the work reported herein has combined nanocomposites of graphene-based quantum dots, gold nanoparticles, phthalocyanines and an aptamer in order to fabricate aptasensors for the electrochemical detection of prostate cancer biomarker. The aptamer is specifically designed to bind to the biomarker, and the nanocomposites are expected to enhance current output thus lowering detection limits and increasing stability and efficiency. Reproducible results are also expected. Prior to the detection of the prostate cancer biomarker, the quantum dots-phthalocyanine nanohybrids were used to detect L-cysteine, which is an amino acid, in order to verify the synergistic effects as electrode modifiers that lead to the enhancement of current output. This increase in current output is then

exploited for the improvement of aptasensor functionality upon incorporation of the aptamer, for the detection of prostate specific antigen. The research in this thesis has been carried out with the intention of contributing to the world of medical research, more so because of the ever-increasing need for medical care to become accessible to all and not only to those who can afford expensive technologies and treatments.

Contents

Table of contents

List of abbreviations

AuNPs = gold nanoparticles

BE = binding energy

BGE = background electrolyte

CE-MS = capillary electrophoresis mass spectrometry

CoPc = cobalt phthalocyanine

CV = cyclic voltammetry

DBU = 1,8-Diazabicyclo [5.4.0]undec-7-ene

DMF = dimethylformamide

DMSO = dimethylsulphoxide

DPV = differential pulse voltammetry

EIS = electrochemical impedance spectroscopy

ESI = electrospray ionization

FTIR = fourier transform infra-red

GCE = glassy carbon electrodes

gCNQDs = graphitic carbon nitride quantum dots

GPES = general purpose electrochemical system

GQDs = graphene quantum dots

MPcs = metallophthalocyanines

NGQDs = nitrogen doped graphene quantum dots

NM = neutral marker

PBS = phosphate buffer saline

PCa = prostate cancer

PSA = prostate specific antigen

SECM = scanning electrochemical microscopy

SEM = scanning electron microscopy

TEM = transmission electron microscopy

tert-butyl = tertiary butyl

UME = ultra-micro electrode

UV/vis = ultraviolet/visible

XPS = X-ray photoelectron spectroscopy

XRD = X-ray diffraction

List of symbols

α = non-peripheral position

A = electrode surface area.

Å = Angstroms

β = peripheral position

b = the Tafel slope

C = concentration

C_{dl}= double layer capacitance

D = diffusion coefficient

ΔE = Peak potential separation

E_{pa}= anodic peak potential

E_{pc} = cathodic peak potential

eV = electron volt

F = Faraday's constant

f = frequency

I_{ac}= anodic peak current.

I_{buf}= currents in the absence analyte

I_{cat}= currents in the presence of analyte

I_D= intensity of Raman D band

I_G= intensity of Raman G band

i_{Lim}= limiting current

I_p= peak current

I_{pc}= cathodic peak current.

k_{app}= apparent rate transfer constant

k_{cat}= the catalytic rate constant

K = constant

n_{α}= number of electrons involved in the rate determining step

R = the universal gas constant

R_{ct}= charge transfer resistance

R_s= solution resistance

δ = standard deviation

Γ = surface coverage

T = temperature (298 K)

ν = scan rate

W = Warburg Impedance

Z' = real impedance.

Z" = imaginary impedance

Abstract

Herein, prostate specific antigen electrochemical aptasensors were fabricated using combinations of novel asymmetrical metallophthalocyanines, graphene-based quantum dots, gold nanoparticles and an aptamer. These nanocomposites were used to fabricate glassy carbon electrodes using adsorption, self-assembly as well as electrochemical grafting and click chemistry. The combination of these nanocomposites with aptamer was to enhance the signal output for improved electrocatalytic detection. The combination of metallophthalocyanine with quantum dots or gold nanoparticles was a novel approach towards developing electrochemical sensors specifically for the electrochemical detection of PSA. Moreover, using electrografting and click chemistry introduced another novel approach to the study of aptasensor fabrication.

For the detection of prostate specific antigen, electrochemical impedance spectroscopy (EIS) as well as differential pulse voltammetry (DPV) were employed to determine detection limits as well as sensitivity and selectivity of the aptasensors. In both analytical techniques, linear calibration curves were observed at a concentration range of 1.2-2.0 pM. The detection limits were much lower than the dangerous levels reported for PSA in males tested for prostate cancer in buffer solutions and spiked serum samples and high percentage recoveries were obtained. These sensors also showed selectivity for PSA in the presence of bovine serum albumin, glucose and L-cysteine. The aptasensor showed good stability, reproducibility and repeatability, deeming it a promising tool for the early detection of prostate cancer.

1. Introduction

This chapter introduces graphene-based quantum dots, gold nanoparticles and their use in combination with metallophthalocyanines and an aptamer for use in electrocatalysis and more specifically, electrochemical biosensing of the prostate cancer biomarker, prostate specific antigen (PSA).

These nanoconjugates are, for the first time, linked to an aptamer and immobilized on glassy carbon electrodes to fabricate prostate cancer diagnostic tools. The importance of using these nanostructures in combination is also described in this chapter.

1.1 Overview of metallophthalocyanines (MPcs)

Phthalocyanines are chemically and thermally stable planar macrocycles with a conjugated 18πelectron system [1]. Amongst their proven characteristics is their ability to coordinate with a number of central metals to form metallophthalocyanines [2,3]. These macrocycles can be substituted peripherally (β) and non-peripherally (α) [4, 5]. Substitution of the rings may also be carried out with the aim of conjugating these macrocycles with other molecules [6-8]. MPcs have been used in areas of study such as photodynamic therapy (PDT) of cancers [9-11], optical limiting and non-linear optics [12, 13], fluorescence imaging [14-16], photocatalysis [17-19] and electrocatalysis [20-23]. In electrocatalysis especially, electroactive central metals such as manganese, cobalt and iron are used in order to catalyze specific reactions and promote charge transfer [24]. These metals have orbitals with energy levels lying between the highest occupied molecular orbital (HOMO) and the lowest unoccupied molecular orbital (LUMO) of the Pc, resulting in redox processes on both the central metal and the Pc ring [25]. The symmetry has shown to influence their performance in applications such as electrocatalysis [26, 27], which is of interest in this work. Asymmetrical MPcs especially, have been shown to improve electrocatalytic ability [28-30].

1.1.1 Synthesis of asymmetric MPcs

Different approaches have been used to synthesize asymmetrical MPcs such as cross condensation between two phthalonitrile components, cross condensation between one phthalonitrile and one non-nitrile component, the sub-phthalocyanine ring-

expansion method, modification of pre-formed symmetric or asymmetric systems [31] and solid-phase synthesis [32]. The most common approach, which is the one that has been used to synthesize the phthalocyanines used in this work, is the cross condensation between two phthalonitrile components, generally using the 3:1 ratio. In most cases, this results in other products forming which can be separated by chromatographic methods [32]. Scheme 1.1 illustrates the possible products that can form from using the aforementioned synthetic approach for mono-MPcs. The desired MPc, which is employed in this work, is the one with the AB_3 symmetry.

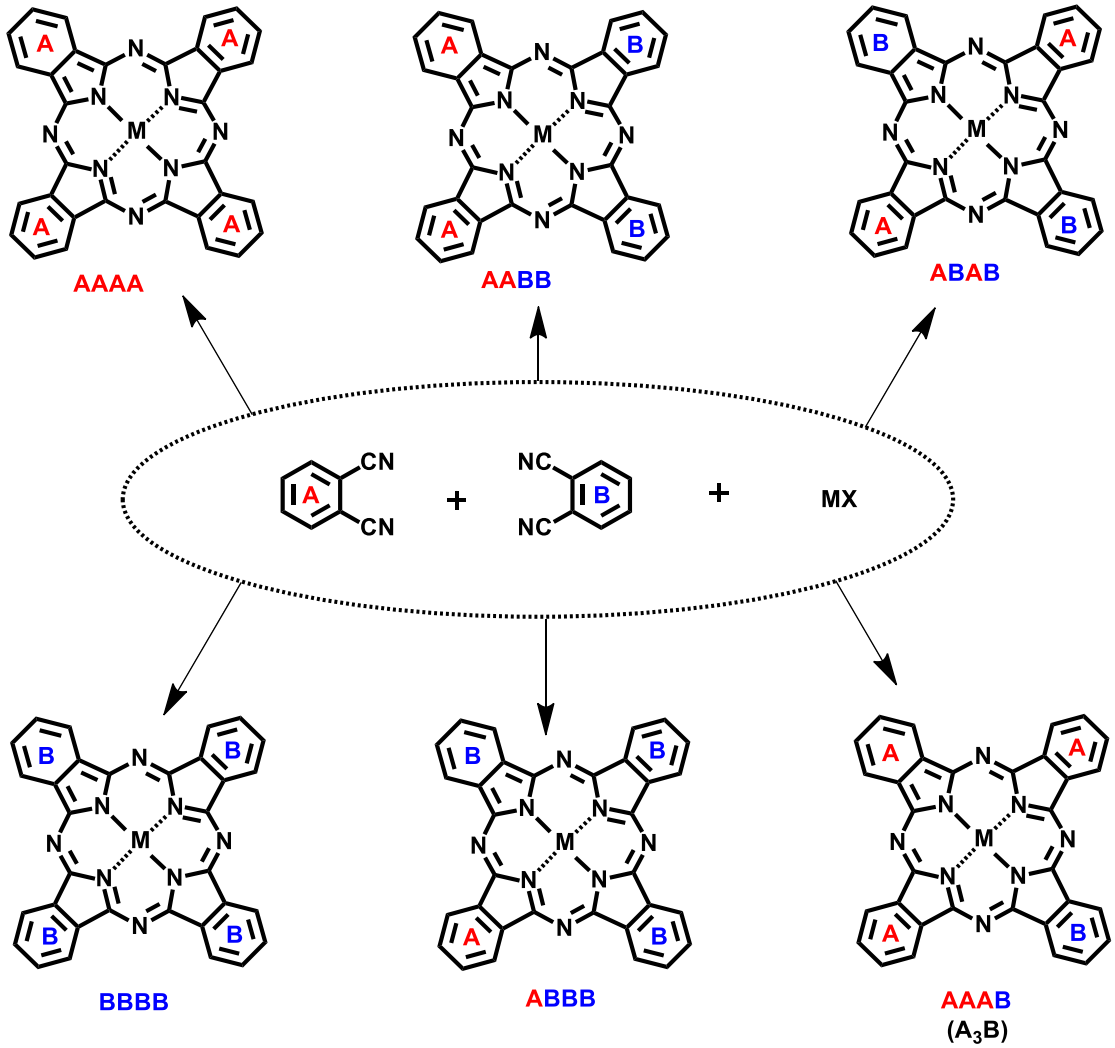

Scheme 1.1: Asymmetric MPc synthesis and other possible formed products. MX refers to the metal salt.

1.1.2 Phthalocyanine complexes used in this work

In this work, the following novel asymmetrically substituted phthalocyanine complexes are employed: 2- benzoic acid-9(10),16(17),23(24)-tris(2,6-di-tert-butyl-4-methylphenoxy) phthalocyaninato cobalt (II) (1) and 2-N,N',N"-hex-5-yn-1-yloxy)-9(10),16(17), 23(24)- tris(benzene-4,1-diyl))triacetamidephthalocyaninato cobalt(II) (2), Fig. 1.1. These asymmetrically substituted Co phthalocyanine derivatives (complexes 1 and 2) are used in combination with quantum dots (QDs), gold nanoparticles (AuNPs) and an aptamer for the electrochemical detection of prostate specific antigen (PSA). They are employed as electrode modifiers towards the development of aptasensors. The combination of MPcs with AuNPs and QDs, as aptamer immobilizers and signal enhancers towards the electrocatalytic detection of PSA, is reported for the first time. Complex 1 has a -COOH substituent which can be used for covalent linking with an NH_2 terminated molecule via an amide bond. Complex 2 on the other hand will be immobilized on an electrode via electrografting and click chemistry before incorporating the aptamer by adsorption. Both complexes are linked to QDs by π-π interactions. The complexes reported herein are novel and reported in this thesis for the first time. Complex 1has substituents (*tert*-butyl) that act as electron donating groups (push) and the single COOH as an electron withdrawing group (pull). Such push-pull substituents have been reported to enhance electron transfer properties of complexes [30]. Complex 2 has electron donating alkoxy groups which lower oxidation potentials. A lower potential difference implies better electron transfer which could affect the performance of the fabricated sensors overall.

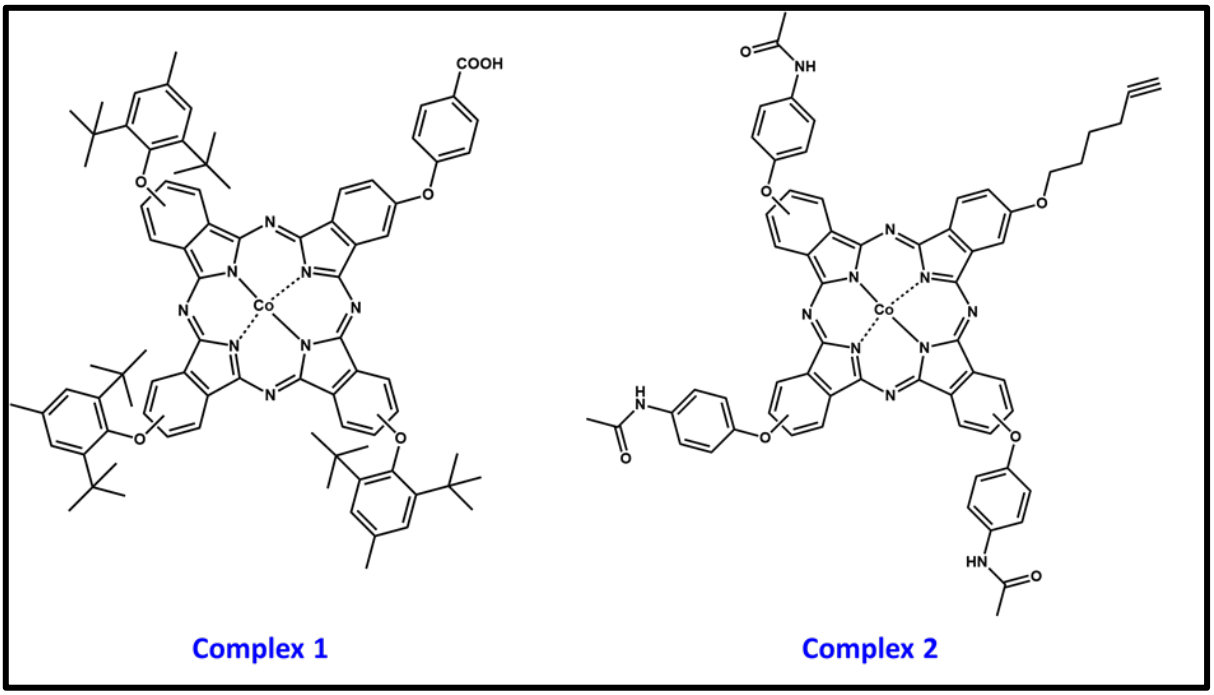

Figure 1.1: Structures of phthalocyanine molecules used in this work.

1.2 Overview of graphene-based quantum dots

Graphene is a 2-dimentional, sp^2 hybridized derivative of graphite made up of covalently linked carbon atoms [33]. Graphite and graphene representations are illustrated in Fig.1.2 [34]. Graphene is characterized by its robustness, good electronic properties and low toxicity in biological applications [35-37]. Graphene and graphene quantum dots (GQDs) can be defined as layered fragments of graphene which are well dispersed in water, biocompatible, easy to functionalize at the surface, and also possess low toxicity, with a size range of 1-20 nm [38]. Different synthetic routes have been followed to obtain these nanostructures. Moreover, their surface functionalization also depends on their intended application.

Doping of GQDs with heteroatoms such as boron, nitrogen, oxygen, phosphorous, and sulphur, has led to improved electrocatalytic activity. Nitrogen lies adjacent

to carbon in the periodic table thus possess similarity in atomic radius (0.70 Å)with carbon (0.77 Å) which makes it easier to incorporate nitrogen into the pristine carbon network. Nitrogen also has a higher electronegativity (3.04) than C (2.55) which promotes altered electron states of graphene and therefore improving electrocatalytic ability of these nanostructures. GQDs, nitrogen doped graphene quantum dots (NGQDs) and graphitic carbon nitride quantum dots (gCNQDs) have all been employed in this work for electrocatalysis in combination with MPcs. The conjugates are expected to perform better than using the nanostructures as individual components. Graphitic carbon nitride quantum dots (gCNQDs) are of particular interest because they possess the layered structure like GQDs, but the difference lies in their exhibition of predominantly π-conjugated framework of C-N layers which are linked covalently [39], Fig.1.3. This nitrogen rich structure will likely play a role in enhancing the electrocatalytic ability of the fabricated sensors. The work reported here shows, for the first time, the use of gCNQDs in the presence of Pcs for electrochemical sensing. The covalent linking of these QDs with an aptamer is also shown herein for the first time although well-known amide coupling is used for conjugation.

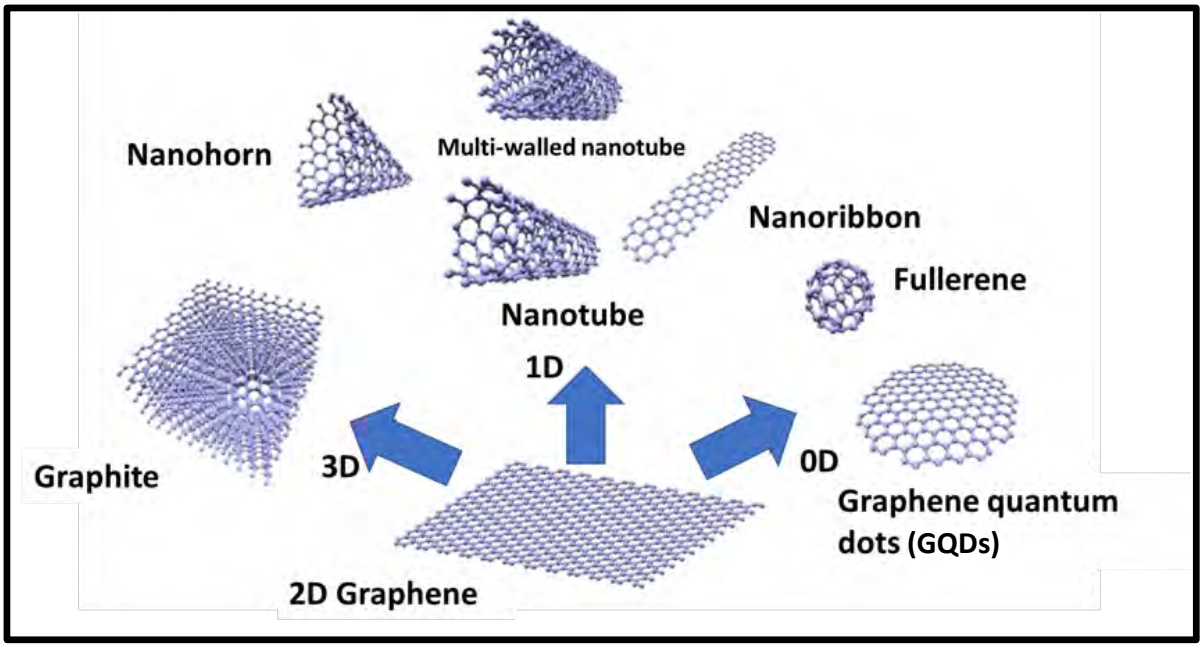

Fig.1.2:Graphite, graphene and their derivatives [34].

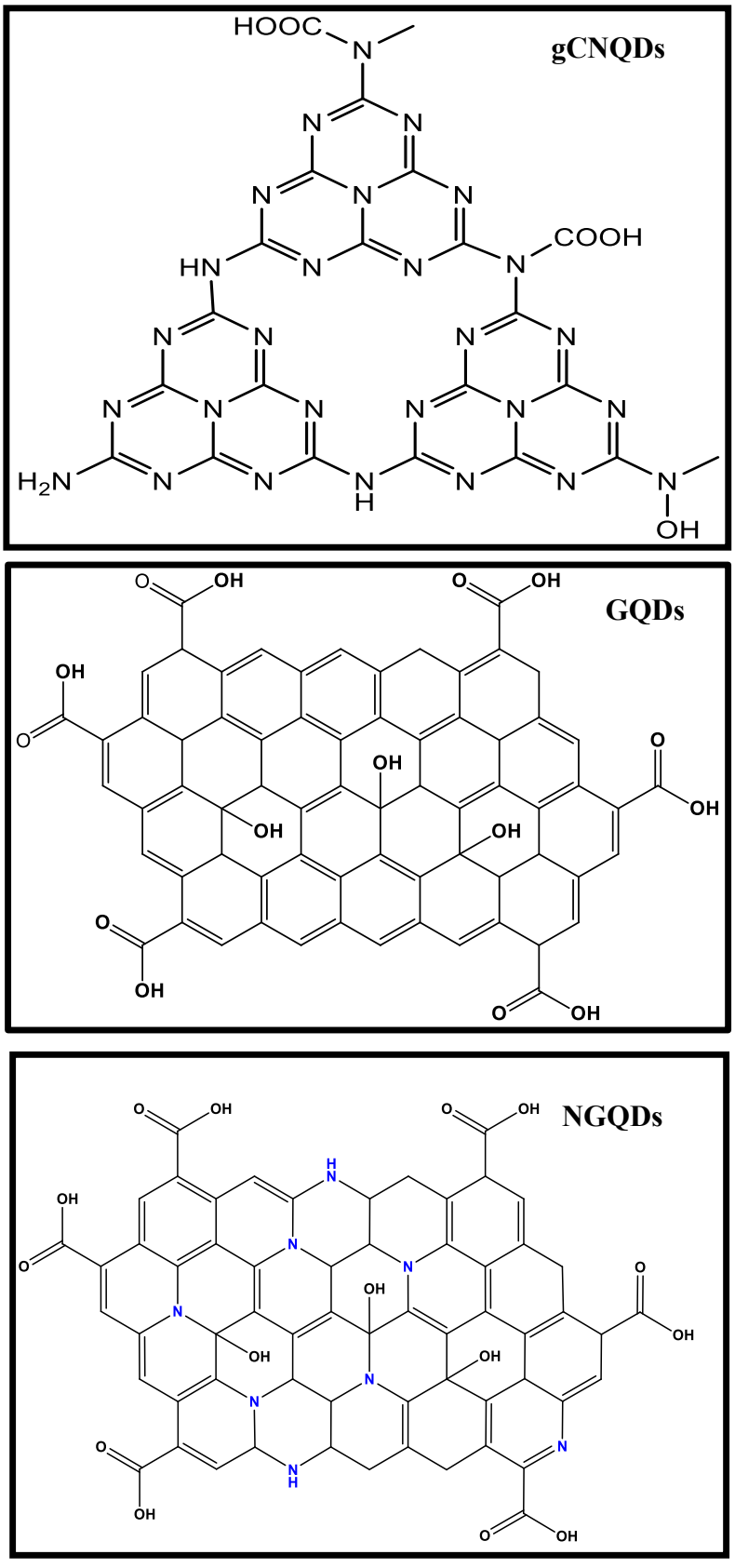

Figure 1.3: Theoretical structural representation of gCNQDs, GQDs and NGQDs.

1.2.1 The synthesis of GQDs, NGQDs and gCNQDs

There are two main approaches to obtaining GQDs. These are the top-down approach and the bottom-up approaches. The top-down approach involves the cutting or breaking down of large materials with graphene-like structures into nanosized (<100 nm) structures and the bottom-up synthetic routes employs carbon-rich precursors to synthesize GQDs [40]. These approaches have been illustrated in Fig. 1.4. Examples of top-down approaches include chemical exfoliation [41], microwave-assisted [42] and solvothermal processes [43]. The bottom-up approach includes hydrothermal [44], microwave-assisted pyrolysis [45] and precursor pyrolysis [46, 47]. The QDs synthesized in this work were obtained by employing the bottom-up hydrothermal approach. Hydrothermal synthesis is achieved in solution under high pressure and high temperatures [48].

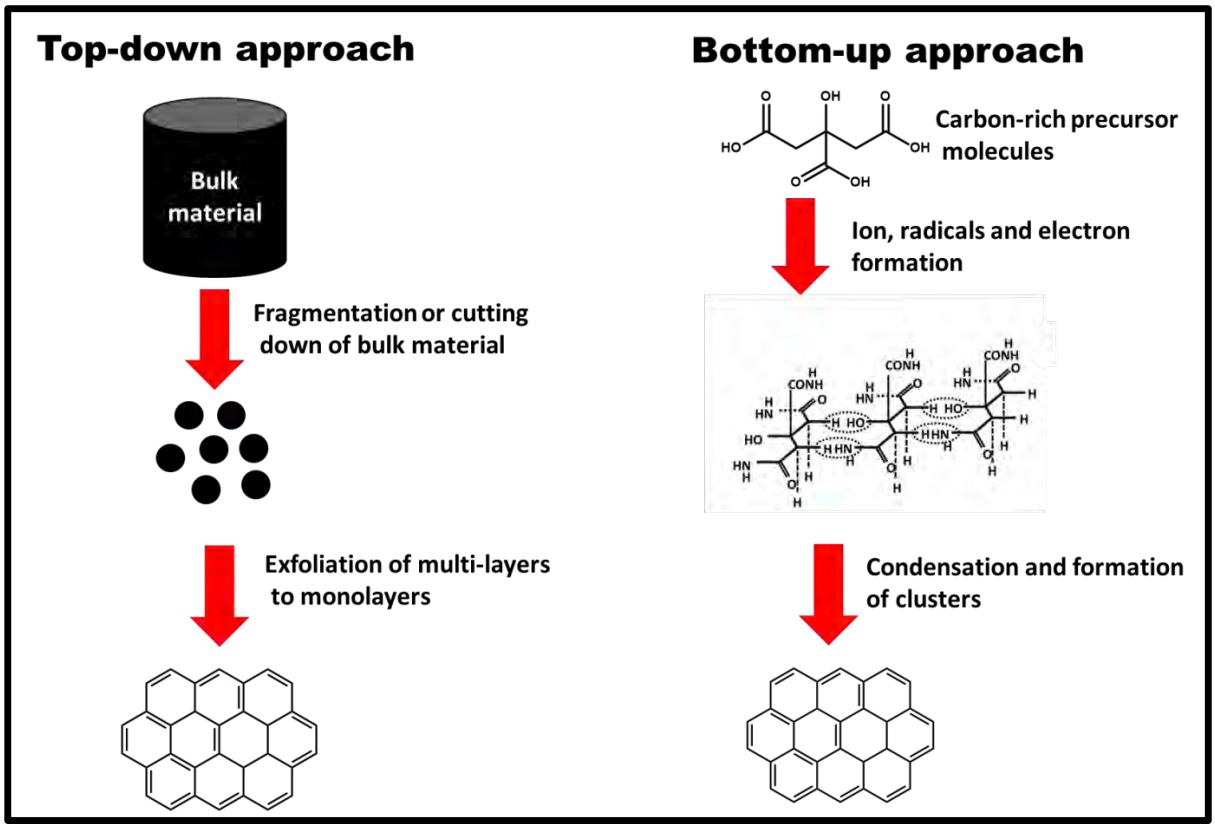

Fig.1.4: GQDs synthetic approaches [47].

1.2.2 GQDs characterization and structural determination

Various spectroscopic techniques have been used to characterize graphene-based QDs such as dynamic light scattering (DLS), energy dispersive X-ray (EDX) microanalysis, Raman, absorption and Fourier transform infrared (FTIR) spectroscopies, just to name a few. These techniques have provided information regarding the physical and optical properties of these QDs. However, with QDs being layered sheets and the synthetic approaches used not being controlled, polydisperse samples are likely to be obtained, meaning that QDs of different structures and extent of functionalization exist in one batch. For this reason, capillary electrophoresis (CE) coupled with electrospray ionization mass spectrometry (ESI-MS) was employed in order to separate QDs in a sample according to their size and surface charge and determine the exact structures and overall surface functionalization of the QDs reported in this thesis. Although methods such as molecular modelling have been used in understanding the structure and chemical composition of graphene-based quantum dots [49], literature rarely reports structural information in detail of the synthesized nanostructures. The list of reports on the optimization of graphene-based quantum dots is a very short one. Some recent reports have shown optimization of quantum dots but only focusing on their fluorescent properties [50, 51]. Herein, it is reported for the first time, on the optimization of the synthetic routes for GQDs, NGQDs and gCNQDs, focusing specifically on the reaction time using CE-ESI-MS.

Electrophoresis coupled to mass spectrometry has become an attractive analytical technique as it combines the advantage of qualitative and quantitative information that would not be obtained if instruments were used separately [52].

In this technique, the sample is injected into the CE instrument through the inlet and is initially separated according to surface charge density and particle size [53]. Fig. 1.5 illustrates the movement of particles within a buffer-filled fused silica capillary where a high voltage is applied, inducing the movement of charge particles. The capillary itself is made up of an internal silanol layer, which becomes negatively charged upon activation. Since size of particles influence their migration, particles that have the same charge will be differentiated according to their size meaning the larger the particle, the slower it will move through the capillary. The advantage of using CE is that it has low sample consumption, short analysis time, high separation efficiency, ease of operation and ability to run automatically once the optimized parameters have been entered into the operating system [54, 55].

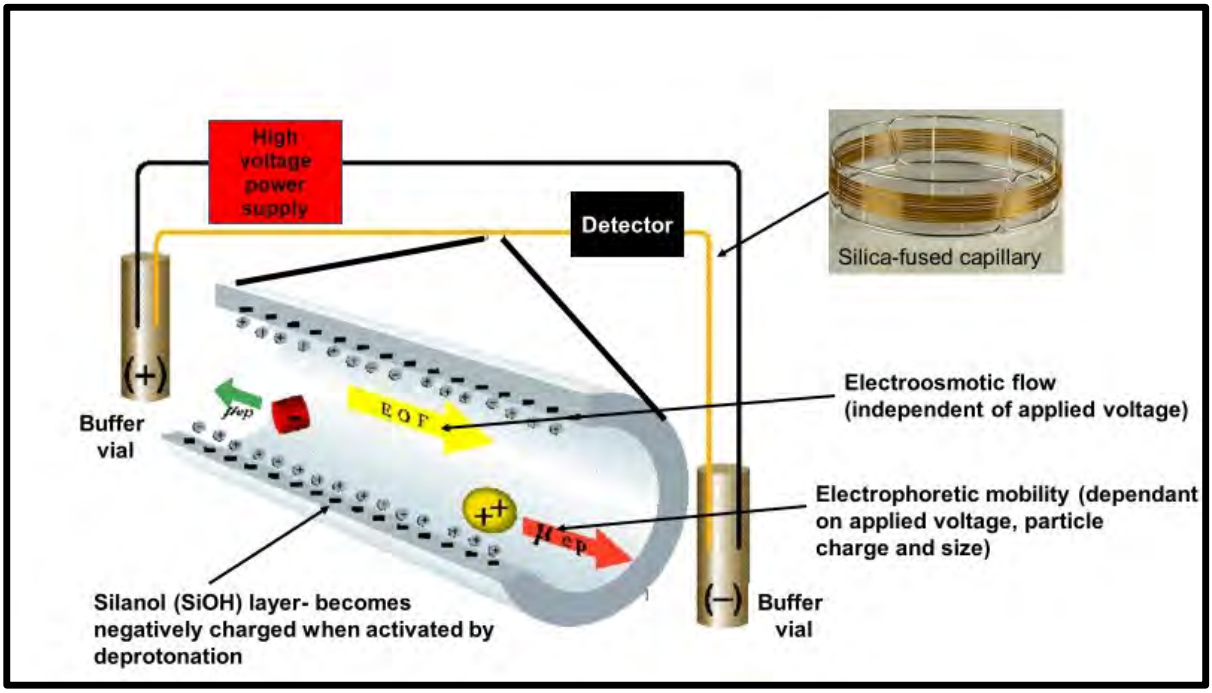

Figure 1.5: Illustration of particle separation in CE [53].

MS then provides a platform to detect the separated nanostructures and gives information via ion mass, which finally allows for the prediction and visualization of the nanostructures of interest. ESI allows for the detection of large molecular species by generating ions with multiple charges [56]. Samples may be analyzed in single ion mode (SIM) or scan mode depending on whether or not expected ions are known. SIM will only show the specified ions in the spectrum whereas scan mode will show all ions detected. Moreover, the analysis setup has to specify positive or negative ion mode depending on the expected charges of the ions. The connection between the CE and MS system is achieved by electrospray ionization, illustrated in Fig. 1.6.to briefly explain how it operates, the electrospray promotes the formation of a stream of charged particles carried through a buffer solution by an applied voltage [57]. For this to be achieved successfully, a number of parameters need to be optimized. Among these parameters is the sheath liquid which needs to be suitable for ionisation and evaporation as well as the nebulizing gas (whose flow rate and temperature needs to be optimized) to evaporate the solvent for ions to be detected and quantified [57]. The sheath gas needs to also be optimized in order to maintain the spray and flow of the sheath liquid through a continuous channel, ensuring the ionized particles reach the detector.

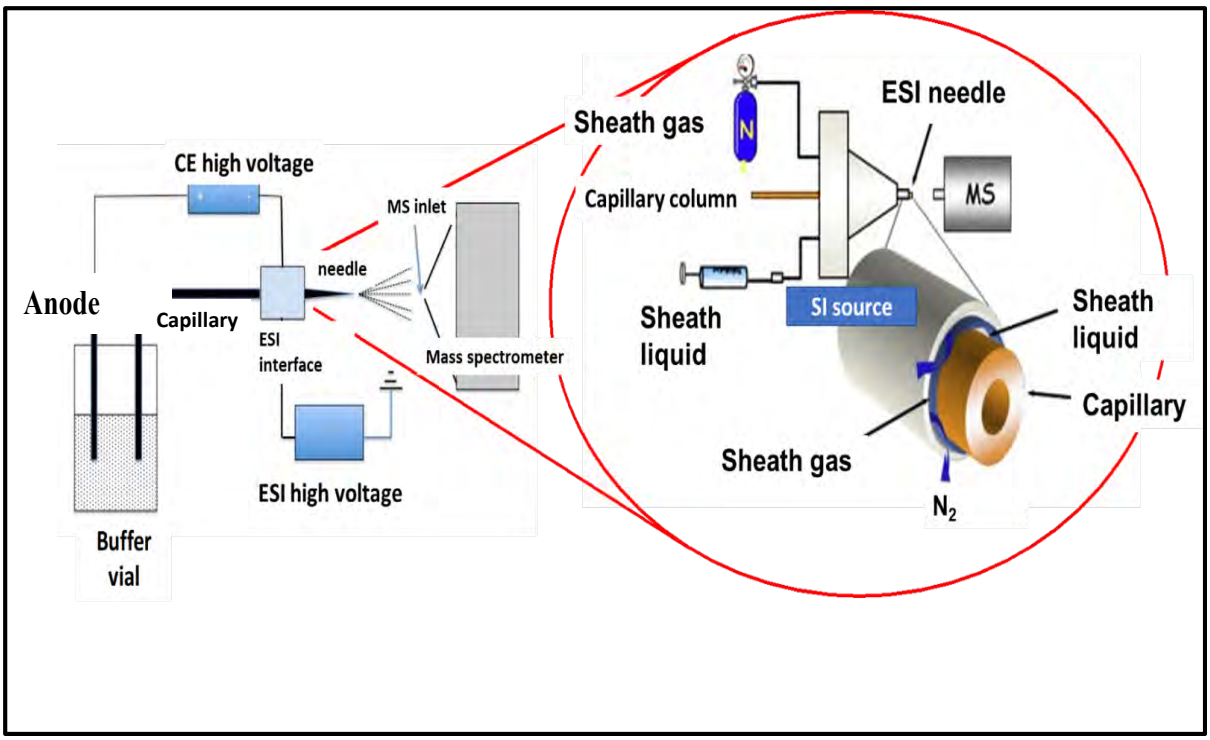

Figure 1.6: Schematic of CE-ESI-MS interface.

1.2.3 General applications of GQDs, NGQDs and gCNQDs

GQDs have been used alone and in combination with other molecules in various fields of study such as bio-imaging [58], photo catalysis [59], photo detection [60], electrochemiluminescence [61], optical sensors [62] and photovoltaic devices [63]. This is owing to their good fluorescence properties. However, GQDs have also become popular in electrocatalysis due to their high stability, high surface area and good charge transfer capabilities [64]. These characteristics have been found to enhance current output which in turn, enhances the performance of electrochemical sensors, hence their use in this work.

The planar structure of graphene based QDs consisting of delocalized π-electrons of graphene enables strong π-π interactions with other π-conjugated aromatic molecules [65]. The presence of carboxyl and hydroxyl groups on the surface

allows for the covalent attachment, electrostatic interactions and hydrogen bonding with other suitable molecules. The combination of graphene based QDs with biomolecule and macrocycles such as MPcs has resulted in changes in their chemical properties, leading to their use in various applications. In this thesis QDs are combined with the MPc complexes for electrocatalysis. Table 1.1 shows examples of graphene based QDs linked to MPcs for sensing [30, 66-70]. As can be seen, a few examples exist where MPcs have been conjugated to graphene-based quantum dots for sensing in general. However, no work has been shown where these nanoconjugates have been used in the fabrication of biomarker detection and is therefore shown herein, for the first time.

Table 1.1: Graphene based quantum dots linked to MPcs for sensing.

Nanoconjugate	QDs-MPc interaction	Application	Reference
NGQDs-CoPc	π-π stacking and covalent linking	Electrochemical sensing of hydrazine	[30]
GQDs-ionic liquid-CoPc	π-π stacking	Electrochemical sensing of glucose	[66]
GQDs-CoPc	π-π stacking	NO_2 gas sensing	[67]
GQDs/SNGQDs-ZnPc	π-π stacking	Optical sensing of ascorbic acid	[68]
GQDs-CoPc	π-π stacking	Fluorescence sensing of CN^- ion	[69]
GQDs-ZnPc	π-π stacking	Fluorescence sensing of biothiols	[70]

1.3 Gold nanoparticles (AuNPs)

1.3.1 Synthesis properties and applications

AuNPs are generally obtained by the chemical reduction of gold salt [71]. Among the reported synthetic procedures of AuNPs, electrochemical methods have been used [72-75]. This involves the electrodeposition of the AuNPs onto substrates via the electrochemical reduction of Au salts. This efficient method has been employed in this thesis. AuNPs, like other precious metals, are known to exhibit completely different properties from bulk gold [76]. This means, a larger fraction

of the active atoms is on the surface. The optical and electronic properties of AuNPs can be adjusted by changing their size, shape and surface chemistry. These properties have been exploited for biological and pharmaceutical applications such as sensing, therapeutics, catalysis and drug delivery [77-80].

1.3.2 AuNPs and their conjugates with MPc in electrocatalysis

The good biological compatibility, conducting capability and high surface-to-volume ratio has resulted in the attraction of AuNPs for electrocatalytic studies [81]. AuNPs have been used in electrocatalysis for the improvement of sensitivity and selectivity of fabricated sensors. Peptides, proteins, polymers, small molecules, drugs, carbohydrates and nucleic acids are often used for the functionalization of AuNPs [82-84]. AuNPs-MPc conjugates have been used for the electrocatalysis of various analytes such as nitrite, hydrazine and bisphenol A [85-87], just to name a few. However, MPcs and AuNPs are rarely used in combination for electrochemical sensing of known cancer biomarkers. The AuNPs-MPc nanoconjugates are used in this work for the first time for the electrocatalytic detection of PSA. Moreover, symmetrical MPcs are commonly used in these rare cases, so the role of symmetry of MPcs is not considered or studied. This work will also highlight the effects the structural makeup of the nanocomposites reported herein have on the efficient functioning of the fabricated aptasensors. Table 1.2 shows examples of MPcs, QDs or AuNPs and their conjugates with other molecules used for the electrocatalytic detection of various biomarkers [88-97]. The list is not exhaustive, thus indicating the room there is to explore these studies further. Moreover, the AuNPs, MPc and QDs are used in conjugation with other molecules and not together as done in this work.

Table 1.2: Examples of MPcs, QDs or AuNPs and their conjugates with other molecules used for the electrocatalytic detection of various biomarkers

Nanostructure/conjugate	Electrode	Target biomarker	Reference
AuPd-ANPs/GQDs/ACF	Microchip	H_2O_2 (Breast cancer)	[88]
Au/fGQDs	Au electrode	Cardiac troponin I	[89]
GQDs-AuNPs	SPGE	Cardiac troponin I	[90]
GQD/AuNP/NG	GCE	CEA	[91]
CuPc	SPGE	ACP	[92]
$Ti_3C_2T_x$MXenes@FePcQDs-cDNA	Au electrode	MicroRNA-155	[93]
Zn-PcTCa-antibody	ITO	KLK4	[94]
N-G/FePc/Nafion/PLL	ITO	NO	[95]
Cr-MOF@CoPc-Aptamer	Au electrode	CT26	[96]
Ab1/AuNPs/PEDOT:PSS	GCE	p53 protein	[97]

Abbreviations: AuPd-ANPs/GQDs/ACF (gold-palladium alloy nanoparticles/ graphene quantum dots/ activated carbon fibres), Au/fGQDs (functionalized graphene quantum dots), SPGE (screen printed gold electrodes), GQD/AuNP/NG (graphene quantum dots/ gold nanoparticles/ nitrogen doped graphene), CEA (carcinoembryonic antigen), ACP (Acid phosphatase), CuPc (copper phthalocyanine), $Ti_3C_2T_x$MXenes@FePcQDs-cDNA (iron phthalocyanine quantum dots-complementary DNA), Zn-PcTCa (zinc(II) phthalocyanine tetracarboxylic acid), ITO (Indium tin oxide), KLK4 (kallikrein-related peptidase 4), N-G/FePc/Nafion/PLL (nitrogen doped graphene/iron phthalocyanine/nafion/poly-L-lysine), NO (nitric oxide), Cr-MOF@CoPc-Aptamer (Chromium metal organic framework@cobalt phthalocyanine-aptamer), CT26 (colorectal cancer cells), Ab1/AuNPs/PEDOT:PSS (Antibody/gold nanoparticles/polymers poly (3, 4-ethylenedioxythiophene): polystyrene sulfonate).

1.4 Overview of aptamers

1.4.1 Discovery and development

Aptamers are acid nucleotides which are identified as short, single-stranded dinucleoribonucleic acid (ssDNA) or ribonucleic acid (RNA) [98, 99]. They are highly selective and specific to a target analyte to which they bind. Aptamers are generated or synthesized through a molecular evolution process or more formally, through the systematic evolution of ligands by exponential enrichment (SELEX) [99-103]. SELEX works by enriching high affinity ligands from randomly selected nucleotides. The binding molecules are subjected to rounds of grammatical rules that are applied repeatedly, increasing the high affinity species in the system until the desired aptamer dominates within the randomly selected species [99-103].

1.4.2 Aptamers as biorecognition elements in biosensing

Aptamers are able to distinguish between closely related molecules such as conformational isomers, targeted molecules possessing different functional groups as well as the mutation of amino acids, which makes them even more interesting molecules to look into [99]. Moreover, using aptamers is more advantageous than using antibodies. Antibodies are proteins that circulate in the blood, which can recognize foreign substances called antigens, and they neutralize them by binding to them, Fig. 1.7. Aptamers work in a similar way and are synthesized to bind to a specific antigen which allows them to be suitable for example, to detect multiple targets and produce little to no batch-to-batch variation. The immobilized aptamer undergoes a conformational change upon PSA binding such that the double stranded DNA is formed with simultaneous binding to (and covering with) PSA [104].

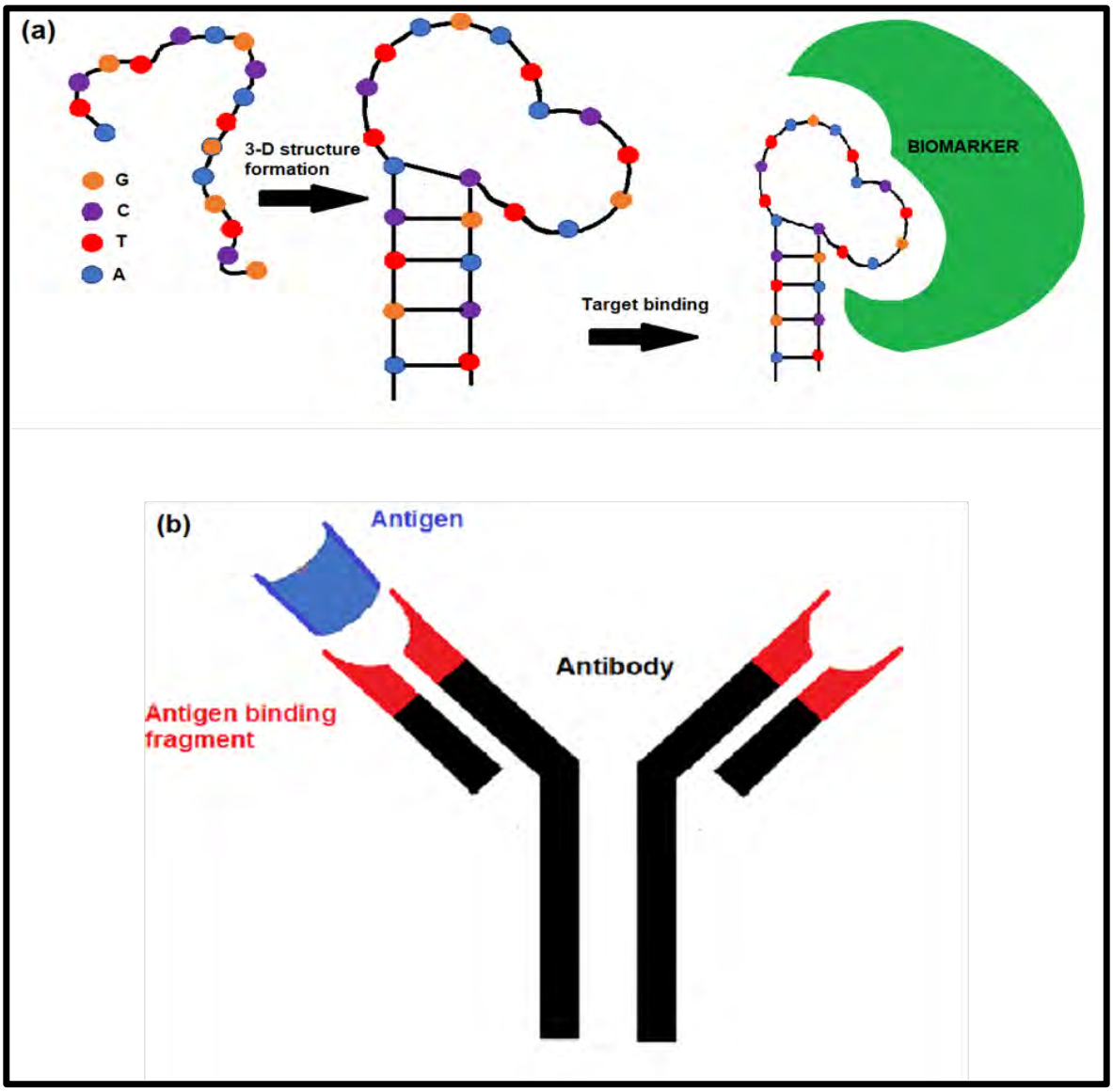

Figure 1.7: Schematic representation of binding of (a) aptamer and (b) antibody to biomarker or target.

1.4.3 Aptamers as bioconjugates for sensing

Aptamers are known to work better upon conjugation with nanocarriers [104-109], which implies that they are also modifiable in order to increase their already high selectivity and specificity. Table 1.3 [110-114] summarizes various aptamer-nanostructure conjugates used as biological sensors, as well as the advantages of these conjugates. Some of the improvements that have been observed regarding

the use of aptamers and nanocarriers in combination are increased sensitivity and selectivity. Reproducibility is also crucial so that accurate results are reported, which some of these conjugates clearly show. It can be seen though, that the list of aptamer conjugates with graphene based QDs is not exhaustive, especially when it comes to the electrochemical detection of biomarkers such as PSA. It is evident from Table 1.3 that no conjugates of QDs with MPcs have been used for aptasensing and therefore it is reported in this thesis for the first time, introducing another novel aspect.

Table 1.3: Aptamer-QDs conjugates for sensing.

Conjugate	Analyte	Advantages	Reference
Aptamer-GQD-Peg-Porphyrin	cancer-related miRNA detection	• good capability of identifying specifically cancer cells rather than somatic cells • good cancer-related miRNA detection	[110]
Aptamer-rGQDs/GO	Lead detection	• good biocompatibility • resistance to photo bleaching • controllable fluorescence turn-on process • high sensitivity and good reproducibility low detection limit	[111]
gCNQDs-CdSe-Aptamer	tetracycline (TET)	• high selectivity • good reproducibility • high stability	[112]
QD-Aptamer	Cocaine	• highly selective quenching of the photoluminescence when QD-aptamer conjugate binds to target	[113]
QD-Aptamer	Doxorubicin (Dox)	• sensitivity, • selectivity, • specificity for cancer imaging, therapy and sensing in vitro	[114]

Abbreviations: Polyethylene glycol (Peg), graphene oxide (GO), microRNA (mRNA), cadmium selenide (CdSe)

1.5 Target analyte used in this work

The main analyte of interest in the work reported herein is PSA. However, in the development of the electroactive nanocomposites and proving that their synergistic effects results in the enhancement of current output, L-cysteine was used as a test analyte. Moreover, this test analyte would later be used to prove selectivity of our aptasensor towards the electrocatalytic detection of PSA.

1.5.1 L-cysteine

L-cysteine is known as an important amino acid that is needed by the human body for tissue growth and repair and the importance of monitoring the levels of L-cysteine in the body has been reported in literature [115]. L-cysteine is one of the important components found in hair, nails and skin cells thus being able to monitor the levels of L-cysteine is essential [115]. L-cysteine has been detected in the presence of MPcs [24] but it is reported for the first time in this thesis, the detection of this analyte using Pcs with GQDs and its derivatives.

1.5.2 PSA

Prostate specific antigen is a biomarker directly linked to prostate cancer [116]. Besides its production in cancerous cells, it can be produced in healthy cells too. However, it has been reported that the leakage volume of PSA from the prostate into the circulatory system increases with the occurrence of prostate cancer [117]. The reported concentration levels of PSA in healthy males, ranges from 0 to 4 $ng.mL^{-1}$ in serum [118], therefore the knowledge of acceptable PSA concentration levels in human serum, using PSA as a biomarker for the diagnosis for prostate cancer has become of great importance.

Early diagnosis of cancers is crucial to avoid costly medical treatment for patients and prevent premature deaths in males. Some diagnostic tools used for PSA detection are summarized in Table 1.4 which includes ELISA, fluorescence and electrochemical immunoassays, chemiluminescence, SPR, SERS and PCR tests [119-131]. These methods allow for the detection of multiple samples at a time and are considered reliable, but they are very expensive and require expensive methods that can only be operated by skilled persons. Electrochemical aptasensors have the least drawbacks and are simple, efficient and can be used anywhere at any given moment. For this reason, the research reported in this thesis involves the fabrication of electrochemical aptasensors as a means to contribute to ongoing research that will allow better access to such medical resources, as well as point-of-care diagnosis preventing extended waiting periods before one can be certain of their health condition. The combination of Pcs with QDs, AuNPs and an aptamer is shown for the first time in this thesis for sensing with the aims of improving the stability, efficiency and overall functionality of the sensor.

Table 1.4: Comparative table PSA detection using electrochemical aptasensors and other reported methods.

Detection method	Advantages	Disadvantages	Reference(s)
ELISA	High throughput Very low detection limits Reliable results	Expensive, complex technologies Large sample volumes required Time consuming &Uses antibodies	[119, 120]
Fluorescence immunoassay	Sensitive and selective Low detection limits can be achieved	quenched fluorescence & Limited scope of practical application	[121, 122]
Electrochemical immunoassay	Can detect analyte in dense samples Low detection limits	Lacks linearity and reproducibility	[123, 124]
CL	Low background signal & High sensitivity	High cost	[125]
SPR	Simple, Efficient, Specific and sensitive	Easily fouled & Poor selectivity in complex mixtures	[126,127]
PCR	Sensitive & Identifies tumour-specific mRNA	Can give false negative results & poor reproducibility	[128]

		of analysis	
SERS	High specificity Low detection limits	Tend to be complex and uses expensive instrumentation	[129, 130]
Chromatography (2D Gel electrophoresis)	Separates different forms of the protein. fPSA/tPSA ratio determines occurrence of PCa Low detection limits	Requires large sample volumes Narrow dynamic range for detection Multi-step protocol	[124]
Electrochemical aptasensor	High selectivity, specificity and stability Low detection limits, efficient and user friendly, Low cost & Point-of-care diagnosis	Method not suitable for follow up after clinical treatment	[124, 131]

Abbreviations: ELISA (enzyme-linked immunosorbent assay), CL (chemiluminescence), SPR (Surface plasmon resonance), PCR (polymerase chain reaction), SERS (surface-enhanced Raman scattering)

Prostate cancer screening using the Digital Rectal Examination (DRE) and PSA blood tests have been reported recently [132]. Although other tools of prostate cancer diagnosis have been developed, the monitoring of PSA concentration levels is still considered necessary as a complementary method of prostate cancer diagnosis [133]. A number of aptasensors have been fabricated for the electrochemical detection of PSA and some have shown very low detection limits [134, 135]. However, the methods of fabrication used are time consuming and quite complicated compared to the procedures developed herein. The electrochemical detection of PSA involving MPcs and QDs has also been reported in the presence of antibodies and not aptamers [136, 137]. Moreover, the studies where phthalocyanines or GQDs are used are based on enzymatic detection and not direct detection of PSA. The examples shown in Table 1.5 [136-140] also look at other detection methods other than electrochemical ones. As can be seen, graphene based QDs and MPcs, especially in combination, are not commonly used for PSA detection. Moreover, the electrochemical detection of PSA using QDs-MPc conjugates is uncommon in literature and explored more deeply in this thesis. AuNPs have never been linked to MPcs for PSA detection as well. Click chemistry is also a new approach to sensor fabrication in this particular application. MPcs on their own with aptamers have not been employed for electrochemical detection of PSA (Table 1.6) [134, 141-146].

Table 1.5: PSA detection using Pcs, AuNPs or QDs with other molecules (no aptamer).

Electrode	Nanoconjugate/Probe	Detection method	Reference
ITO	G–CdS/CoTAPc-(anti-PSA)antibody	Photoelectrochemical	[136]
GCE	Au/Ag-rGO/Aminated-GQDs/Carboxyl-GQDs-antibody	ECL	[137]
-	g-CNQDs/Pd TPs-PA	Fluorescence	[138]
FTO	rGO-$BiFeO_3$-DNA	Photoelectrochemical	[139]
GCE	Au-CoS/graphene-TB/M-CeO_2/CMC/ILs-Antibody	Electrochemical	[140]

Abbreviations: G–CdS/CoTAPc-(anti-PSA)antibody (graphene-cadmium selenide/cobalt tetraamino phthalocyanine),Au/Ag-rGO/Aminated-GQDs/Carboxyl-GQDs-antibody, ECL(Electrochemiluminescence),Pd TPs-PA (palladium triangular plates-PSA aptamer), FTO (Fluorine-doped tin oxide), rGO-$BiFeO_3$-DNA (reduced graphene oxide- Bismuth ferrite-DNA), Au-CoS/graphene-TB/M-CeO_2/CMC/ILs (gold-cobalt suflide/graphene-toluidine blue/mesoporous-Cerium(V) oxide/carboxymethyl chitosan/ionic liquids-antibody).

Table 1.6: Electrochemical PSA detection using aptamer in combination with porphyrin-type complexes, AuNPs or graphene nanomaterials.

Electrode	Conjugates	Modification method	Reference
PGE	AuNPs@GMCs-Aptamer	Adsorption	[134]
AuE	AuNPs-Aptamer	Self-assembly	[141]
SPCE	Au NPs/C_{60}-CS-IL/MWCNTs-Aptamer	Adsorption and electrochemical deposition	[142]
AuE	MoS_2QDs@g-C_3N_4@CS-AuNPs-Aptamer	Adsorption	[143]
AuE	Au nanospheres-Aptamer	Electrodeposition and self-assembly	[144]
GCE	rGO-MWCNT/AuNPs-aptamer	Adsorption and self-assembly	[145]
GCE	H-Gr/PdNPs-Aptamer	Adsorption	[146]

Abbreviations: AuE (gold electrode), SPCE (screen-printed carbon electrode), AuNPs/C60-CS-IL/MWCNTs (Au nanoparticles/fullerene C_{60}-chitosan-ionic liquid/multiwalled carbon nanotubes), PGE (pyrolytic graphite electrode), AuNPs@GMCs (gold nanoparticles@graphetasizedmesocarbons), MoS_2QDs@g-C_3N_4@CS-AuNPs (Molybdenum sulfide quantum dots-graphitic carbon nitride@chitosan-gold nanoparticles), H-Gr/PdNPs (hemin-functionalized graphene-conjugated palladium nanoparticles)

1.6 Methods of electrode surface modifications

1.6.1 Adsorption by 'drop and dry' modification technique

Physical adsorption involves the interaction between the surface and the molecule without structural changes. In this work, the drop and dry method was employed by dissolving the different modifiers in a suitable solvent and applying a drop of a certain volume on the electrode surface. Herein, all electrode modifications that did not involve electrografting and click chemistry were achieved by adsorption of composites at the electrode surface. Moreover, the aptamer was placed on the electrografted and clicked surfaces using the drop-and dry method.

1.6.2 Electrodeposition & self-assembly

Using electrodeposition and self-assembly as a method of electrode modification has its advantages such as low cost, high growth rate at room temperature, reproducibility, environmental friendliness and easier control of size and shape. Electrodeposition was used to synthesize and immobilize AuNPs at the GCE surface. Thereafter, the electrode was immersed in an aptamer solution to induce self-assembly as N is known to have an affinity for Au [147]. The electrode fabricated using this technique is illustrated in Fig. 1.8. Using Au surfaces for the immobilization of aptamer has been reported [141, 144,145]. This work has taken the study further by combining AuNPs and an MPc for the first time towards the fabrication of a PSA aptasensor to study their synergistic effects towards the electrocatalytic detection of PSA.

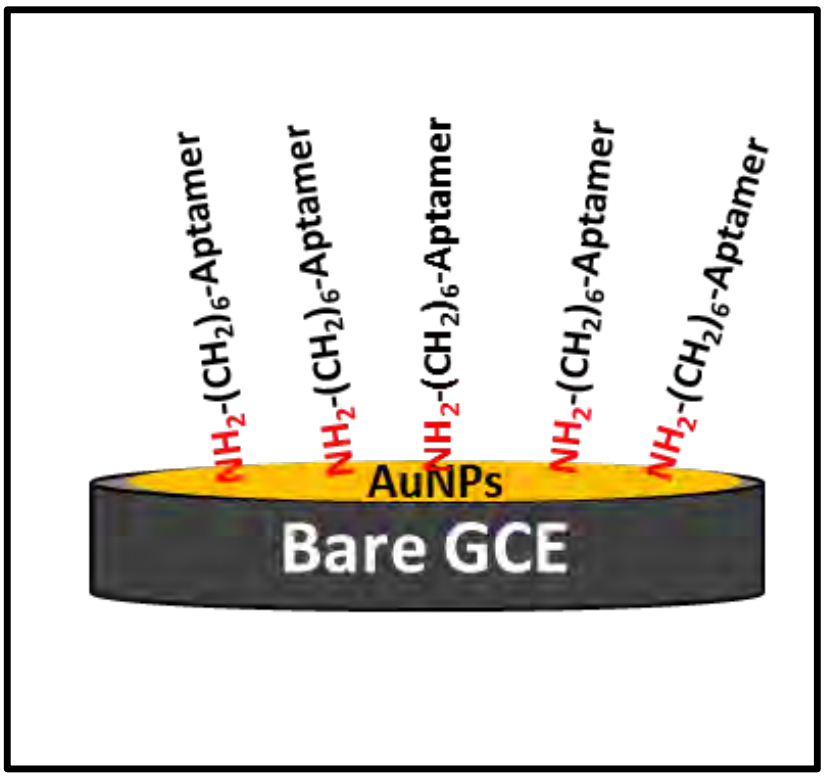

Figure 1.8: AuNPs-modified GCE with self-assembled amine-terminated aptamer molecules.

1.6.3 Electrochemical grafting by reduction and 'click' reaction

Reducing phenyl azide or phenyl acetylene diazonium salts by electrochemical methods results in the grafting of azido or ethynyl groups onto electrode surfaces [148]. Grafting involves the immobilization of molecules at the electrode surface via covalent linkage. It is achieved by electrochemical reduction of compounds in solution forming radicals which simultaneously form covalent bonds between the electrode surface and the reduced molecule. Herein, electrografting of 4-azidobenzenediazonium salt is used to obtain terminated azide groups on a glassy carbon electrode for these groups to react with the terminal alkyne groups of Complex 2. Figure 1.9 illustrates the reaction that occurs on the electrode surface during electrografting using the diazonium salt. Although the number of phenyl

azide groups on the electrode surface is unknown, attachment of molecules by covalent bonding increases the stability of the sensor which promotes the reproducibility of the electrocatalyst.

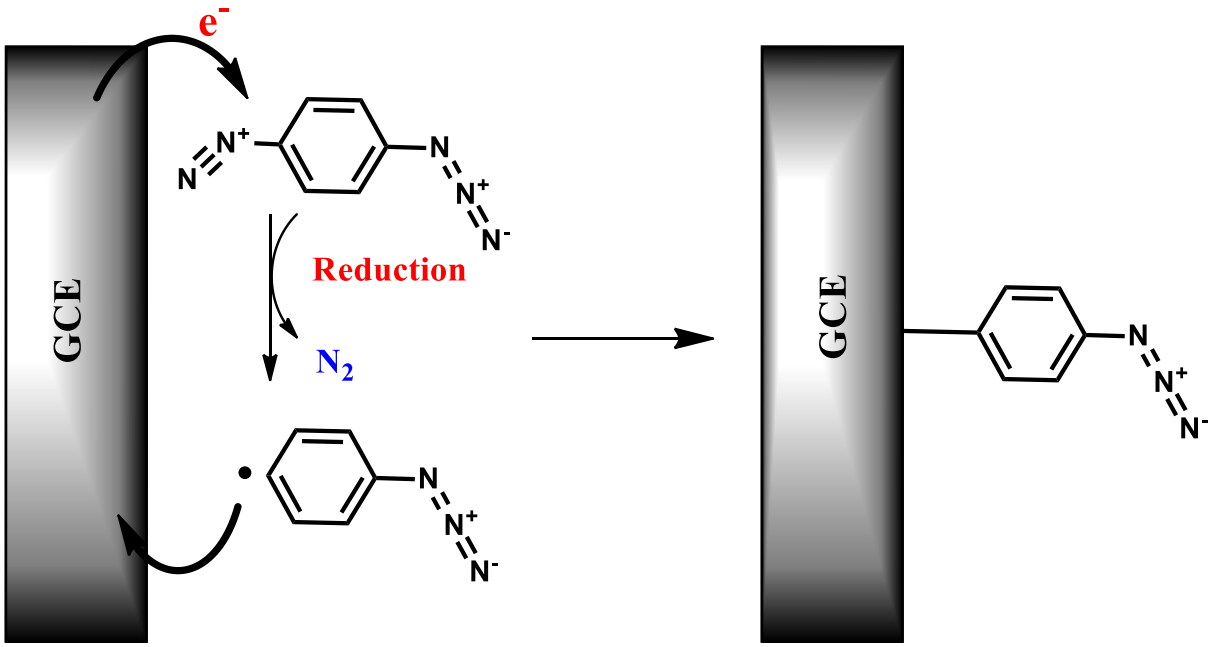

Figure 1.9: Approach to attachment of phenyl azide groups onto a GCE by electrochemical reduction.

The Sharpless Cu(I) catalyzed click reaction [149] is a useful and convenient method as it can be carried out at room temperature and does not require inert conditions, while forming strong covalent bonds with other molecules. Fig.1.10 illustrates the process of how the reaction takes place, where the copper temporarily coordinates with the terminal alkyne group displacing a ligand, followed by the azide group displacing another ligand and in turn coordinating with the copper. Thereafter ring contraction takes place, forming a 1,2,3-triazole ring which is then completed by protonolysis. Initially the copper that is used is in

its2^{+}state and therefore a reducing agent is used to form Cu(I). Fig. 1.11, thus illustrates the click reaction on a GCE which was done in this work. It is important to note that this is not the true representation of the electrode surface since the reaction may occur with more than one immobilized phenyl azide group.

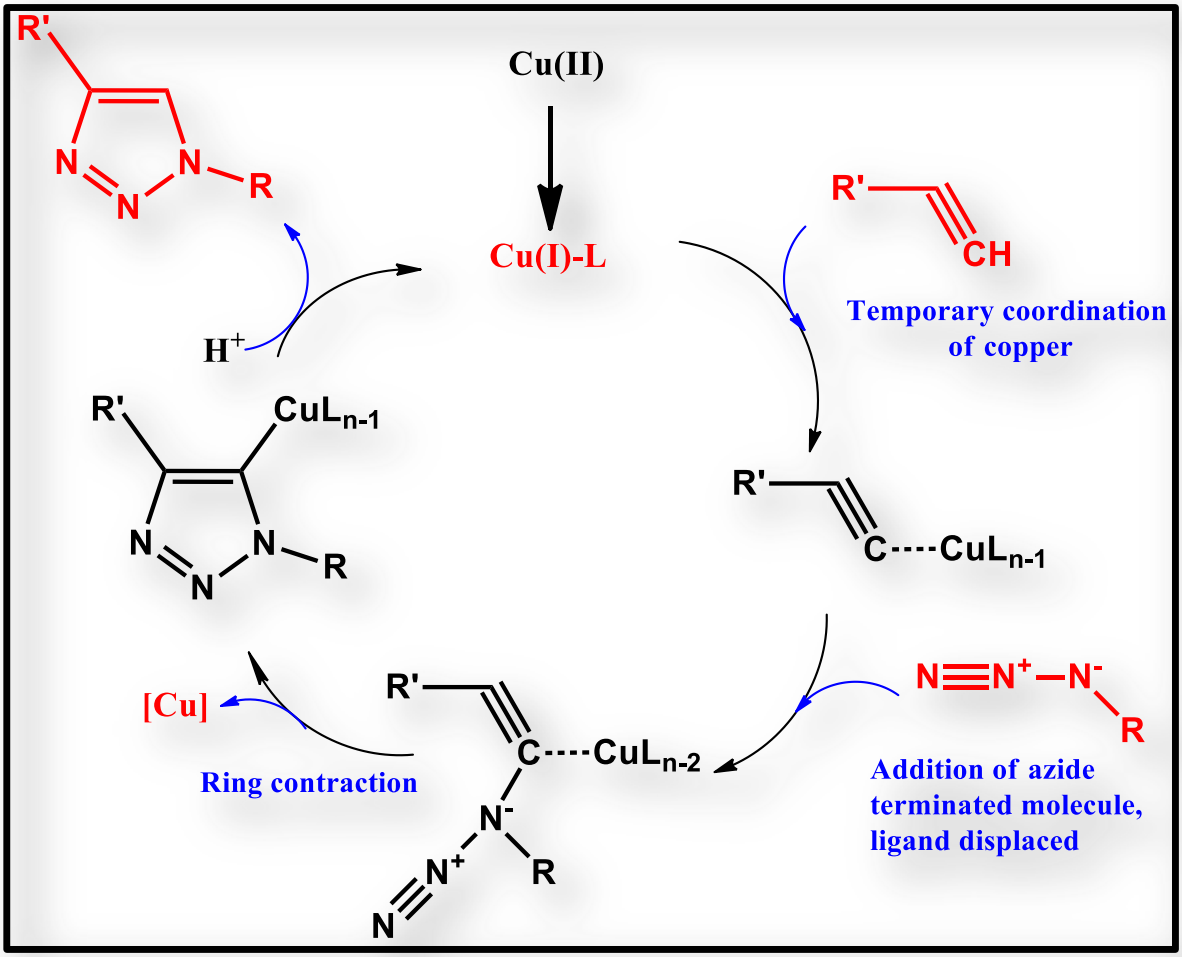

Figure 1.10: Basic illustration of Cu(I)-catalyzed Huisgen 1,3 dipolar cycloaddition. R= functional group, L= ligand.

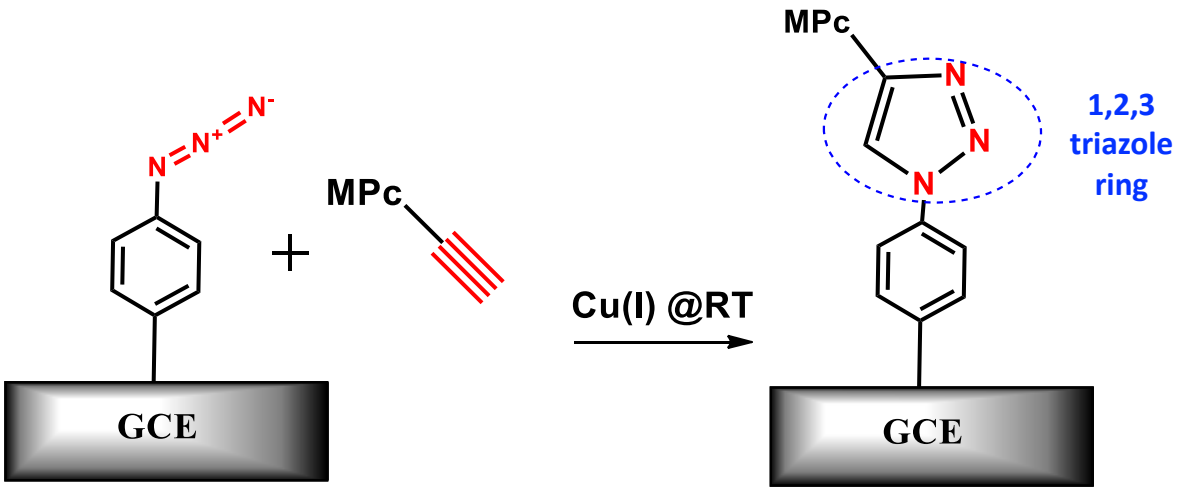

Figure 1.11: Click reaction between terminal alkyne groups of an MPc and phenyl azide groups immobilized on a GCE.

Click chemistry is used in this work to immobilize an alkyl terminated MPc onto a GCE or a GCE with AuNPs electrodeposited on the surface. Once the MPc is immobilized, the aptamer is dropped and dried on the fabricated electrodes to finally obtain the aptasensors. The electrodes are further compared to prove that the use of MPcs and AuNPs together results in the improved performance as PSA aptasensor modifiers.

Table 1.7 [150-154] illustrates the alkyne terminate phthalocyanine molecules used for electrode surface modification via click chemistry. As can be seen, this technique has rarely been used for electrode surface modification and never been used for the fabrication of PSA aptasensors leaving room to further explore its usefulness in sensor fabrication for the electrochemical detection of biomarkers.

Table 1.7: Terminal alkyne functionalized MPcs used for electrode surface modification via click chemistry

Alkynyl MPc	Analyte	reference
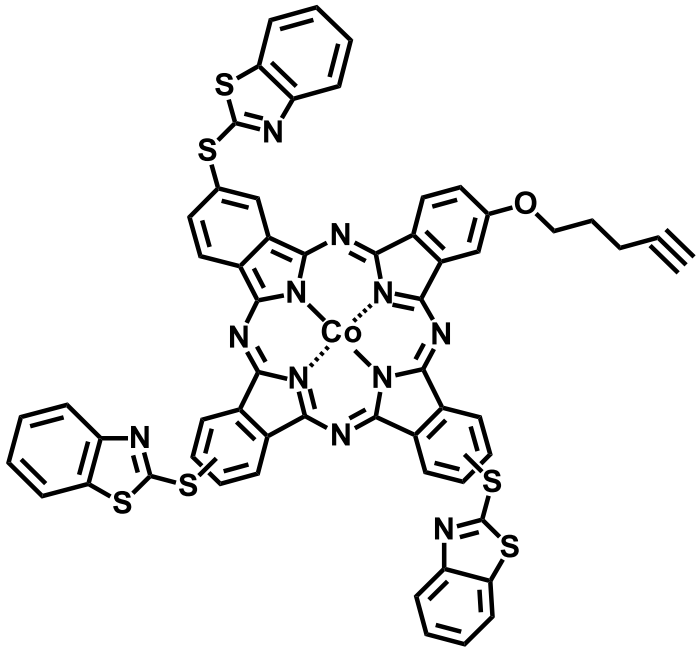	Heavy metals	[150]
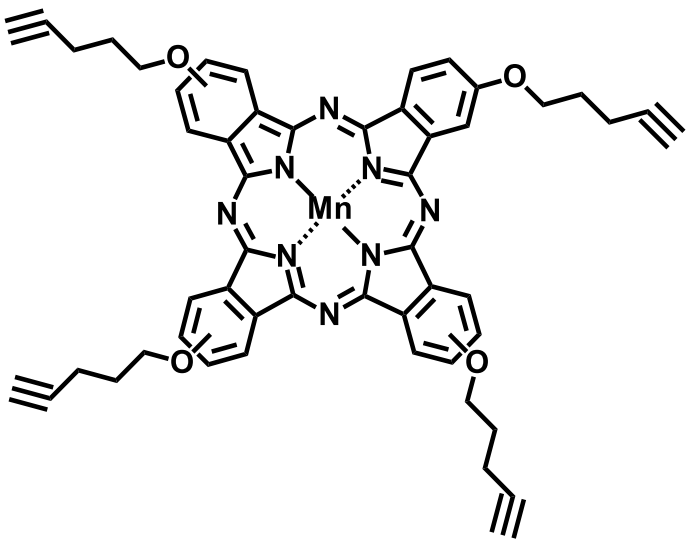	Pesticides	[151]

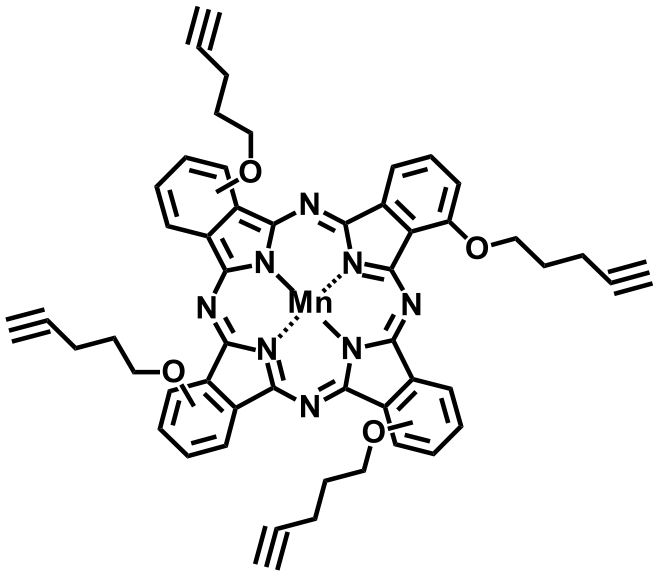	Oxygen reduction	[152]
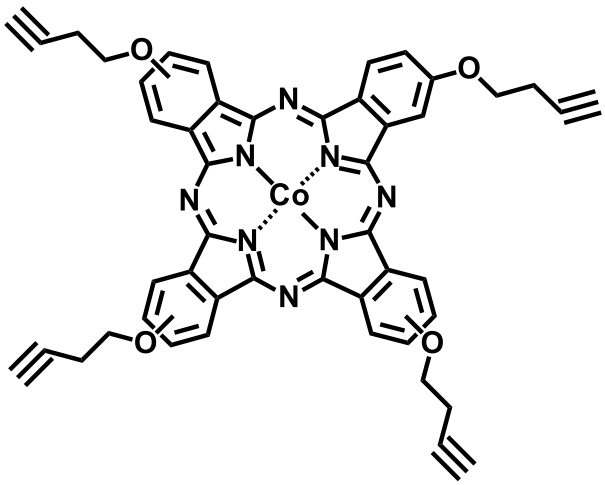	Tested in various electrolyte systems	[153]
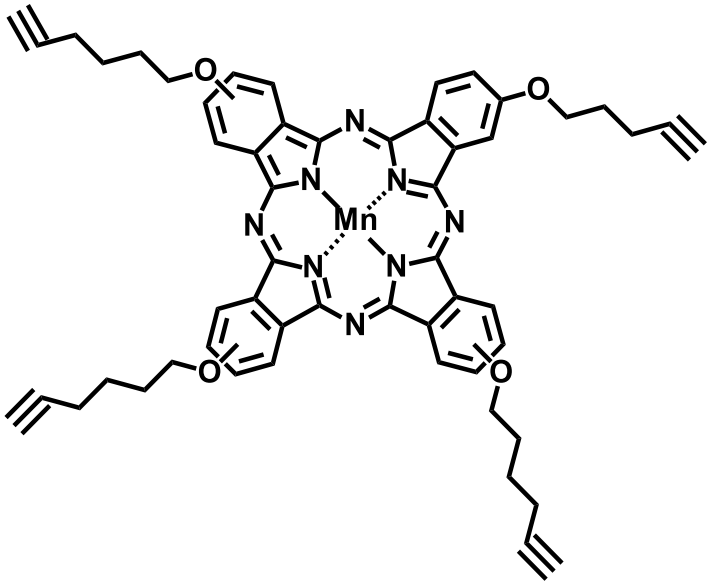	Hydrazine	[154]

1.7 Summary of aims of this thesis

The general aims of the research conducted and reported in this thesis is to fabricate and develop efficient, low-cost, simple and stable diagnostic tools for prostate cancer, which will yield low detection limits with high specificity and selectivity. All modifiers and electrode surfaces modified were characterized fully prior to using them for sensing. Moreover, the feasibility and reliability of the fabricated aptasensors will be determined by testing the sensors in spike serum samples. The aims of the thesis are therefore as follows:

1. Synergistic effects of Complex (1)-quantum dots nanoconjugates:

L-cysteine is used as test analyte to validate the effectiveness of using GQDs, NGQDs and gCNQDs in combination with complex 1, as signal amplifiers and stable platforms prior to using them to fabricate aptasensors.

2. Aptasensing capabilities of complex (1)-quantum dots nanoconjugates in combination with aptamer:

GQDs are used as a base point to test different combinations of the conjugates with aptamer and MPc to suite the application. The combined nanostructures are immobilized on glassy carbon electrodes using the drop-and-dry method. The best performing electrode will be used to do a comparative study of the synthesized QDs, where the NGQDs and gCNQDs replace the GQDs, and then their electrocatalytic response studied and compared.

3. Influence of quantum dots composition and structure on aptasensing capabilities-a comparative study:

A comparative study of QDs influence on aptasensing capabilities in terms of structure and composition is conducted once best adsorption combination is determined as outlined in point number 2.

4. Influence of phthalocyanine substitution on aptasensor performance:

The influence of MPc, complexes (1) and (2), on the performance of an aptasensor in terms of substituents is studied and determined.

5. Synergistic effects of complex (2) and Au nanoparticles on aptasensor performance:

Synergistic effects on the aptasensor performance of AuNPs-MPc conjugate via covalent linkage i.e., electrochemical grafting and click chemistry is studied and determined.

6. Verification of feasibility of fabricated sensors in real samples:

In each case where the aptamer is included, the best performing sensor (unless stated otherwise) is testing in spiked serum samples to verify the feasibility and potential to be used in clinical studies.

2. Materials, equipment and experimental

This chapter outlines the materials and equipment used in the work reported. It also outlines the synthesis, conjugation and electrode modification protocols followed.

2.1 Materials

2.1.1 Solvents and general materials

Chloroform and methanol (MeOH) were procured from SAARCHEM. Potassium chloride (KCl) was purchased from MINEMA. Dimethyl sulfoxide (DMSO), ethanol (EtOH), N, N-dimethylformamide (DMF) and acetonitrile (ACN) was purchased from Merck. Tetrahydrofuran (THF) was purchased from EMSURE. Potassium hexacyanoferrate (II) ($K_4[Fe(CN)_6]$), potassium hexacyanoferrate (III) ($K_3[Fe(CN)_6]$) and ethylenediaminotetraacetic acid (EDTA) were purchased from Sigma Aldrich. Ultra-pure water was obtained from a Milli-Q Water system (Millipore Corp. Bedford, MA, USA).

2.1.2 Synthesis of MPcs and conjugates

N-hydroxysuccinimide (NHS),1-ethyl-3-(3-dimethylaminopropyl)-carbodiimide (EDC), 1,8-diazabicylo[5.4.0]-undec-7-ene (DBU), and cobalt(II) chloride were purchased from Sigma-Aldrich.

2.1.3 Quantum dots

Sodium hydroxide, citric acid, urea, diaminomaleonitrile (DAMN) were purchased from Sigma Aldrich.

2.1.4 Biological samples

Tris-HCl, prostate specific antigen (PSA) and human serum (from male AB clotted whole blood, USA origin, sterile-filtered) were purchased from Aldrich. Magnesium chloride was purchased from SAARCHEM. The amine-functionalized aptamer was synthesized by (and purchased from) Integrated DNA technologies (IDT) and purified using high-performance liquid chromatography and its sequence is listed as

follows: single stranded DNA (ssDNA): 5′-NH_2-$(CH_2)_6$-TTT TTA ATT AAA GCT CGC CAT CAA ATA GCT TT-3′ (235 nmol, >90% purity).

2.1.5 Capillary electrophoresis-mass spectrometry (CE-MS)

Paracetamol, ammonium carbonate, ammonium bicarbonate, ammonium hydroxide, triethylamine (TEA), and formamide (FA) were purchased from Sigma-Aldrich.

2.1.6 Electrode modification

4-Azidoaniline hydrochloride, tetrabutylammonium tetrafluoroborate ($TBABF_4$), gold salt ($HAuCl_4$), sodium nitrate ($NaNO_3$) and bromotris(triphenylphosphine)copper(I)($Cu(PPh_3)_3Br$) were purchased from Aldrich. 4-Azidobenzenediazonium tetrafluoroborate was synthesized from 4-azidoanaline hydrochloride as reported in literature [155].

2.2 Solution preparation

2.2.1 Capillary electrophoresis-mass spectrometry (CE-MS)

The analyte solutions for CE-MS analyses were prepared by dissolving the quantum dots at a concentration of *ca.* 1mg/mL in water. Deionized water was obtained from an Alpha-Q system (Millipore, Saint-Quentin-en-Yvelines, France). The background electrolyte (BGE) was composed of 150 mM ammonium carbonate and 150 mM ammonium bicarbonate, which were mixed and diluted to make a pH 7.4 solution with an ionic strength of 10 mM. Electrolytes were sonicated and filtered through a 0.45 mm polyvinylidene fluoride (PVDF) membrane filters (Pall Life Sciences, MI, USA) before use.

2.2.2 Aptamer

The aptamer solution was prepared in a Tris-EDTA buffer as recommended by supplier as follows: A 100 mL stock solution of pH 8 was prepared in Tris-HCl (1 mL, 1 M) and EDTA (0.2 mL, 0.5 M) and topped up 100 mL. The stock solution was adjusted accordingly to make a 10 mM buffer solution, which was stabilized by adding 10 mM KCl, and 10 mM $MgCl_2$, both had a pH of 8. The solution was stored at 4°C.

2.2.3 Electrocatalytic detection

A phosphate buffer saline (PBS) solution of pH 7.4, 30 mM, was employed in this work. The pH of PBS was adjusted using 0.1 M HCl or NaOH where necessary. $[Fe(CN)_6]^{3-/4-}$ solution (1 mM in 0.1 M KCl) was used for the characterization of the modified electrodes in cyclic voltammetry. The solvent used was deionized water.

2.3 General equipment

- Ground state electronic absorption spectra were recorded on a Shimadzu UV-2550 spectrophotometer in the range of 300-800 nm.
- X-ray powder diffraction (XRD) patterns were recorded on a Bruker D8 discover equipped with a Lynx Eye detector, using Cu-Kα radiation (λ = 1.5405 Å, nickel filter). Data was collected in the range from 2θ = 10 to 100°, scanning at 1 min with a filter time-constant of 2.5s per step and a slit width of 6.0 mm.
- Transmission Electron Microscopy (TEM) images were obtained from a Zeiss Libra TEM 120 model operated at 90 kV.
- Dynamic light scattering (DLS) zeta potential measurements were done on a Malvern zetasizer nanoseries, Nano-ZS90. The assumption of a graphite

structure (carbon) refractive index of 2.417 [156] and a dispersant refractive index of 1.332 with a viscosity of 0.8872 cP was made consistently across all the dispersions. Zeta potentials were measured using a Malvern zetasizer nanoseries, Nano-ZS90.

- Infra-red spectra were collected on a Bruker Alpha model FT-IR Spectrometer with platinum-ATR.
- Raman spectrum was obtained with a Bruker Vertex 70-Ram II spectrometer (equipped with a 1064 nm Nd:YAG laser and liquid nitrogen cooled germanium detector). Solid samples were diluted with KBr.
- Scanning electron microscope (SEM) images were obtained using a JOEL JSM840 scanning electron microscope.
- Energy-dispersive X-ray spectroscopy (EDX) analysis was run using a JEOL JSM 840 scanning electron microscope (SEM)) operating at an accelerating voltage of 20 kV.

- X-ray photoelectron spectroscopy (XPS) analysis for the characterization of covalently linked conjugates was done using an AXIS Ultra DLD (supplied by Kratos Analytical) using Al (monochromatic) anode equipped with a charge neutralizer, the following parameters were used: the emission was 10 mA, the anode (HT) was 15 kV and the operating pressure below 5×10^{-9} Torr. A hybrid lens was used and resolution to acquire scans was at 160 eV pass energy in slot mode. The centre used for the scans was at 520 eV (width of 1205 eV) with steps at 1 eV and dwell time at 100 ms. The high-resolution scans were acquired using 80 eV pass energy in slot mode. The chemically distinct peaks were resolved using a non-linear least squares curve fitting

procedure. The core level binding energies (BEs) were aligned with respect to the C 1 s binding energy (BE) of 284.5 eV.

- Cyclic voltammetry (CV), differential pulse voltammetry (DPV) and chronoamperometric experiments were run using Auto lab potentiostat PGSTAT 302 (Eco Chemie, Utrecht, The Netherlands) driven by the General Purpose Electrochemical System data processing software (GPES, software version 4.9).
- Electrochemical impedance spectroscopy (EIS) experiments were run using an Autolab potentiostat PGSTAT30 equipped with Nova software version 2.1 and measurements were performed between 1 Hz and 10 KHz using a 5 mV rms sinusoidal modulation. EIS was used to measure the changes in capacitance on the substrate surface due to the binding or lack thereof of the PSA.
- Scanning electrochemical microscopy (SECM) experiments were carried out using Uniscan Model 370 equipment and a 15 μm Pt microelectrode (Uniscan) as the tip. SECM approach curves were done using the Pt microelectrode with a Pt counter electrode and Ag|AgCl wire as the pseudo-reference electrode. SECM images were obtained by maintaining the tip at a constant Z position and scanning in the X–Y plane over the desired area (constant-height mode of SECM) and monitoring changes in the steady-state current of $K_3[Fe(CN)_6]$ oxidation at -0.1 V vs. Ag|AgCl (as pseudo reference electrode) as the tip travels. Approach curve analysis and constant height imaging was employed using the 15 μm Pt ultra-microelectrode (UME) together with a Pt counter electrode and Ag/AgCl wire as the pseudo-

reference electrode. For surface imaging, the microelectrode tip was maintained at a constant height (z-axis) and the desired area scanned along the X-Y plane. Changes were monitored in the steady state current of $K_3[Fe(CN)_6]$ oxidation at 0.1 V vs. Ag/AgCl as the tip travels.

- Glassy carbon plates (GCP, Goodfellow, UK) of 1×1cm and 2mm thick were also used as substrates for SECM, SEM and XPS analyses.

2.4 Capillary electrophoresis-mass spectrometry (CE-MS) experiments

The equipment employed for CE-MS experiments is shown in Fig. 2.1.

Figure 2.1: CE-ESI MS instrumentation used for the separation of the QDs synthesized in this work.

2.4.1 CE-UV experiments

CE was performed with an HP^{3D}CE instrument (Agilent Technologies, Massy, France) equipped with a UV absorbance diode array detector (DAD). Separations were achieved using bare fused- silica capillaries (Photonlines, Marly-le-Roi, France) with the following dimensions: 75 mm internal diameter (360 mm outer diameter) 100 cm (26.5 cm effective length). HP^{3D}CE chemstation software was used for instrument control, data acquisition and data handling. Paracetamol (5 mM in the BGE was used as neutral marker to determine electroosmotic flow (EOF). Analytes were hydrodynamically injected (50 mbar, 16 s) and separation voltage was at 20 kV in positive polarity (unless otherwise specified). UV absorption detection at 200 nm is used in this work. Detection is achieved through a 'window' obtained by burning (or scraping) off the polyimide external coating. The high transparency of the fused-silica capillaries wall allows the use of low UV wavelengths. New capillaries were conditioned by successive flushes with water (50 mbar, 300 s), 0.1 M NH_4OH (50 mbar, 300s), water (50 mbar, 300 s) and then the capillary filled with BGE by flushing for 600 s at 50 mbar. The temperature in the capillary cassette was set at 25 °C. The acquisition rate was 10 points/s. Analytes were detected by UV absorbance at 200 nm. Between runs, capillaries were rinsed using the same preconditioning methods. Capillaries were rinsed with 0.1 M NH_4OH and water and dried by air when not in use.

2.4.2 MS detection

An Agilent Series 1100 MSD single quadrupole mass spectrometer (Agilent Technologies) equipped with an orthogonal electrospray ionization (ESI) source was used in the negative ionization mode. The upper mass limit of the instrument was 2000 amu. A coaxial triple-tube ESI-MS interface was used to maintain the connection between the CE and MS systems by providing the necessary sheath liquid and nebulizing gas. In the scan mode, scans were run between m/z = 0-2000 unless stated otherwise. In the analysis of the selected ions in single ion mode (SIM), the selected masses were used with a dwell time of 40 ms on each mass. Nitrogen was used as nebulizing gas at a temperature of 300°C (pressure in the 0 to 100 kPa range) and as drying gas at 300 °C (flow rate in the 0 to 8 L/min range). Optimized ESI voltage was 3000 V. Skimmer voltage was 10 V. Peak width and dwell time were set to 0.3 min and 880 ms, respectively. CE-MS coupling was carried out using a coaxial ESI interface (Agilent Technologies). MS detection of the compounds by direct injection was performed by continuously flushing the sample from the separation capillary to the MS detector under pressure *via* the ESI interface. The sheath liquid (SL) (50:50 v/v MeOH: H_2O mixture containing 0.01% v/v triethylamine) was delivered by an Agilent 1100 series isocratic HPLC pump (flow rate in the 0–10 mL/min range). Some parameters are later optimized for better detection and characterization of the samples.

Prior to introducing the quantum dots samples into the CE-MS (Fig. 2.1) system for analysis, the analytical conditions needed to be optimized. The neutral marker was used as a test sample for all optimizations and introduced by an internal pressure of 50 mbar at the inlet end. The conditions optimized were the nebulizing gas

pressure, electrospray voltage, drying gas flow rate, drying gas temperature, sheath liquid flow rate, applied voltage in CE for separation and effects of changing internal pressure at a constant applied potential. The initial setpoint were varied one parameter at a time while keeping the other parameters constant. The signal to noise ratio was determined to see the effects of these parameters on measurements. Once those conditions were optimized, the samples were introduced into the CE-MS system. The optimized parameters are summarized in Table 2.1.

Table 2.1: Summary of optimized analytical conditions for ESI-MS.

ESI-MS Parameter	Set point
Nebulizing gas pressure	8 psi
Electrospray voltage	3000 V
Capillary-electrospray interface	0.2mm protrusion of capillary
Drying gas flow rate	12 l/min
Drying gas temperature	300°C
Sheath liquid flow rate	6 µl/min

2.5 Synthesis

2.5.1 Complex (1), Scheme 3.2

The syntheses of 2,6-di-*tert*-butyl-4-methylphenoxy phthalonitrile (i) [157] and 4-(4-carboxyphenoxy) phthalonitrile (ii) [158] have been reported in literature. The

synthesis of complex (1) was carried out as follows: phthalonitrile (i) (0.39 g, 1.14 mmol), phthalonitrile (ii) (0.1 g, 0.36 mmol) and $CoCl_2$ (0.178 g, 1.37 mmol) were dissolved in hexanol. DBU was then added, and the mixture was refluxed at 150 °C under inert conditions for 24 h. The product was then dried and subsequently purified by aluminium oxide 90 active neutral packed column chromatography with a gradient eluent mixture of methanol and $CHCl_3$. Since Cobalt is paramagnetic, this complex could not be characterized using nuclear magnetic resonance (NMR) analysis.

Yield: 35 % (w/w); UV-vis ($CHCl_3$): λ_{max}/nm (log ε): 600(3.27), 665(3.05). IR [(KBr)ν_{max}/cm^{-1}]: 1600 (–C–C–), 1470 (–C–H–), 1360 (–C–N–), 1225 (–C–O–C–), 1170 (–C–O–). (Calculated for $C_{84}H_{86}N_8O_6Co$; (C 74.04 H 6.36 N 8.22)%, Found C 74.52 H 7.26 N 8.54) %; MS (MALDI-TOF) (m/z): calcd. for $C_{84}H_{86}N_8O_6$; 1361.60; found: [M]. 1361.34.

2.5.2 Complex (2), Scheme 3.3

The phthalonitriles 4-(hex-5-yn-oxy) phthalonitrile (iii) [159] and *N*-(4-(3,4-dicyanophenoxy)phenyl)acetamide (iv) [160] were also synthesized as reported in literature. The synthesis of complex (2) was carried out as follows: phthalonitrile (iv) (0.40 g, 1.4 mmol), phthalonitrile (iii) (0.065 g, 0.29 mmol) and $CoCl_2$ (0.094 g, 0.72 mmol) were added to dry DMF(15 mL) and DBU (0.5 mL). The mixture was refluxed over a period of 18 h in an argon atmosphere. Following the completion of the reaction, the product was allowed to cool to room temperature after which the crude sample was precipitated using methanol and water and then dried in an oven at 120 °C. The desired compound was separated from the tetra substituted A_4 Pcs (structural isomers) and other impurities using column chromatography with a

gradient eluent mixture of 9:1 tetrahydrofuran: methanol solvent system. This complex was not characterized using NMR for the same reason stated for complex 1. Yield: 0.0394 g, 12.3 % (w/w); UV/vis (DMF): λ_{max}/nm (log ε): 667 (4.86), 608 (4.31), 327 (4.71). IR [(KBr), ν_{max}/cm^{-1}]: 746, 795 (aromatic C-H_{str}), 1087 (C-O-C), 1258 (C-N), 1464 (C=C), 1501 (C-H), 1537 (N-H), 1662 (C=O), 2849, 2916 (aliphatic C-H_{str}), 3273 (C≡C-H). Anal.calc. for $C_{62}H_{45}CoN_{11}O_7.5H_2O$: C, 61.80; H, 4.57; N, 11.46. Found: C 61.70, H, 3.60; N, 10.90. MS (MALDI-TOF) (*m/z*): calc.: 1114.28 amu; found: 1114.34 amu $[M]^+$.

2.5.3 Quantum dots, Scheme 3.1

The synthesis of gCNQDs has been reported in literature [161]. Briefly, diaminomaleonitrile (1 g, 9.25 mmol), EDTA (0.5 g, 1.34 mmol), and NaOH (5 mL of 1 M) were added to 100 mL of millipore water and the mixture stirred for 1 h to ensure complete dispersion of the compounds. The resulting mixture was then transferred to a 400 mL capacity teflon-lined hydrothermal reactor (Fig. 2.2) and was heated at 200 °C for 2, 4, 6 and 8 h. After cooling to room temperature, the resulting brown-green product was filtered through a 0.22 µm cellulose membrane, followed by the addition of ethanol. The product was centrifuged at 15000 rpm for 15 min. The collected solid was re-dispersed in Millipore water and further dialyzed against ultrapure Millipore water for 24 h to get rid of excess starting materials and by-products. The synthesis of GQDs and NGQDs have been reported [162]. Briefly for GQDs, citric acid (4.2 g, 1 mmol) and NaOH (2.4 g, 3 mmol) were dissolved in 100 mL water, and stirred to form a clear solution. Then the solution was transferred into a 400 mL Teflon lined stainless autoclave. The sealed autoclave was heated to 160 °C for 2, 4, 6 and 8 h. The final product was

collected by adding ethanol into the solution and centrifuged at 5000 rpm for 15 min. The solid was re-dispersed into water and was dialyzed for two days using a dialysis membrane (MW 1.5 kDa) to remove excess salts. The NGQDs were prepared as described above for pristine GQDs, using urea (3.6 g, 3 mmol) in place of NaOH.

Fig. 2.2: Berghof high pressure reactor employed for the hydrothermal synthesis of the QDs used in this work.

2.5.4 Conjugation of nanocomposites

The conjugates used in this work are listed in Table 2.2.

Table 2.2: Conjugates used in this work (excluding ones directly conjugated on the electrode surface).

Modifier	Method of conjugation
GQDs-CoPc(1)(ππ)	ππ interactions
NGQDs-CoPc(1)(ππ)	ππ interactions
gCNQDs-CoPc(1)(ππ)	ππ interactions
CoPc(1)@Aptamer	Covalent bonding
GQDs@Aptamer	Covalent bonding
gCNQDs@Aptamer	Covalent bonding
gCNQDs@Aptamer-CoPc(1) (ππ)	Covalent bonding and ππ interactions
gCNQDs@Aptamer-CoPc(2) (ππ)	Covalent bonding and ππ interactions

2.5.4.1 Conjugation of QDs to CoPc(1), Scheme 3.5

Where the nature of the quantum dots used for sensor fabrication was studied, the non-covalent coordination (ππ stacking) between the quantum dots and the CoPc(1) derivative was achieved as follows:

CoPc(1) derivative (10 mg, 0.07 mmol) was dissolved in 2 mL of DMSO, followed by mixing with 5 mg (each) of GQDs, NGQDs, and gCNQDs, in 2 mL of water. The mixtures were then sonicated at room temperature for 1 h. Following that, the mixtures were left to stir at room temperature for 24 h. A mixture of DMSO, water

and ethanol (1:5:3) was used to repeatedly wash the products to try get rid of the excess uncoordinated QDs or CoPc(1). The conjugates are represented as GQDs-CoPc(1) (ππ), NGQDs-CoPc(1) (ππ) and gCNQDs-CoPc(1) (ππ), Table 2.2.

2.5.4.2 Conjugation of aptamer to QDs and CoPc(1), Scheme 3.4

Covalent linking to form an amide bond between COOH functional groups with the NH_2 group of the aptamer, was achieved by carbodiimide coupling chemistry and the method derived from literature reports [163, 164]. The CoPc(1), GQDs and gCNQDs were used as examples therefore NGQDs were not covalently linked to the aptamer. Briefly, for the formation of the amide linkage, the procedure was as follows: of N-hydroxysuccinimide (NHS) (5 mL, 0.02 M) and 1-ethyl-3-(3-dimethylaminopropyl)-carbodiimide (EDC) (5 mL, 0.02 M) each, both prepared in a pH 8 Tris-HCl buffer solution were mixed together and then GQDs/gCNQDs (5 mL, 20 mg/mL) were added to the mixture. These solutions were stirred for 12 h to activate the carboxylic acid groups in preparation for conjugation with the aptamer. After 12 h, aptamer (2 mL, 1.0 μM) was added and the solution further stirred for 24 h, at room temperature, resulting in GQDs@Aptamer and gCNQDs@Aptamer, Table 2.1. For the covalent linkage of CoPc(1) with aptamer, CoPc(1) (5 mL, 0.1 M) was added to the EDC/NHS mixture (same amounts as stated above) followed by the addition of aptamer (2 mL, 1.0 μM) to form CoPc(1)@Aptamer (The '@' symbol represents covalent conjugation).

Ethanol (20 mL) was used to precipitate the conjugates out of solution which were further washed using a DMSO (10mL) and water (50 mL) to remove unreacted QDs and CoPc molecules, resulting in GQDs@Aptamer, gCNQDs@Aptamer and CoPc(1)@Aptamer, Table 2.2.

2.5.4.3 Non-covalent combination of gCNQDs@Aptamer with complex (1) and (2)

The covalently linked gCNQDs@Aptamer was used for the MPc complex comparative study as examples since the ππ-conjugates of the QDs with complex 1 had already been extensively studied in combination with aptamer. The comparison of the MPc complexes in this work is therefore not limited to just the gCNQDs but could also be carried out with the other QDs structures. Where the nature of substituents on the asymmetrical MPcs was compared, the non-covalent coordination of the complexes with gCNQDs@Aptamer was achieved as follows: CoPc (1) (10 mg, 0.07 mmol) and CoPc (2) (10 mg, 0.01 mmol) derivatives were dissolved in 2 mL of DMSO, followed by mixing with 5 mg of the gCNQDs@Aptamer in 2 mL of water. Purification was achieved as described above. The conjugates are represented as gCNQDs@Aptamer-CoPc(1) (ππ) and gCNQDs@Aptamer-CoPc(2) (ππ).

2.6 Electrode modification

A three-electrode system comprising of an Ag|AgCl (3M KCl) as the reference electrode, a platinum (Pt) wire counter electrode and a glassy carbon electrode (GCE) as the working electrode was employed. Prior to modification, the electrode surface was cleaned by means of polishing on a SiC-emery paper in slurry made from alumina nano powder (Sigma-Aldrich) and rinsed with Millipore water several times. In addition, all analytical solutions were purged with argon gas for 20 min to eliminate the dissolved oxygen before each cyclic voltammetry analysis, and the argon atmosphere was maintained throughout the period of analysis to ensure that no disturbances occurred during the analyses due to oxygen.

2.6.1 Drop and dry electrode modification

Each of the conjugates listed in Table 2.2 were used to modify the electrode using the drop and dry method. Experiments where individual components of the conjugates were employed alone or in sequence to modify electrodes, were also conducted. Table 2.3 then lists the modifiers, the solvents they were prepared in and the amounts of modifier used for surface fabrication. 10 µL of each solution was placed on the GCE, followed by drying in the oven at 60°C.

Table 2.3: Summary of amounts of modifiers (2 mg of each) dispersed in different solvents in preparation for electrode surface modification.

Modifier	Solvent	Volume/ mL	Concentration/ mg/mL
QDs	H_2O	2	1
CoPc	DMSO	2	1
Aptamer	Tris-HCl buffer	2	1
GQDs-CoPc(1)($\pi\pi$)	H_2O/DMSO mixture	1	2
NGQDs-CoPc(1)($\pi\pi$)	H_2O/DMSO mixture	1	2
gCNQDs-CoPc(1)($\pi\pi$)	H_2O/DMSO mixture	1	2
CoPc(1)@Aptamer	H_2O/DMSO mixture	1	2
GQDs@Aptamer	H_2O	1	2
gCNQDs@Aptamer	H_2O	1	2
gCNQDs@Aptamer-CoPc(1) ($\pi\pi$)	H_2O/DMSO mixture	1	2
gCNQDs@Aptamer-CoPc(2) ($\pi\pi$)	H_2O/DMSO mixture	1	2

2.6.2 Electrodeposition and self-assembly, Scheme 4.2 (a)

The modification of GCE using gold nanoparticles was achieved by electrodeposition using literature methods [165] as follows: A de-aerated solution of 1 mM $HAuCl_4$ in 0.1 M $NaNO_3$ was cycled at a scan rate of 50 mV/s for 10 scans from 1 V to 0 V. The resulting GCE-AuNPs was then activated using 0.5 M H_2SO_4 by scanning the electrode from 0.2 V to 1.4 V for another 10 scans. The GCE-AuNPs-Aptamer was obtained by immersing the GCE-AuNPs in the aptamer solution (2 mL, 1.0 µM) stirring for 24 h, at room temperature to allow for the self-assembly of the aptamer at the electrode surface forming the N-Au bond [166].

2.6.3 Electrografting and click chemistry, Scheme 4.2 (b, c)

First the bare GCE surface was grafted onto the bare using 4-azidobenzenediazonium tetrafluoroborate (Scheme 4.2(b)) by reductive electrodeposition by scanning three cycles from -1.0 V to 0.2 V at 50 mV/s in a 1 mM solution of the diazonium salt (1 mM in 0.1 M $TBABF_4$ in 96 % ACN: 4 % HCl (0.1M)), following literature methods [167-169] to give the grafted GCE. For the electrode containing AuNPs, the AuNPs were first electrodeposited of the GCE as stated above, followed by grafting azidobenzenediazonium salt onto the AuNPs, to give grafted GCE-AuNPs. The grafted GCEs were then rinsed thoroughly with milli-Q water. The grafted electrodes were then further modified with CoPc(2) using click chemistry as reported in literature [170] by immersing them in 5 mL DMF containing alkynyl CoPc(2) (1 mM), triethylamine (10 mM) and $Cu(PPh_3)_3Br$ (2 mM) for 18 h at room temperature, Scheme 4.2 (b) and (c). The electrodes were thoroughly rinsed using milli-Q water and are represented as GCEØCoPc(2) and GCE-AuNPsØCoPc(2), where Ø represents the clicking step. The GCEØCoPc(2)-

Aptamer and GCE-AuNPsØCoPc(2)-Aptamer were obtained by immobilizing the aptamer on the GCEØCoPc(2) and GCE-AuNPsØCoPc(2) using the drop and dry method (Scheme 4.2 (b) and (c)), using aptamer at 5 µL of 1.0 µM.

2.7 Electrode and solution preparation for detection of PSA

Regarding the detection of PSA using EIS and DPV, the modified electrodes were first incubated for 2 h in a 2 µM PSA solution in 10 mM phosphate buffer solution of pH 7.4 at room temperature after which the impedance measurements were performed. For concentration studies using EIS and DPV, the stock solution was further diluted to produce samples with concentrations ranging from 1.2 to 2.0 pM. The electrodes used for concentration studies were also incubated in each solution prior to EIS and DPV measurements being recorded.

Publications

Publications in peer-reviewed journals from the results presented in this thesis are listed below. These articles are however, not referenced in this thesis.

1. S.R. Nxele, D.O. Oluwole, T. Nyokong, Electrocatalytic activity of a push pull Co(II) phthalocyanine in the presence of graphitic carbon nitride quantum dots, Electrochim. Acta 326 (2019) 134978.

2. S.R. Nxele, T. Nyokong, The electrochemical detection of prostate specific antigen on glassy carbon electrode modified with combinations of graphene quantum dots, cobalt phthalocyanine and an aptamer, J. Inorg. Biochem.(2021) 111462.

3. S.R. Nxele, T. Nyokong, The effects of the composition and structure of quantum dots combined with cobalt phthalocyanine and an aptamer on the electrochemical detection of prostate specific antigen, Dye. Pigment.192 (2021) 109407.

4. S.R. Nxele, T. Nyokong, The composites of asymmetric Co phthalocyanines-graphitic carbon nitride quantum dots-aptamer as specific electrochemical sensors for the detection of prostate specific antigen: Effects of ring substituents. J. Electroanal. Chem. 900 (2021) 115730.

5. S.R. Nxele, T. Nyokong, Time-dependent characterization of pristine and N-doped graphene quantum dots and graphitic carbon nitride quantum dots synthesized by bottom-up hydrothermal methods. Diamond and related materials. Accepted with revisions.

6. S.R. Nxele, T. Nyokong, The synergistic effects of coupling Au nanoparticles with an alkynyl Co(II) phthalocyanine on the detection of prostate specific antigen. Talanta. In press.

3. Characterization

This chapter outlines the characterization of nanomaterials, MPcs and their conjugates employed in this thesis. Schematics of protocols followed are shown for illustration purposes.

3.1 Characterization of GQDs, NGQDs and gCNQDs

The synthesis pathways of the metal-free quantum dots reported herein is shown in Scheme 3.1. These nanostructures were characterized using various techniques, which verified the success of the synthesis as well as their general structure and present functional group.

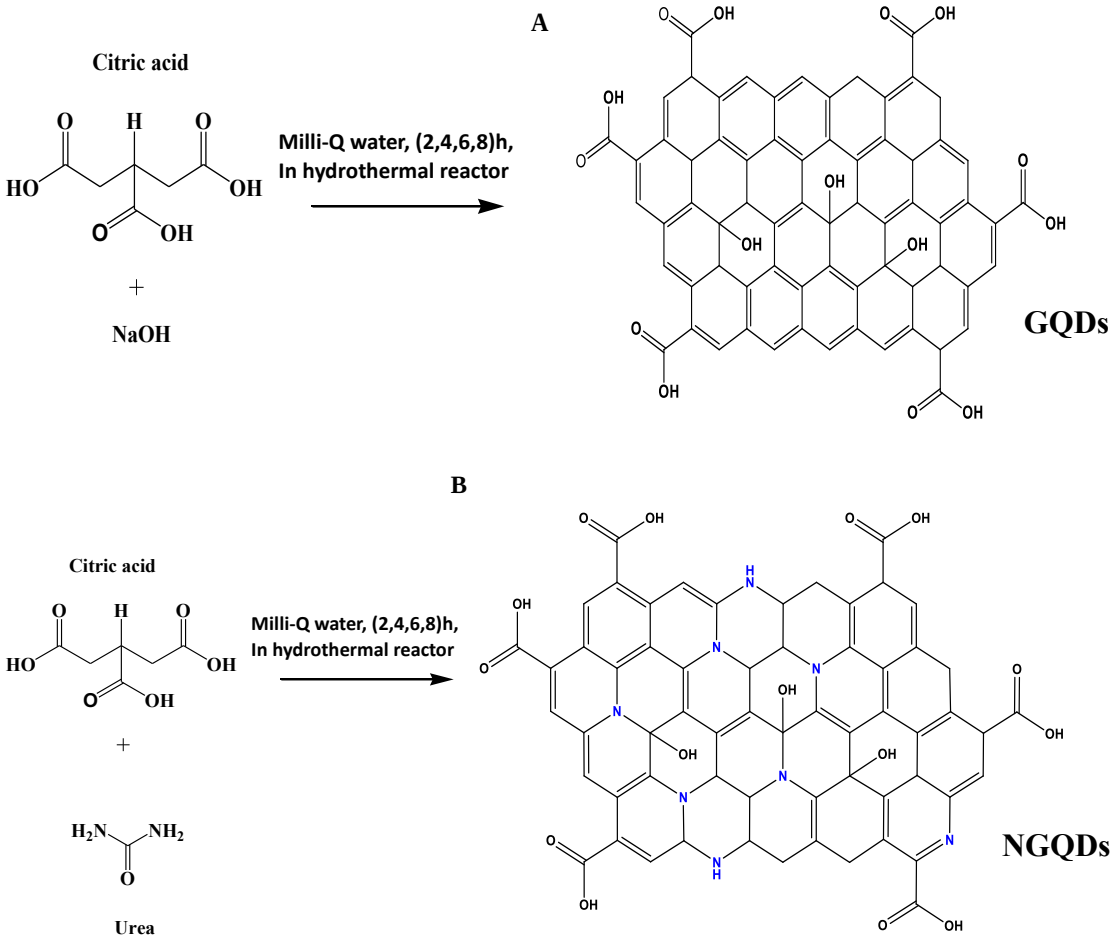

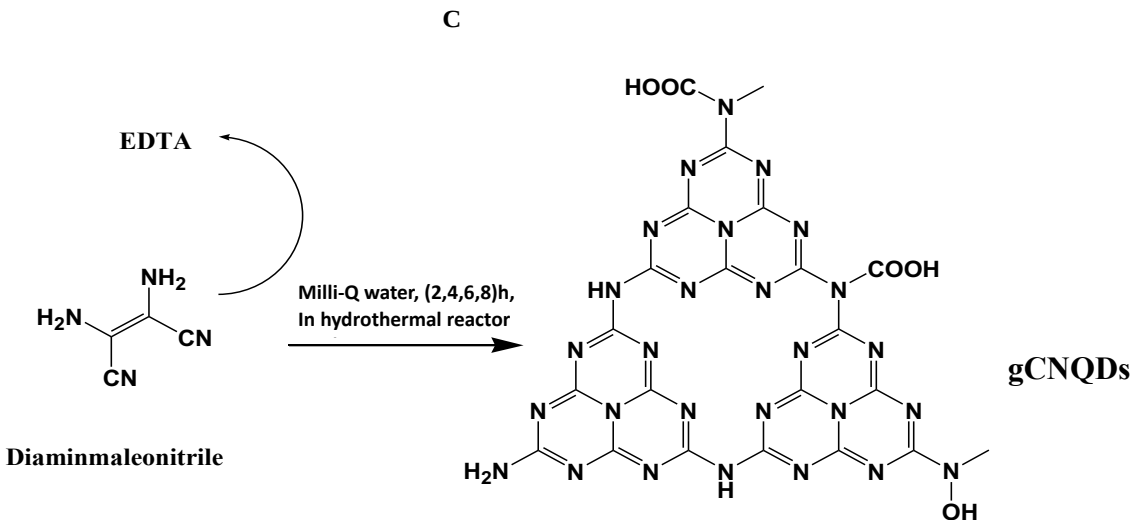

Scheme 3.1: Optimized synthetic route of (A) GQDs (B) NGQDs and (C) gCNQDs and their proposed structures.

3.1.1 Dispersity and size distribution

3.1.1.1 TEM images

TEM images for all QDs samples obtained to get a visual representation of the dispersity of the nanostructures as well as average diameter.

The size of quantum dots can influence their behaviour in different environments and therefore it is important to determine this characteristic [171, 172]. The samples were dispersed in solution (EtOH: H_2O mixture, 50:50 v/v) and then dropped on copper grids where they were left to dry prior to conducting the measurements. The obtained images are shown in Figure 3.1 with their corresponding distribution curve and average diameters.

For the GQDs produced after 2 and 4 h reaction times, a mixture of non-aggregated and aggregated particles were observed, making it difficult to measure the diameters. The distribution curves shown represent non-aggregated particles population. After a 6 h synthesis time, a better dispersity of particles was

observed. The particle sizes did not vary significantly for 2 h, 4 h, 6 h synthesis times, with an average diameter being determined as of 8.4 ± 2 nm, Table 3.1. At a synthesis time of 8 h however, a clear spatial distribution of the GQDs is observed with an average diameter of 4.9 ± 1.6 nm. Upon doping the pristine GQDs with nitrogen atoms (NGQDs), the TEM images obtained show similar spatial distribution across all synthesis times, with minimal aggregation. The average diameters of 6.3 ± 2.4 nm at 2h, 8.3 ± 3.1 nm at 4h, 5.9 ± 2.6 nm at 6 h and 6.0 ± 2.1 nm at 8 h synthesis time were determined, Table 3.1.

The TEM images for gCNQDs showed aggregation of the samples at 2h, 4h and 6 h reaction times. After 8 h synthesis time, there is improved dispersity of the particles with an average diameter of 6.9 ± 1.4 nm, Table 3.1. It is evident that the optimization of the synthesis achieved by changing the synthesis time affected the dispersity and average diameters of the QDs. Determining the best synthesis time of these nanostructures is important in this work, especially when it comes to CE-MS analysis as well as applications.

GQDs


2h

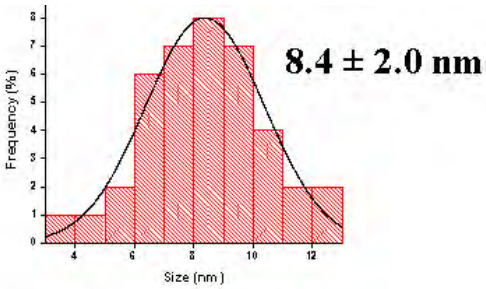
Frequency (%)
Size (nm)
8.4 ± 2.0 nm


4h

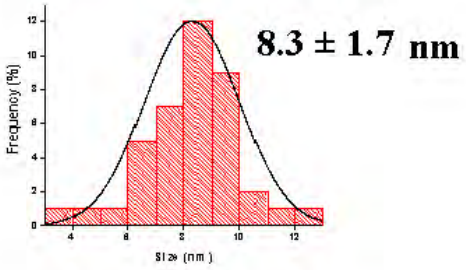
Frequency (%)
Size (nm)
8.3 ± 1.7 nm

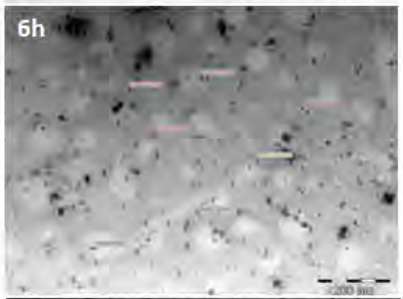
6h

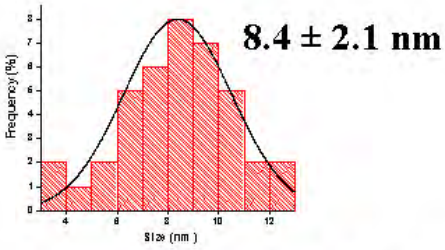
Frequency (%)
Size (nm)
8.4 ± 2.1 nm

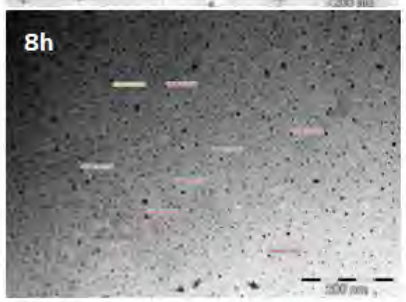
8h

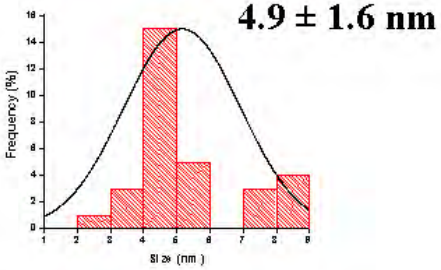
Frequency (%)
Size (nm)
4.9 ± 1.6 nm

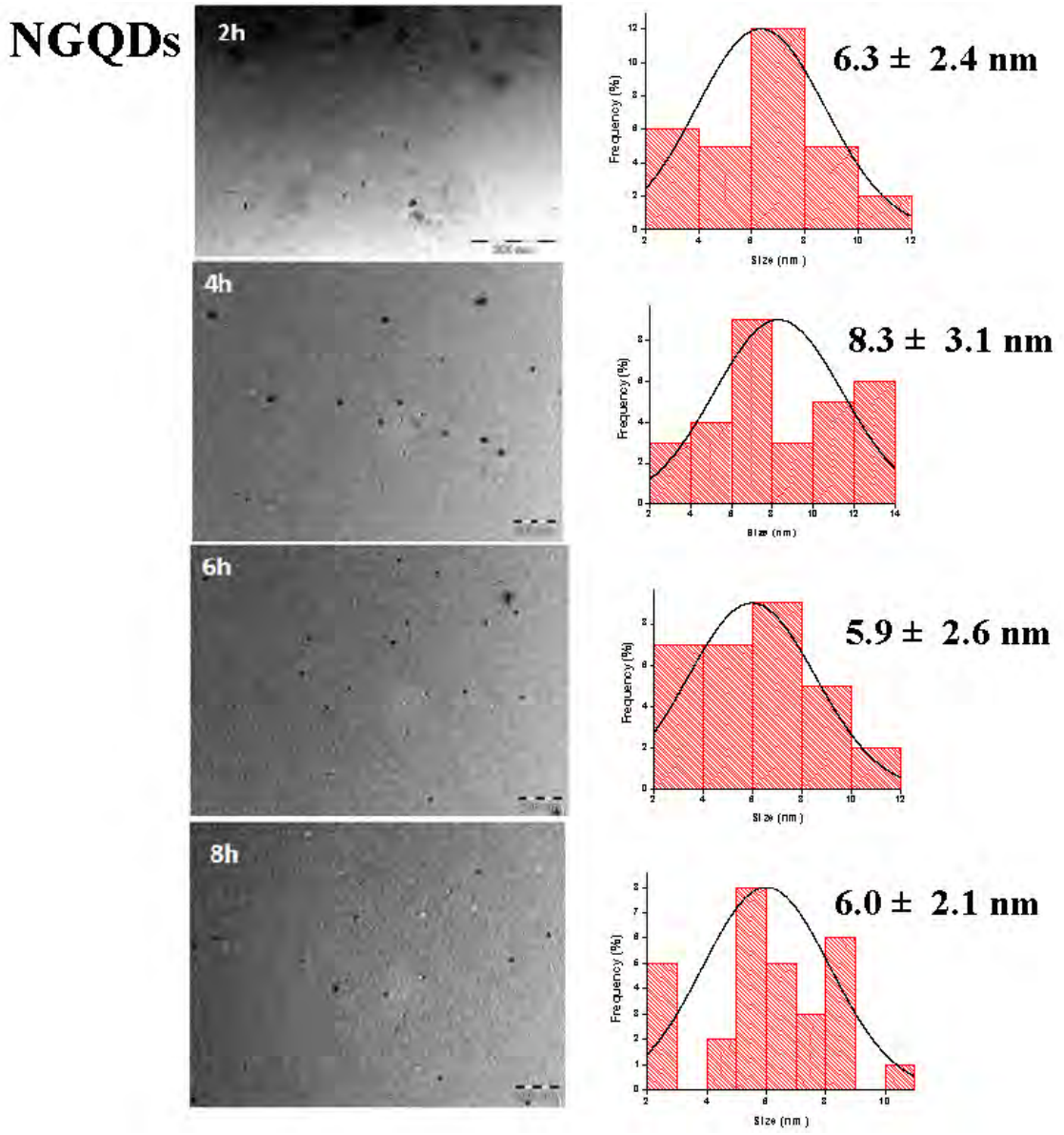
NGQDs
2h
6.3 ± 2.4 nm
Frequency (%)
Size (nm)
4h
8.3 ± 3.1 nm
Frequency (%)
Size (nm)
6h
5.9 ± 2.6 nm
Frequency (%)
Size (nm)
8h
6.0 ± 2.1 nm
Frequency (%)
Size (nm)

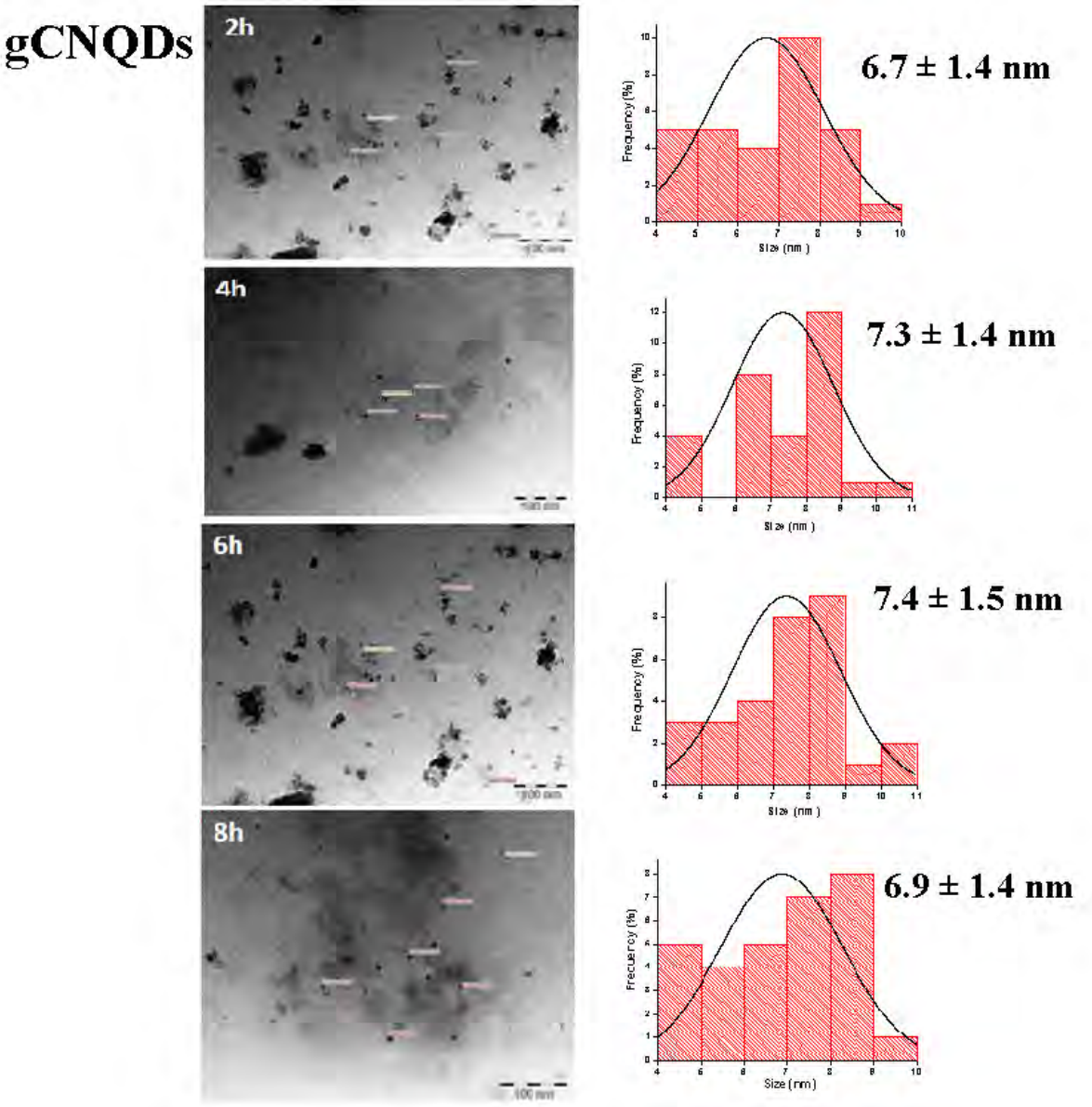

Figure 3.1: TEM images with corresponding distribution curve of GQDs, NGQDs and gCNQDs at different synthesis times. Samples prepared in EtOH: H_2O mixture (50:50) then drop-casted on a copper grid for analysis.

3.1.1.2 DLS

DLS was also employed in order to determine the hydrodynamic size distribution of the synthesized QDs. Contrary to TEM, these experiments are performed in solution, which can help provide the hydrodynamic radius as well as extent of aggregation in solution. As quantum dots are known to be well dispersed in water, each QDs sample was dissolved in water and sonicated to ensure homogeneity in solution. Figure 3.2 shows the DLS plots of each type of QDs samples after 2 h, 4 h, 6 h and 8 h synthesis with the particle sizes as well as the polydispersity index (PDI) values summarized in Table 3.1. The PDI values are determined by the instrument depending on the average sizes measured. The sizes recorded herein are those extracted from the peak maxima. For the GQDs, a decrease in the hydrodynamic radius is observed as the reaction time is increased, as well as a decrease in polydispersity indices, leading to a value close to 0.5 for 8 h, which is in accordance with what was observed in TEM. At 8 h synthesis time, the hydrodynamic radius obtained in DLS and TEM are similar with values of 4.9 nm in DLS and 4.9 ± 1.6 nm in TEM. Moreover, the trend of decreasing size with increasing synthesis time for the GQDs is an indicator of an increase in COOH groups, which when deprotonated create an overall negative charge, leading to repulsion between QDs and reduced aggregation which can be seen in TEM images. The results obtained for the NGQDs showed no significant trend when correlating the reaction times with the particle sizes, which is in agreement with the TEM experiments. The lack in trend may be that there is no control in extent of doping in each batch as QDs are formed. For gCNQDs, the lowest size and PDI are measured after 2 h reaction time. However, the diameter determined using TEM at 2 h synthesis is larger than that obtained from DLS experiments, which is an

indication of possible aggregation. Therefore, the optimization of the synthetic routes by varying the synthesis time did result in changes of size and polydispersity. There was no trend observed for the gCNQDs which may be a result of aggregation within the sample batches, thus creating inconsistencies in the measurements performed.

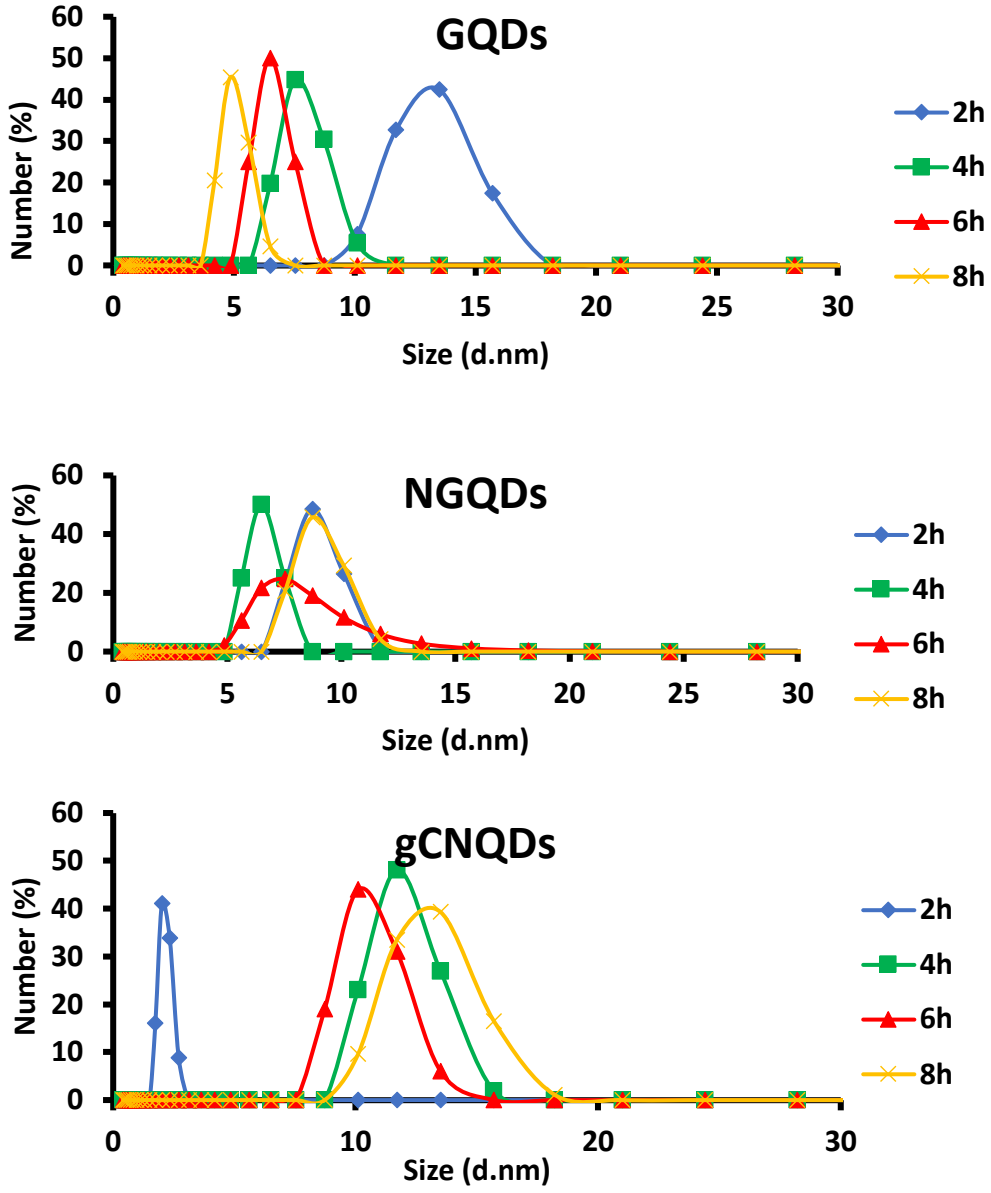

Figure 3.2: DLS plots for GQDs, NGQDs and gCNQDs dispersed in water and sonicated to promote solubilization (2mg/mL).

Table 3.1: Summary of DLS sizes and polydispersity indices (PDI) of synthesized quantum dots in water. Values in brackets are sizes from TEM.

QDs/Size (nm)	2 h	PDI	4 h	PDI	6 h	PDI	8 h	PDI
GQDs	13.5(8.4)	0.94	7.5 (8.3)	0.85	6.5 (8.4)	0.71	4.9 (4.9)	0.52
NGQDs	8.7 (6.3)	0.58	6.5 (8.3)	0.98	7.5 (5.9)	0.51	8.7 (6.0)	0.96
gCNQDs	2.0 (6.7)	0.49	11.7 (7.3)	0.63	10.1 (7.4)	0.62	13.5 (6.9)	0.65

3.1.2 Elemental composition and structure

3.1.2.1 Energy dispersive X-ray (EDX) analysis

Figure 3.3 shows the obtained EDX results for the QDs samples analyzed. This technique is a qualitative measure providing the elemental composition of samples. The expected elements were carbon and oxygen for the three QDs structures and nitrogen for NGQDs and gCNQDs, which were observed in the results obtained.

(a)

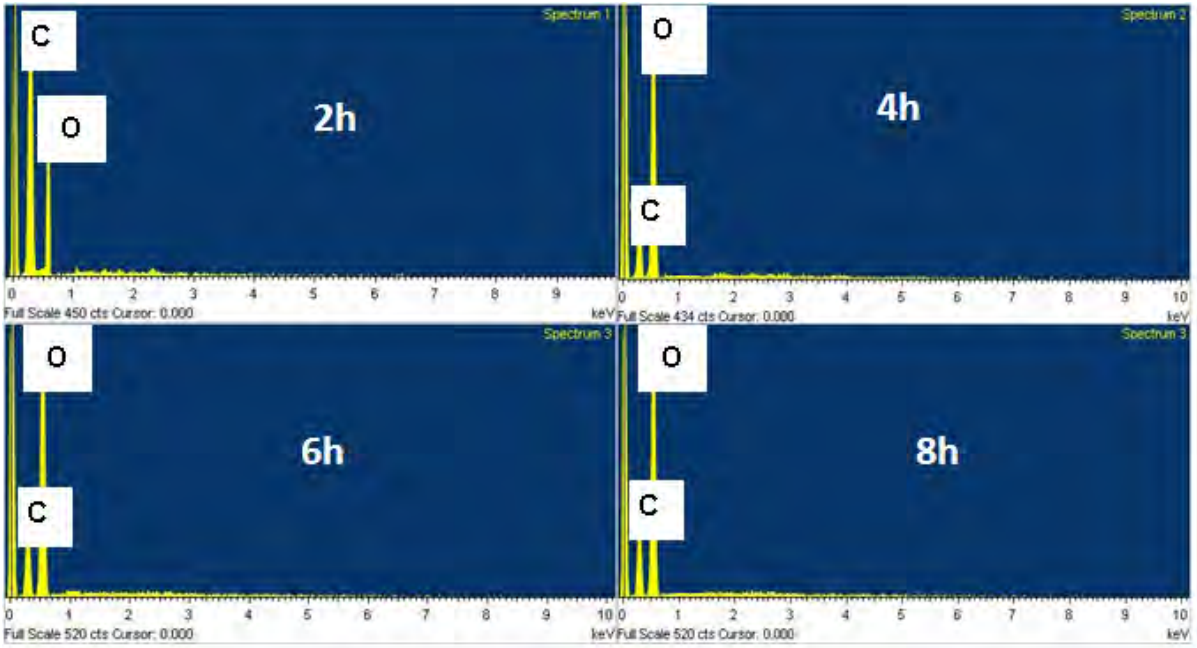

(b)

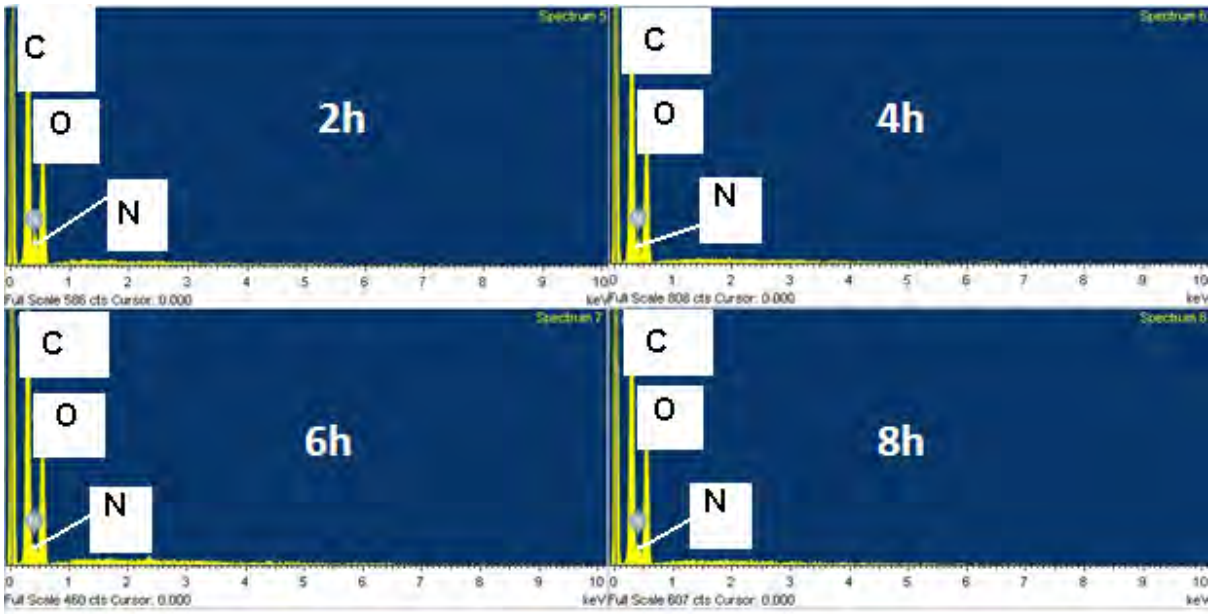

(c)

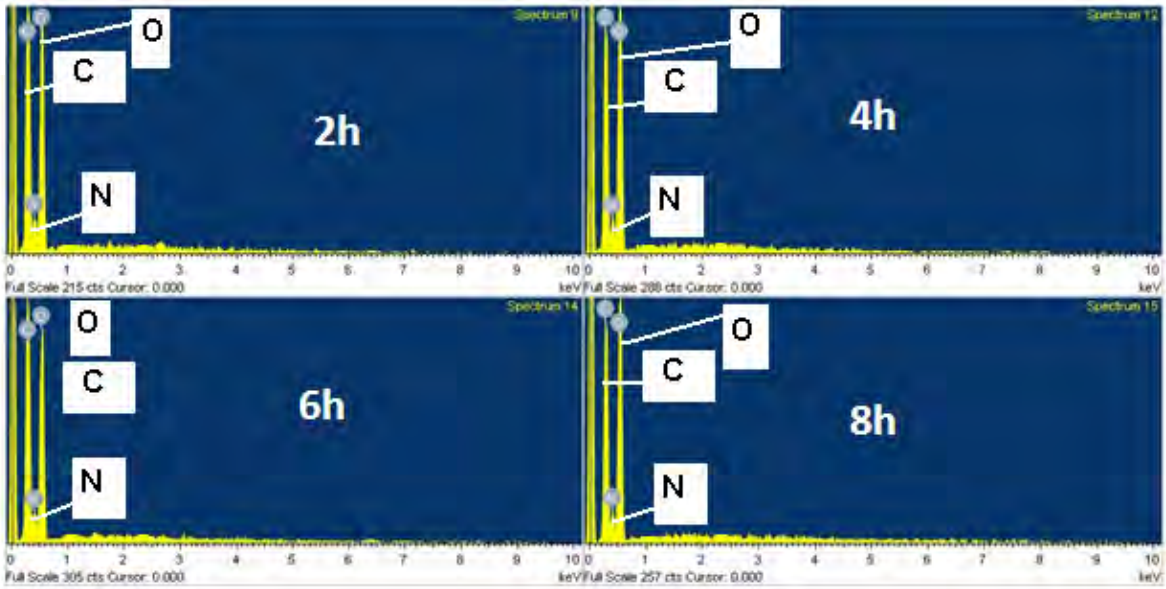

Figure 3.3: EDX spectra for (a) GQDs, (b) NGQDs and (c) gCNQDs at 2,4,6 and 8 h synthesis.

3.1.2.2 Raman spectra

Raman spectroscopy was employed to prove the presence of structural differences between pristine GQDs and its derivatives. Pristine GQDs are used as a reference for the NGQDs and gCNQDs as they ideally have a graphitic structure with no additional elements that could cause defects to the original structure [173]. The peaks of interest in Raman spectra are the disorder (D) sp^3 and graphitic (G) sp^2 peaks from in plane vibrations, which were observed for GQDs, gCNQDs and N-GQDs. The results are summarized in Figure 3.4. In the case of the NGQDs, the D and G bands were slightly shifted in terms of wavenumber compared to the pristine GQDs, Table 3.2. These shifts are likely due to the defective nature caused by the presence of nitrogen atoms introduced into the lattices and stretching of the graphene layers [174]. From these results, the I_D: I_G (sp^3: sp^2) ratios are determined, which determine the extent of functionalization of the carbon nanomaterials or introduction of heteroatoms in the prisitine structure.

Noticeable patterns were observed in the I_D: I_G (sp^3: sp^2) ratio of each type of quantum dots sample analyzed while varying the synthesis time, Table 3.2.

For the GQDs, the ratios decrease with increasing synthesis time. This is expected as it implies that with time, there is an increase in the spatial distribution of the π-conjugated structure. The ratios obtained for NGQDs increase with increasing synthesis time indicating an increase in the extent of doping with the nitrogen atoms. The longer the synthesis takes place, the greater the extent of doping of the graphene structure, resulting in greater spatial disorder. For the gCNQDs, the ratios also increase with increasing synthesis time, indicating the presence of more triazine groups forming as the synthesis time is increased. These results are a clear indication of the QDs structural dependence on the duration of the synthesis.

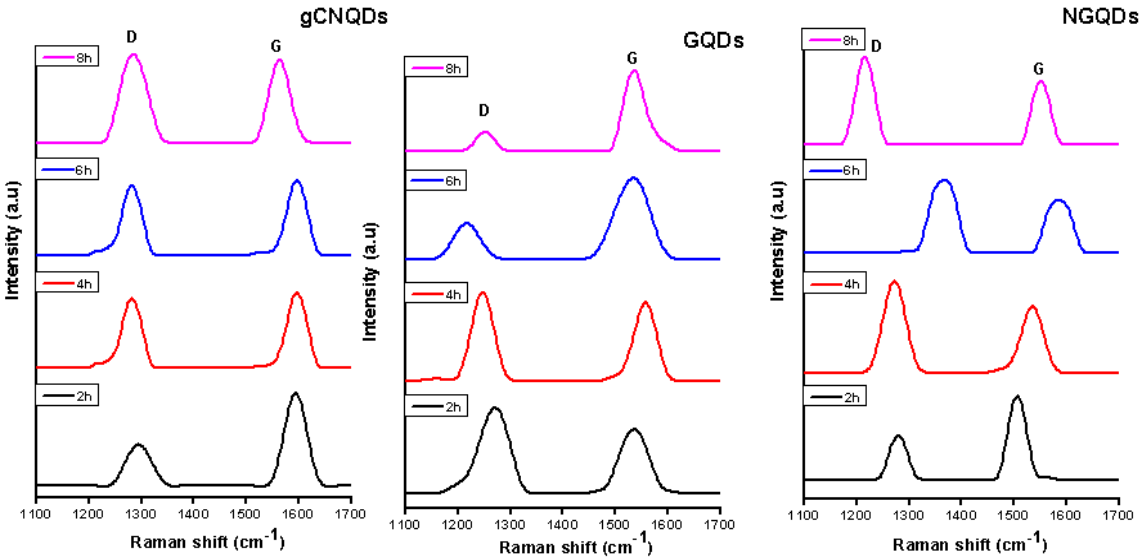

Figure 3.4: Raman spectra of synthesized GQDs, NGQDs and gCNQDs in solid state.

Table 3.2: Summary of Raman stretches of D and G bands and I_D/I_G ratios. Analyses run in solid state.

Synthesis time	D band cm^{-1}	G band cm^{-1}	$I_D:I_G$
	GQDs		
2h	1275	1525	1.33
4h	1250	1550	1.14
6h	1220	1525	0.34
8h	1250	1525	0.17
	NGQDs		
2h	1280	1500	0.56
4h	1280	1550	1.33
6h	1375	1600	1.50
8h	1225	1560	1.56
	gCNQDs		
2h	1300	1590	0.50
4h	1300	1590	0.83
6h	1300	1590	0.83
8h	1280	1550	1.31

3.1.2.3 FTIR spectra

FTIR provides information on the bonds present within each structure, as well as their functional groups the QDs possess. Figure 3.5 summarizes the results obtained. The spectra of the GQDs show the presence of the vibrations, which are typical of the O-H vibration observed between 3000-3500 cm^{-1} [51]. The vibrations at 1250 cm^{-1} and 1262 cm^{-1} are attributed to the C-C and C-O bonds respectively, and the vibration at 1430 cm^{-1} is characteristic of the C=C bond. The vibration identified at 1620 cm^{-1} characterizes the C=O bond which confirms the presence of the expected carboxylic acid groups as well. The spectra of the NGQDs are characterized by vibrations observed in regions of 2500-3500 cm^{-1} which is a broader window compared to GQDs. These vibrations are typical of the O-H/N-H

vibration. At 1430 cm^{-1} and 1400 cm^{-1} are the C=O and C=C vibrations respectively and at 1210 cm^{-1} and 1125 cm^{-1} are vibrations due to C-O and C-C respectively. These findings also correspond to those reported in literature [175]. As stated in the introduction, the gCNQDs have a different base structure compared to the other quantum dots. Therefore, there will be differences in the FTIR spectrum of these nanostructures. Vibrations observed at around 774 cm^{-1} are characteristic of the heptazine units, which the other quantum dots do not possess. At 1415 cm^{-1} and 1315 cm^{-1} vibrations are characteristic of the C=N and C-N bonds respectively as the structure of these quantum dots is predominantly nitrogen based and the 1627 cm^{-1} stretch is characteristic of the C=O of the carboxylic acid groups. Finally, the broad peak between 2750 and 3750 cm^{-1} is characteristic of the N-H/O-H groups. Literature reports also show similar findings and therefore in agreement with the peak assignments made in this work [176, 177]. These results confirm the presence of the expected functions on each of the three QDs synthesized herein.

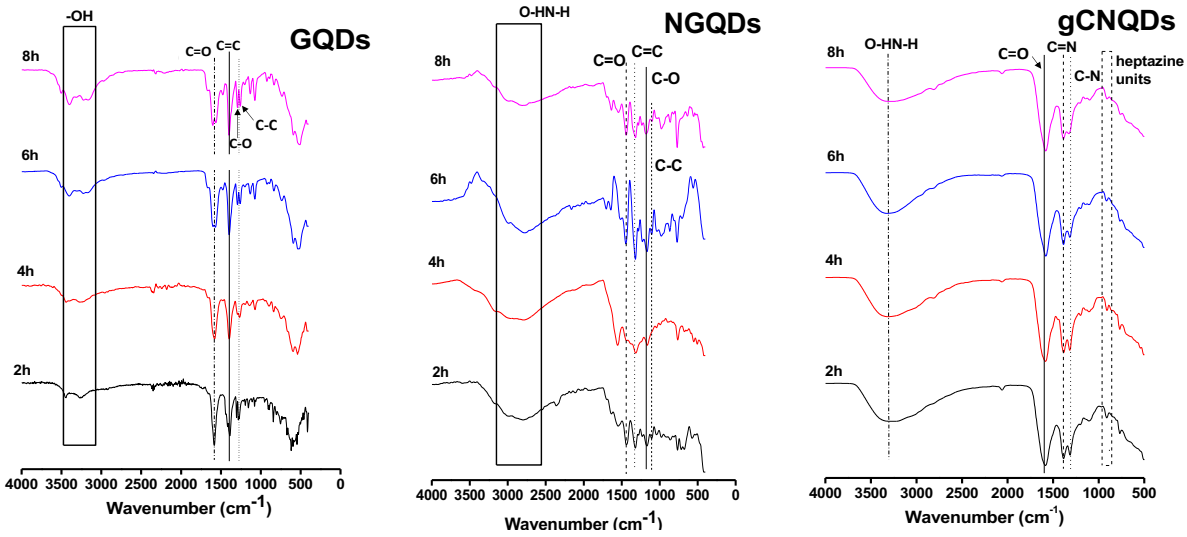

Figure 3.5: FTIR spectrum of GQDs, NGQDs and gCNQDs synthesized at varying times for optimization of synthetic routes. Analyses run in solid state.

3.1.2.4 XPS spectra

XPS is another technique that provides information on the types of bonds and atoms present in the molecular structure, which allows for the determination of extent of functionalization. The wide scan analyses allow for the determination of the general elemental composition of the sample. Thereafter, the peaks due to the elements of interest are deconvoluted in order to determine the exact bonds that exist within the structure and what functional groups are present. Figure 3.6 shows the wide scans for all the synthesized dots at 2 h, 4 h, 6 h and 8 h reaction times. These survey scans confirm the presence of the expected elements comprised within the QDs structures. For GQDs, the expected carbon (C1s) and oxygen (O1s) peaks were observed with an additional sodium (Na) peak, probably due to excess NaOH used during synthesis. It is unclear where the silica peaks come from as there is no silica used in the starting materials and no silica was observed in the EDX spectra already discussed. Therefore, the assumption is that the impurity was picked up during XPS analysis. High-resolution scans were then obtained and deconvoluted and the results are summarized in Table 3.3. The C1s spectra were deconvoluted in order to confirm which other atoms the carbon atoms were bonded to, as well as to prove the presence of the –COOH groups. At all GQDs synthesis times, three peaks were observed at binding energies of about 294 eV, 292 eV and 290 eV corresponding to C=C/C-C which are the sp^2 carbons, C-O which are the sp^3 carbons and C=O, Table 3.3(a). The C-O and C=O peaks also confirm the presence of –COOH groups [176]. While varying the synthesis time, no effect on the binding energies was observed. For the NGQDs samples, the wide scans only showed peaks corresponding to the nitrogen (N1s), carbon (C1s) and oxygen (O1s) with no peak due to possible contaminants. The C1s (Table 3.3(a))

and N1s (Table 3.3(b)) peaks were further analyzed by plotting and deconvoluting the high-resolution scans. Under the C1s scan, three prominent peaks were observed at binding energies of 286 eV, 284 eV and 282 eV corresponding to O-C=O, C-N/C=N and the sp^2 hybridized C-C/C=C [176]. For the high resolution N1s scan, four peaks were observed at binding energies of 401 eV, 400 eV, 399 eV and 398 eV corresponding to N-C=O, N-H, C=N and C-N-C bonds [176]. Thus, for the NGQDs the synthesis time did not affect the binding energies of the peaks. The wide scans for the gCNQDs show the expected O1s, N1s and C1s peaks. Very weak signals corresponding to Si are observed. However, no Si was used in the synthesis of the QDs indicating that this contamination did not come from these nanostructures. The deconvoluted C1s scans of the gCNQDs samples synthesized at 2h, 6h and 8h revealed three peaks at binding energies of 294 eV, 293 eV and 291eV which correspond to C-O, C=N and C-C/C-N respectively. The binding energies of the peaks observed for the sample at 4h synthesis time were observed at 289 eV, 287 eV and 285 eV. The same trend is observed for the N1s deconvoluted scans where for the samples obtained at 2h, 6h and 8h synthesis time peaks were observed at binding energies of 399 eV, 397 eV and 396 eV corresponding to C-N-H, $N(C)_3$ and C-N=C [160]. For the sample reacted for 4h, the peaks were observed at 404 eV corresponding, according to reported works [178], to N-oxide, the charging effects in the cyano group and heterocycles or π-excitations, 401 eV corresponds to the quaternary nitrogen bonded terminal amino group (C–H–N) and 399 eV corresponds to the tertiary nitrogen bonded to carbon atoms in the form of $N(C)_3$ bonds.

These results confirmed the presence of the synthesized quantum dots in greater details than FTIR did, providing more information on the structural formation of these nanostructures.

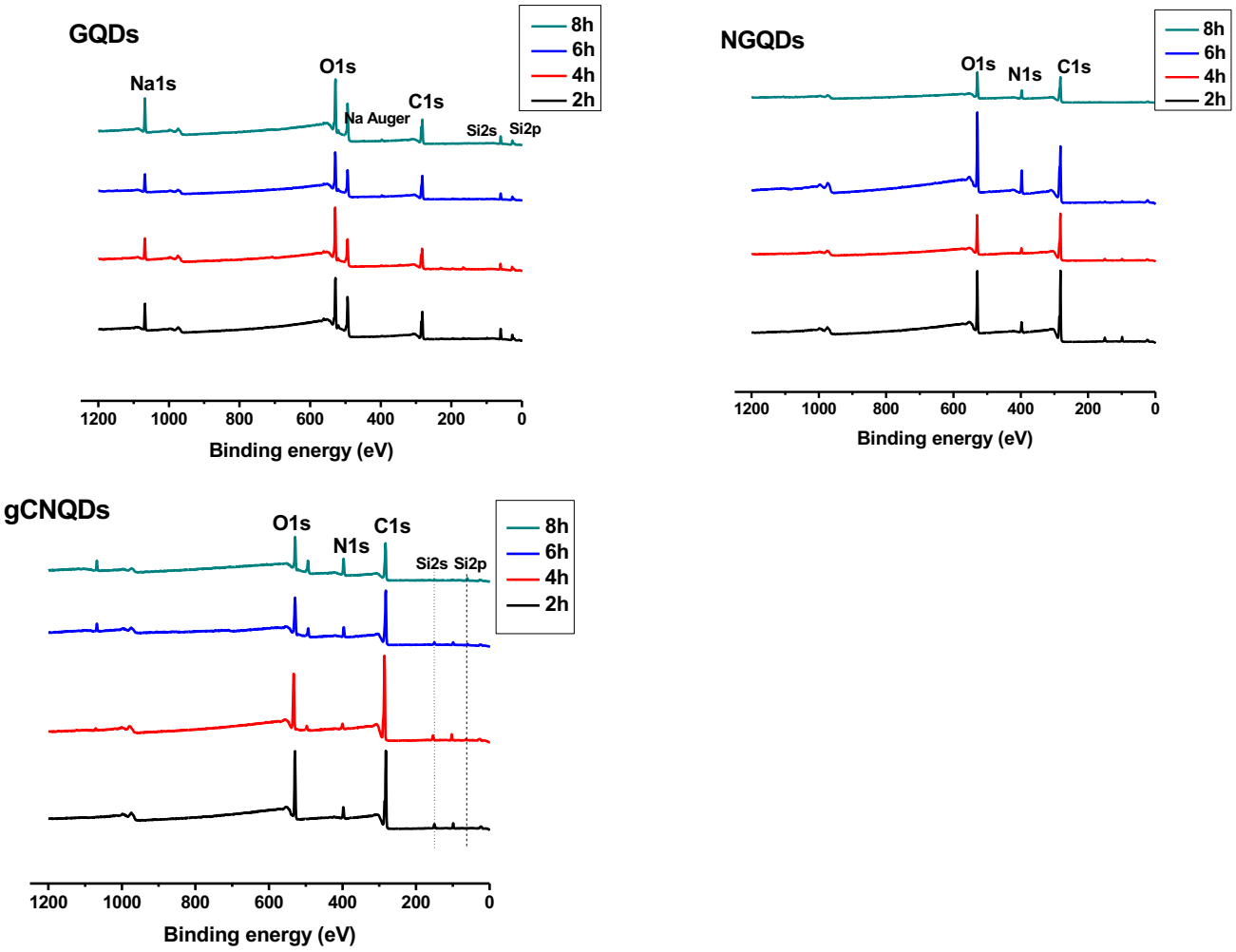

Figure 3.6: XPS wide scans of GQDs, NGQDs and gCNQDs.

Table 3.3(a): C1s deconvoluted peak assignments (binding energy/BE) of GQDs, NGQDs and gCNQDs.

GQDs	**C=C/C-C**	**C-O**	**C=O**
2-8h	294	292	290
NGQDs	**O-C=O**	**C-N/C=N**	**C-C/C=C**
2-8h	286	284	282
gCNQDs	**C-O**	**C=N**	**C-C/C-N**
2h, 6h, 8h	294	293	291
4h	289	287	285

Table 3.3(b): N1s deconvoluted peak assignments of NGQDs and gCNQDs.

NGQDs	**N-C=O**	**N-H**	**C=N**	**C-N-C**
2-8h	401	400	399	398
gCNQDs	**C-N-H**	**$N(C)_3$**	**C-N=C**	-
2h, 6h, 8h	399	387	396	-
	N-oxide	**C-H-N**	**$N(C)_3$**	-
4h	404	401	399	-

Moreover, the % oxygen and carbon present in the GQDs, NGQDs and gCNQDs synthesized at 2, 4, 6 and 8 h were also determined (Table 3.4). For the GQDs and NGQDs samples, there was no trend observed that could help in differentiating the structures at the different synthesis times. However, the gCNQDs showed an increase in % oxygen as synthesis time increased and a decrease in % carbon. This may imply an introduction of more triazine groups within the gCNQDs structure as well as more -COOH groups in the periphery.

Table 3.4: Summary of % Oxygen and Carbon present in the GQDs, NGQDs and gCNQDs synthesized at 2, 4, 6 and 8 h.

Synthesis time	Atomic conc. % Carbon	Atomic conc. % Oxygen
	GQDs	
2h	55.51	44.49
4h	63.09	36.91
6h	51.77	48.23
8h	60.25	39.75
	NGQDs	
2h	73.80	26.20
4h	76.90	23.10
6h	66.42	33.58
8h	72.96	27.04
	gCNQDs	
2h	83.75	16.82
4h	81.07	18.93
6h	80.67	19.33
8h	75.88	24.12

3.1.3 Dispersity, charge density and colloidal stability

3.1.3.1 Zeta potential (ζ)

Zetametry provides information on the charge density of the QDs, which relates to their surface functionalization as well as their colloidal stability in solution [179]. In other words, the higher the zeta potential value, the more stable the particles are in solution. Water was used as the analysis medium. The obtained data is summarized in Table 3.5 alongside the mobility and conductivity obtained from the zetametry instrumentation. All synthesized quantum dots were negatively charged at all synthesis times in the -18 to -40 mV range (Table 3.5). For gCNQDs however, the zeta potential is recorded as less negative at 8h synthesis, which is unexpected. This could be caused by aggregation if the NH_2 groups are protonated while COOH or OH groups deprotonated in this sample. Indeed, the classical proposed structure in the literature of gCNQDs contains NH_2 groups at their periphery and possibly COOH or OH groups, Scheme 3.1. On the other hand, GQDs and NGQDs present COOH and OH groups and additional NH groups for NGQDs. These functional groups, when deprotonated, generate an overall negative surface charge. Moreover, the literature reports pKa value of 4.3 for COOH near-OH in graphene oxide (GO) [180] and 5.2 for $-NH_2$ [181]. The differences in conductivity indicate how the synthesis time will affect their size and therefore electronic properties. Moreover, the negative mobility indicates the presence of negative particles in solution.

Table 3.5: Summary of Zeta (ζ) potential data and mobility of synthesized quantum dots in water.

	Zeta (ζ) potential/mV	Conductivity/ mS.cm^{-1}	Mobility/ μmcm.Vs^{-1}
		GQDs	
2h	-20.9	9.61	-1.76
4h	-26.4	9.91	-1.70
6h	-27.6	10.2	-1.61
8h	-30.1	16.1	-1.71
		NGQDs	
2h	-18.4	0.22	-1.54
4h	-19.7	0.08	-1.60
6h	-24.5	0.15	-2.76
8h	-37.5	0.44	-3.02
		gCNQDs	
2h	-31.8	0.32	-2.50
4h	-33.2	0.40	-2.60
6h	-40.0	0.30	-3.14
8h	-26.1	0.057	-2.0

3.1.3.2 Capillary electrophoresis coupled with electrospray ionization-mass spectrometry (CE-ESI-MS)

From the results obtained after optimizing the synthesis of the QDs, the samples used for further studies throughout this thesis were GQDs 8h, NGQDs 6h and gCNQDs 6h. The GQDs batch at the above-mentioned synthesis time was chosen as it showed the lower PDI valuein DLS which is ideal for CE analysis. It was also clear from the TEM images that this batch was well dispersed compared to the other batches. It also showed a high zeta potential value at this time which was an indicator of better stability in solution compared to the other batches synthesized for different lengths of time. The NGQDs also showed the lowest PDI value and hydrodynamic size in DLS at 6 h synthesis time compared to the other batches and therefore was chosen for further studies in the thesis. Moreover, in XPS, it showed the highest concentration % of oxygen at 6 h synthesis which suggests more COOH groups available for amide bonding in later studies. Although the gCNQDs showed the lowest PDI value and size in DLS at 2 h synthesis time, the batch synthesized for 6 h was chosen for further studies as it showed the highest value in zeta potential measurements, which was an indicator of better stability in solution compared to the batch synthesized for only 2 h. In-solution stability is crucial in CE-MS studies. In addition, DLS and TEM were in agreement at these reaction times. An attempt was therefore made to further characterize the selected QDs using CE-ESI-MS.

Capillary electrophoresis (CE) is an electrokinetic method that was proved powerful analytical tool to separate and characterize nanostructures, allowing for their discrimination in size, surface charge density and functionalization as well as for understanding their behaviour in different environments to allow for further

applications [182-184]. The detection was performed by UV-Vis at 200 nm detection wavelength. As expected, all the QDs showed negative mobilities. Fig. 3.7 shows the electropherogram of the GQDs as an example. As can be seen, the mobility was negative indicating negatively charged particles in solution, which are in agreement with the results obtained from zeta potential measurements.

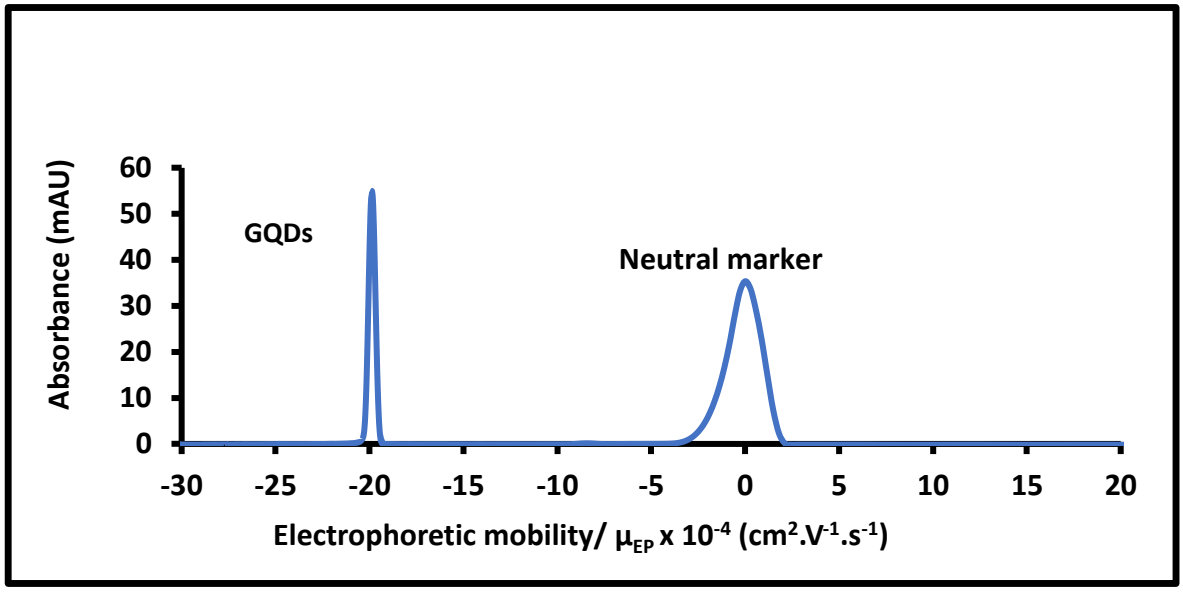

Figure 3.7: Electropherogram of neutral marker and GQDs simultaneous injection; 18 kV electrokinetic separation; 200 nm detection.

Once the analyses were conducted in CE alone, the samples were prepared for separation and characterization using CE-ESI-MS. The effect of pH was one of the parameters studied as it plays a role in the surface charge of the nanostructures in solution and therefore the recorded mobilities. The pH of the buffer was increased from pH 7 to 10 to see if it could improve the ionization of the carboxylic groups known to occur at the surface of the QDs. Figure 3.8 shows the electropherograms obtained after running each sample at increasing pH from 7 to 10. The electropherograms obtained from CE are marked (i) and those obtained from MS

detection are marked (ii). For the GQDs (Fig. 3.8(a)), the electropherograms from UV detection are broad and suggest nanostructures with varying surface charge. Under mass detection, the peaks are not as broad, but the electrophoretic mobility shifts towards the negative region with increasing pH. This implies more ionization with increasing pH levels. For the NGQDs shown in Fig. 3.8(b), the profiles of the electropherograms in CE have no defined trend, however, the mobilities at pH 9 and 10 overlap. For the gCNQDs (Fig. 3.8(c)), there was no defined trend observed, but pH 9 and 10 showed broad peaks in the same mobility regions. Thus, the change in pH did not result in any changes that may help improve the analysis or separation of the QDs in MS detection.

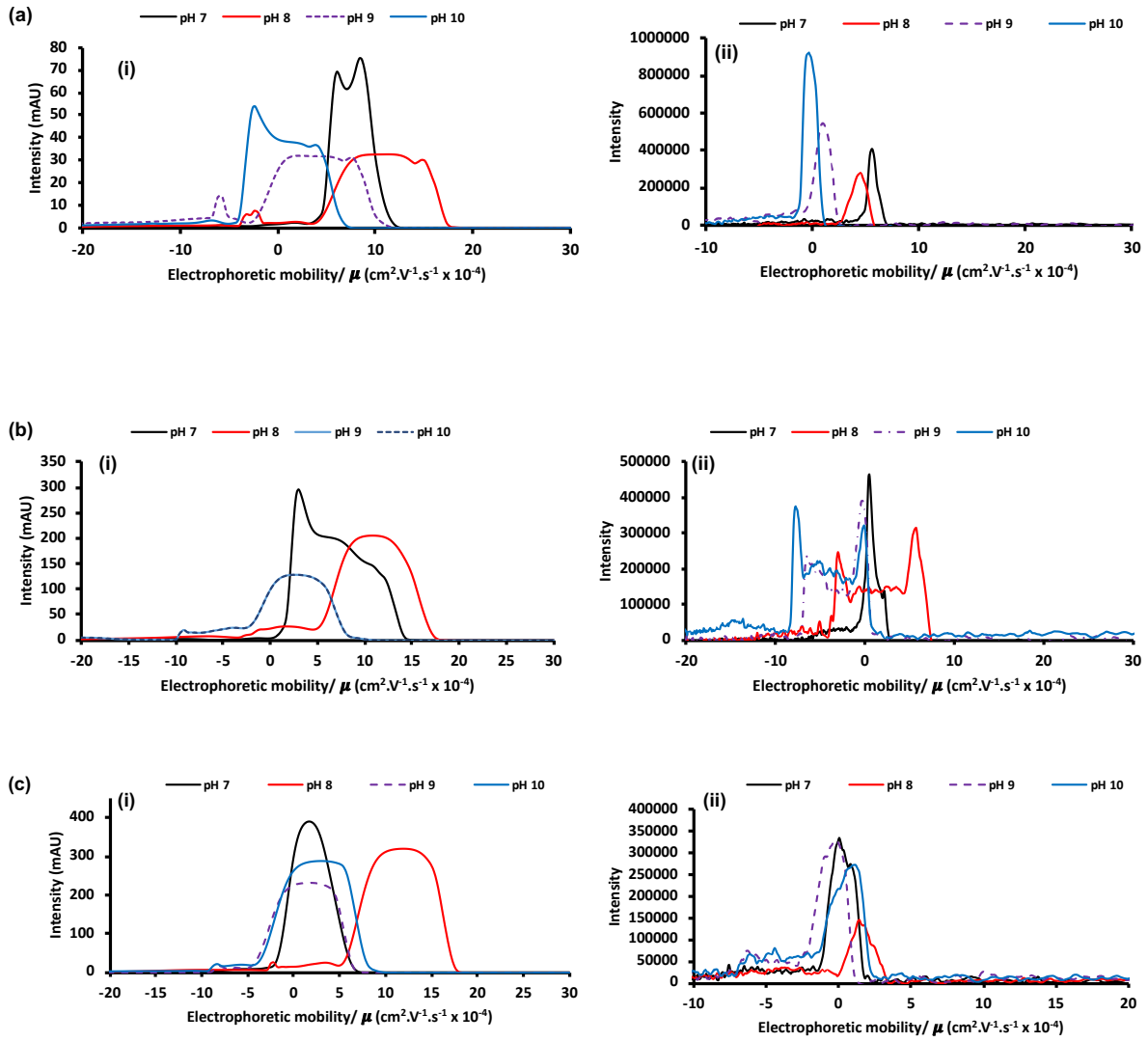

Figure 3.8: Electropherograms of (a) GQDs, (b) NGQDs and (c) gCNQDs (1mg/mL BGE) recorded at pH 7.4 -10 of run buffer. Injections done at 50 mbar for 16 s for QDs. (i) CE electropherograms and (ii) MS electropherograms.

3.2 Characterization of MPcs, Complex (1) and complex (2)

Complexes 1 and 2 were synthesized by a statistical cross-condensation reaction using two phthalonitrile derivatives illustrated in Schemes 3.2 and 3.3.

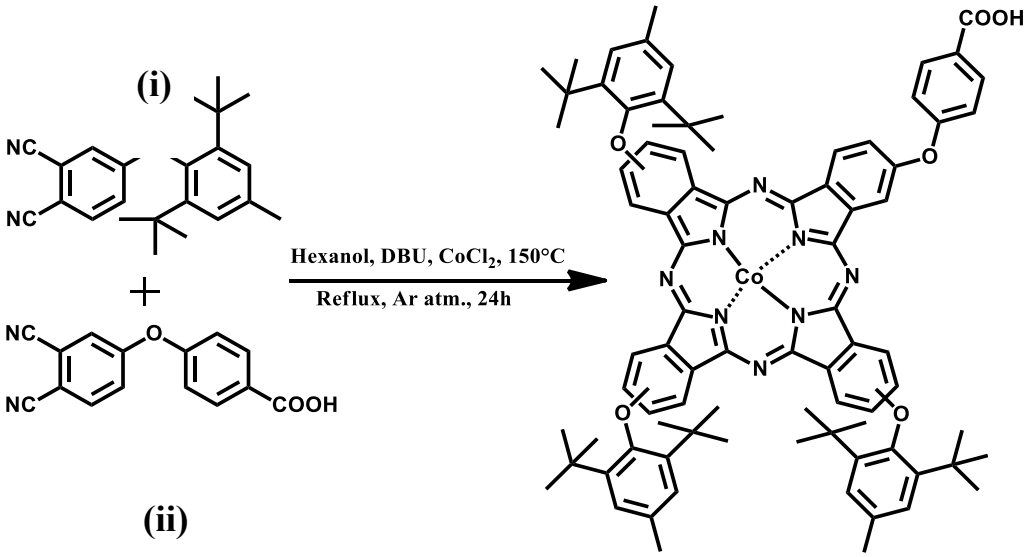

Scheme 3.2: Synthesis of complex 1.

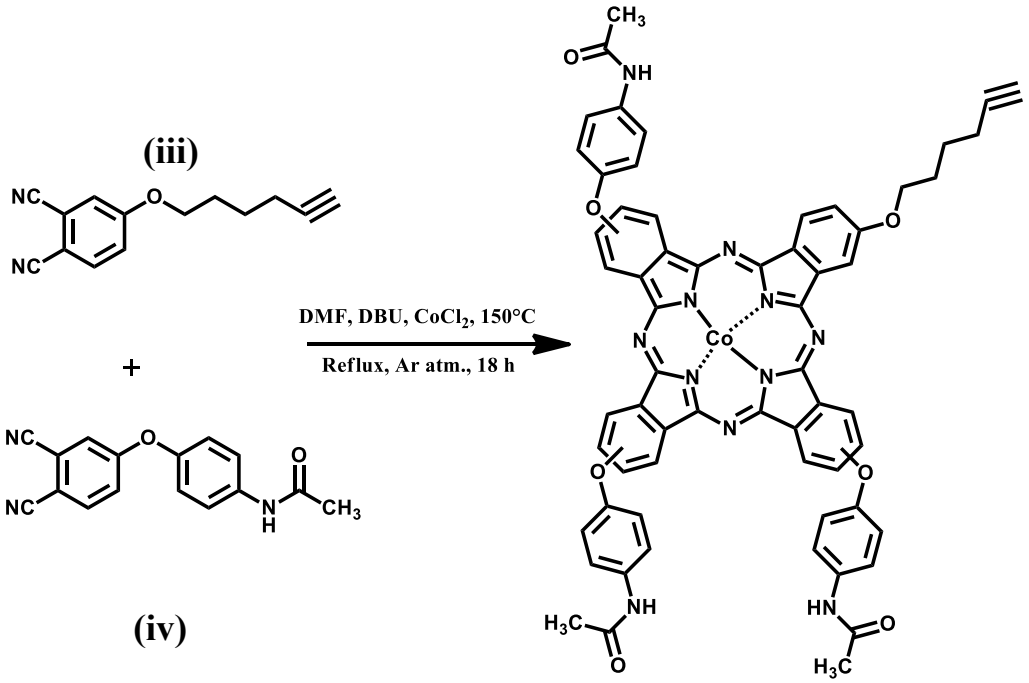

Scheme 3.3: Synthesis of complex 2.

The obtained products were characterized using various analytical techniques such as UV/vis, FTIR, MALDI-TOF as well as elemental analysis, which gave an indication of the success of the reaction. Complexes 1 and 2 gave a mass of 1361.34 for [M] and 1114.34 for $[M]^+$ respectively, verifying the success of the syntheses. Fig. 3.9 shows the absorption spectra of MPc complexes 1 and 2 in DMF. The Q band is broad probably due to aggregation for complex 1. A broad or split Q band indicates aggregation in Pc complexes, with the low energy band being due to the aggregate and the high-energy band being due to the monomer [185]. Q bands and B bands associated with metalated Pcs are observed, where complex 2 achieves its Q band maximum at 667 nm while the B band is the most pronounced at 327 nm. The Q band of complex 1 was observed at 665 nm in DMF.

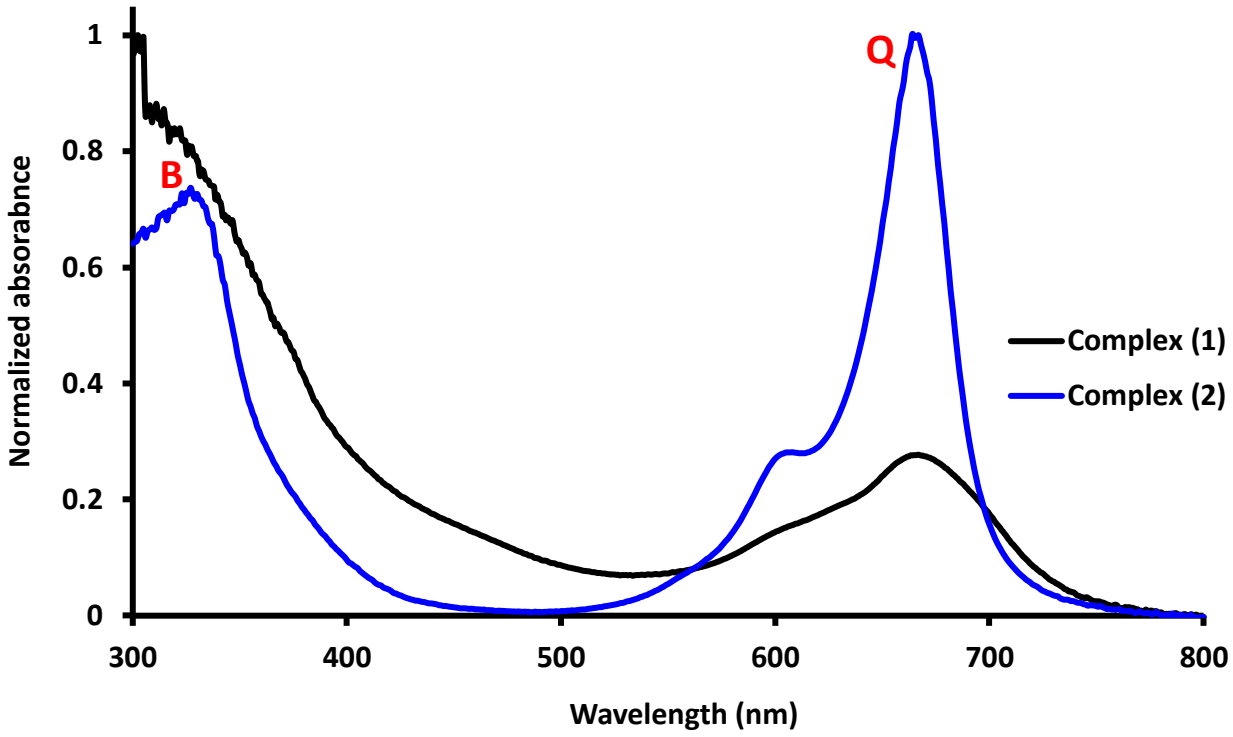

Figure 3.9: Absorption spectrum of complex 1 and 2 in DMF (~ 10^{-5} M).

3.3 Characterization of conjugates

Two-component systems were formed in this work prior to combining the GQDs, MPcs and aptamer to finally form the three-component systems. The conjugates formed are listed in Table 3.6 with some data summarized, which will be further elaborated on in this sub-section.

Table 3.6: Summarized spectral, DLS and zeta potential data of quantum dots, phthalocyanine and their conjugates with aptamer.

Sample	Loading (mg/mg)	λ_{max} (nm)	Hydrodynamic size/ nm (PDI)[d]	Zeta (ζ) potential/mV
GQDs, 8 h	-	348[a]	4.9 (0.52)	-30.1
NGQDs, 6 h	-	344[a]	7.5 (0.51)	-24.5
gCNQDs, 6 h	-	378[a]	10.1 (0.62)	-40.0
CoPc(1)	-	660[b]	Unstable in solution	Unstable in solution
CoPc(2)	-	667[b]	Unstable in solution	Unstable in solution
Aptamer	-	622[a]	Unstable in solution	Unstable in solution
GQDs-CoPc(1) ($\pi\pi$)	0.08	639[c]	18.2 (0.66)	-33.9
NGQDs-CoPc(1) ($\pi\pi$)	0.39	629[c]	15.7 (1.0)	-34.7
gCNQDs-CoPc(1)($\pi\pi$)	0.21	660[c]	18.2 (0.67)	-76.0
CoPc(1)@Aptamer	-	400, 625[c]	37.8 (0.97)	-46.4
GQDs@Aptamer	-	629[a]	68.1 (0.74)	-39.3
gCNQDs@Aptamer	-	620[a]	58.8 (1.0)	-51.2

[a]in water, [b]in DMSO, [c]in DSO/water mixture, [d]PDI in brackets

3.3.1 Verification of covalently linked conjugates GQDs@Aptamer, gCNQDs@Aptamer and CoPc(1)@Aptamer

The covalent conjugation of the QDs and CoPc(1) with aptamer was achieved via amide coupling which is illustrated in Scheme 3.4 using gCNQDs as the example. This subsection highlights various analytical techniques used to fully characterize these composites.

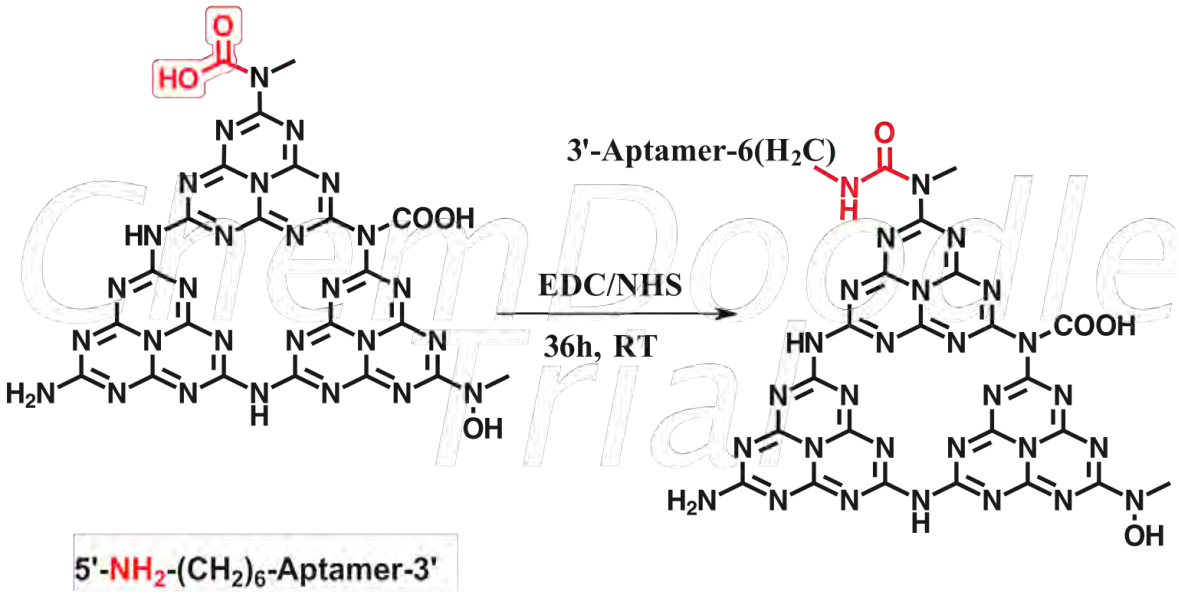

Scheme 3.4: Amide coupling procedure of gCNQDs and amine-terminated aptamer.

3.3.1.1 XPS spectra

XPS was used to verify the success of covalent linking of the aptamer with the chosen quantum dots samples and the CoPc(1). The XPS results obtained are shown in Figure 3.10. The analyzed samples are GQDs@Aptamer, gCNQDs@Aptamer and CoPc(1)@Aptamer ('@' representing covalent amide linking of molecules).

The wide survey scans showed the expected peaks which were attributable to the covalent conjugates presented in this work. The observed peaks on the wide scan were the N1s at 400 eV, C1s at 300 eV, O1s around 550 eV, P2s at 197 eV and P2p around 150 eV all wide scans. The difference in the survey scans was just the peak due to cobalt, which is the central metal of the phthalocyanine used, observed at around 791 eV which is the region where Co is observed on XPS analyses of CoPc(1)@Aptamer [186]. The P is said to be due to the DNA phosphate group [187]. P has been observed at binding energies of 150-200 eV [187].

The peaks due to nitrogen, carbon and oxygen were further studied as high-resolution scans and deconvoluted to confirm the covalent conjugation of the aptamer with the QDs and CoPc(1). All data from deconvoluted spectra are summarized in Table 3.7. For the GQDs@Aptamer conjugate, the deconvoluted N1s spectrum showed two main peaks underneath the original peak at binding energies of 399 eV and 401 which are attributable to N-H and N-C=O respectively and these bonds at these binding energies has been reported [188]. The presence of N-C=O confirms the formation of an amide bond. The C1s spectrum showed three peaks after deconvolution at binding energies of 283.5 eV, 285.0 eV and 287.0 eV attributable to graphitic carbon, C-N and C=O respectively, Table 3.7. The O1s spectrum showed three peaks under the main peak at binding energies of 529.0 eV, 531.0 eV and 531.8 eV which may be attributed to C-O-C/C=O, C=O/P=O and C-O-P respectively. A similar finding for aptamer-based work has been reported in literature [189]. For the gCNQDs@Aptamer conjugate, the deconvoluted N1s spectra showed three peaks at binding energies of 398.5 eV, 401.0 eV and 402.0 eV which may be attributed to C-N, N-H and N-C=O respectively [188]. The C1s spectra for this samples showed three peaks after deconvolution at binding

energies of 285.5, 286.5 eV and 288.0 eV attributable to graphitic carbon, C-N and C=O respectively. The O1s spectrum showed three peaks under the main peak at binding energies of 530.5 eV, 532.0 eV and 533.0 eV which may be attributed to C-O-C/C=O, C=O/P=O and C-O-P respectively. Compared to the GQDs, the other QDs samples have the nitrogen atoms present within their structures and thus contain more defects than the GQDs which may be the cause of shifts in binding energies. For the CoPc(1)@Aptamer conjugate, the deconvoluted N1s spectrum showed peaks at binding energies of 397.0 eV, 399.0 eV and 401.0 eV which may be attributed to C=N, N-H and N-C=O respectively [190]. For the C1s and O1s spectra, similar results were observed as was for GQDs@Aptamer which confirms the presence of the new amide bond formed by covalent linkage as well as presence of N-C=O bond.

A

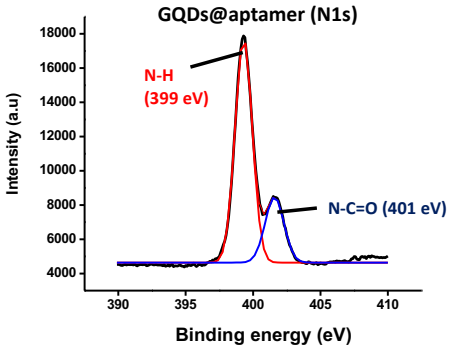
GQDs@aptamer (N1s)
N-H
(399 eV)
N-C=O (401 eV)
Intensity (a.u)
Binding energy (eV)

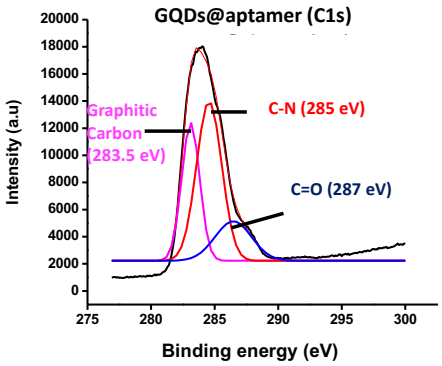
GQDs@aptamer (C1s)
Graphitic
Carbon
(283.5 eV)
C-N (285 eV)
C=O (287 eV)
Intensity (a.u)
Binding energy (eV)

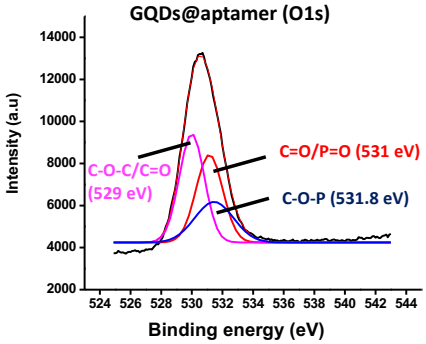
GQDs@aptamer (O1s)
C-O-C/C=O
(529 eV)
C=O/P=O (531 eV)
C-O-P (531.8 eV)
Intensity (a.u)
Binding energy (eV)

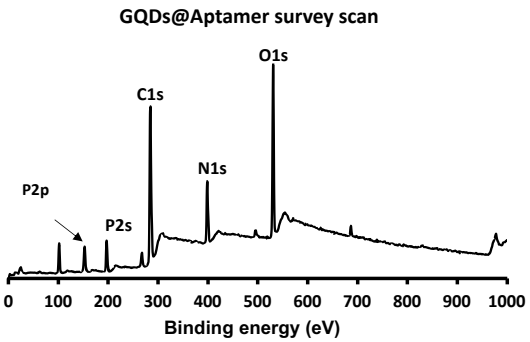
GQDs@Aptamer survey scan
O1s
C1s
N1s
P2p
P2s
Binding energy (eV)

B

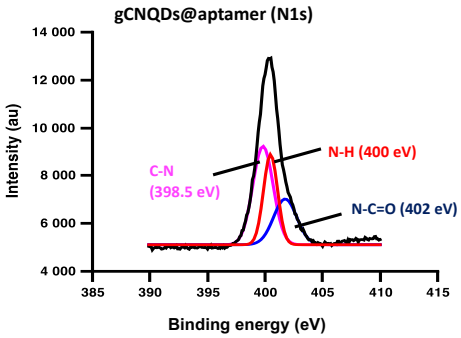
gCNQDs@aptamer (N1s)
C-N
(398.5 eV)
N-H (400 eV)
N-C=O (402 eV)
Intensity (au)
Binding energy (eV)

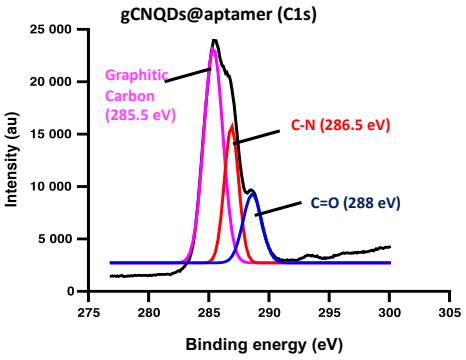
gCNQDs@aptamer (C1s)
Graphitic
Carbon
(285.5 eV)
C-N (286.5 eV)
C=O (288 eV)
Intensity (au)
Binding energy (eV)

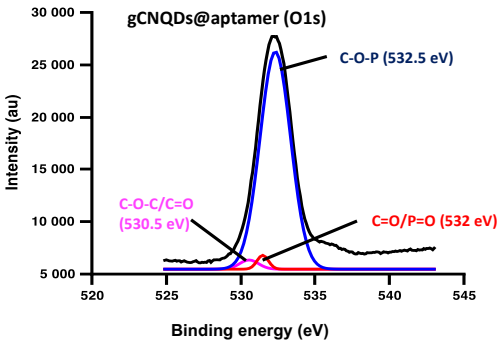
gCNQDs@aptamer (O1s)
C-O-P (532.5 eV)
C-O-C/C=O
(530.5 eV)
C=O/P=O (532 eV)
Intensity (au)
Binding energy (eV)

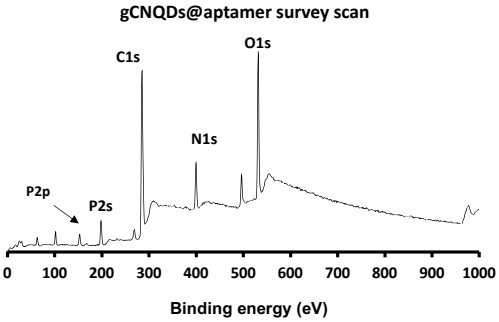
gCNQDs@aptamer survey scan
O1s
C1s
N1s
P2p
P2s
Binding energy (eV)

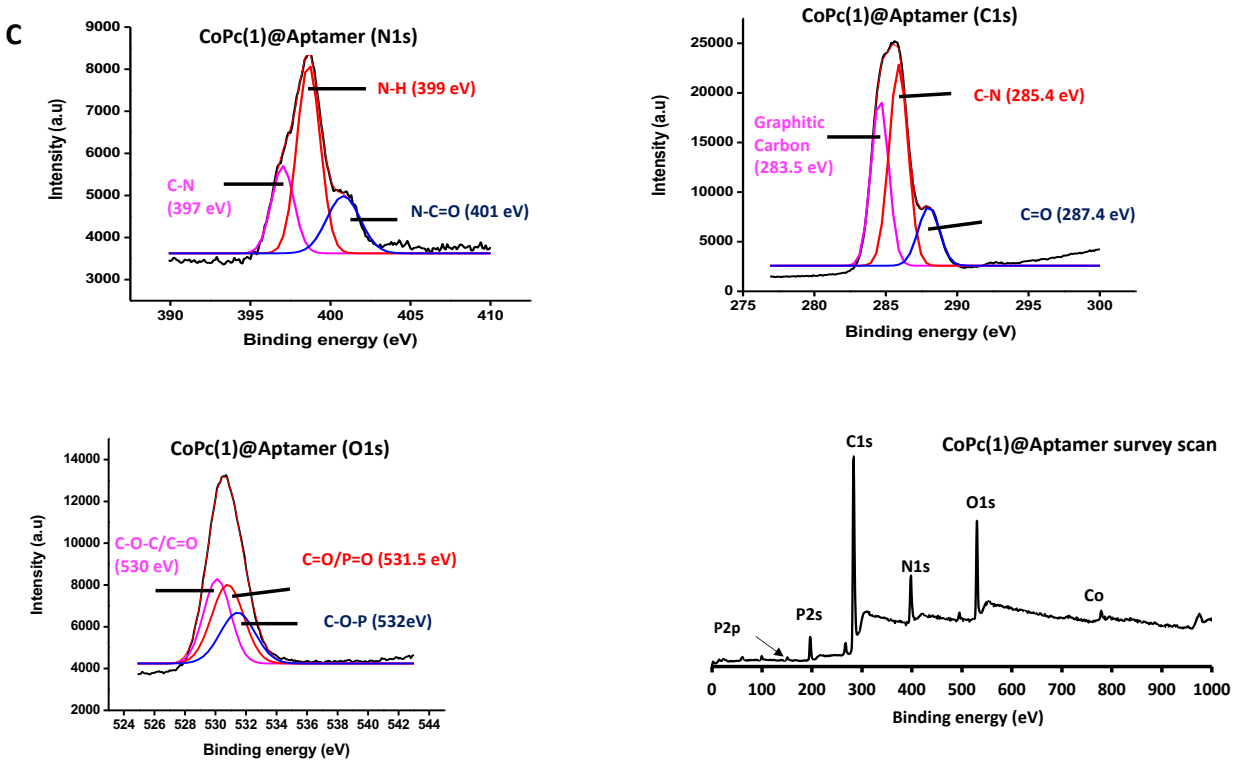

Figure 3.10: XPS survey and high-resolution scans for GQDs@Aptamer, gCNQDs@Aptamer and CoPc(1)@Aptamer for the verification of covalent bonding.

Table 3.7: Summary of binding energies determined from deconvoluted high-resolution spectra, corresponding to bonds forming the structures reported and their conjugates.

	N1s			C1s			O1s		
Peak assignments	C-N	N-H	N-C=O	Graphitic carbon	C-N	C=O	C-O-C/ C=O	C=O/P=O	C-O-P
GQDs@Aptamer	-	399.0	401.0	283.5	285.0	287.0	529.0	531.0	531.8
gCNQDs@Aptamer	398.5	401.0	402.0	285.5	286.5	289.0	530.5	532.0	533.0
CoPc(1)@Aptamer	397.0	399.0	401.0	283.5	285.4	287.4	530.0	531.5	532.0

3.3.1.2 DLS and zetametry

Figure 3.11 shows the profiles obtained for the QDs and their conjugates with aptamer dispersed in a de-ionized water. For the GQDs (Fig. 3.11(a)), (Tables 3.1 and 3.6) the size determined in DLS was 4.9 nm for the sample synthesized for 8 h. Upon covalently linkage to the aptamer (GQDs@Aptamer), a very broad peak is observed with a size of about 68.1 nm at the peak maxima, Table 3.6. Sizes this large in DLS analyses are an indication of high aggregation of these conjugates in the buffer solution. The gCNQDs (Fig. 3.11(b)), were found to be 10.1 nm for the sample synthesized for 6 h, with its conjugate with aptamer being 58.8 nm, Tables 3.1 and 3.6. For the aptamer alone, obtaining a value was difficult which was an indication of low stability of this molecule in solution. However, when conjugated to the QDs, negative values were obtained which indicated the ability of these QDs of interest to stabilize the aptamer in solution. The zeta potential values of the GQDs and gCNQDs prior to conjugation were -30.1 and -40.0 mV, Table 3.6. When conjugated to the aptamer, the zeta potential values were measured as -39.3 and -51.2 mV respectively. The higher zeta potentials for the covalently conjugated molecules indicates good in-solution stability. The CoPc(1)@Aptamer conjugate in particular showed a hydrodynamic radius of 37.8 nm with a zeta potential value of -46.4 mV which indicates a stable conjugate in solution compared to the CoPc(1) alone which was unstable in solution.

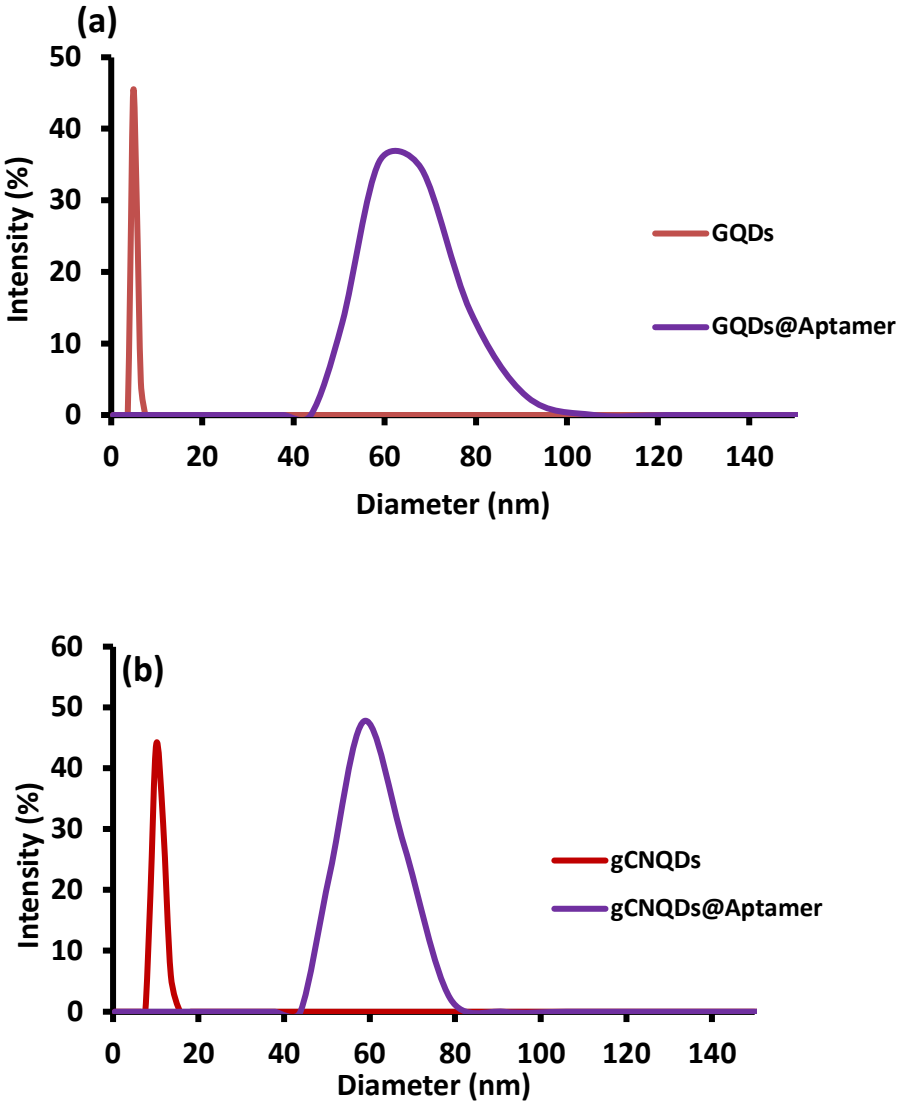

Figure 3.11: DLS plots of (a) GQDs and (b) gCNQDs and their conjugates with aptamer in deionized water.

3.3.1.3 FTIR spectra

The presence of the QDs and aptamer within the covalent conjugate was also validated using FTIR analysis. The conjugation between the GQDs and aptamer was used as an example to illustrate the results obtained for all covalent conjugates reported in this thesis. These results are shown in Figure 3.12. The stretches due to the backbone of the aptamer are identified in the region of 1084/1225 cm^{-1}

where they are expected. These peaks are not observed in the GQDs spectrum. More importantly, in the region between 3000-3500 cm^{-1} of the conjugate a distinct peak at 3300 cm^{-1} due to NH(C=O) can be seen, as well as spectral shift which are an indication of amide bond formation [191].

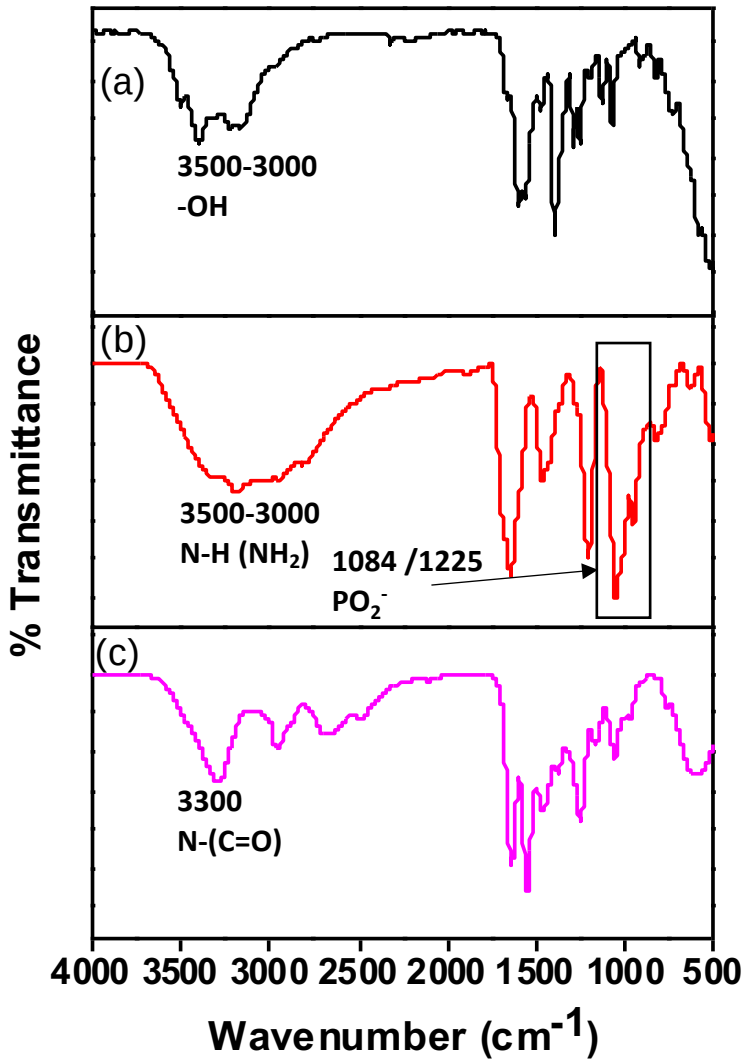

Figure 3.12: FTIR spectra of (a) GQDs, (b) aptamer and (c) their covalent conjugates. Samples studied in solid state.

3.3.1.4 Raman spectra

Raman results are shown in Fig. 3.13 for the GQDs, aptamer and GQDs@Aptamer. Their I_D/I_G ratios were determined using peak areas. The peak due to the aptamer was observed at 1285 cm^{-1} that has been reported in literature to occur in this region [192, 193]. The effect of covalently conjugating the QDs to the aptamer is discussed using GQDs@Aptamer as an example. When the GQDs are covalently bonded to the aptamer, there is a shift of the D band to a lower frequency and G band of the GQDs to a higher frequency. The aptamer peak still appears at 1285 cm^{-1}. The D band of the GQDs also intensifies upon conjugation of the aptamer with the GQDs, indicating an interaction between the two molecules. The I_D/I_G ratio of GQDs@Aptamer was found to be 0.67 which is an increase from the ratio determined for the GQDs alone, determined as 0.17 (Table 3.8). This is one of the indicators that there is interaction between the aptamer and the GQDs.

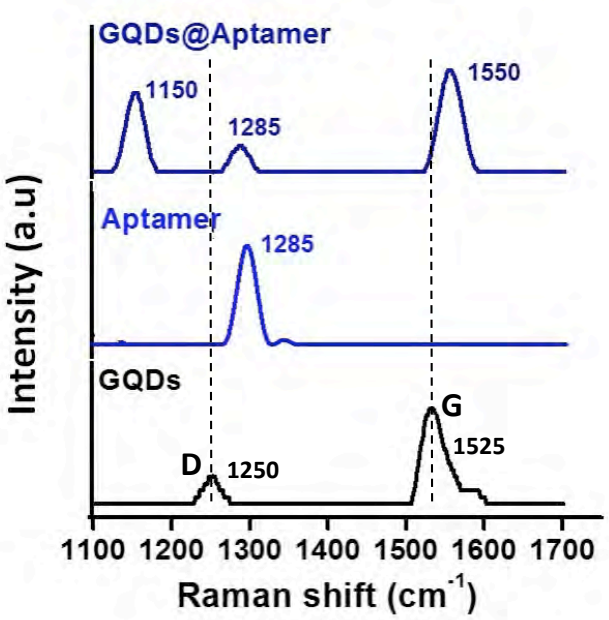

Figure 3.13: Raman of aptamer with its covalent conjugates with selected QDs. All samples analyzed in solid state.

Table 3.8: Aptamer and its covalent conjugates with selected QDs.

Electrode modifier	Raman D (cm^{-1})	Raman G (cm^{-1})	Aptamer Raman (cm^{-1})	Raman (I_D/I_G)
GQDs (8 h)	1250	1525	-	0.17
NGQDs (6 h)	1375	1600	-	1.50
gCNQDs (6 h)	1300	1590	-	0.83
GQDs-CoPc(1) ($\pi\pi$)	1300	1623	-	0.50
NGQDs-CoPc(1) ($\pi\pi$)	1280	1550	-	0.40
gCNQDs-CoPc(1) ($\pi\pi$)	1325	1600	-	0.50
Aptamer	-	-	1285	-
GQDs@Aptamer	1150	1550	1285	0.67
gCNQDs@Aptamer	1650	1750	1400	0.86

3.3.2 Conjugation by ππ interactions

3.3.2.1 UV/vis spectroscopy

The ππ interaction between the CoPc(1) and QDs of interest is illustrated in Scheme 3.5 using GQDs as an example.

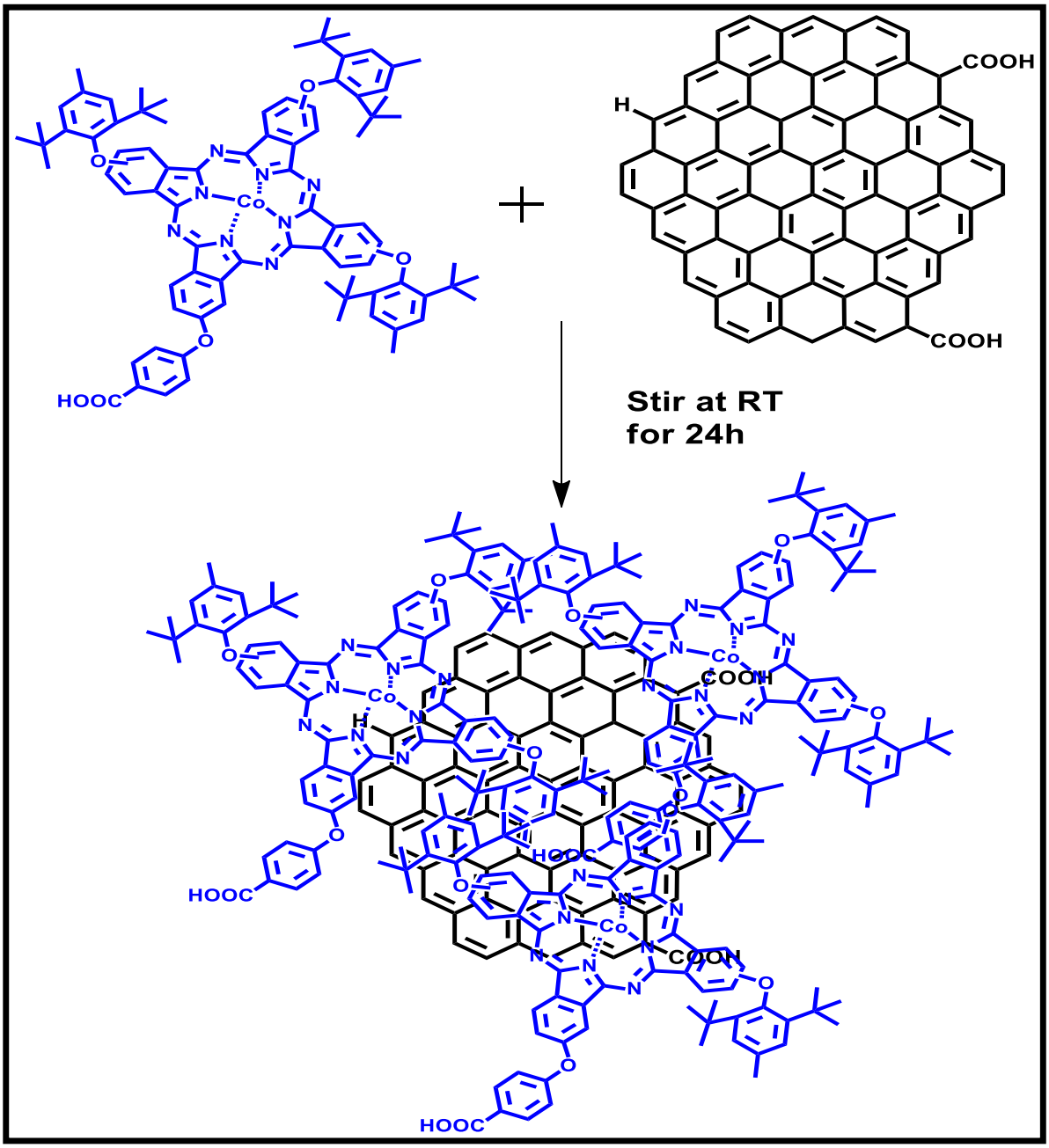

Scheme 3.5. The ππ conjugation of CoPc(1) with GQDs to form GQDs-CoPc(1) (ππ).

The NGQDs and gCNQDs were combined with the CoPc(1) in the same manner. The UV/vis spectra are shown in Figure 3.14 where comparative plots show how the CoPc(1) spectrum changes when conjugated to the QDs. QDs alone were dissolved in water (5 mg/mL), the Pc in DMSO (5 mg/mL) and the conjugates (2 mg/mL) in DMSO and water solvent mixture (3:1 v/v). The quantum dots synthesized in this work showed absorption peaks at 348 nm (GQDs), 344 nm (NGQDs) and 378 nm (gCNQDs), Table 3.6. GQDs-CoPc(1) ($\pi\pi$) and NGQDs-CoPc(1)($\pi\pi$) showed extensive aggregation with only the peak due to the aggregate being observed. These peaks are also blue shifted. For gCNQDs-CoPc(1) ($\pi\pi$), both the CoPc(1) monomer and aggregate peaks are observed and there is no change in peak position of the monomer following conjugation.

The loading of the CoPc(1) onto the QDs was investigated following previous studies using absorption instead of fluorescence [194]. This involves comparing the Q band absorbance intensities of the conjugate (QDs-CoPc(1)($\pi\pi$)) with that of the CoPc(1) before the conjugation. Equal masses (mg) for CoPc(1) and QDs-CoPc(1)($\pi\pi$) conjugates were weighed and separately dissolved in the same volume of the solvent. The loading values were determined to be 0.08, 0.39 and 0.21 mg/mg for the GQDs-CoPc(1) ($\pi\pi$), NGQDs-CoPc(1)($\pi\pi$) and gCNQDs-CoPc(1)($\pi\pi$), respectively. The low loading of the Pc on the GQDs could be due to repulsion in solution of deprotonated carboxylic acid groups on the Pc and on the GQDs. The NGQDs and gCNQDs have NH and NH_2 functions respectively, which, upon deprotonation become positively charged. Should this occur in solution, there is a possible attraction between the deprotonated COOH groups of the Pc and the

deprotonated NH and NH_2 groups of the NGQDs and gCNQDs, hence increasing the loading.

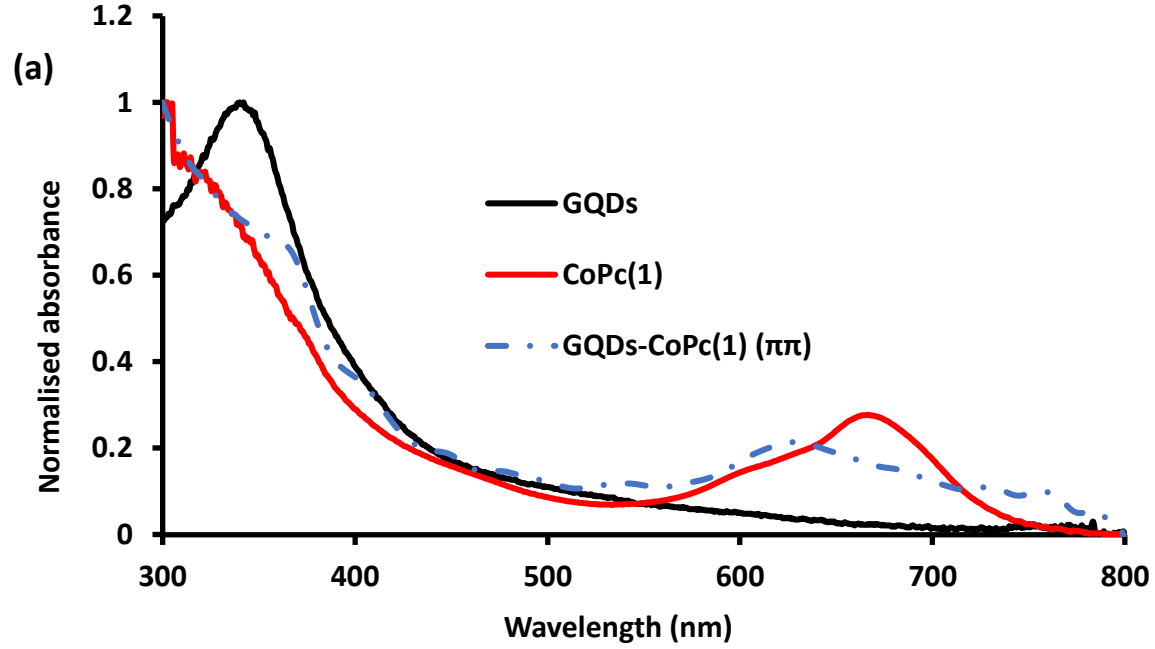

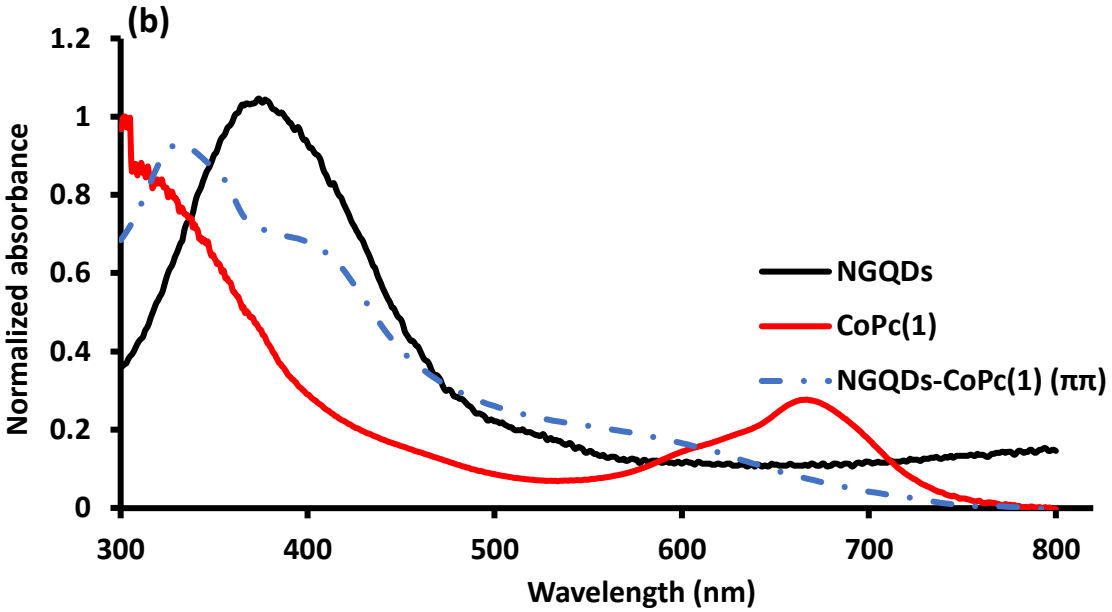

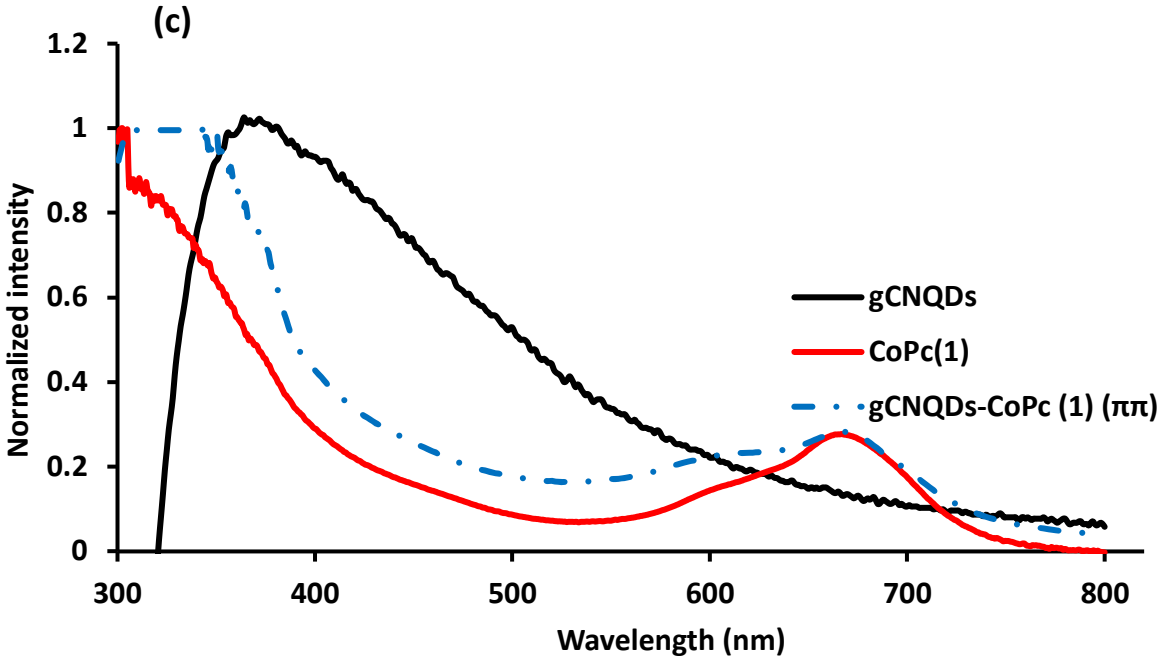

Figure 3.14: UV/vis spectra of (a) GQDs, (b) NGQDs and (c) gCNQDs and their conjugates with CoPc(1). All QDs were dispersed in water, CoPc(1) was dispersed in DMSO and the conjugates were dispersed in a DMSO/water mixture.

3.3.2.2 DLS and zetametry

Figure 3.15 illustrates the change in DLS distribution curve from the unconjugated quantum dots to the QDs-MPc conjugate. For analysis, the QDs were dispersed in water and their conjugates with CoPc(1) dispersed in a DMSO/water mixture. The profiles observed are broad indicating high polydispersity (PDI values and hydrodynamic radii shown in Table 3.6). Moreover, the conjugation of the QDs with the MPc resulted in an increase in the hydrodynamic radius measured for the QDs alone. For the GQDs (Fig. 3.15(a)), the size determined in DLS was 4.9 nm as stated above, Table 3.6. Upon conjugation with the CoPc(1), the hydrodynamic size increased to about 18.2 nm. The NGQDs Fig. 3.15(b)), showed hydrodynamic

sizes of 7.5 nm for the QDs alone and 15.7 nm when ππ conjugated to the CoPc(1). The gCNQDs, Fig. 3.15(c)), measured a hydrodynamic size of 10.1 nm with its CoPc(1)(ππ) conjugate measured at 18.2 nm. The zeta potential values of the GQDs, NGQDs and gCNQDs prior to conjugation were -30.1, -24.5 and -40.0 mV. When ππ conjugated to the CoPc(1), the zeta potential was increased to -33.9, -34.7 and -76.0 mV respectively. This shows improved stability in solution upon conjugation of the QDs to the MPc.

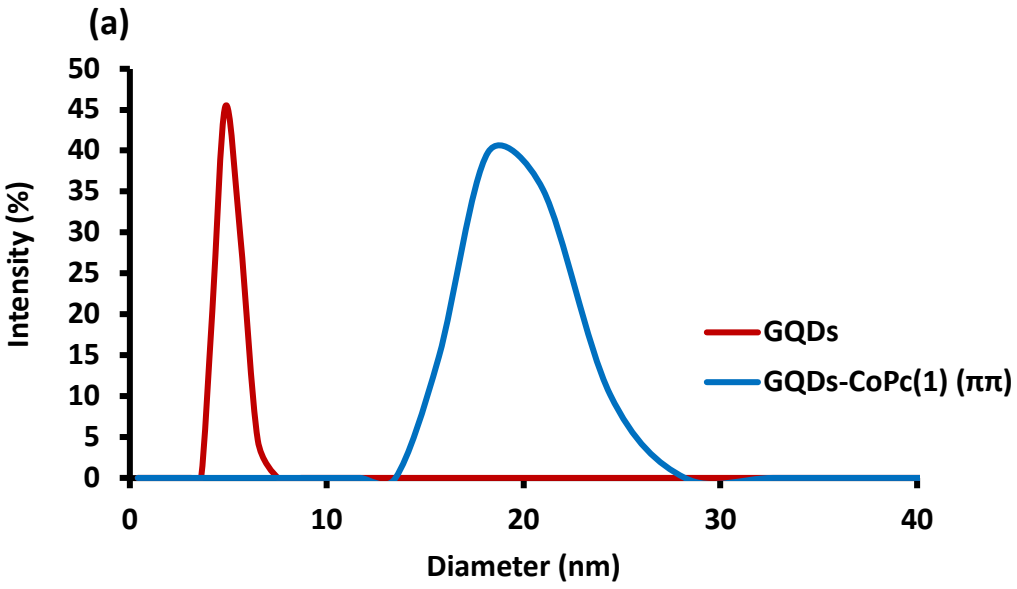

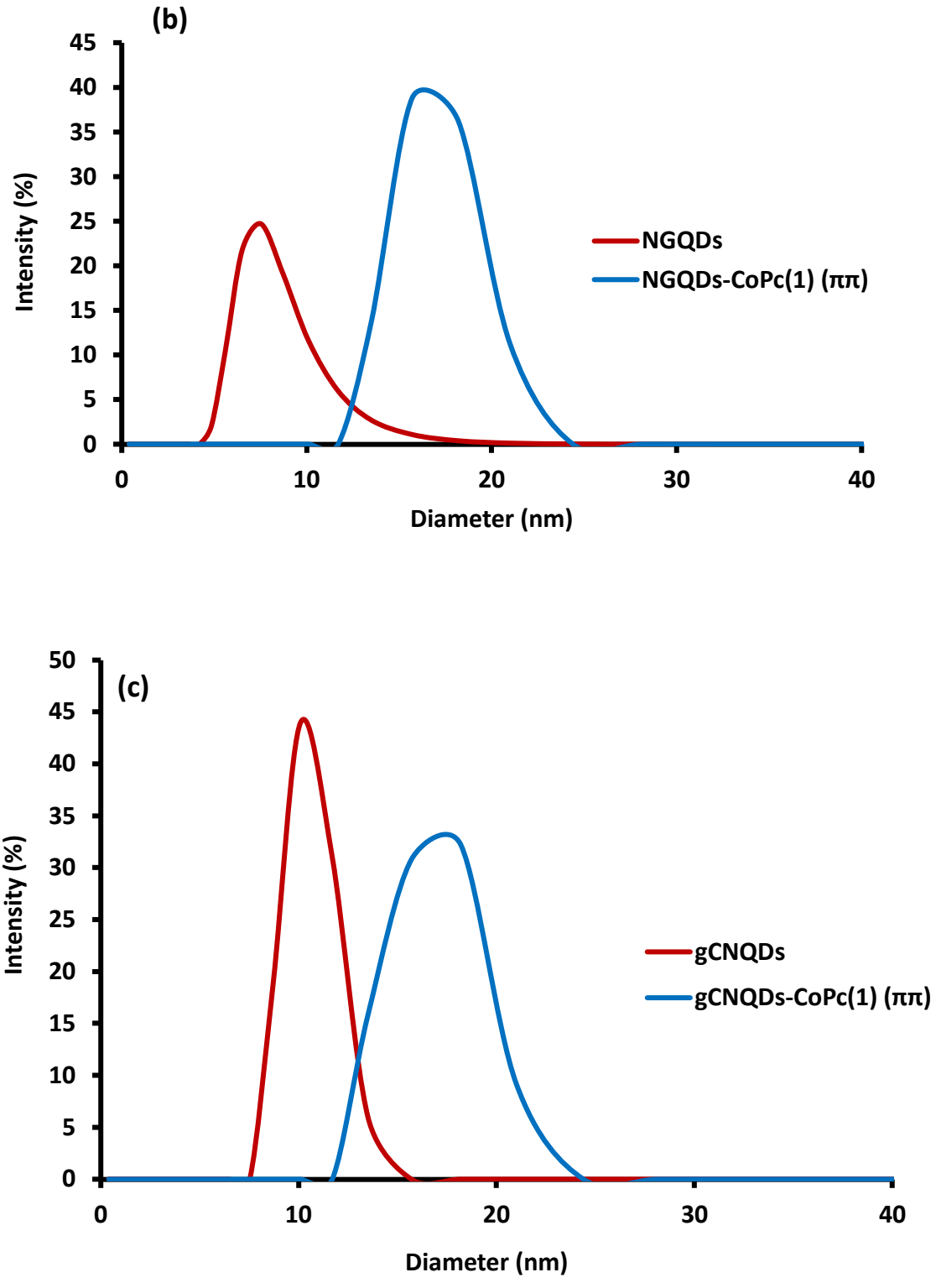

Figure 3.15: DLS plots of (a) GQDs, (b) NGQDs and (c) gCNQDs and their conjugates with CoPc (1). QDs alone were dispersed in water and QDs-Pc conjugates in DMSO/water (3:1 v/v) mixture.

3.3.2.3 Raman spectra

Raman was used to characterize the QDs and their conjugates with Complex 1. The spectra are shown in Figure 3.16. For the GQDs, the D band is observed at 1250 cm^{-1} and the G band at 1525 cm^{-1} with an I_D/I_G ratio of 0.17, Table 3.8. Upon conjugation with the CoPc(1) by $\pi\pi$ interactions, there is a shift to higher frequencies of 1300 cm^{-1} and 1623 cm^{-1} for the D and G bands, respectively with the I_D/I_G ratio determined as 0.50. Moreover, the decrease of the intensity of the G band is an indicator of the disorder occurring on the pristine GQDs structure and the shift in frequency is a result of strong interactions. The D and G bands of the NGQDs are observed at 1275 cm^{-1} and 1540 cm^{-1} respectively with an I_D/I_G ratio of 1.50, shifting to higher frequencies of 1280 cm^{-1} and 1550 cm^{-1} upon $\pi\pi$ conjugation with the CoPc(1). The G band intensity increases, however which is not expected when conjugation of the composites occurs. The I_D/I_G ratio for NGQDs-CoPc(1) ($\pi\pi$) was determined as 0.40. Regarding the gCNQDs, the D and G bands for this sample are observed at 1300 cm^{-1} and 1590 cm^{-1} respectively. Upon $\pi\pi$ conjugation with the CoPc(1) shifts of the peaks to higher frequencies of 1325 cm^{-1} and 1600 cm^{-1} are observed. The I_D/I_G ratio decreased from 0.83 to 0.50.

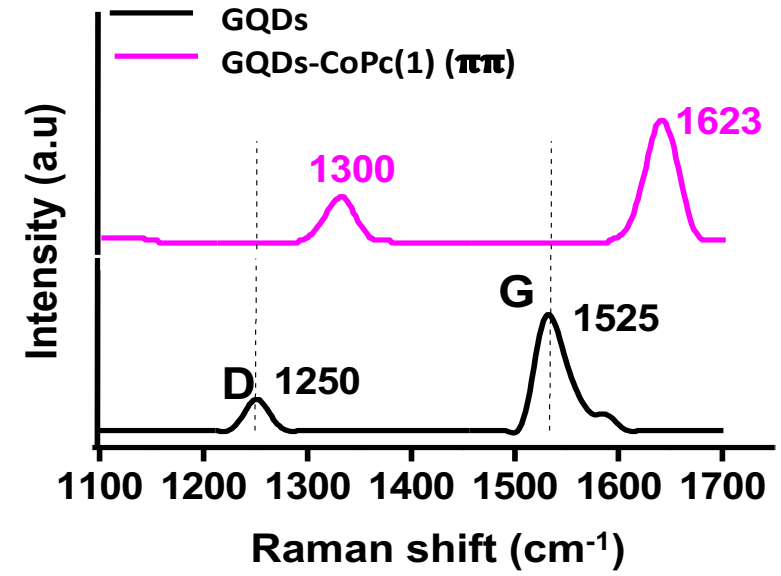
GQDs
GQDs-CoPc(1) (ππ)
Intensity (a.u)
1623
1300
G
1525
D
1250
1100 1200 1300 1400 1500 1600 1700
Raman shift (cm-1)

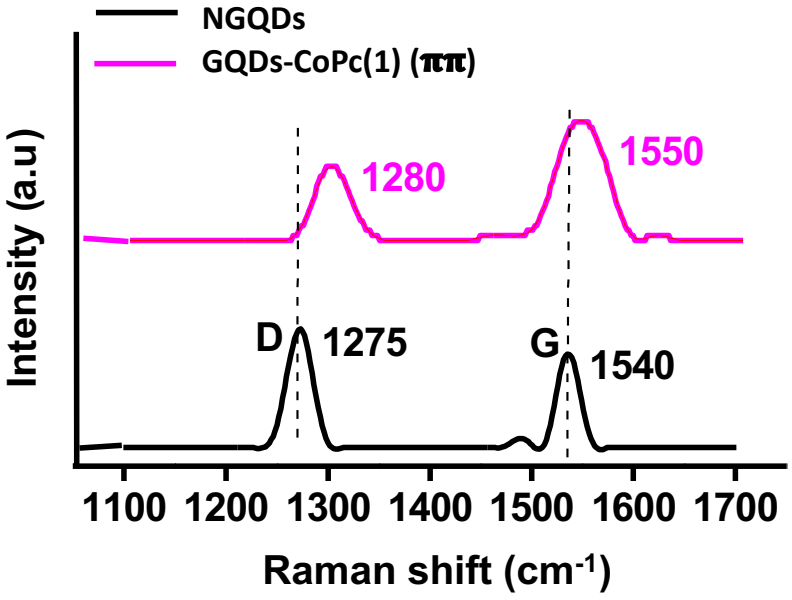
NGQDs
GQDs-CoPc(1) (ππ)
Intensity (a.u)
1550
1280
D
1275
G
1540
1100 1200 1300 1400 1500 1600 1700
Raman shift (cm-1)

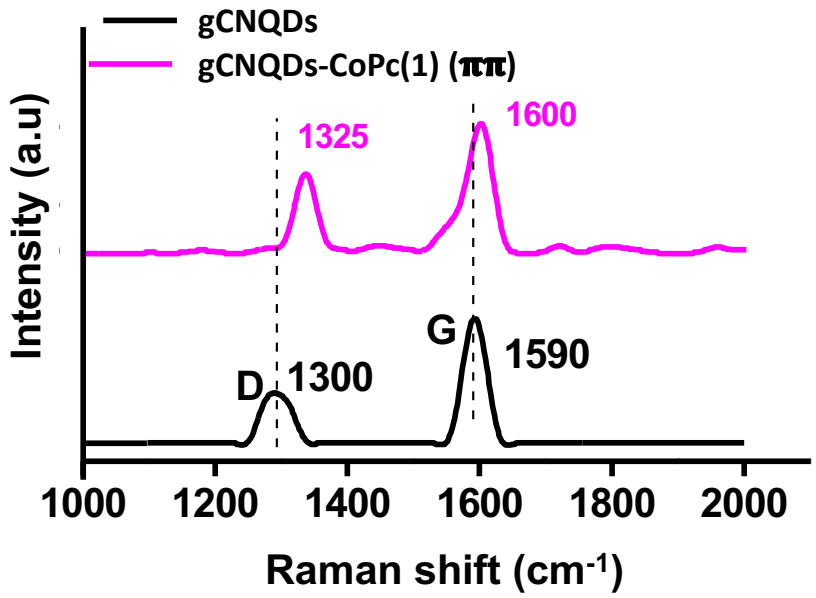

Figure 3.16: Raman spectra of QDs and their conjugates with CoPc(1).

3.4 Conclusion

The MPc complexes 1 and 2 were successfully synthesized, purified, and characterized using various techniques. Besides their obvious structural differences, their optical properties differed as well as seen in UV/vis spectral analyses. The synthesized gCNQDs, GQDs and NGQDs were characterized in their physical dry form and in solution. The optimization of the synthesis time proved useful in obtaining well dispersed nanostructures which could be further analyzed and characterized using electrophoretic separation analyses. The obtained results provided proof of the presence of the expected functional groups as well as overall structures. TEM images showed samples of differing dispersity but helped in deciding on the best dispersed samples to use going forward in this work. Moreover, the behavior of these nanostructures in solution such as their hydrodynamic size, surface charge and mobilities agreed with the presence of functional groups determined from structural characterization techniques. Capillary electrophoresis results obtained also showed that the samples had a high polydispersity which affected the separation efficiency. The synthesis optimization studies also showed that the synthesis time influences the quantum dots size, extent of functionality as well as in-solution behavior.

4. Electrode modification and characterization

This chapter outlines the electrode modification protocols as well as the characterization of these electrodes using surface characterization techniques and electrochemical methods. Methods of electrode modification include adsorption, electrodeposition, electrochemical grafting and click chemistry.

Table 4.1: List of modifiers and conjugates used for electrode fabrication.

Conjugates	**ΔE (mV)**	**Γ (x10^{-10} mol.cm^{-2})**
Bare GCE	77	-
GQDs-CoPc (**1**) (ππ)	161	0.09
• GQDs	321	1.59
• CoPc(**1**)	158	0.33
• GQDs-CoPc(**1**) (sequential)	107	6.50
NGQDs-CoPc (**1**) (ππ)	100.1	15.5
• NGQDs	466	3.1
• NGQDs-CoPc(**1**) (sequential)	615	8.2
gCNQDs-CoPc (**1**) (ππ)	100	30.2
• gCNQDs	90.4	39.3
• gCNQDs-CoPc(**1**) (sequential)	174	12.0
GQDs-CoPc (**1**) (ππ)-aptamer	361.5	2.99
NGQDs-CoPc (**1**) (ππ)-aptamer	139.1	28.1
gCNQDs-CoPc (**1**) (ππ)-aptamer	202.6	39.6
CoPc(**1**)@Aptamer	166	0.96
• CoPc(**1**)-Aptamer (sequential)	300	3.00
• CoPc(**1**)-Aptamer (premixed)	262	0.55
GQDs@Aptamer	617	1.99
• aptamer	178	0.11
• GQDs-Aptamer (sequential)	68	1.57
• GQDs-Aptamer (premixed)	262	0.009
gCNQDs@Aptamer	292	-
gCNQDs@Aptamer-CoPc(**1**) (ππ)	288	0.151
gCNQDs@Aptamer-CoPc(**2**) (ππ)	356	0.215
• CoPc(**2**)	169	0.066

4.1 Electrode modification by adsorption: Table 4.1

This method of electrode modification applies to the composites listed in Table 4.1 and depicted in Scheme 4.1 for gCNQDs-CoPc(1) (sequential) as an example. This includes the individual components as well as the covalently linked and ππ conjugated modifiers. Individual components were placed sequentially, by first placing the QDs on the electrode surface followed by the CoPc(1) or the aptamer. The components with aptamer were also premixed in addition to their sequential deposition onto the electrode surface. Literature has shown electrode modification using premixed composites, as well the sequential immobilization of nanostructures [195].

Preliminary studies of this work involved the study of the synthesized QDs and complex 1 as individual modifier and in combination, to determine the changes in current output. This was to validate the use of these nanocomposites as signal enhancers for the fabricated sensors towards the electrocatalytic detection of PSA.

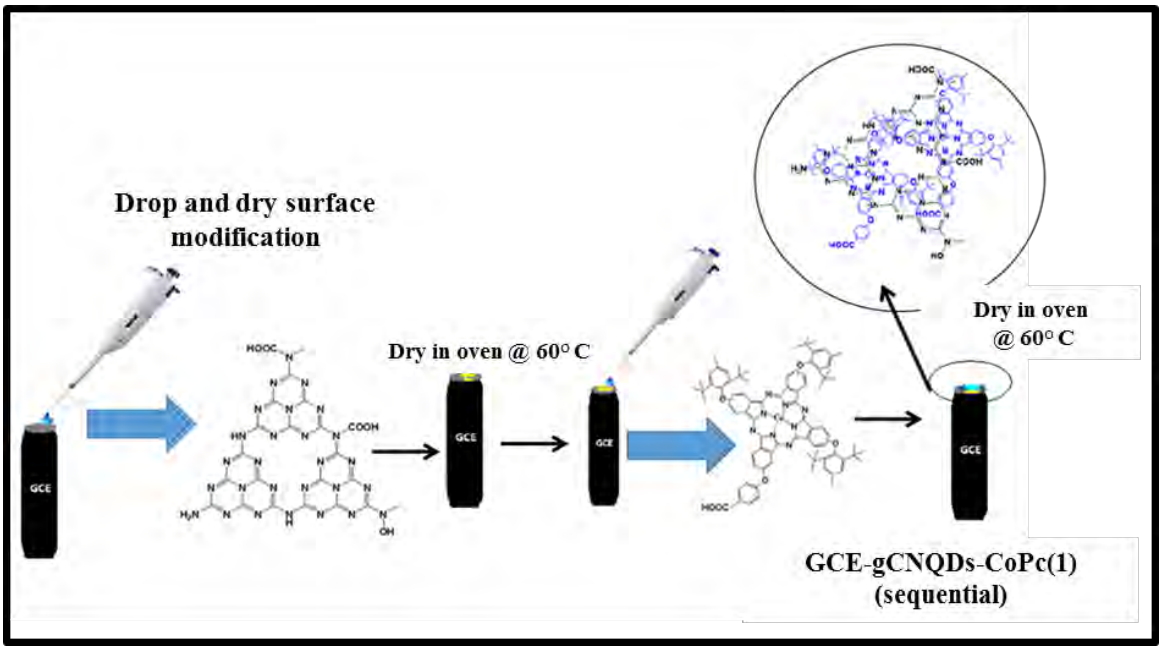

Scheme 4.1: Example of GCE fabricated in this work using sequential drop-dry electrode modification.

4.1.1 Cyclic voltammetry

Cyclic voltammetry was used to characterize the electrode surface to better observe the electrocatalytic ability of the modified electrodes. Peak separations are recorded in Table 4.1, which indicate that there has been a change on the electrode surface compared to that of the bare electrode.

To avoid congestion within one plot, only some of the cyclic voltammograms are shown in Fig. 4.1(a) where electrodes are tested in a 0.1 M KCl solution containing 1 mM ferricyanide (pH 7.5). Peaks near a potential of -0.5 V (I) are due to electrode modifiers associated with the redox processes of GQDs and have been observed before for modified electrodes containing GQDs [196]. GQDs possess oxygen-rich groups at the surface, which may result in their oxidation, making them good redox mediators. Moreover, their tunability allows them to act as

multivalent redox species. Moreover, peaks in the -0.5 V (I) region for electrodes containing CoPc(1) could be due to the $Co^{II}Pc^{-2}/Co^{I}Pc^{-2}$ redox couple [197].The DNA also show the peaks in this region [198], hence a peak is observed for the aptamer alone. The peaks labelled (II)are due to $[Fe(CN)_6]^{3-/4-}$ redox couple. Peaks at 0.70 V (III) can be assigned to ring based process in electrodes containing CoPc(1) [197]. However, the oxidation of amino acids such as guanine, which constitute the aptamer also occur in this region [199]. Although it may be of low intensity, the electrode containing aptamer alone also shows this peak (III). The lower ΔE_p is related to better charge transfer processes.

Comparing the different combinations of electrodes using GQDs and aptamer, the increase in ΔE_p is as follows: GCE-GQDs-Aptamer (sequential) (68 mV) < GCE-GQDs-Aptamer (premixed) (262 mV) <GCE-GQDs@Aptamer (617 mV), Table 4.1. These results show an improvement in charge transfer when the electrode is modified sequentially. The ΔE_p for GCE-GQDs-Aptamer (sequential) is near the Nernstian value. The GCE-GQDs@Aptamer with a higher ΔE_p, suggests bonding of the aptamer to more than one carboxylic acid functional group around the GQDs, hindering the GQDs from being able to mediate the transfer of electrons as it usually would when used to modify the electrode surface, therefore allowing for less electron transfer between the analytical solution and electrode. The GCE-GQDs-Aptamer (premixed) (262 mV) showing the second highest ΔE_p in this group indicates strong adsorption of aptamer on the GQDs thus hindering the electron transfer process compared to the sequentially modified electrode with the same components. The combination of the CoPc(1) with the aptamer showed a reverse trend where the increase in $\Delta E_p$is as follows: CoPc(1)-Aptamer (sequential) (300

mV) < CoPc(1)-Aptamer (premixed) (262 mV) < CoPc(1)@Aptamer (166 mV). This trend suggests that the CoPc(1) may not be lying flat on the electrode surface for the covalently linked molecule (CoPc(1)@Aptamer), leaving unmodified spaces to for charge transfer to take place. Thus, it can be said that the bonded aptamer does not passivate the electrode surface due to its orientation, as much as the aptamer on the surfaces of the premixed and sequential combinations does.

Of the QDs alone, the largest ΔE_p is observed for NGQDs (466 mV), showing poor charge transfer in ferricyanide, Table 4.1. The CoPc(1) alone has a ΔE_p of 158 mV, which improves in the presence of NGQDs when conjugated by $\pi\pi$ interactions. Moreover, in ferricyanide, the electrodes modified with combinations of QDs and MPcs by $\pi\pi$ interactions, compared to the sequentially combined modifiers, show a lower peak potential difference indicating better electrocatalytic activity, in the absence of any analyte. Therefore, in ferricyanide, GCE-GQDs-CoPc(1)($\pi\pi$), GCE-NGQDs-CoPc(1)($\pi\pi$) and GCE-gCNQDs-CoPc(1)($\pi\pi$) perform as better electrocatalysts compared to GCE-GQDs-CoPc(1) (sequential), GCE-NGQDs-CoPc(1) (sequential) and GCE-gCNQDs-CoPc(1) (sequential).

It is also important to test all electrodes in the absence of the analyte to ensure there are no interferences with the detection of the analyte of interest in solution. Fig. 4.1(b) shows the responses of the selected electrodes in the buffer in the absence of analytes. The peaks observed in these studies can then be used to determine surface coverages of the fabricated electrodes. When determining the electrochemical properties of a modified electrode surface, non-specific adsorption is one of the factors that need to be considered, hence the

determination of the electrode surface coverage values (amount of modifier per square centimeter) in this work.

The Randles-Sevcik Eqn.4.1 can be applied on $[Fe(CN)_6]^{3-/4}$ redox couple (Fig. 4.1(a)) to determine the effective electrode area.

$$I_p = 2.69 \times 10^5 n^{3/2} ACD^{\frac{1}{2}} v^{1/2} \qquad (4.1)$$

where I_p, A, C, D, n, and v are the peak current, the effective surface area, concentration of $[Fe(CN)_6]^{3-/4}$, diffusion coefficient of $[Fe(CN)_6]^{3-/4}$, the number of electrons involved, and scan rate, respectively. The literature value for D = 7.6×10^{-6} cm^2s^{-1} [200] for $[Fe(CN)_6]^{3-/4}$ was used. By using the effective area of the modified electrodes determined using Eqn. (4.1) above, and the total charge determined by integrating the anodic peak area of peaks (ii) in Fig. 4.1(b) and then by employing Eqn. (4.2), surface coverages were calculated.

$$\Gamma = \frac{Q}{nFA} \qquad (4.2)$$

where n is the number of electrons transferred (~ 1), F the Faraday constant (96,485 C mol^{-1}), A is the effective surface area obtained from Eqn. (4.1) and Γ is the surface coverage. The surface coverages calculated are shown in Table 4.1 and were generally higher than the reported value for phthalocyanines lying flat on the surface of the electrode (1×10^{-10} mol cm^{-2}) [201]. The higher surface coverages imply the increase in the electrode surface area, which offers more

electrocatalytic surface. For CoPc(1) $\pi\pi$ linked with QDs, the GQDs containing electrodes show the lowest coverages followed by NGQDs, with the gCNQDs containing electrodes showing the highest values. This then means that the gCNQDs are expected to perform better. The NGQDs are expected to perform better than the GQDs due to the addition of heteroatoms (nitrogen atoms) to the pristine graphitic structure, which is known to enhance electrocatalytic activity. Therefore, higher signal amplification is expected from the NGQDs-based electrode compared to the GQDs-based electrode. At first glance, better performance would be expected from the gCNQDs due to their predominantly nitrogen rich structure, as observed by the largest surface coverage value of the gCNQDs-CoPc(1)($\pi\pi$) modified electrode.

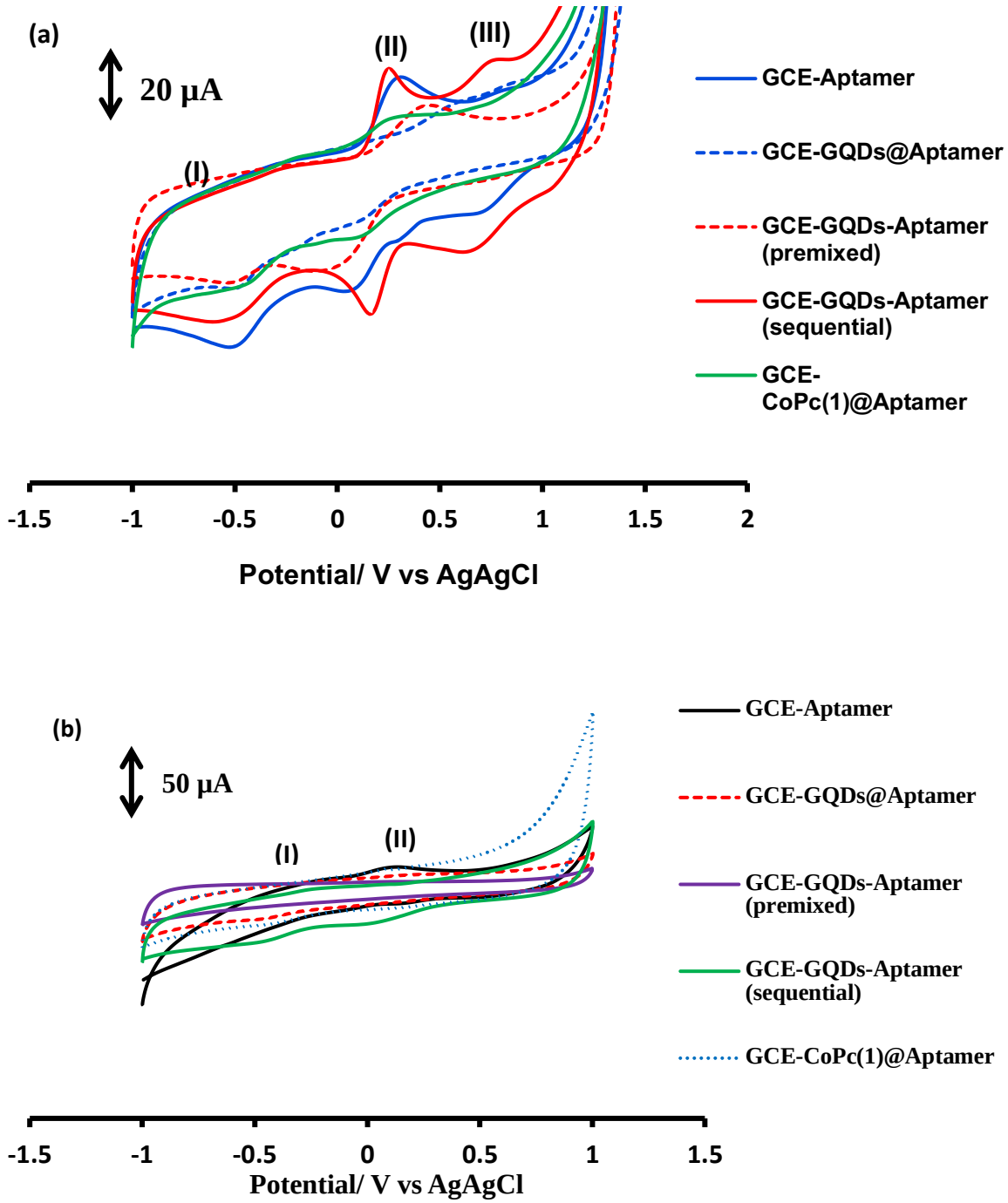

Figure 4.1: Electrodes in (a) 0.1M KCl containing 1mM $[Fe(CN)_6]^{3-/4-}$ and (b) 30 mM PBS solution of pH 7.4. Scan rate =100 mV/s. (Starting potential of scans = −1.0 V).

Following the study of the effects of QDs structure on composition on the behavior of the aptasensor, complex 2 was introduced to determine the effects of MPc substitution on the aptasensor behavior while keeping the nature of the QDs constant. As an example, covalently linked gCNQDs@Aptamer was used as the constant and complex 1 and complex 2 incorporated onto the modifier by ππ interactions. These composites were immobilized on the electrode surface using the drop-dry method. The modified electrodes for this part of the study are listed in Table 4.1. A higher surface coverage was obtained for GCE-gCNQDs@Aptamer-CoPc(2) ($\pi\pi$).

4.1.2 SECM

SECM was used for further probing of the behaviour of the modified surfaces. The CoPc(1), QDs and aptamer composites are used as examples. The analyses were done in a ferricyanide solution as was done for cyclic voltammetry. Fig. 4.2 shows the approach curves which provide information on the changes in tip current as the ultra-micro electrode (UME) tip approaches the substrate glassy carbon plate (GCP) in a feedback mode experiment in the presence of Fe^{2+}/Fe^{3+} redox mediator. The current generated at the tip of the electrode is determined by the substrate, the distance between the tip of the electrode and the substrate as well as the composition of the redox mediator. When the tip is closer to a conductive substrate surface, an increase in the current is observed while an insulating substrate is accompanied by a decline in the current [202].

The approach curves show an enhancement in current output of the QDs-CoPc(1)($\pi\pi$) compared to the bare GCP which contradicts the trends observed in

ΔE_p values where the bare GCE has a lower ΔE_p value which implies better conductivity. This contradiction may arise due to the nature of electrodes being used as well as the area in which the analysis is taking place, where greater aggregation may have occurred on the GCE surface compared to the analyzed area on the GC plate. In SECM, a GC plate is modified and a UME is used to analyze the conductivity of a specific area on the substrate in solution. With CV, the electrode is modified and used as the working electrode to determine extent of electron transfer between substrate and solution. These differences may be the reason contradictions are observed. In summary, the approach curves obtained for the different surfaces show that the bare GCP as well as the surface modified with the QDs-CoPc(1)($\pi\pi$) conjugate are conducting, with increasing normalized current as the UME approaches the GCP surface. Once the aptamer is incorporated in all cases, a drop in current is observed. The aptamer evidently has a passivating effect on the electrode surface.The area scans are shown in Fig. 4.3 for the bare GCP, GCP-QDs-CoPc(1)($\pi\pi$) and the GCP-QDs-CoPc(1)($\pi\pi$)-Aptamer. These scans illustrate the topography of the modified electrode surface as well as its conducting or insulating nature within the area analyzed. For GQDs-CoPc(1)($\pi\pi$), there is a slight reduction in current of the modified region compared to the bare GCP, which may indicate passivation of the GCP surface upon modification, confirming ΔE_p values. When the aptamer is immobilized at the surface, the surface conductivity is further passivated which correlates with the results obtained for the approach curves. For NGQDs-CoPc(1)($\pi\pi$), and gCNQDs-CoPc(1)($\pi\pi$), there is an enhancement in surface conductivity compared to bare GCP, contradicting ΔE_p values as discussed for the approach curves as well. The

current decreased however, upon immobilization of the aptamer, which was expected as the same trend was observed on the approach curves.

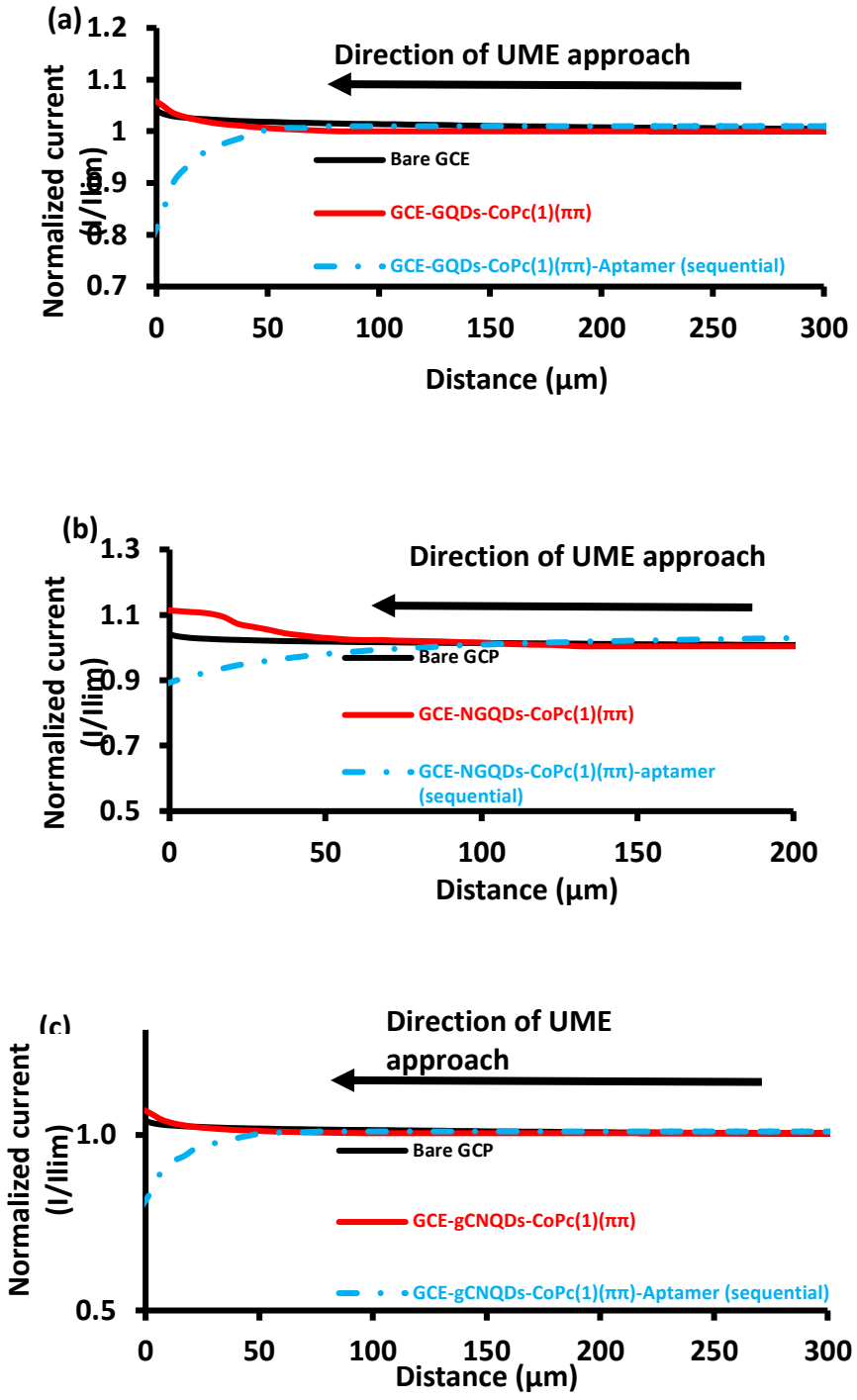

Figure 4.2: Approach curves of bare GCPs with (a) GQDs, (b) NGQDs and (c) gCNQDs based conjugates.

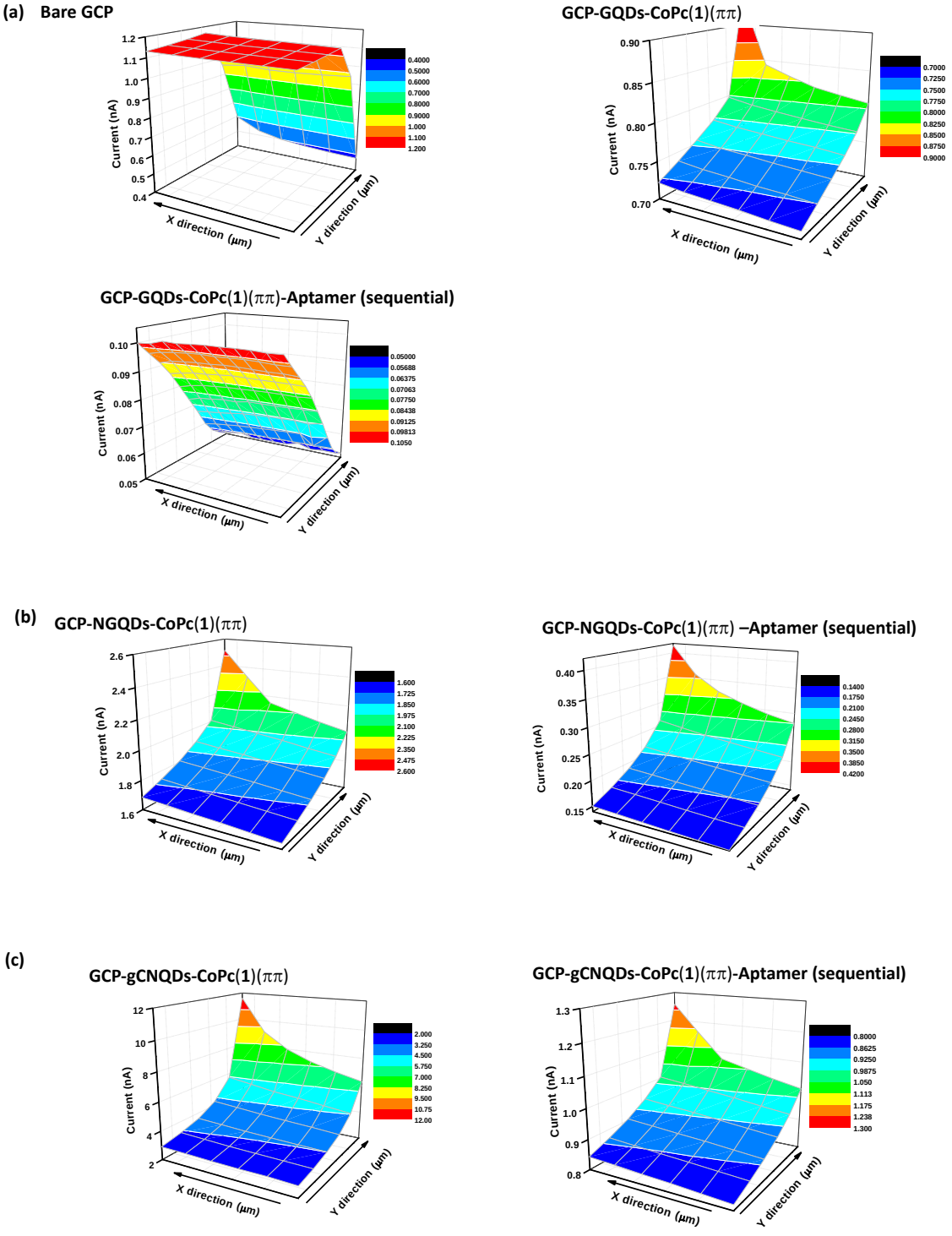

Figure 4.3: Area scans of bare GCPs with (a) GQDs, (b) NGQDs and (c) gCNQDs based conjugates.

4.2 Preparation and characterization of AuNPs, CoPc(2) and aptamer-based electrodes

This section shows the use of complex 2 and Au nanoparticles (AuNPs) as nanoplatforms for the immobilization of an aptamer to prepare novel aptasensors. The synergistic effects of these complex 2 and AuNPs are studied. Literature has shown the use of AuNPs-containing nanoconjugates as platforms for the immobilization of PSA-binding aptamer towards the detection of PSA [134, 141-144, 203]. These nanoconjugates have aided in improving the stability and sensitivity of the fabricated devices. Although these aptasensors have shown good promise as potential early diagnostic tools for PSA, the combination of electrodeposited AuNPs and phthalocyanines with aptamer, has not been studied, thus introducing another novel aspect to this thesis. Moreover, electrochemical grafting and click chemistry are employed, in order to fabricate these aptasensors. This technique has not been used to fabricate PSA aptasensors before. Scheme 4.2 illustrates the fabricated aptasensors as well as the protocol followed in achieving this.

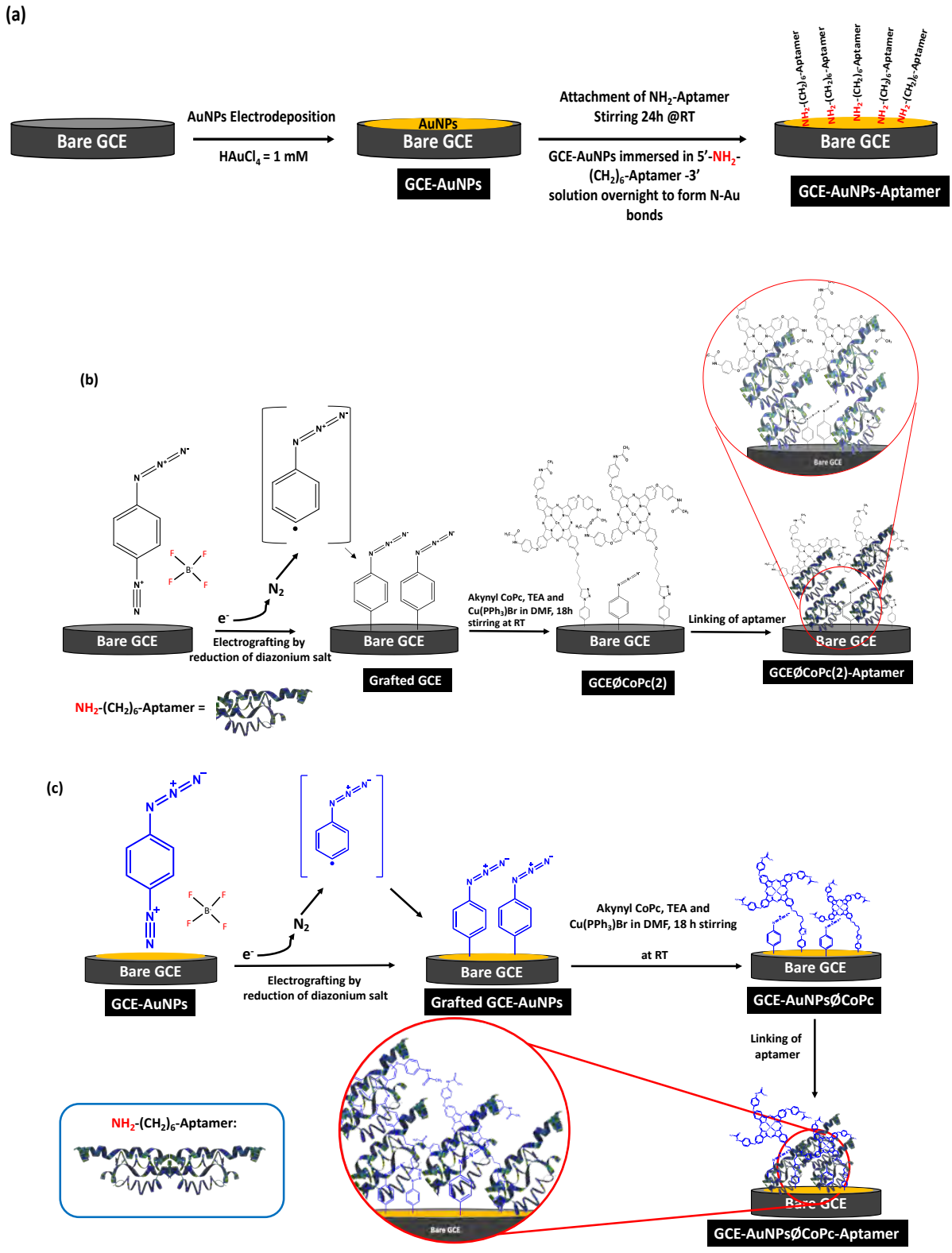

Scheme 4.2: Fabrication process of (a) GCE-AuNPs-aptamer, (b) GCEØCoPc(2)-Aptamer and (c) GCE-AuNPsØCoPc(2)-Aptamer.

4.2.1 Electrodeposition of AuNPs, Scheme 4.2(a)

4.2.1.1 Cyclic voltammetry

AuNPs were obtained via the electroreduction of the gold salt in 0.1 M $NaNO_3$ by cyclic 10 scans using the cyclic voltammetry technique shown in Fig. 4.4. After cycling, the electrode surface appeared gold in color confirming the success of the deposition (Fig. 4.4). The formation AuNPs is represented in Fig. 4.5. The forward scan shows the reduction of Au(III) to Au(0) with a cathodic peak at 0.41 V, resulting in the deposition of AuNPs onto the GCE surface (GCE-AuNPs), Fig. 4.4. Literature reports have recorded a value of 0.48 V, which is close to the value obtained in this work [165]. The decrease in current following electrodeposition has also been reported [165], which is due to the consumption of the gold salt. The electrodeposited AuNPs were then activated, following literature methods [165] using 0.5 M H_2SO_4 by cyclizing (10 scans) from 0.2 V to 1.4 V. Fig. 4.4(b) shows the cyclic voltammogram of the 10^{th} scan. The anodic and cathodic peaks increased with the increase of the number of scans. The anodic peaks between 1.0 and 1.3 V correspond to Au oxidation. The presence of two oxidation peaks suggests the formation of different types of Au oxides [165]. However, AuO is formed as the main oxide according to Eqn. (4.3):

$$Au + H_2O \rightarrow AuO + 2H^+ + 2e^- \qquad (4.3)$$

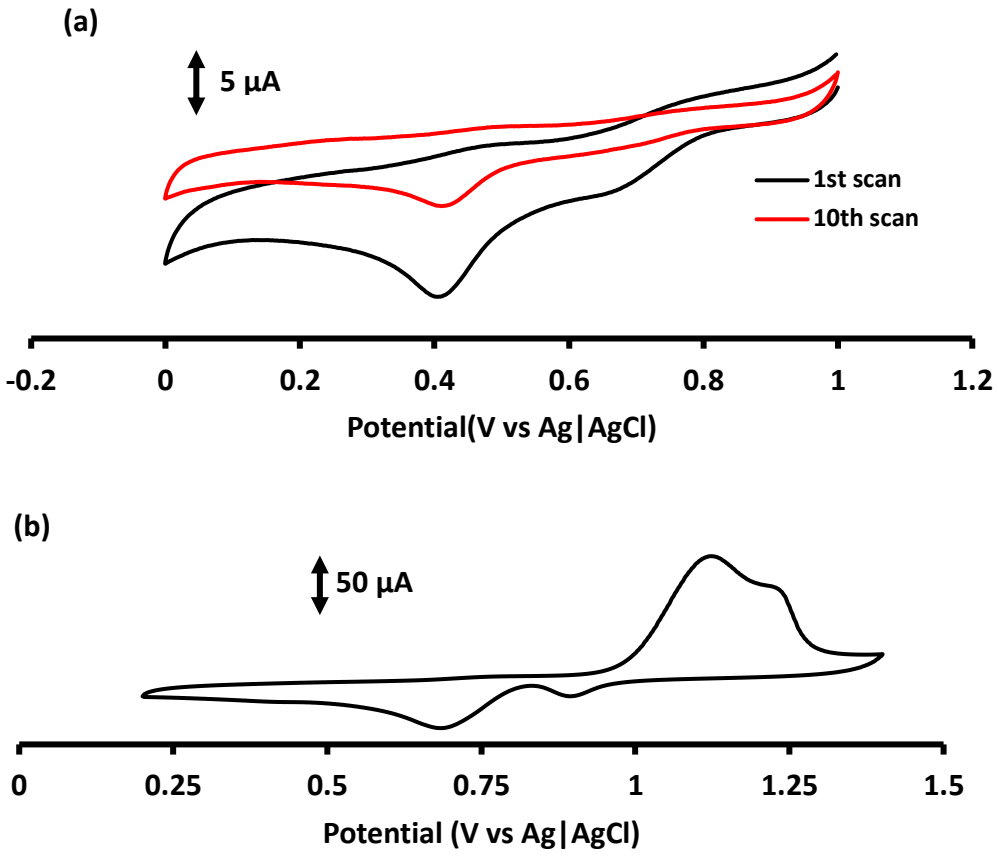

Figure 4.4: Cyclic voltammograms of (a) the first and the last scan of 1 mM $HAuCl_4$ in 0.1 M $NaNO_3$ (scan rate 50 mV/s) and (b) GCE-AuNPs in 0.5 M H_2SO_4 solution (activated AuNPs at scan rate= 100 mV/s).

Figure 4.5: Images of a bare GCE and the GCE after cycling in 1 mM $HAuCl_4$ in 0.1 M $NaNO_3$.

4.2.1.2 Energy dispersive X-ray (EDX) spectroscopy and scanning electron microscopy (SEM)

To verify the formation of AuNPs on glassy carbon surfaces, scanning electron microscopy (SEM) was used to analyze a bare glassy carbon plate as well as the one modified with AuNPs. The GCP was modified in the same manner as the GCE was. Verification of the elemental composition at the substrate surface was achieved using EDX, illustrated by Fig. 4.6. In Fig. 4.6(a), the bare plate is shown with the EDX spectrum showing only carbon which is due to the carbon surface. The EDX spectrum in Fig. 4.6(b), shows the presence of Au. Fig. 4.6(b) also shows the SEM image of the electrodeposited AuNPs which appear well distributed spherical. The EDX spectrum confirms the presence of the AuNPs thus proving the success of the electrodeposition of these nanostructures on a glassy carbon plate.

The AuNPs formed by electrodeposition on the electrode surface were thereafter collected for UV characterization by sonicating the electrode in DMF. The color in DMF was pale purple as expected [204]. The absorption spectrum was obtained and is shown in Fig. 4.7. The absorption peak is recorded at 436 nm, which is surface plasmon resonance band.

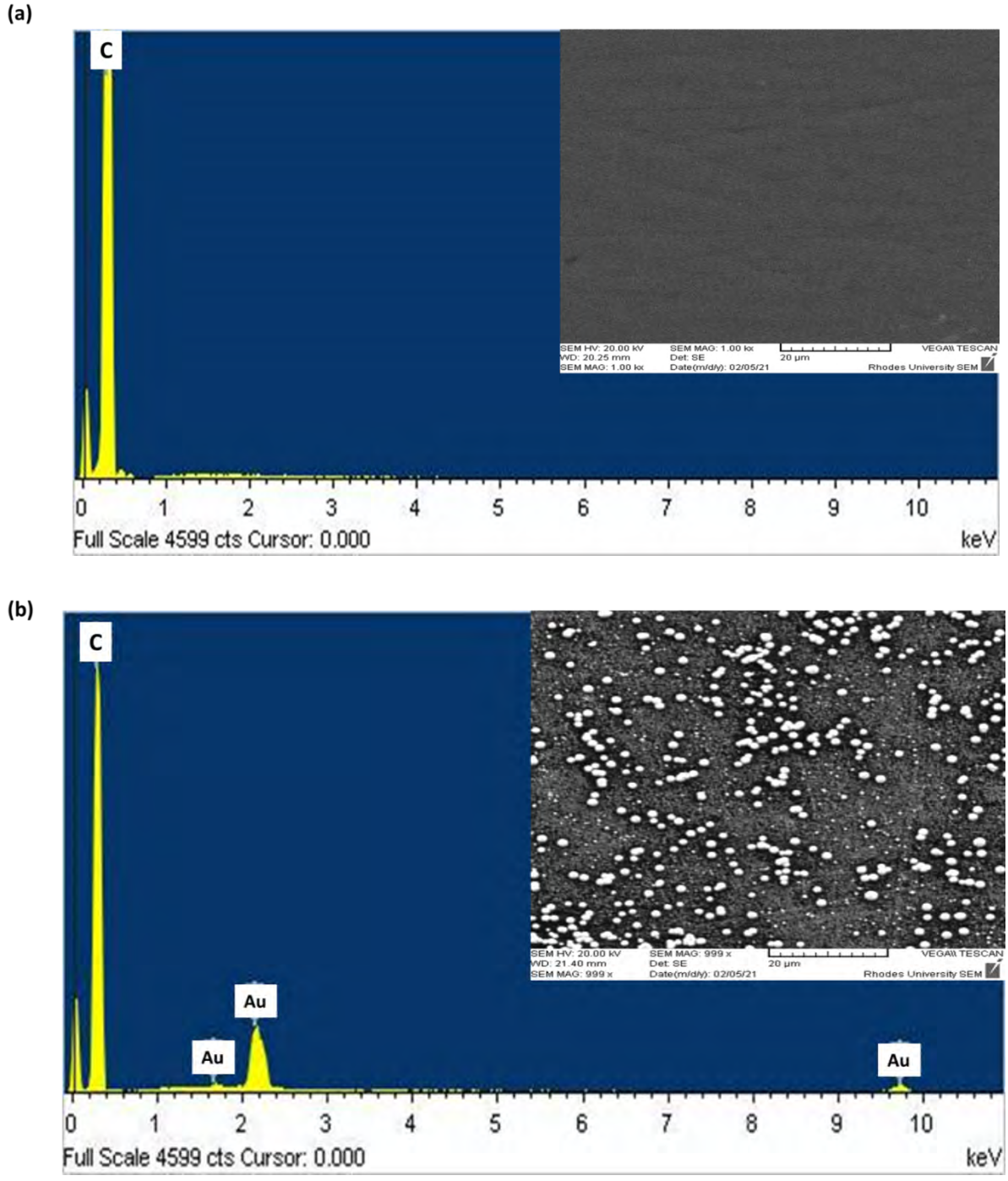

Figure 4.6: EDX analysis spectra of (a) Bare GCP and (b) GCP-AuNPs. Inserts: Corresponding SEM images.

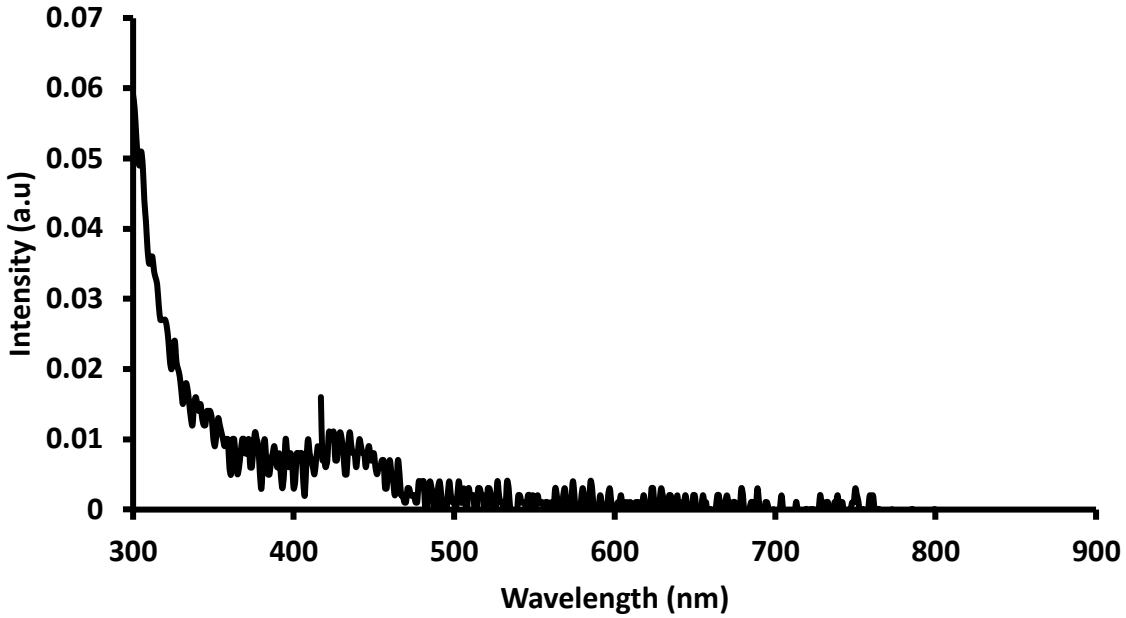

Figure 4.7: Absorption spectrum of AuNPs in DMF.

4.2.2 Self-assembly (Scheme 4.2(a)), electrochemical grafting and click chemistry, Scheme 4.2 (b, c)

The GCE-AuNPs was then linked to aptamer via the NH_2 functional group by self-assembly, as nitrogen is known to have an affinity for Au. Scheme 4.2(a) illustrated the fabrication of GCE-AuNPs-Aptamer. The evolution of the cycling voltammograms due to the electrografting of the GCE is shown in Fig. 4.8. This was achieved in a solution of 1 mM 4-azidobenzenediazonium tetrafluoroborate in 0.1 M $TBABF_4$ in acetonitrile, within a potential window of -1.0 V to 0.2 V at 50 mV/s. A reduction peak is observed at -0.79 V on the first cycle of the bare GCE and completely disappears on the 3rd cycle confirming passivation of the electrode surface by azide groups [205]. The gold surface was also electrografted the same way the bare GCE was. For the GCE-AuNPs, the reduction peak is also observed at around -0.79 V but the peak only disappears on the 5th cycle which is not

uncommon [206]. The electrografting of gold surfaces has been reported in literature, however, the reduction peak observed at -0.35 V [167]. Both the grafted GCE and the GCE-AuNPs were then linked to CoPc(2) via click chemistry to form GCEØCoPc(2) and GCE-AuNPsØCoPc(2). To immobilize the aptamer on these surfaces, the aptamer was adsorbed at the GCEØCoPc(2) and GCE-AuNPsØCoPc(2) surfaces to give GCEØCoPc(2)-Aptamer (Scheme 4.2 (b)) and GCE-AuNPsØCoPc(2)-Aptamer (Scheme 4.2(c)). Both electrodes were tested in an electroactive solution to confirm the passivation of their surface and the data reported in the next section.

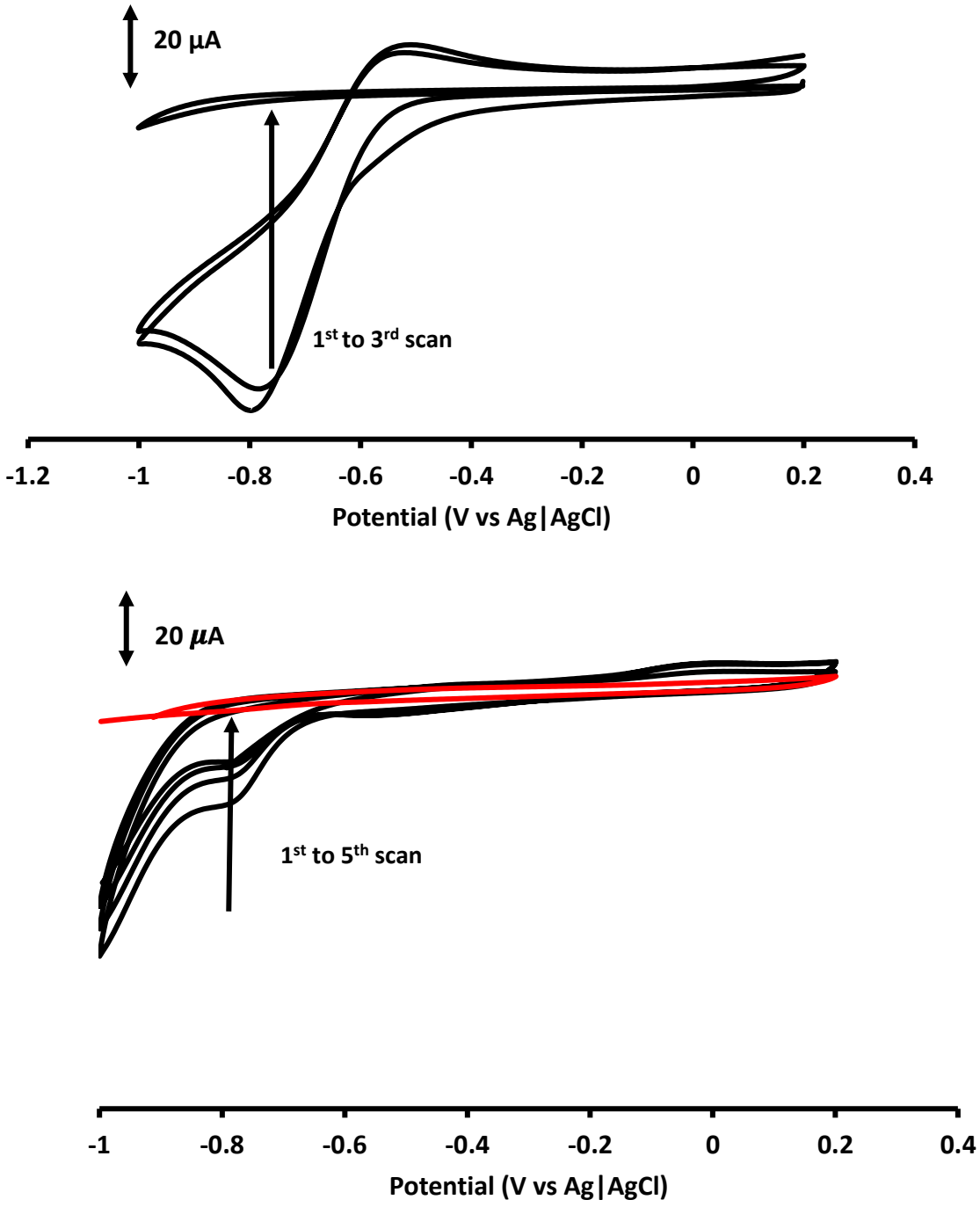

Figure 4.8: Cyclic voltammograms evolving during electrografting of (a) bare GCE and (b) GCE-AuNPs.

4.2.3 Cyclic voltammetry characterization

All the electrode surfaces were tested using cyclic voltammetry analysis in a 0.1 KCl solution containing 5 mM $K_3[Fe(CN)_6]$ and the results are shown in Fig. 4.9(a-c). From these figures, the peak separation values, **Δ**E, are recorded in Table 4.2. The modified electrodes were also tested in a buffer solution (PBS pH 7.4) before addition of the analyte and the selected CVs are shown in Fig. 4.9(d).

When looking at the results obtained from characterizing the electrodes in the ferricyanide solution, the aptamer was expected to passivate the electrode completely; however, results showed that there was still some current output, which is indicative of some exposed areas of the GCE after the modification of the surface, Fig. 4.9(a). Fig. 4.9(b) shows complete passivation due to grafting the electrode surface as well as when the aptamer is immobilized at the surface of the electrode. Fig. 4.9(c) shows that the combination of AuNPs and CoPc(2) enhances current output, and upon immobilization of the aptamer there is a significant decrease in the peak current indicating the success of immobilization of the aptamer on the electrode surface. From these cyclic voltammograms, ΔE values were determined. As previously mentioned, an increase in this value implies a decrease in current output due to blocking of electroactive sites at the electrode surface. The highest value was determined for GCE-AuNPsØCoPc(2)-Aptamer and the lowest value was obtained for the GCE-AuNPsØCoPc(2) which agree with what is observed in the voltammograms.

When the electrodes were studied in the buffer solution, no peaks were observed for the bare GCE, electrografted GCE, GCE-Aptamer, GCEØCoPc(2)-aptamer and GCE-AuNPsØCoPc(2)-Aptamer. The peaks in the circled part of Fig. 4.9(d) could be due to $Co^{III}Pc^{-2}/Co^{II}Pc^{-2}$processes in CoPc(2) containing electrodes. The peaks that

were observed were quite broad and flattened but attempts to integrate them were made to estimate the surface coverage. The effective electrode area and surface coverages were calculated as done for the electrodes already mentioned in this chapter. The calculated parameters are summarized in Table 4.2. The highest surface coverage value was obtained for GCE-AuNPsØCoPc(2) indicating that the combination of the AuNPs with the phthalocyanine enhances the surface area of the electrode, which is what is needed in order to achieve the maximum output and efficiency of the sensor.

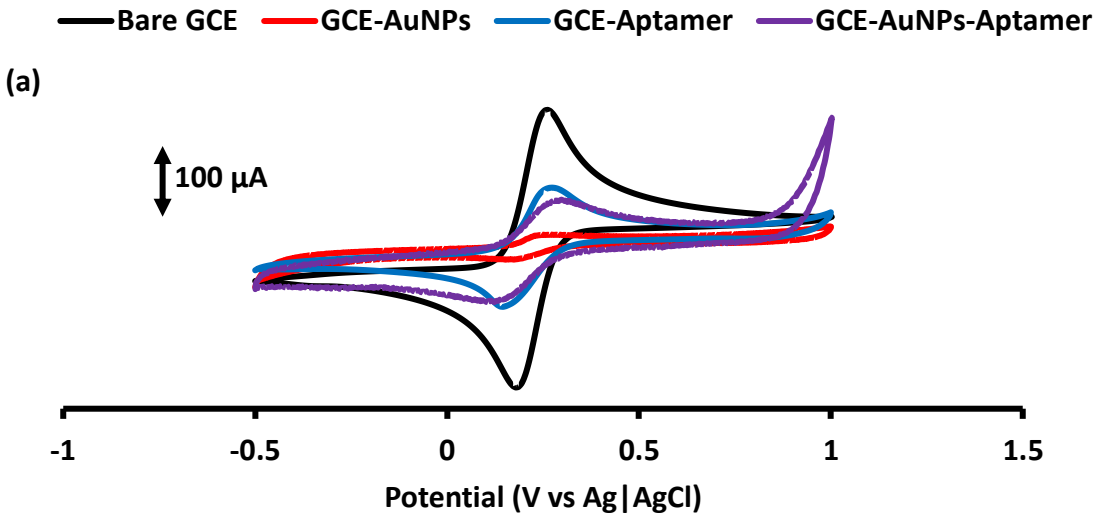
Bare GCE
GCE-AuNPs
GCE-Aptamer
GCE-AuNPs-Aptamer
(a)
100 µA
-1
-0.5
0
0.5
1
1.5
Potential (V vs Ag|AgCl)

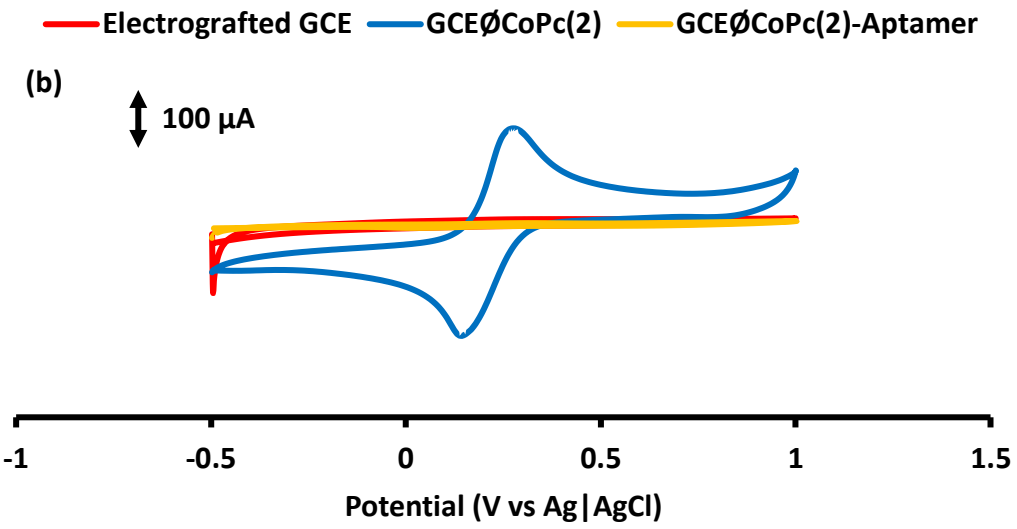
Electrografted GCE
GCEØCoPc(2)
GCEØCoPc(2)-Aptamer
(b)
100 µA
-1
-0.5
0
0.5
1
1.5
Potential (V vs Ag|AgCl)

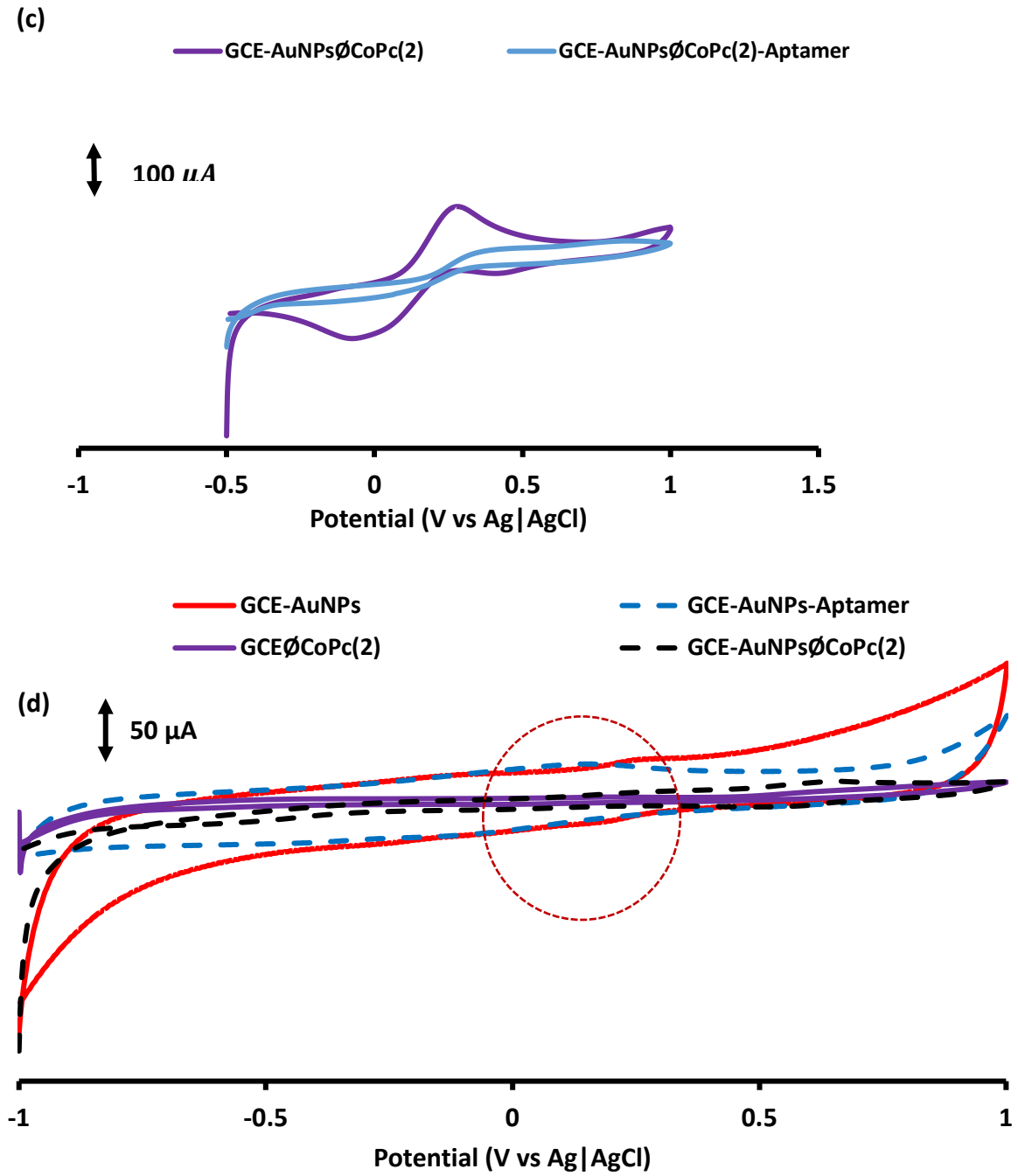

Figure 4.9: Cyclic voltammograms of bare and modified electrodes in (a), (b) and (c) 5 mM $K_3[Fe(CN)_6]$ containing 0.1 KCl solution containing and (d) in PBS solution pH 7.4. Scan rate = 100 mV/s.

Table 4.2: Summarized cyclic voltammetry data for the electrodes in 0.1M KCl containing 1mM $[Fe(CN)_6]^{3-/4-}$ solution.

Electrode	**Δ**E/ mV $K_3[Fe(CN)_6]$ in 0.1 M KCl	**Γ** mol.cm^{-2} (x 10^{-9}) in pH 7.4 buffer
Bare GCE	77	-
GCE-AuNPs	83	1.19
GCE-Aptamer	134	-
GCE-AuNPs-Aptamer	164	1.23
GCEØCoPc(2)	147	2.34
GCEØCoPc(2)-Aptamer	273	-
GCE-AuNPsØCoPc(2)	56	7.12
GCE-AuNPsØCoPc(2)-Aptamer	573	-

4.2.4 Scanning electrochemical microscopy (SECM) characterization

Further characterization of the modified surfaces was done using SECM. The studies were done in ferricyanide, as it is a conductive solution. Approach curves were recorded and are shown in Fig. 4.10. The bare and electrodes modified with AuNPs, CoPc(2) and AuNPsØCoPc(2) were conducting. The grafted electrodes showed a drop in normalized current as the UME approached the surface. This was expected and in agreement with the results obtained in the same solution using cyclic voltammetry as the analytical technique. The introduction of the aptamer also indicated a passivated surface.

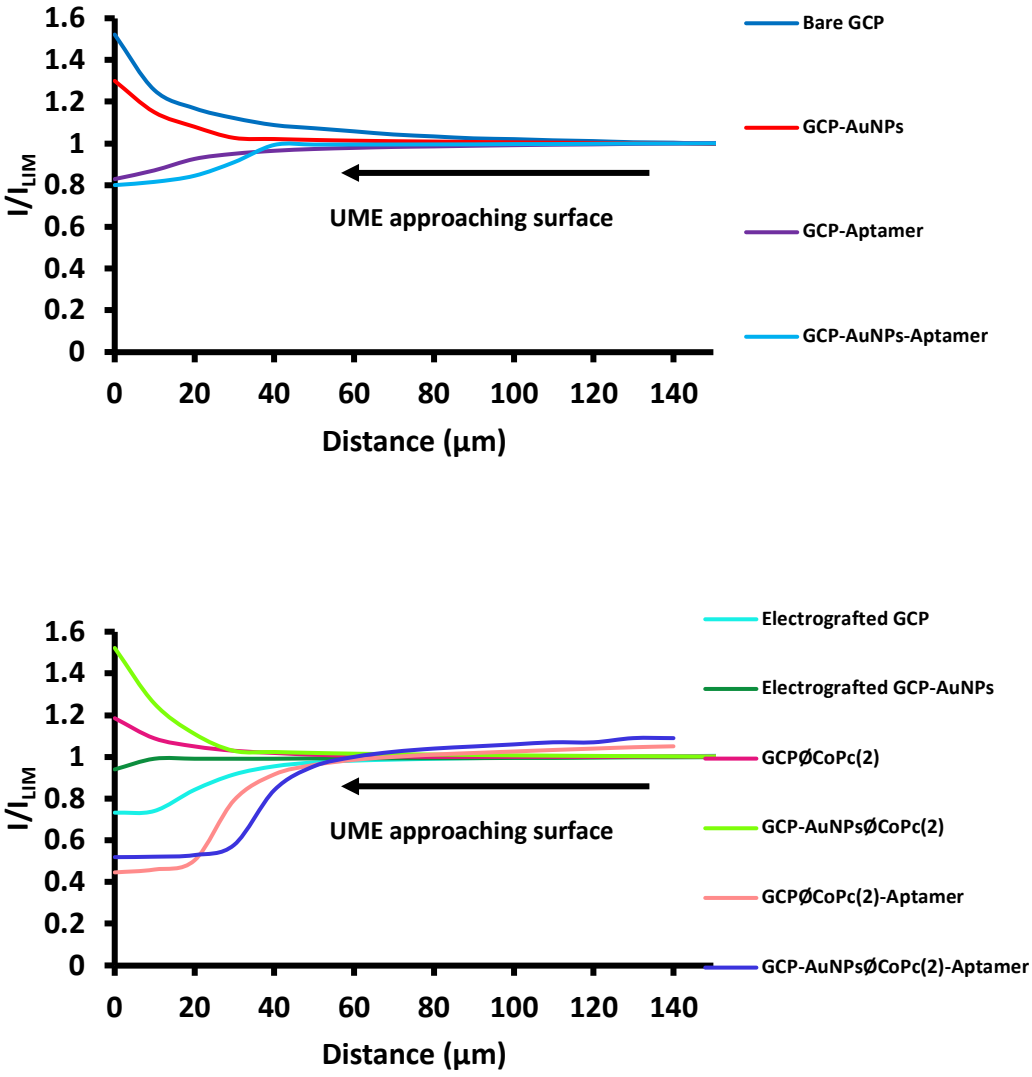

Figure 4.10: Approach curves of bare and modified electrodes in 0.1 KCl solution containing 5 mM $K_3[Fe(CN)_6]$. Curves are plotted separately to avoid crowding on one plot.

4.2.5 XPS spectra

XPS analyses was carried out to validate some of the conjugations performed in the electrode fabrication process. Initially, wide scans were obtained to see if all expected elements were present on each fabricated surface. The survey scans of the fabricated aptasensors are shown in Fig. 4.11. The analyzed surfaces are the GCP-AuNPs-Aptamer, grafted AuNPs surface, grafted GCP, the GCP-AuNPsØCoPc(2)-Aptamer and the GCPØCoPc(2)-Aptamer. Fig. 4.11(a) shows the survey scan for GCP-AuNPs-aptamer sensor. All expected elements were observed as also reported in literature [207]. The nitrogen peak is likely due to the amine groups on the aptamer. The Au4f high resolution scan for GCP-AuNPs-Aptamer (Fig. 4.12(a)) was deconvoluted to assign the peaks associated with the expected AuN bond since N (in the aptamer) has an affinity for Au. Four peaks were extracted at binding energies of 84.0, 86.0, 87.5 and 89.6 eV, Table 4.3(a). These peaks have been assigned to AuN ($Au4f_{5/2}$), Au^0 ($Auf_{5/2}$), AuN ($Auf_{7/2}$) and Au^0 ($Auf_{7/2}$) respectively [208]. The presence of AuN confirms that the aptamer is linked to AuNPs through the N groups on the aptamer.

Fig. 4.11(b) shows the survey scans for the electrografted GCP and GCPØCoPc(2)-aptamer. The presence of Co in the clicked surface at 683.8 eV was an indication of the presence of the CoPc(2) at the GCP surface. The P atom from the backbone of the aptamer, confirmed the adsorption of aptamer at the electrode surface. The high-resolution spectra of the N1s peaks (Fig. 4.12(b)) from the grafted and clicked electrode were extracted and deconvoluted to verify the success of the click reaction. The identified peaks and their assignments are summarized in Table 4.3(b) with the spectra shown in Fig. 4.12(b). The N1s spectrum of the grafted

GCP showed two peaks after deconvolution at binding energies of 399.5 and 402.5 eV which have been assigned to the azide nitrogen atoms of the terminal azide groups. The lower intensity peak at higher binding energy is due to the electron deficient central nitrogen [209]. The clicked surface showed four peaks after deconvolution at binding energies of 398.5, 399.5, 401.0 and 402.5 eV, Table 4.3 (b). The peaks due to the azide groups at 399.5 eV and 402.5 eV are still visible showing that not all azide groups were part of the click reaction. However, they were reduced to intensities of 7000 cps and 7400 cps respectively, compared to the intensities observed for the grafted GCP which were at 10800 cps and 8900 cps respectively. The lower intensities prove that some of the azide groups were 'clicked' to the alkynyl group of the MPc. The peaks at 398.5 and 401 eV have been assigned to N-N and N-C respectively [210].

Fig. 4.11(c) shows the survey scans of the grafted gold surface as well as the GCP-AuNPsØCoPc(2)-aptamer and grafted GCP-AuNPs. Herein, the appearance of Co on the clicked surface confirms the presence of the CoPc(2) on the electrode surface. However, the high intensity of the peaks due to Au over-shadow the peak expected after grafting due to nitrogen at 400 eV. The presence of nitrogen on the gold surface due to electrografting is only confirmed upon obtaining high-resolution scans shown in Fig. 4.12(c) for the grafted GCP-AuNPs with the peak assignments summarized in Table 4.3(c). To validate the success of the grafting process, the C1s spectra were extracted and deconvoluted for grafted GCP-AuNPs, Fig. 4.12(c). For the C1s spectrum, peaks were observed at 285.5, 287 and 289 eV. These peaks are attributed to C-N, C-Au bond, and C-C respectively [211]. The C-Au bond confirms the success of the electrografting process. The deconvoluted N1s spectrum was too broad to provide useful information.

Fig. 4.12(d) then shows the N1s spectrum of the clicked gold surface, with the peak assignments summarized in Table 4.3(c) for AuNPsØCoPc(2)-Aptamer. The N1s spectrum showed peaks at 400.0, 402.5 and 407.0 eV after deconvolution. The peaks at 400.0 (10 600 cps) and 402.5 eV (8500 cps) have been earlier assigned to azide peaks which also shows that not all azide groups were clicked to the MPc. The peak at 407 eV can be assigned to N=C which may be a contribution from the CoPc(2) at the surface. The N1s spectrum of the grafted gold surface also showed very high intensities of about 23 900 cps at around 400 eV (data not shown) therefore it can also be noted that the highly reduced N1s intensities from the grafted electrode to the clicked electrode indicates the success of the click reaction.

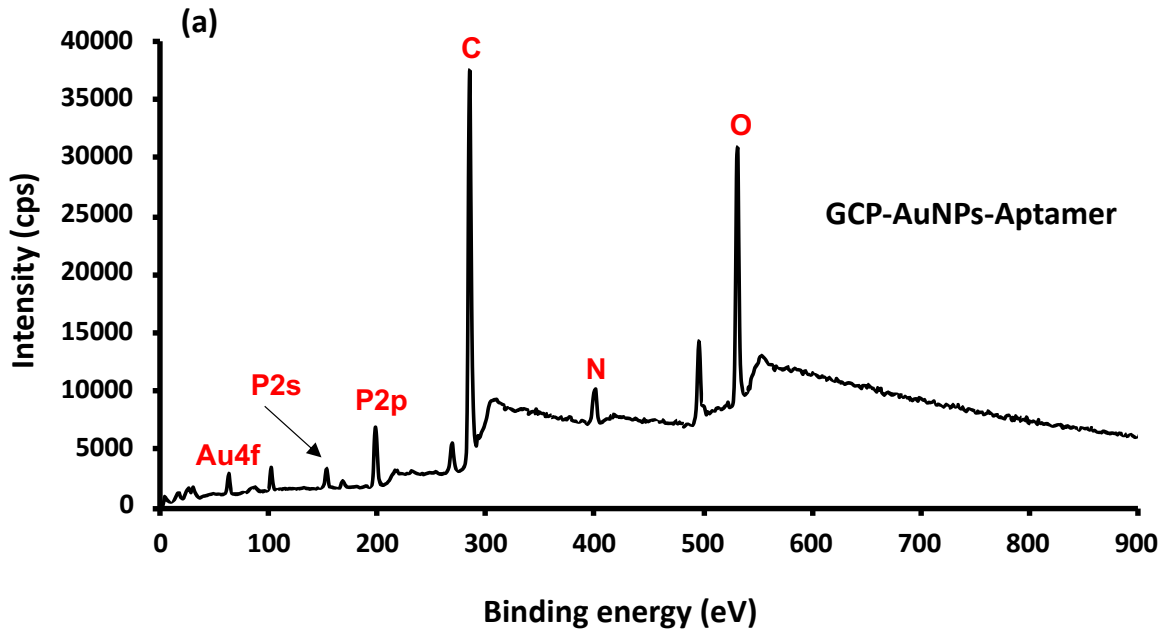

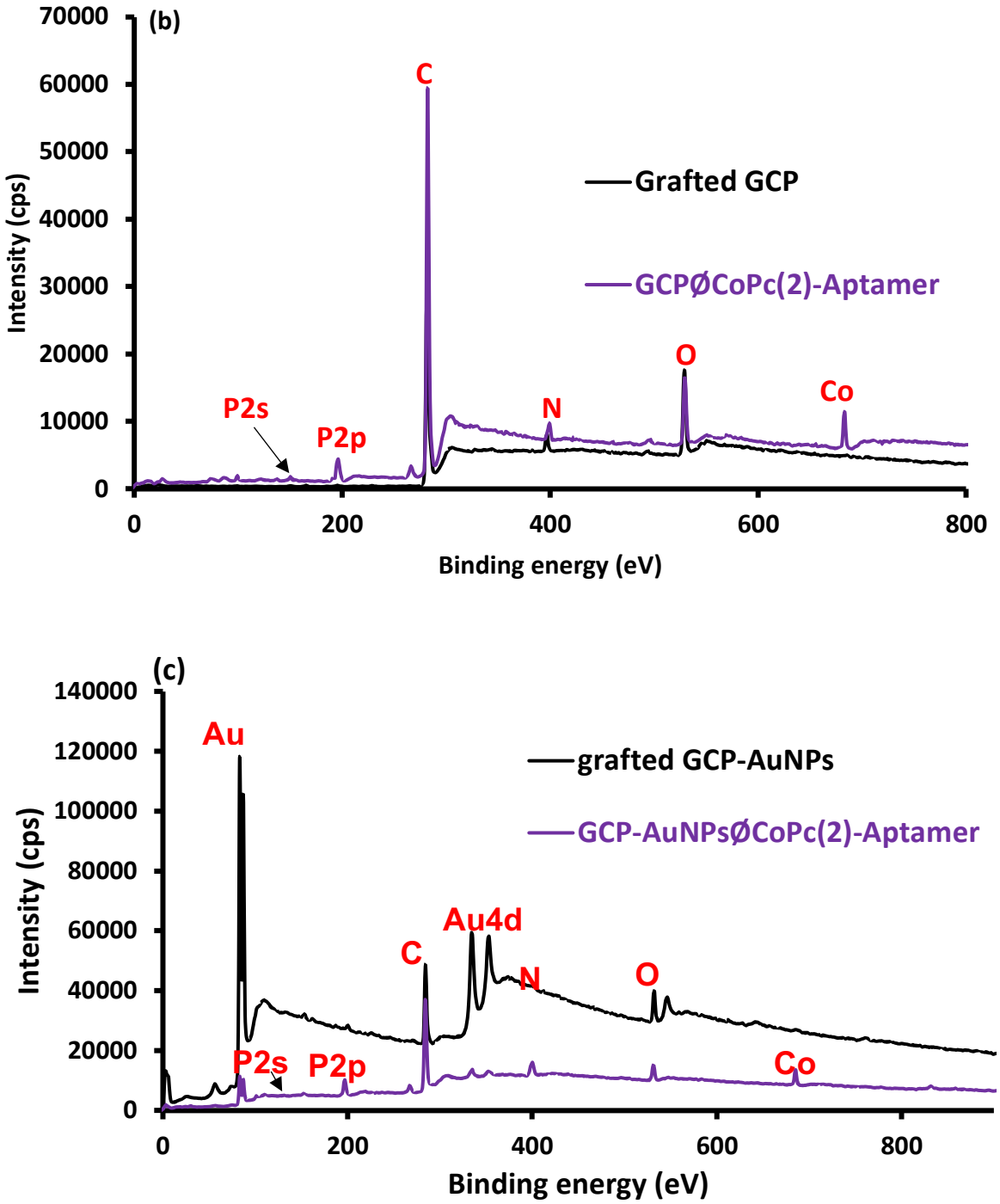

Figure 4.11: Survey scans of (a) GCP-AuNPs-Aptamer, (b) grafted GCP and GCPØCoPc(2)-Aptamer and (c) grafted GCE -AuNPs and GCP-AuNPsØCoPc(2)-Aptamer.

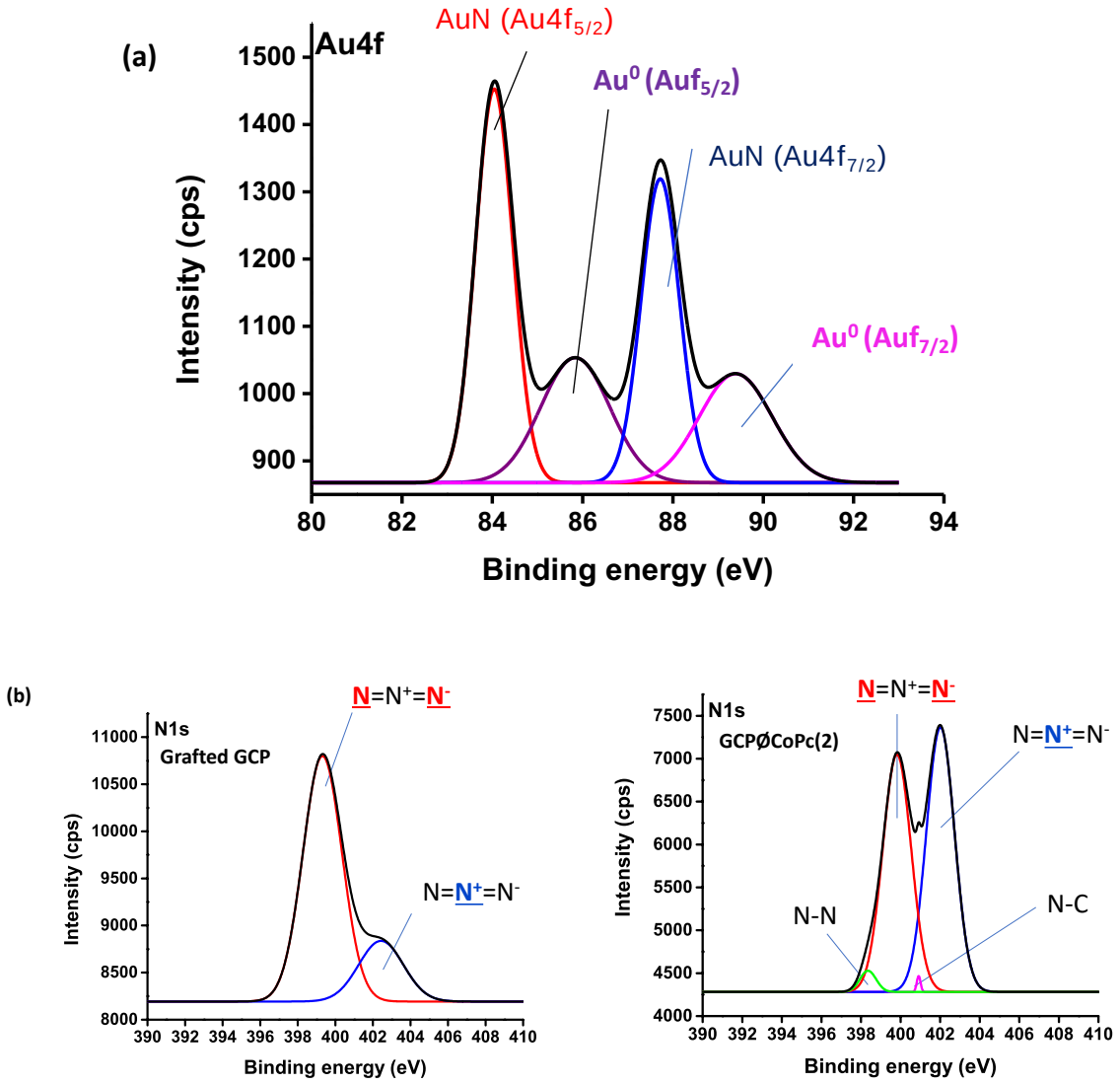
(a)
Au4f
AuN (Au4f5/2)
Au0 (Auf5/2)
AuN (Au4f7/2)
Au0 (Auf7/2)
Intensity (cps)
Binding energy (eV)
(b)
N1s
Grafted GCP
N=N+=N-
N=N+=N-
Intensity (cps)
Binding energy (eV)
N1s
GCPØCoPc(2)
N=N+=N-
N=N+=N-
N-N
N-C
Intensity (cps)
Binding energy (eV)

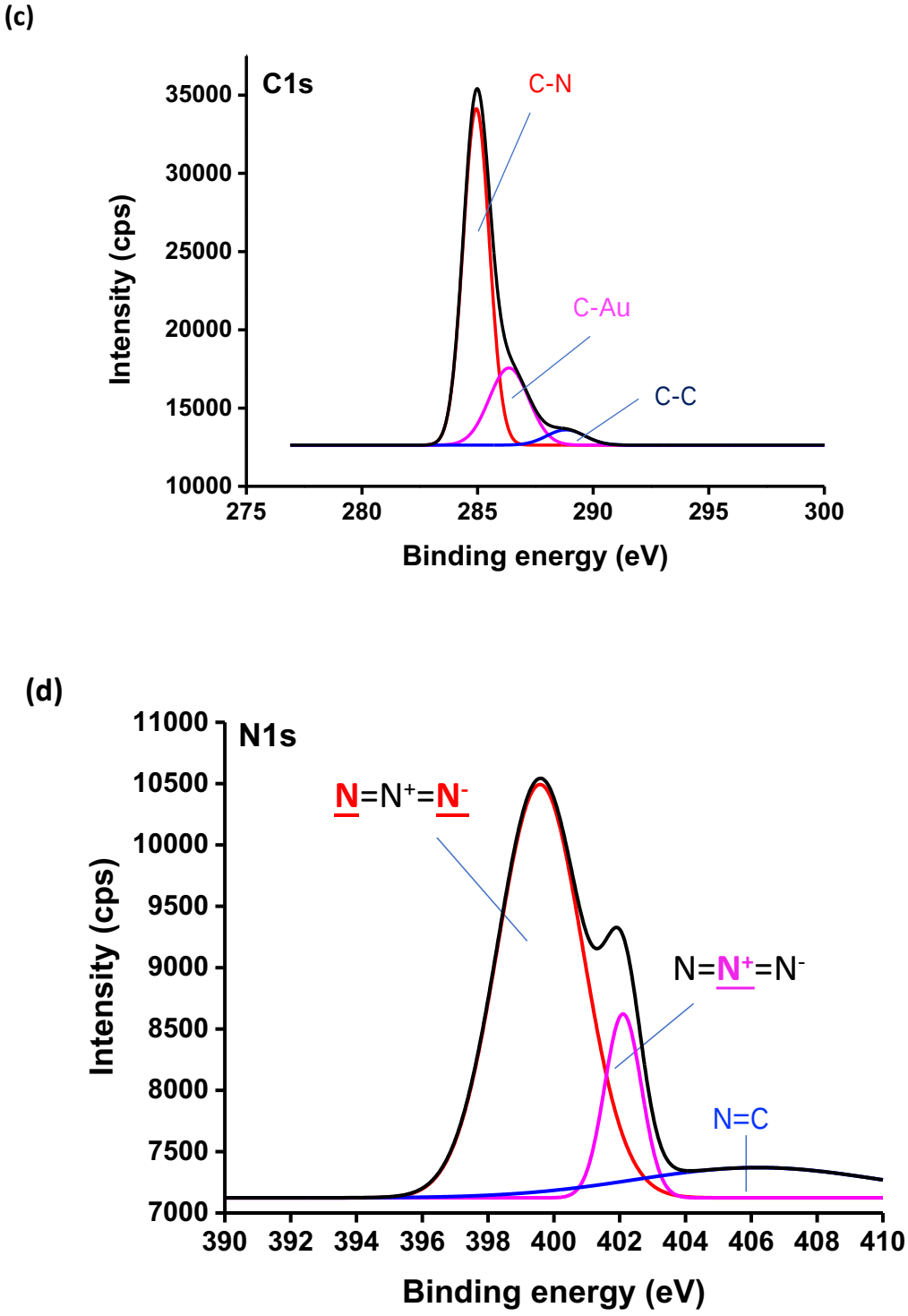

Figure 4.12: High resolution scans obtained for (a) Au4f of GCP-AuNPs-Aptamer, (b) N1s of Grafted GCP and GCPØCoPc(2) (c) C1s of grafted GCP-AuNPs and (d) N1s of GCP-AuNPsØCoPc(2).

Table 4.3(a): XPS peak assignments for electrode modification verification for GCP-AuNPs-Aptamer.

Surface	Element	Binding energy/ eV	Assignment
GCP-AuNPs-Aptamer	Au4f	84.0	AuN ($Au4f_{5/2}$)
		86.0	Au^0 ($Auf_{5/2}$)
		87.5	AuN ($Auf_{7/2}$)
		89.6	Au^0 ($Auf_{7/2}$)

Table 4.3(b): XPS peak assignments for electrode modification verification for GCPØCoPc(2)-Aptamer

Surface	Element	Binding energy/ eV	Assignment
Grafted GCP	N1s	399.5	$\underline{N}=N^+=\underline{N}$
		402.5	$N=\underline{N^+}=N^-$
GCPØCoPc(2)	N1s	398.5	N-N
		399.5	$\underline{N}=N^+=\underline{N}$
		401.0	N-C
		402.5	$N=\underline{N^+}=N^-$

Table 4.3(c): XPS peak assignments for electrode modification verification for GCP-AuNPsØCoPc(2)-Aptamer.

Surface	Element	Binding energy/ eV	Assignment
Grafted GCP-AuNPs	C1s	285.5	C-N
		287.0	C-Au
		289.0	C-C
GCP-AuNPsØCoPc(2) (Clicked GCP-AuNPs)	N1s	400.0	$\underline{N}=N^{+}=\underline{N}$
		402.5	$N=\underline{N^{+}}=N^{-}$
		407.0	N=C

4.3 Conclusions

GCEs and GCPs were used as immobilization platforms for composites with the aims of fabricating electrochemical sensors. Moreover, it was also proven that using QDs and AuNPs in combination with MPcs rather than individually resulted in enhanced signal output. The nature of the QDs affected the performance of the modified electrode. When AuNPs were combined with Complex 2 directly on the electrode surface, the synergistic effects were observed when the electrode surface was characterized. The electrode surfaces were successfully coated with AuNPs and complex 2 successfully clicked onto the bare GCE and GCE-AuNPs, followed by the adsorption of the PSA binding aptamer.

5. Electrocatalytic detection

Successful sensor fabrication was achieved by adsorption, electrodeposition, electrografting and click chemistry as discussed in Chapter 4. These fabricated sensors were then employed for the electrochemical detection of L-cysteine and PSA. The electrochemical detection of L-cysteine was carried out to prove the signal enhancement capabilities of the QDs-MPc conjugates rather than using these nanocomposites on their own. This is the first time an MPc or QDs are linked to an aptamer for the detection of PSA and it is the first time where all three (MPc, aptamer and QDs) are employed together for sensing. Moreover, the combination of AuNPs and MPc using electrografting and click chemistry for PSA sensing is employed here for the first time using complex 2.

5.1 Electrocatalytic detection of L-cysteine

Complex (1), the selected QDs and their conjugates were immobilized on a GCE and tested in a buffer solution containing L-cysteine to further prove the improved electrocatalytic ability or signal response, as opposed to using them as individual components. These results are also shown to validate the use of these conjugates as signal amplifiers for the PSA aptasensors and determine the best QDs for this application. L-cysteine is used as a test analyte since it is also later used for selectivity studies using the mixed solutions methods.

5.1.1 Cyclic voltammetry

In this study, L-cysteine is analyzed in a buffer solution of pH 4 due to good solubility of analyte at this pH. Fig. 5.1 shows the responses of the modified electrodes in the presence of 2 mM L-cysteine. Double oxidation peaks were observed for GCE-CoPc(1) as well as the electrodes modified sequentially using the NGQDs, gCNQDs and CoPc(1). The gCNQDs show a small peak at a potential of 0.83 V, Table 5.1, which is attributable to the electrocatalysis of L-cysteine. The NGQDs also show an oxidation peak at 0.28 V with the GQDs showing no interpretable peaks in the presence of the analyte. As explained in previous studies, the oxidation on both the forward and reverse scans is attributed to regeneration of the active catalyst responsible for the oxidation of L-cysteine [212]. The GCE-GQDs-CoPc(1)($\pi\pi$), GCE-NGQDs-CoPc(1)($\pi\pi$) and GCE-gCNQDs-CoPc(1)($\pi\pi$) showed peak potentials at 0.38, 0.76 and 0.61 V, respectively. Compared to the sequentially modified electrodes, the drastic shift was observed for the GQDs-based electrode where the peak potential was 0.61 V but shifted to 0.38 V when the GQDs and CoPc(1) were combined by $\pi\pi$ interactions. The

sequentially modified electrodes in general, show a higher current response than their counterparts combined by ππ interactions. The mechanism behind the electrocatalysis of L-cysteine by CoPc's has been reported in literature [213].

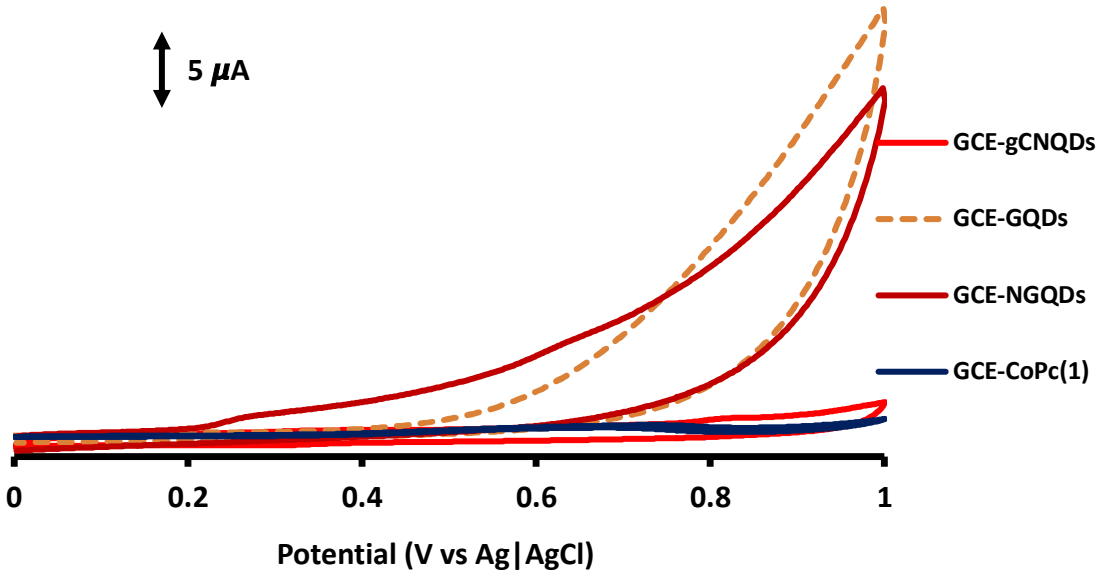

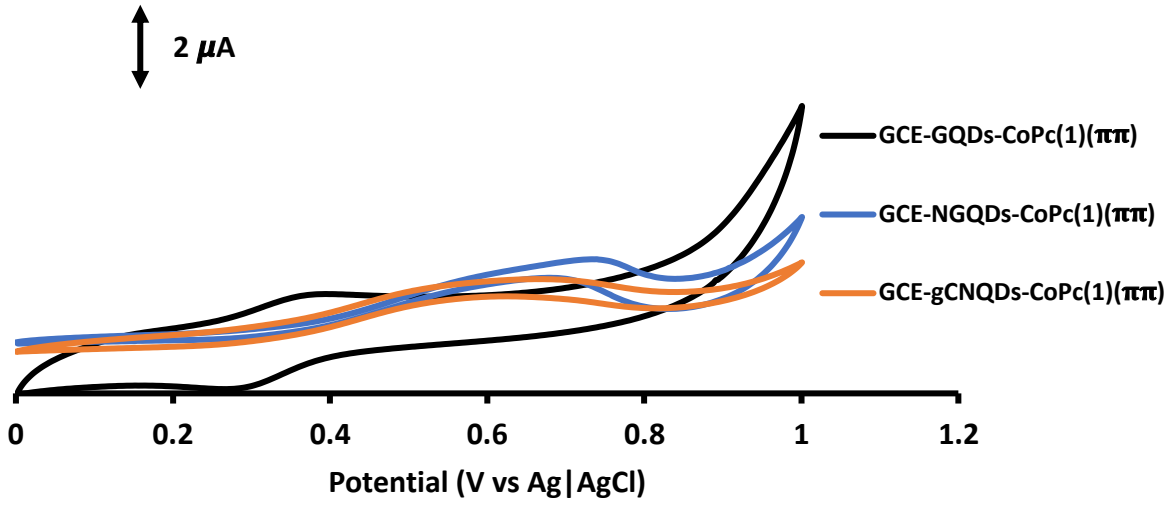

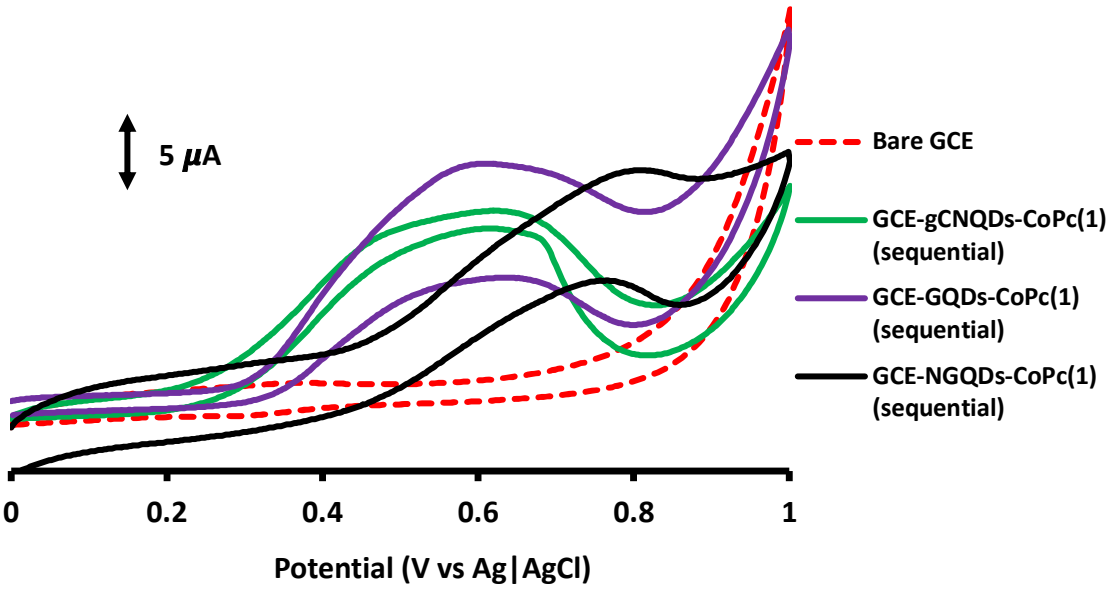

Figure 5.1: Cyclic voltammograms of de-aerated pH 4 buffer solution in the presence of 2 mM L-cysteine. Scan rate= 100 mV/s.(Plots separated for better visibility of peaks).

5.1.2 Chronoamperometry

Chronoamperometry allows for the determination of the behavior of the electrocatalysts employed in the presence of the analyte at different concentrations and how the electrocatalytic effects evolve with increasing concentration of the analyte of interest.

Fig. 5.2(a) shows the chronoamperograms obtained from electrocatalytic responses of gCNQDs-CoPc(1) (sequential) as an example, in the presence of L-cysteine at different concentrations. The potential was held constant at 0.6 V vs Ag/AgCl for the gCNQDs and GQDs based electrodes and at 0.8 V vs Ag/AgCl for the electrode containing NGQDs, based on Fig. 5.1. Linear responses of concentration vs current response are observed as illustrated in Fig. 5.2(b). The limits of detection (LOD) were obtained using 3δ/slope ratio notation, where δ is the

standard deviation of the blank and 3 is a recommended factor that gives a practical confidence of 90 % to 99.7 % [214]. The sensitivity of the sensors were determined as 38.2 μA.mM^{-1} and the limit of detection (LoD) as 0.16 μM for GCE-GQDs-CoPc(1) (sequential), 39.9 μA.mM^{-1} and 0.11 μM for GCE-NGQDs-CoPc (1) (sequential) and 100.5 μA.mM^{-1}, 0.02 μM for GCE-gCNQDs-CoPc(1) (sequential), 12.4 μA.mM^{-1} and 1.09 μM for GCE-GQDs-CoPc(1)(ππ), 18.6 μA.mM^{-1} and 0.52 μM for GCE-NGQDs-CoPc(1)(ππ) and 23.4 μA.mM^{-1} and 0.41 μM for GCE-gCNQDs-CoPc(1)(ππ). It is evident that the sequentially modified surfaces performed better than their ππ counterparts. Table 5.2. The LoD is the lowest on GCE-gCNQDs-CoPc(1) (sequential). Fig. 5.2(c) shows plots of I_{cat}/I_{buf} versus $t^{1/2}$ for the sequentially modified electrodes that are useful for the determination of the rate constant according to Eqn. (5.1) [215]:

$$\frac{I_{cat}}{I_{buff}} = \gamma^{1/2}\pi^{1/2} = \pi^{1/2}(k_{cat}Ct)^{1/2} \qquad (5.1)$$

where I_{cat} and I_{buf} are currents in the presence and absence of L-cysteine respectively, k_{cat} is the catalytic rate constant, C is the concentration of L-cysteine and t is the time elapsed in seconds. By plotting the square of the slopes obtained from Fig. 5.2(c) for GCE-gCNQDs-CoPc(1) (sequential) versus concentration of the analyte, a linear relationship may be observed (Fig. 5.2(d)) and is represented by Eqns. (5.2):

$$y = 1.02\text{x}10^4\,[L\text{-}cysteine](s^{-1}mM) + 420.92\ s^{-1},\quad R^2 = 0.9693 \quad (5.2)$$

where the slope of this plot is equivalent to πk. The value of k_{cat} in this work was found to be 1.3 × 10^5 M^{-1} s^{-1} for GCE-GQDs-CoPc(1) (sequential), 3.9 × 10^5 M^{-1} s^{-1} for GCE-NGQDs-CoPc(1) (sequential) and 1.0 × 10^7 $M^{-1}.s^{-1}$ for GCE-gCNQDs-CoPc(1) (sequential), Table 5.1. Here again, the electrode containing the gCNQDs shows better results than the other surfaces.

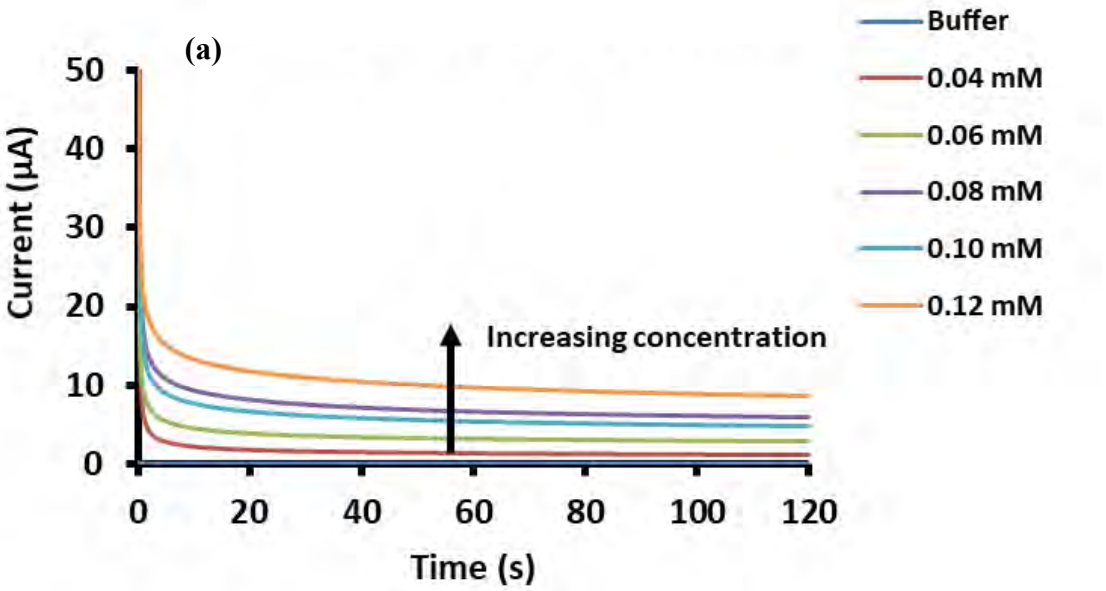

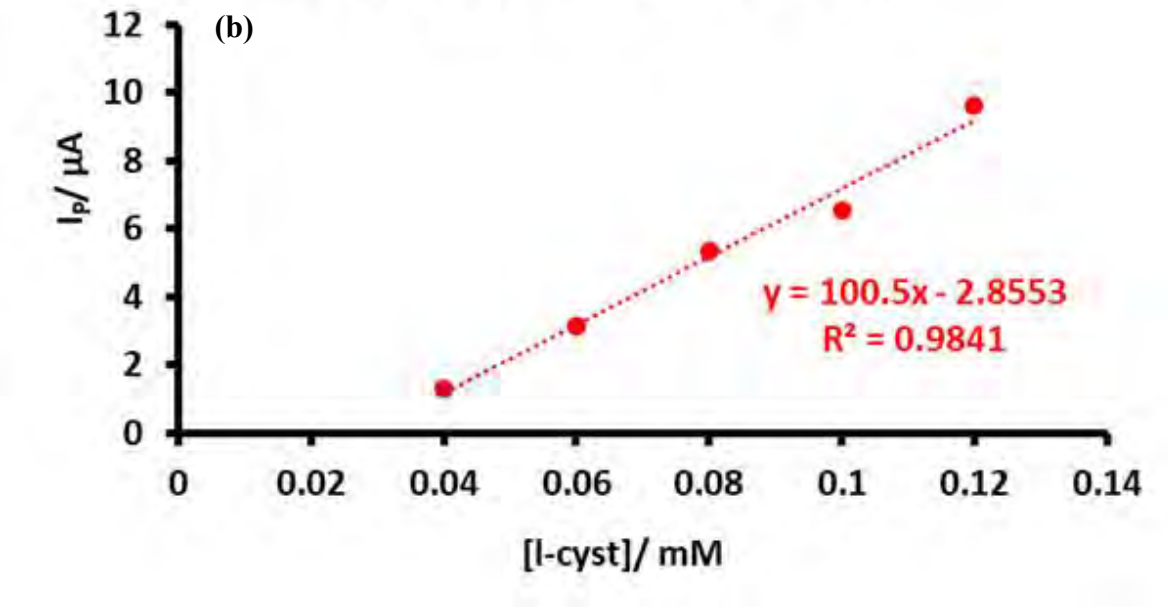
(b)
12
10
8
6
4
2
0
I_p/ µA
y = 100.5x - 2.8553
R² = 0.9841
0
0.02
0.04
0.06
0.08
0.1
0.12
0.14
[l-cyst]/ mM

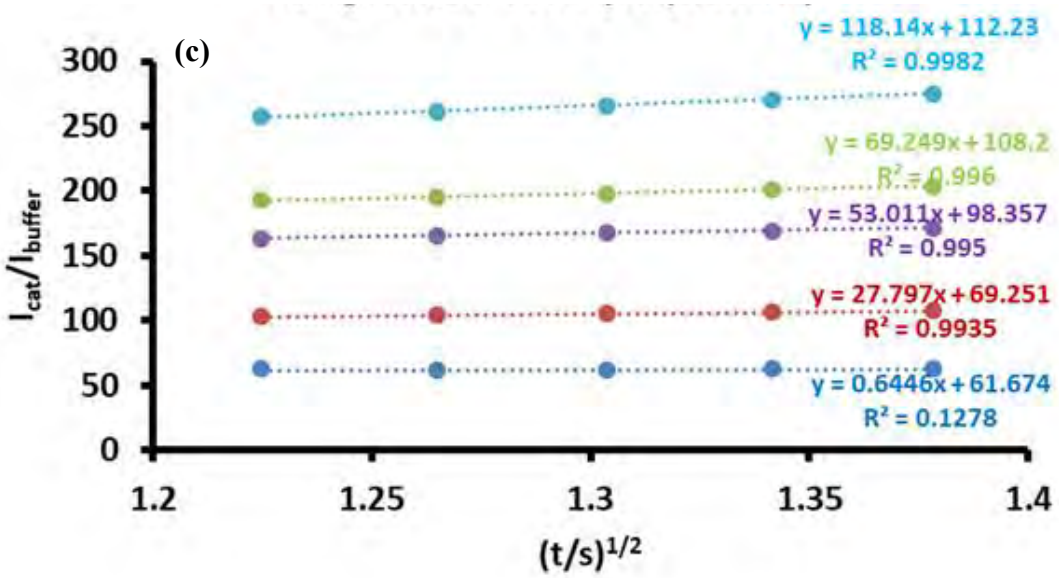
(c)
300
250
200
150
100
50
0
I_{cat}/I_{buffer}
y = 118.14x + 112.23
R² = 0.9982
y = 69.249x + 108.2
R² = 0.996
y = 53.011x + 98.357
R² = 0.995
y = 27.797x + 69.251
R² = 0.9935
y = 0.6446x + 61.674
R² = 0.1278
1.2
1.25
1.3
1.35
1.4
$(t/s)^{1/2}$

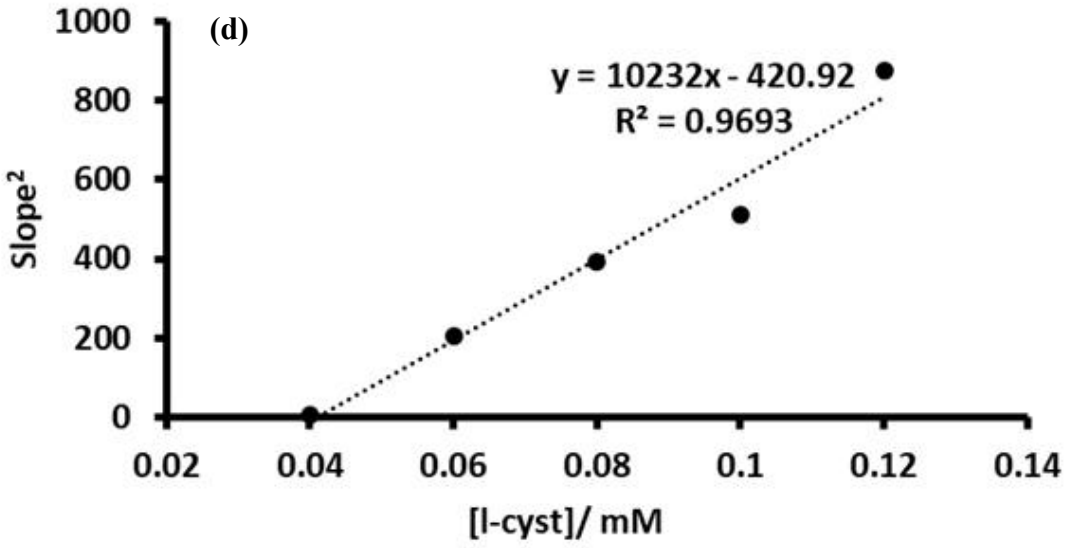

Figure 5.2: (a) Chronoamperograms of modified electrodes in pH_4 buffer with L-cysteine concentration ranging from 0.04-0.12 mM, (b) plots of [L-cysteine] vs I_p, (c) I_{cat}/I_{buffer} vs $\sqrt{t}$ and (d) plots of $Slope^2$ vs concentration of analyte. GCE-gCNQDs-CoPc(1) (sequential) used as an example. Scan rate= 100 mV/s.

Table 5.2 then compares the best electrode surface obtained in this work used for the electrooxidation of L-cysteine with other fabricated electrodes for the detection of L-cysteine reported in literature [195, 216-218]. To highlight an important difference, one report [216] has used multiwalled carbon nanotubes (MWCNTs) and a tetrasubstituted phthalocyanine (symmetrical) whereas in this work gCNQDs quantum dots with a predominant nitrogen rich structure and an asymmetrical phthalocyanine. As stated in the introduction of this work, asymmetry improves electrocatalytic behavior of porphyrin-type complexes and the presence of nitrogen in the gCNQDs results in an electron rich structure which is expected to enhance the electrocatalytic activity of MPcs to a larger extent than GQDs which are also carbon based nanostructures, therefore it is expected that

the combination of the novel asymmetric CoPc(1) and the gCNQDs to be an improved electrocatalyst for the electrooxidation of L-cysteine compared to some literature reports.

Table 5.1: Summary of determined characteristics of fabricated electrodes for L-cysteine detection in this work.

GCE surface	E_p (V) (L-cysteine)	Background corrected current (μA)	$k_{cat}/M^{-1}s^{-1}$	LoD/ μM	Sensitivity/ $\mu A.mM^{-1}$
CoPc(1)	0.74	1.53	1.9×10^4	0.96	0.65
GQDs	No peak	No peak	1.3×10^3	112.1	2.5
GCE-GQDs-CoPc(1) (sequential)	0.61	8.64	1.3×10^5	0.16	38.2
GCE-GQDs-CoPc(1) (ππ)	0.38	3.38	5.4×10^5	1.09	12.4
NGQDs	0.28	2.92	2.01×10^3	109.3	2.9
GCE-NGQDs-CoPc(1) (sequential)	0.80	8.62	3.9×10^5	0.11	39.9
GCE-NGQDs-CoPc(1) (ππ)	0.76	3.95	4.2×10^5	0.52	18.6
gCNQDs	0.83	1.85	3.1×10^3	101.3	3.5
GCE-gCNQDs-CoPc(1) (sequential)	0.63	8.46	1.0×10^7	0.02	100.5
GCE-gCNQDs-CoPc(1) (ππ)	0.61	3.62	2.2×10^6	0.41	23.4

Table 5.2: Comparison of results obtained for L-cysteine electrocatalysis by sequentially modified electrode surfaces in this work and those reported in literature.

Electrode surface	LoD/ μM	Sensitivity/ $\mu A.mM^{-1}$	Reference
GCE-gCNQDs-CoPc(1) (sequential)	0.02	100.5	This work
GCE-GQDs-CoPc(1) (sequential)	0.16	38.2	This work
GCE-NGQDs-CoPc(1)(sequential)	0.11	39.9	This work
CoTAPc–MWCNTs–GCE(sequential)	0.28	0.0007×10^{-6}	[195]
MWCNT-FeTsPc-GCE	1.00	0.175	[216]
PPy- MWCNT-CoPc	200	1.15	[217]
CoPc-SPEs	4.00	0.78	[218]

Abbreviations: Multiwalled carbon nanotubes (MWCNTs), polypyridine (PPy), screen printed electrodes (SPEs)

5.1.3. Kinetics: Scan rate studies

The response of the modified electrodes was observed as the scan rate was increased. An increase in current response was observed with increasing scan rate, Fig. 5.3(a). From these results, the peak current was plotted against the scan rate (I_P vs ν), the peak potential against the log of scan rate (E_P vs log ν) and the peak current was plotted against the square root of the scan rate (I_P vs $\nu^{1/2}$) shown by Fig 5.3 (b). The linear relationship observed in the plot of I_P vs $\nu^{1/2}$ suggests that the catalytic response of the electrode is a diffusion-controlled process [216].

The plot of E_P vs log ν gave a linear relationship (for which is a characteristic of a diffusion-controlled process) and allows for the determination of the Tafel slope, Eqn. (5.3) [217]:

$$\boldsymbol{E_P = \frac{b}{2} log\, \nu + K} \qquad (5.3)$$

Where *b* is the Tafel slope and *v* is the scan rate. The gradient of the slope can be defined as $\frac{b}{2}$. The Tafel slopes for the electrodes modified with GQDs-CoPc(1) ($\pi\pi$), NGQDs-CoPc(1)($\pi\pi$)and gCNQDs-CoPc(1)($\pi\pi$) were determined as 143, 217 and 73 mV/decade respectively. The determined value for the gCNQDs based electrode lies in the expected range of 30-120 mV/decade since it has shown the best performance throughout the studies conducted in this work. Moreover, low Tafel slopes are an indication of high current density at low potentials which is ideal for a good electrocatalyst.

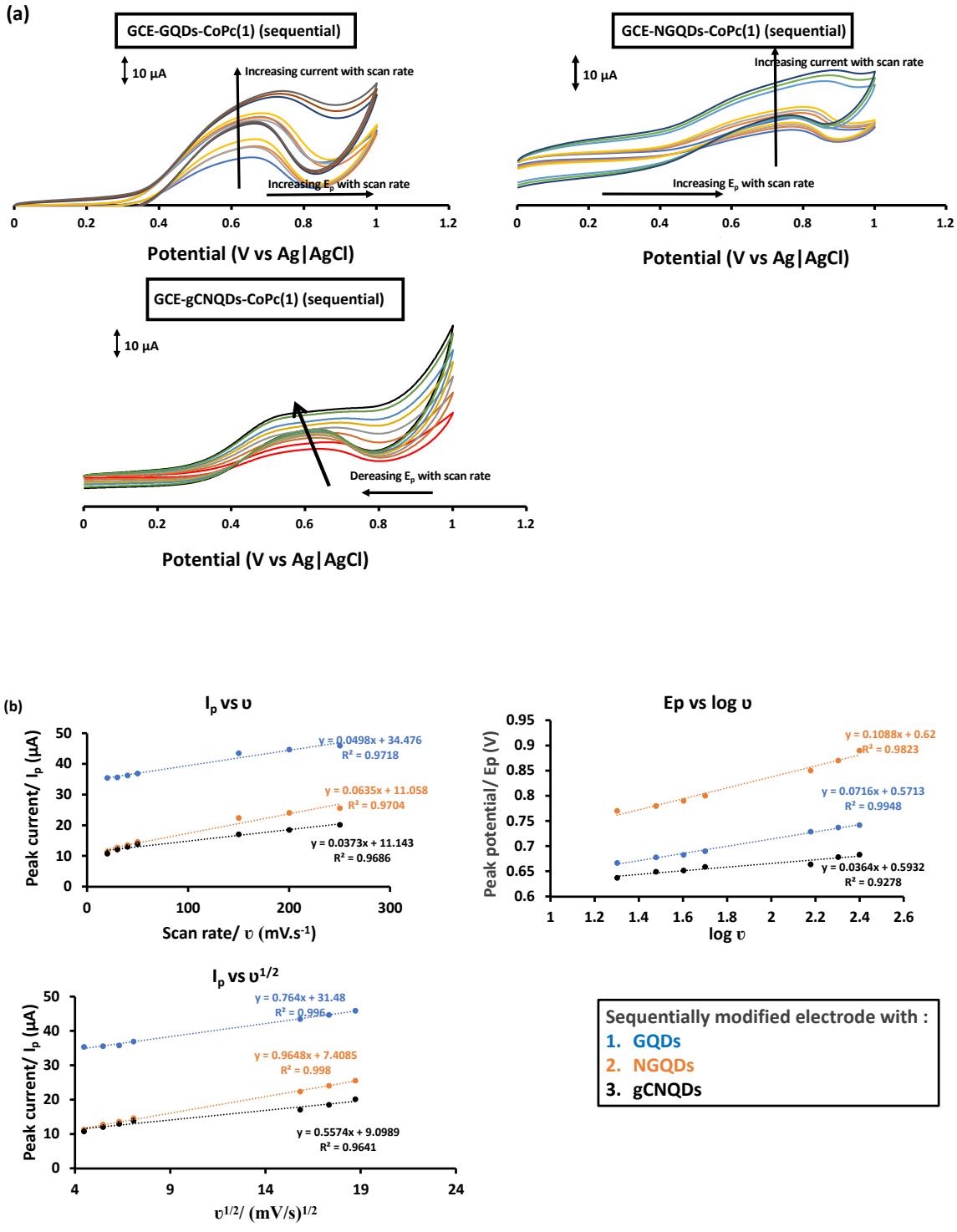

Figure 5.3: (a) Cyclic voltammograms of sequentially modified electrodes at changing scan rates (20, 30, 40, 50, 150, 200, 250 mV/s) and (b) I_p vs υ, Ep vs log υ and I_p vs$\upsilon^{1/2}$ for the sequentially modified electrodes in in de-aerated pH 4 buffer solution in the presence of 2 mM L-cysteine.

5.1.4 Stability

The modified electrodes were continuously cyclized in the presence of L-cysteine to test the stability of the electrocatalyst on the electrode surface as well as the repeatability of the detection. The more cycles run on the electrode, the more enhanced the current response as shown in Fig. 5.4, using the sequentially modified electrodes as examples. These results also prove that the electrode surfaces are resistant to fouling and passivation.

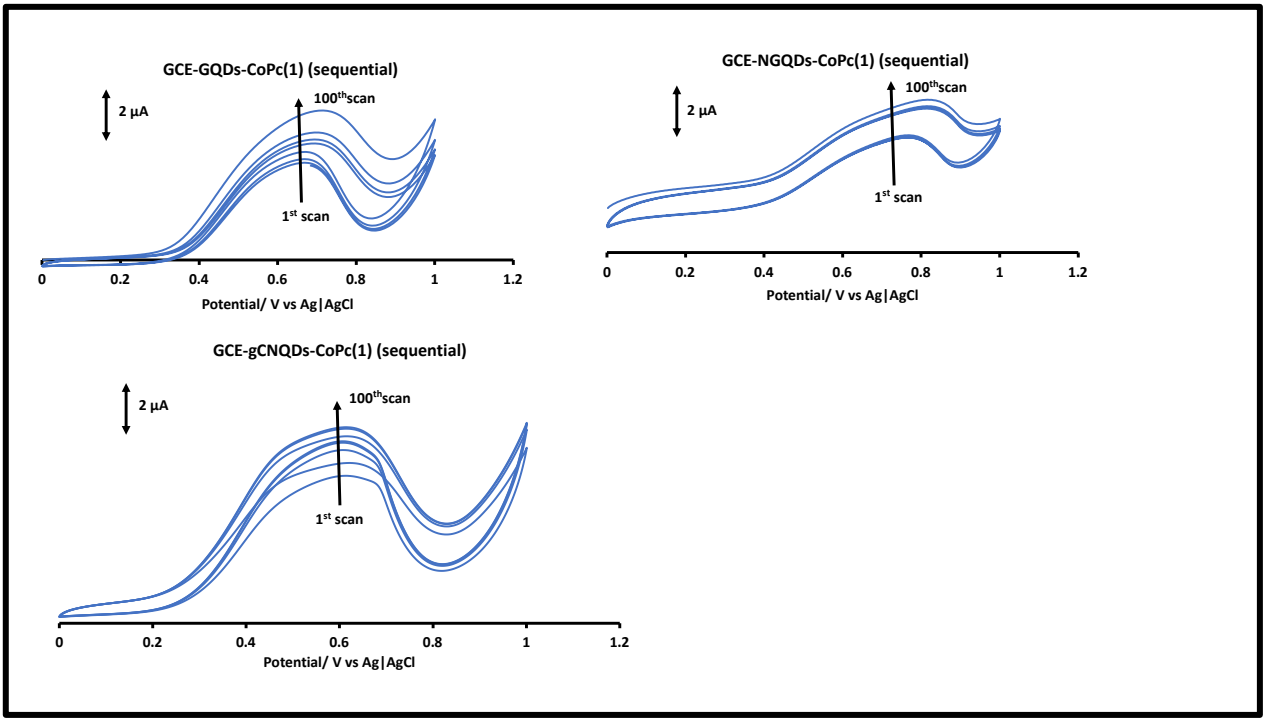

Figure 5.4: Continuous cyclization of sequentially modified electrodes in de-aerated pH_4 buffer solution in the presence of 2 mM L-cysteine. Scan rate = 100 mV/s, 100 cycles.

5.2 The electrochemical detection of PSA

Various aptasensors were fabricated in this work to determine the combinations of nanocomposites and aptamer that would generate low detection limits and good sensitivity. From these results, the best performing sensors would be used to determine sensor characteristics such as stability, selectivity, repeatability and reproducibility. Moreover, these sensors would also be used to determine their feasibility and potential use in clinical applications by detecting PSA in spiked serum samples. It should be noted that GQDs were used for the initial study to determine the combination sequence of the modifiers that would yield the best results for the electrochemical detection of PSA.

5.2.1 GQDs-CoPc(1)-Aptamer conjugates

5.2.1.1 EIS

Although this section focuses on PSA sensing and should only focus on aptamer-based electrodes, the behaviour of individual components of QDs-CoPc(1)($\pi\pi$) are included. Electron transfer kinetics in the presence of PSA were determined using EIS. Nyquist plots (Fig. 5.5(a)) were used to determine R_{ct} values by fitting the Randles equivalent circuit (Fig. 5.5(b)). The impedance spectra were fitted using a Randles electronic equivalent circuit, which is often used in diffusion-controlled electrochemical systems [219, 220] where a well-defined semi-circle followed by a linear segment is observed. This model includes the solution resistance (R_s), the electron transfer resistance (R_{ct}), the double-layer capacity element (C_{dl}) and a Warburg element (Z_w) to quantify the diffusion processes of the ionic species. However, the results obtained in this work showed suppressed semi-circles and thus a constant phase element (CPE) was used following the observation of similar

behaviour in literature reports [220]. It is also reported that using a CPE accounts for the irregularities on the electrode surface that are a result of roughness and inhomogeneities on the modifiers [220], where the plot starts to appear more linear than the semi-circle with a defined linear segment [219].

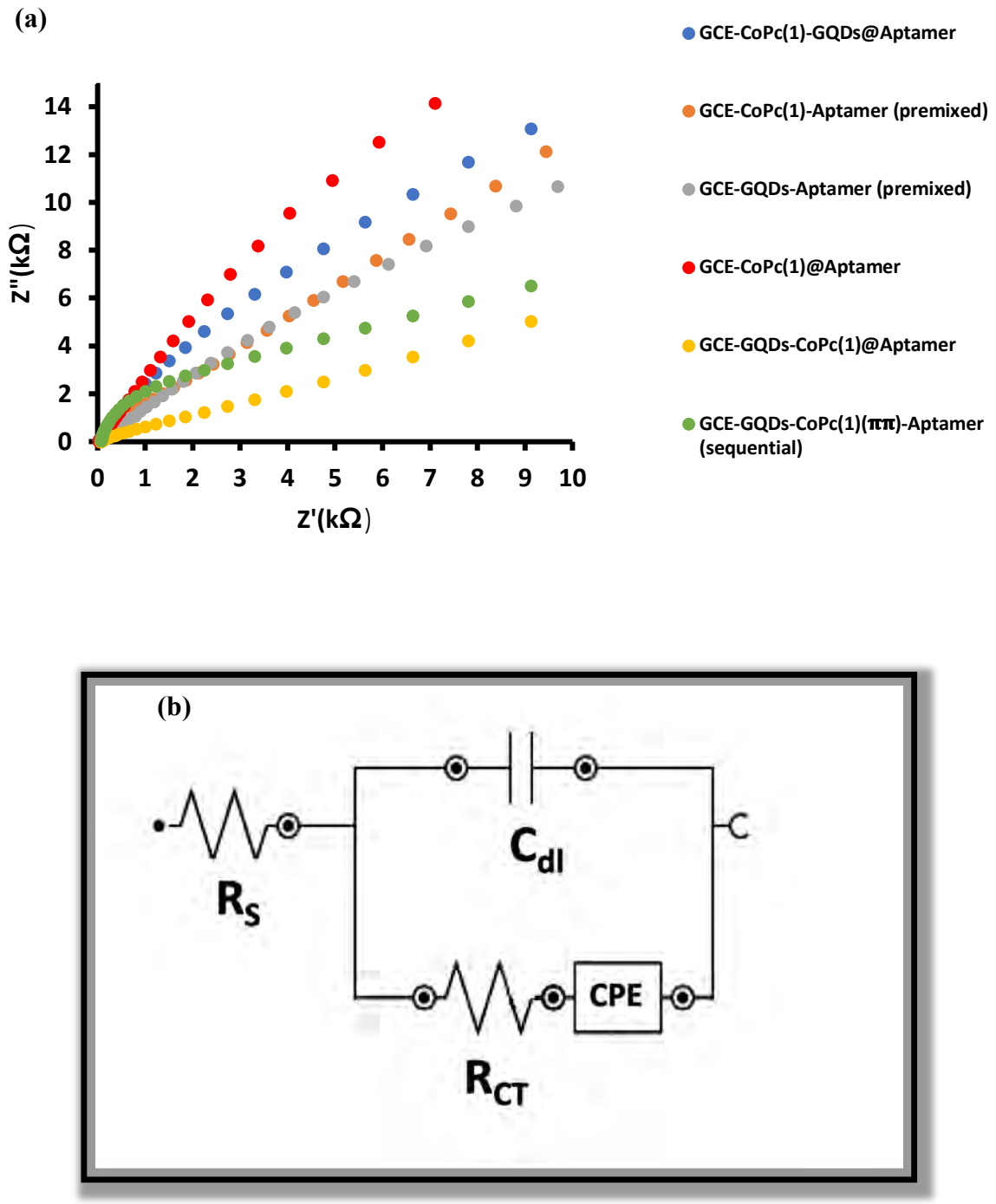

Figure 5.5: (a) Nyquist plots of some aptamer-modified electrodes in a 2 μM PSA solution in 30 mM phosphate buffer solution of pH 7.4. Plots separated into three groups for ease of comparison. (b) Circuit fitting model used.

The R_{ct} values are summarized in Table 5.3. The highest R_{ct} values were observed for the bare GCE, GCE-GQDs, GCE-CoPc(1) and the GCE-GQDs-Aptamer (sequential). For the bare GCE and the GCE-GQDs, the R_{ct} values decreases slightly for the latter, possibly due to only a slight enhancement in electron transfer caused by the GQDs. The slight increase in R_{ct} at the GCE-GQDs-Aptamer (sequential) surface may possibly be a result of how the adsorbed aptamer is assembled at the GCE surface, which only causes a slight increase in resistance to charge transfer.

Comparing the combinations of electrodes using GQDs and aptamer only, the R_{ct} values increase as follows:

GCE-GQDs-Aptamer (sequential) >GCE-GQDs@Aptamer> GCE-GQDs-Aptamer (premixed).The GCE-GQDs-Aptamer (sequential) sensor performed poorly in the presence of PSA even though it showed good charge transfer in terms of ΔE_p when the electrodes were characterized in the $[Fe(CN)_6]^{3-/4-}$ solution, Table 4.1. The large R_{ct} suggest faster passivation, hence better binding of PSA to aptamer and better detection. Thus, the electrode surface modified with GCE-GQDs-Aptamer (sequential) showing poor charge transfer in the presence of PSA is an indication of good binding of PSA to the aptamer, which hinders electron transfer. The combination of CoPc(1) and aptamer(CoPc(1)-Aptamer (sequential)) showed the largest R_{ct} value, followed by CoPc(1)-Aptamer (premixed), with CoPc(1)@Aptamer being the least resistant. Lower R_{ct} values suggests less binding of PSA to aptamer. The orientation of the electrocatalyst on the electrode surface may explain this in terms of how well the aptamer at the surface may be exposed, to be able to bind to the PSA in solution.

The apparent charge transfer rate constant (k_{app}) was also calculated using Eqn.5.4 [221] and the results are summarized in Table 5.3.

$$k_{app} = \frac{RT}{F^2 A R_{ct} C} \qquad (\mathbf{5.4})$$

where C is the concentration of the PSA, A = real surface area in cm^2 and other symbols retain their usual scientific meaning. The real surface area was obtained using Eqn. 4.1. The k_{app} values are inversely proportional to $R_{ct,}$ which validates the results obtained where high k_{app} values corresponded to low R_{ct} values.

Table 5.3: Summary of determined R_{ct} and k_{app} values determined from Nyquist plots (in order of increasing R_{ct} values). (Modified electrodes in the presence of PSA).

Electrode	R_{CT}/ kΩ	k_{app} $(cm/s)^2/s)$
Bare GCE	77.64	5.14×10^{-3}
GCE-GQDs	74.84	5.75×10^{-3}
GCE-CoPc(1)	85.87	4.37×10^{-3}
GCE-Aptamer	10.31	3.64×10^{-1}
GCE-GQDs-CoPc(1)(ππ)	12.44	2.79×10^{-1}
GCE-GQDs-CoPc(1) (sequential)	8.13	4.61×10^{-1}
GCE-GQDs@Aptamer	16.10	1.46×10^{-1}
GCE-GQDs-Aptamer (premixed)	10.62	3.53×10^{-1}
GCE-GQDs-Aptamer (sequential)	79.12	4.74×10^{-3}
GCE-CoPc(1)-GQDs@Aptamer (sequential)	41.68	1.11×10^{-2}
GCE-CoPc(1)@Aptamer	13.90	2.54×10^{-1}
GCE-CoPc(1)-Aptamer (premixed)	27.50	5.11×10^{-2}
GCE-CoPc(1)-Aptamer (sequential)	30.20	4.98×10^{-2}
GCE-GQDs-CoPc(1)@Aptamer (sequential)	26.30	5.23×10^{-2}
GCE-GQDs-CoPc(1)(ππ)-Aptamer (premixed)	3.15	1.19
GCE-GQDs-CoPc(1)(ππ)-Aptamer (sequential)	19.13	8.34×10^{-2}
GCE-GQDs@Aptamer-CoPc(1)@Aptamer (premixed)	11.41	$2.98 \quad 10^{-1}$

Note: Sequential modification involves placing the QDs first on the electrode surface. For premixed (ππ interactions), the CoPc(1) and GQDs are mixed with aptamer then placed on the electrode surface.

5.2.1.2 Concentration studies: DPV and EIS

A stock solution of PSA with a concentration of 2 µM was diluted to concentrations ranging from 1.2-2.0 pM to determine the effects concentration of the analyte would have on the current output or resistance to charge transfer. Electrodes with the PSA specific aptamer at the surface were selected for this study. Although several electrodes were tested, the DPV and EIS of the best performing electrodes are shown in Fig. 5.6. The DPV plots of the electrode containing aptamer alone (GCE-Aptamer) is illustrated by Fig. 5.7. As can be seen, this plot shows two peaks near 0 V (III), which are known for DNA [198]. These peaks are observed on all electrodes containing aptamer. Peaks near zero will overlap with the $Co^{III}Pc^{-2}/Co^{II}Pc^{-2}$ processes for electrodes containing CoPc(1). For all electrodes containing GQDs, there is a peak near -0.65 V (I) , which has been assigned to GQDs. DPV peaks near -0.65 V (due to GQDs) and the sharp one near -0.25 V (II) due to $Co^{II}Pc^{-2}/Co^{I}Pc^{-2}$ were used for the determination the detection limits.

The DPV results illustrated in Fig. 5.6(a), showed that the peak currents decreased with increasing PSA concentration. Fig. 5.6(b) showed an increasing in resistance to charge transfer with increasing concentration. It is reported that the immobilized aptamer undergoes a conformation change upon PSA binding such that the double stranded DNA is formed with simultaneous binding to (and covering with) PSA that decrease the charge transfer rate, between redox probe and electrode surface [144]. Therefore, there is an expected increase in resistance and decrease in current as PSA concentrations increase. The calibration plots (inserts) were linear in the ranges from 1.2 to 2.0 pM (0.2 pM increments) and the detection limits were calculated.

The electrodes GCE-Aptamer (sequential) and GCE-GQDs-CoPc(1)(ππ)-Aptamer (sequential) gave the lowest detection limits compared to the other electrodes tested, Table 5.4. Similar values were obtained in EIS analyses with the same electrodes showing better detection limits. The detection limit of the best surface tested using EIS, GCE-GQDs-CoPc(1)(ππ)-Aptamer (sequential), was determined as 0.79 pM (0.022 ng/mL). The best performing surface in DPV was GCE-GQDs-CoPc(1)(ππ)-Aptamer (sequential) with LoD values of 0.66 (0.018 ng/ml) and 0.73 pM (0.021 ng/mL) determined using peaks (I) and (III). Again, sequential modification proved superior, with the combination of MPc and QDs showing the best performance overall.

A three-component system showing higher detection limits than the one developed in this work is reported by Liu *et al*. [134] where AuNPs are also used and fabrication involves multiple steps whereas the fabrication process reported in this work is much simpler and shorter for the best performing aptasensor developed. Another aptasensor reported in literature is one developed by Hu and co-workers [135] where PSA was detected at femtomolar level concentrations by cleavage-based electrochemical detection using eATRP-based (eATRP = electrochemically mediated atom transfers radical polymerization) method for signal amplification. The major drawback, however, is that the fabrication process is quite time consuming and the use of gold electrodes in their method is at a cost higher than that of carbon electrodes which are used in this work. Amongst good sensitivity and low detection limits, cost effectiveness as well as ease of use are important when developing biosensors so that they may be more accessible and user friendly.

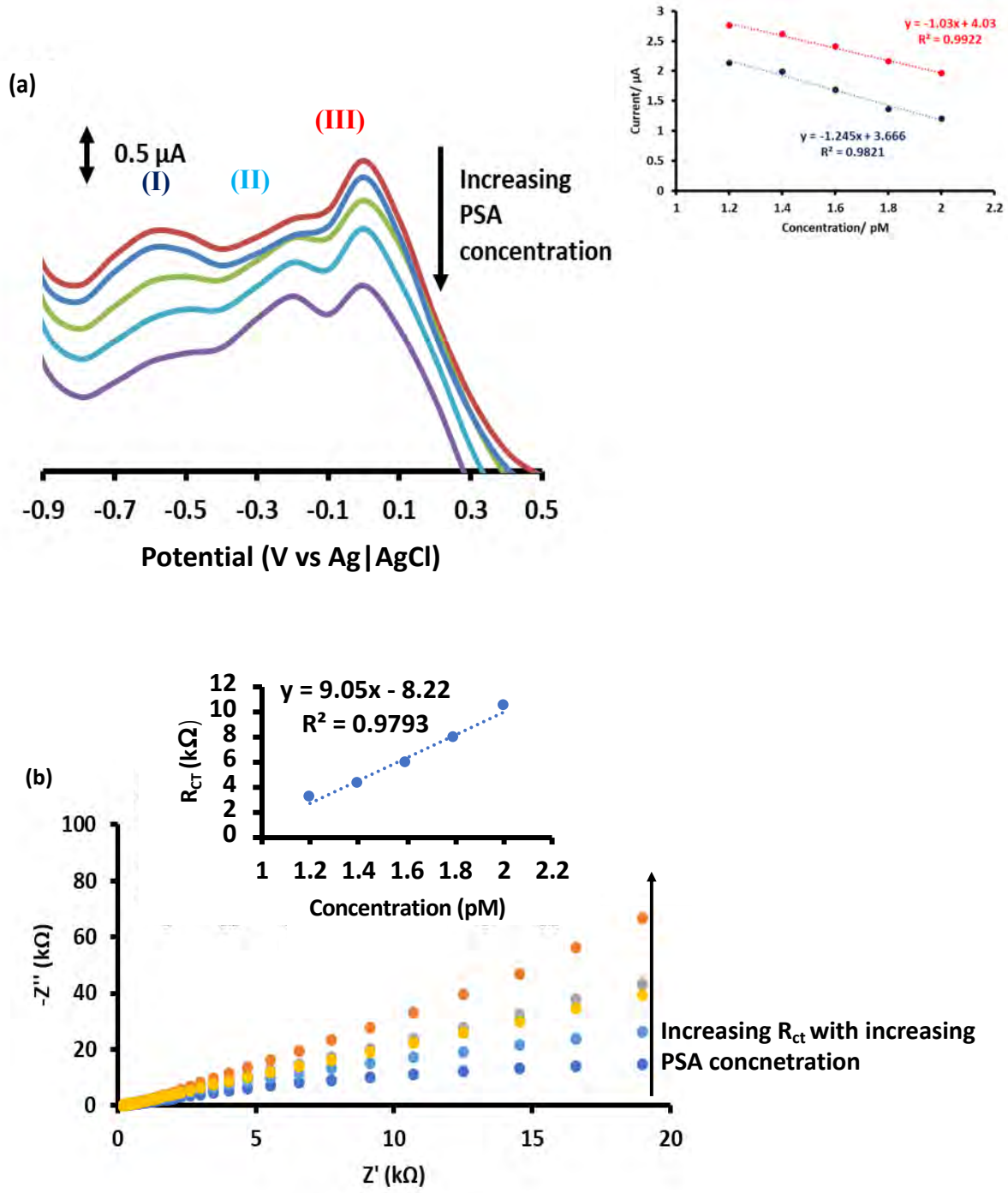

Figure 5.6: (a) Differential Pulse Voltammograms (DPV) and (b) Electrochemical impedance (EIS) Nyquist plots of GCE-GQDs-CoPc(1)(ππ)-Aptamer (sequential) in a 30 mM phosphate buffer solution of pH 7.4 with PSA concentrations ranging from 1.2-2.0 pM. Inserts: Linear responses of currents and resistance to changing concentrations.

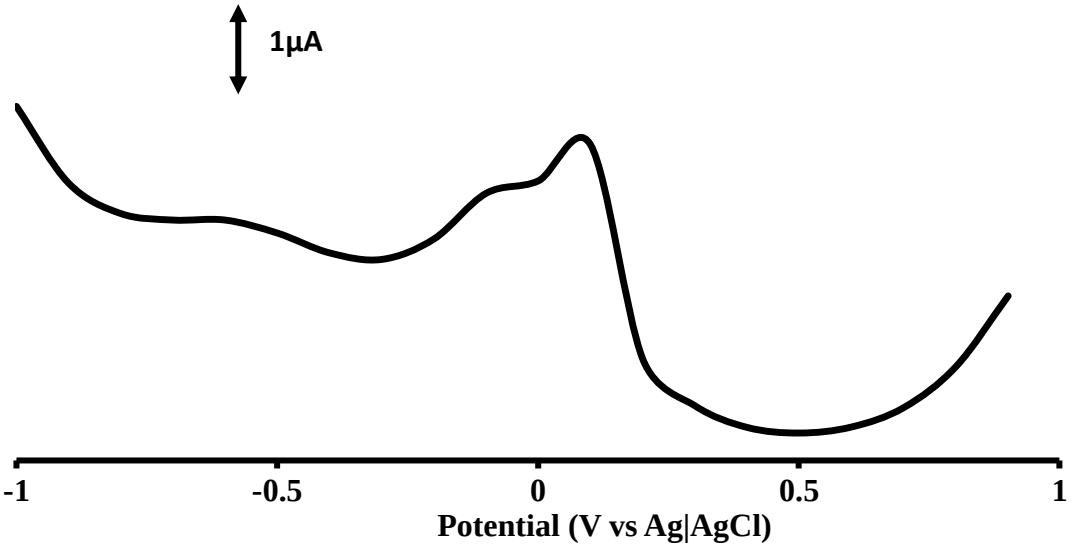

Figure 5.7: DPV of GCE-aptamer in PSA.

Table 5.4: Summary of limits of detection (LoD) of selected electrode surfaces determined from EIS and DPV measurements (Linear detection range: 1.2-2 pM).

Electrode	LoD (EIS)/ pM	Peak (I)LoD (DPV) / pM	Peak (III)LoD (DPV) / pM
GCE-Aptamer	1.15	1.02	1.10
GCE-GQDs@Aptamer	1.18	1.27	1.36
GCE-GQDs-Aptamer (sequential)	1.51	-	1.23
GCE-CoPc(1)@Aptamer	1.40	1.70	-
GCE-GQDs-CoPc(1)@Aptamer(sequential)	1.41	1.60	1.80
GCE-GQDs-CoPc(1)(ππ)-Aptamer (sequential)	0.79	0.73	0.66

5.2.1.3 Stability, selectivity, and reproducibility studies

The stability, selectivity, and reproducibility of the proposed electrochemical aptasensor were also investigated by DPV using a 2 pM PSA in PBS solution of pH 7.4 (30 mM). The electrode GCE-GQDs-CoPc(1)($\pi\pi$)-aptamer is used as an example.

The same electrode was fabricated on three different occasions and tested in the PSA solution of same concentration (2 pM). The results are illustrated in Fig. 5.8. There were slight differences in current output, however no changes were observed in terms of peak potential. The relative standard deviations (RSD %) were determined from peaks at -0.6 V and at 0 V, and were found to be 4.43 % and 3.77 %, respectively. After incubation in the PSA solution, the DPV scans were run for 50 cycles and the change in current response was monitored (Fig. 5.9). The first and the last scan were compared and it was found that the current response at the most prominent peak (0 V) decreased by only 3.9 %. When the electrode was not in use, it was stored at 4 ^{o}C. After a week of storage, the final scan in the repeatability test was compared to an initial run done at the same scan rate (Fig. 5.10). By looking at the difference between peak currents at -0.6 V and 0 V, this electrode maintained approximately 89 % of its performance ability proving to be quite stable in that time frame.

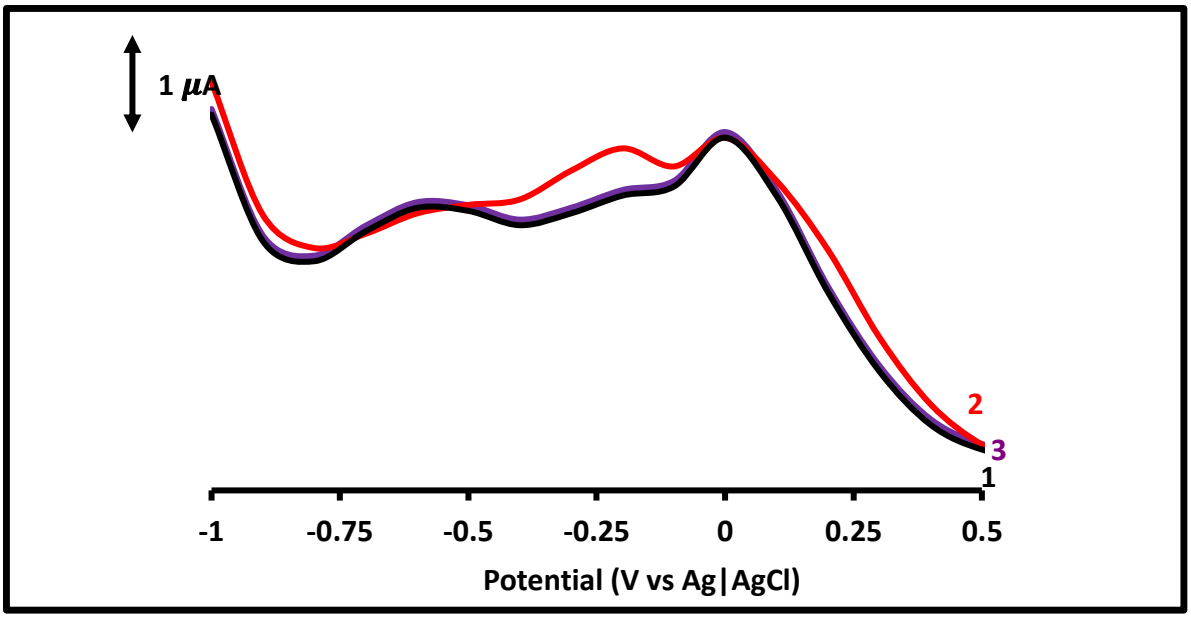

Figure 5.8: Differential pulse voltammograms of three different GCE-GQDs-CoPc(1)(ππ)-Aptamer (sequential) in a PSA solution of concentration 2.0 pM to determine reproducibility.

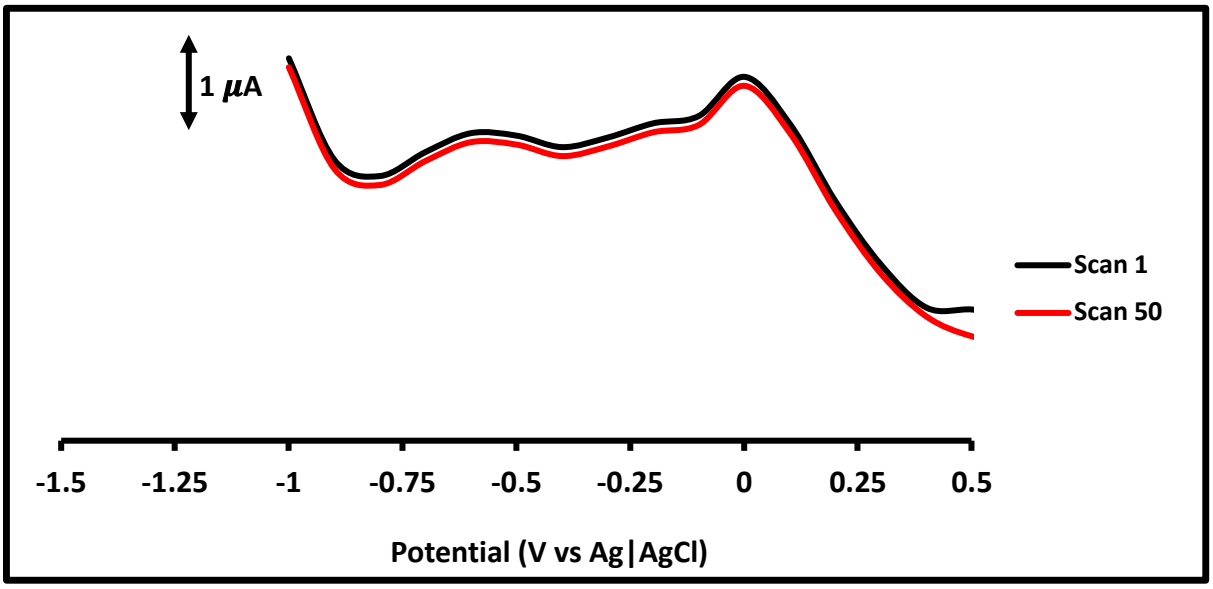

Figure 5.9: Differential pulse voltammograms of GCE-GQDs-CoPc(1)(ππ)-Aptamer (sequential) in a PSA solution of concentration 2.0 pM before and after 50 cycles to test electrode repeatability.

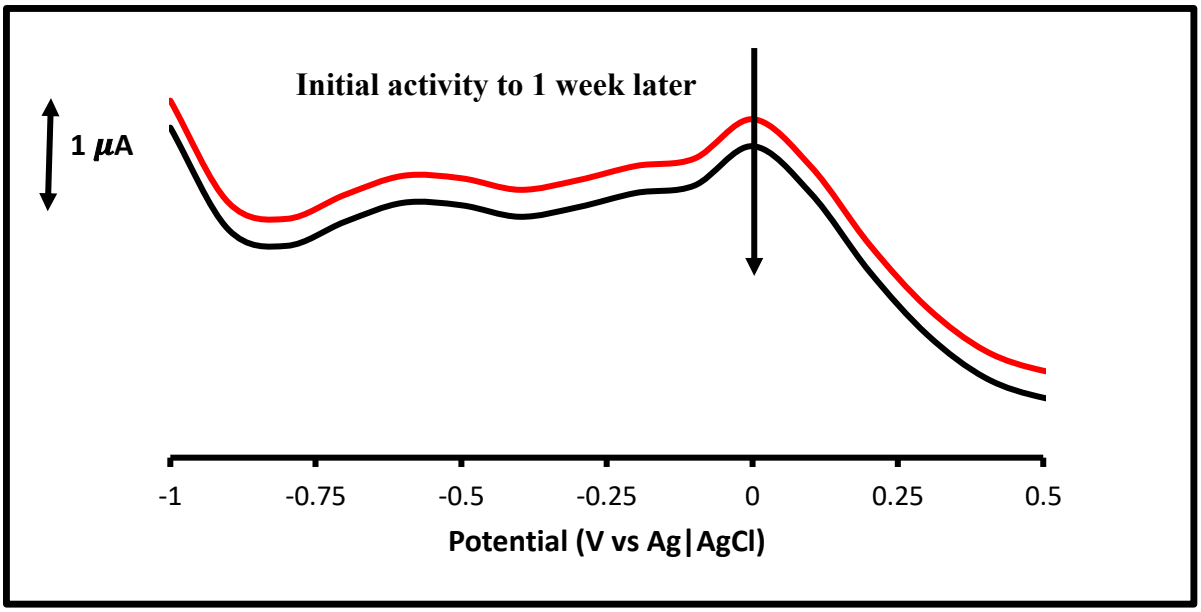

Figure 5.10: Differential pulse voltammograms of GCE-GQDs-CoPc(1)(ππ)-Aptamer (sequential) tested in a PSA solution of concentration 2.0 pM 1 week apart to determine stability of electrode.

Biological samples exist as complex mixtures therefore the fabricated sensors need to be tested against potential interferences in order to validate their reliability to target a specific analyte, irrespective of what other analytes may be present in a sample. The mixed solution method [222] and DPV (Fig. 5.11) was used to determine the selectivity of the best performing electrode towards PSA, in the presence of other analytes that could possibly be detected in a real sample with PSA, namely bovine serum albumin (BSA), L-cysteine and glucose. The chosen test analytes BSA, L-cysteine and glucose were mixed in excess, in the buffer solution with PSA. Other than being easily accessible in the laboratory, BSA was chosen so as to determine how other proteins expressed in biological samples could affect the aptasensor functionality. Glucose was chosen as it is possible to detect it in seminal samples and the level may vary depending on the health of the patient. L-

cysteine was chosen as a test analyte as it is an amino acid, which can be found in the human body, or a variant thereof may be ingested as a supplement to enhance sperm quality [223].The concentration of PSA used was 2.0 pM and 2.0 nM of interfering analyte was added for non-specific binding determination. The interferants were added in access (x10^{-3} higher than analyte) to ensure a high enough concentration for the sensor to pick up should it be sensitive to the interferences. The fabricated electrodes were incubated in the solutions as was done for PSA studies in earlier sections. Eqn. (5.5) was used to determine values of the selectivity coefficients (K_{amp}) which will give a measure of the degree of interference.

$$K_{AMP} = \left(\frac{I_{MIXTURE}}{I_{PSA}} - 1\right)\frac{[PSA]}{[INTERFERANT]} \qquad (5.5)$$

where $I_{mixture}$ and I_{PSA} are background corrected current responses of PSA in the presence and absence of the interferent, respectively. A K_{amp} value in the order of magnitude higher than 10^{-2} indicates strong interference and a value close to 10^{-3} indicates weak interference [224]. From the peaks observed at about -0.6 V (Fig. 5.11(I)), a K_{amp} value of 0.17 × 10^{-3}, 0.08 × 10^{-3} and 0.04 × 10^{-3} were obtained for BSA, glucose and L-cysteine, respectively. At the potential close to 0 V (Fig. 5.11 (II)) where the more prominent peak is observed, K_{amp} value of -0.46 × 10^{-3}, -0.64 × 10^{-3} and 0.68 × 10^{-3} were obtained for BSA, glucose and L-cysteine, respectively. Therefore, this sensor platform can be applied without any pre-separation procedures for the determination of PSA in the presence of the tested interferents with no need for pre-treatment of sample.

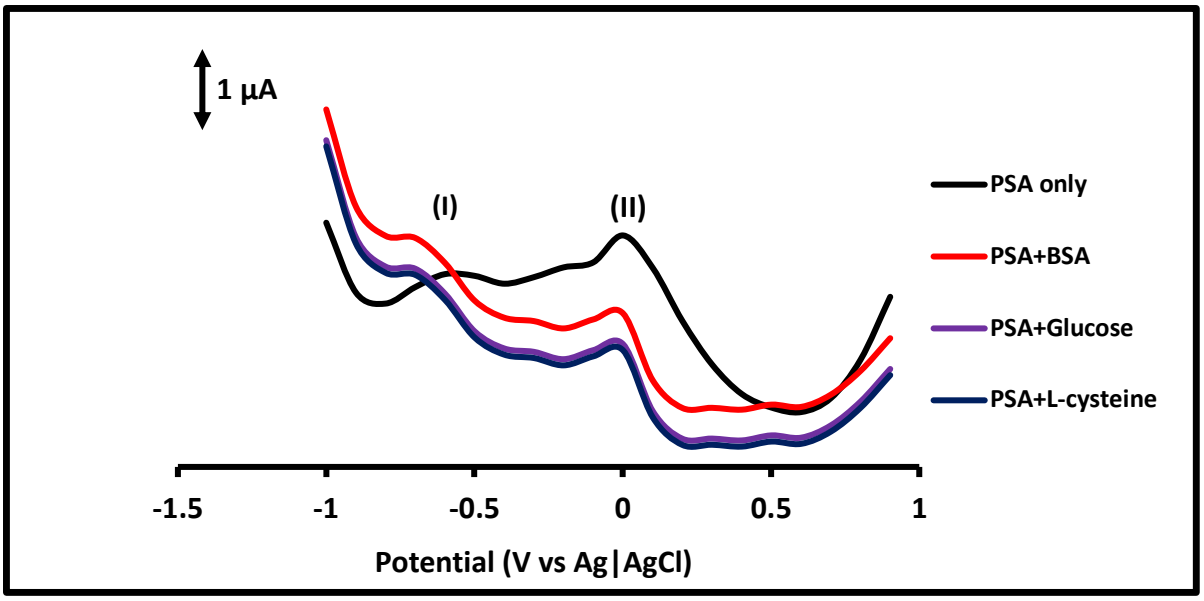

Figure 5.11: Differential pulse voltammograms of GCE-GQDs-CoPc(ππ)-Aptamer (sequential) in the absence and presence of interferents (2 nm of BSA, glucose, and L-cysteine) in a PSA solution of concentration 2.0 pM.

The best performing aptasensor showed one of the lowest detection limits using DPV and comparable reproducibility and repeatability relative standard deviations (RSD) % compared to other similar works reported in literature [134, 142, 144, 145, 225, 226]. Table 5.5 summarizes this data and the data from the above-mentioned literature reports related to the detection of PSA.

Table 5.5: Summary of results obtained in this work for GCE-GQDs-CoPc(1)(ππ)-Aptamer (sequential) compared to electrochemical PSA aptasensors reported in literature (units used in this work converted from pM to pg/mL for ease of comparison with literature values).

Electrode	Linear range	LoD	Repeatability (RSD%)	Reproducibility (RSD%)	Reference
Biotin-Aptamer/streptavidin/AuNPs@GMCs on polygraphite electrode	0.005-20 ng/mL	1.0 ng/mL	4.7	4.40	[134]
APT/AuNPs/C_{60}-CS-IL/MWCNTs/SPCE	0.05-5 ng/mL	13 pg/mL	-	5.00	[142]
AuE-nAu-Aptamer	0.25-200 ng/mL	0.25 ng/mL	4.2	5.40	[144]
GCE- rGO-MWCNT/AuNPs/Aptamer	0.14-11.6 ng/mL	0.14 ng/mL	3.0	4.50	[145]
GCE-GS-MB-CS film	0.125-200 ng/mL	50 pg/mL	4.5	5.50	[225]
IDE/APTES/EDC-NHS/anti-PSA aptamer	2.5-90 ng/mL	1.5 ng/mL	3.3	3.10	[226]
GCE-GQDs-CoPc(1)(ππ)-Aptamer (sequential)	0.035-0.057 ng/mL	0.018 ng/mL	3.9	3.77	This work

Abbreviations:Reduced graphene oxide (rGO), multi-walled carbon nanotubes (MWCNTs), gold nanoparticles (AuNPs), GMCs (graphitized mesoporous carbon), gold nanospheres (nAu), graphene sheets–methylene blue–chitosan (GCE-GS-MB-CS), Au nanoparticles/fullerene C_{60}-chitosan-ionic liquid/multiwalled carbon nanotubes/screen printed carbon electrode (APT/Au NPs/C_{60}-CS-IL/MWCNTs/SPCE), Interdigitated electrode/ Aminopropyltrimethoxysilane / EDC-NHS/anti-PSA aptamer(IDE/APTES/EDC-NHS/anti-PSA aptamer)

5.2.2 The effects of QDs composition and structure: Comparing GQDs, NGQDs and gCNQDs

Once the best modification approach was determined, the nature of the QDs used was changed and the aptasensors compared. The aim of this sub-study was to verify the influence the structure and composition of the QDs has on the overall performance of the aptasensors fabricated herein.

5.2.2.1 EIS

The electrodes used for this sub-study were GCE-GQDs-CoPc(1)($\pi\pi$)-Aptamer (sequential), GCE-NGQDs-CoPc(1)($\pi\pi$)-Aptamer(sequential) and GCE-gCNQDs-CoPc(1)($\pi\pi$)-Aptamer (sequential). The Nyquist plots Fig. 5.12(a) were used to determine R_{ct} values by fitting the Randles equivalent circuit (Fig. 5.5(b)) as previously carried out. The R_{ct} values are summarized in Table 5.6. The highest R_{ct} values were observed for the NGQDs-based electrode followed by the GQDs-based electrode, with the gCNQDs-based electrode having the lowest values. A higher R_{ct} suggests more PSA binding hence better detection activity. Thus, the electrode containing NGQDs show better PSA detection. This electrode also had a low ΔE (Table 4.1) in the 1 mM $[Fe(CN)_6]^{3-/4-}$ solution before incubation with PSA which further validates the result obtained.

The apparent charge transfer rate constant (k_{app}) was calculated using Eqn.5.4. The gCNQDs-CoPc(1)($\pi\pi$)-Aptamer (sequential) combination had the highest k_{app} value (1.78×10^{-1} cm/s) which implies a less passivated electrode surface compared to the other two electrodes hence minimal binding of PSA to the aptamer or more exposure of the conductive regions of the electrode surface compared to the GQDs

and NGQDs-based surfaces. This means the gCNQDs-CoPc(1)(ππ)-Aptamer is less effective at detecting PSA, even though it has a larger surface coverage, Table 4.1.

A plot of phase-shift against log frequency Fig. 5.12(b) provides further characteristic information on the frequency, which cannot be obtained from the Nyquist plot. All electrodes showed the phase angle less than the ideal 90° indicative of a true capacitor (Table 5.6) [227]. Shift of phase angles towards lower frequencies in the Bode plots are an indication that the electrocatalyst gives more efficient catalytic activity [228]. The Bode plots show broad peaks suggesting complicated relaxation behaviour. This has been observed before and related many factors including film thickness [229], which could result in different diffusion processes within the film.

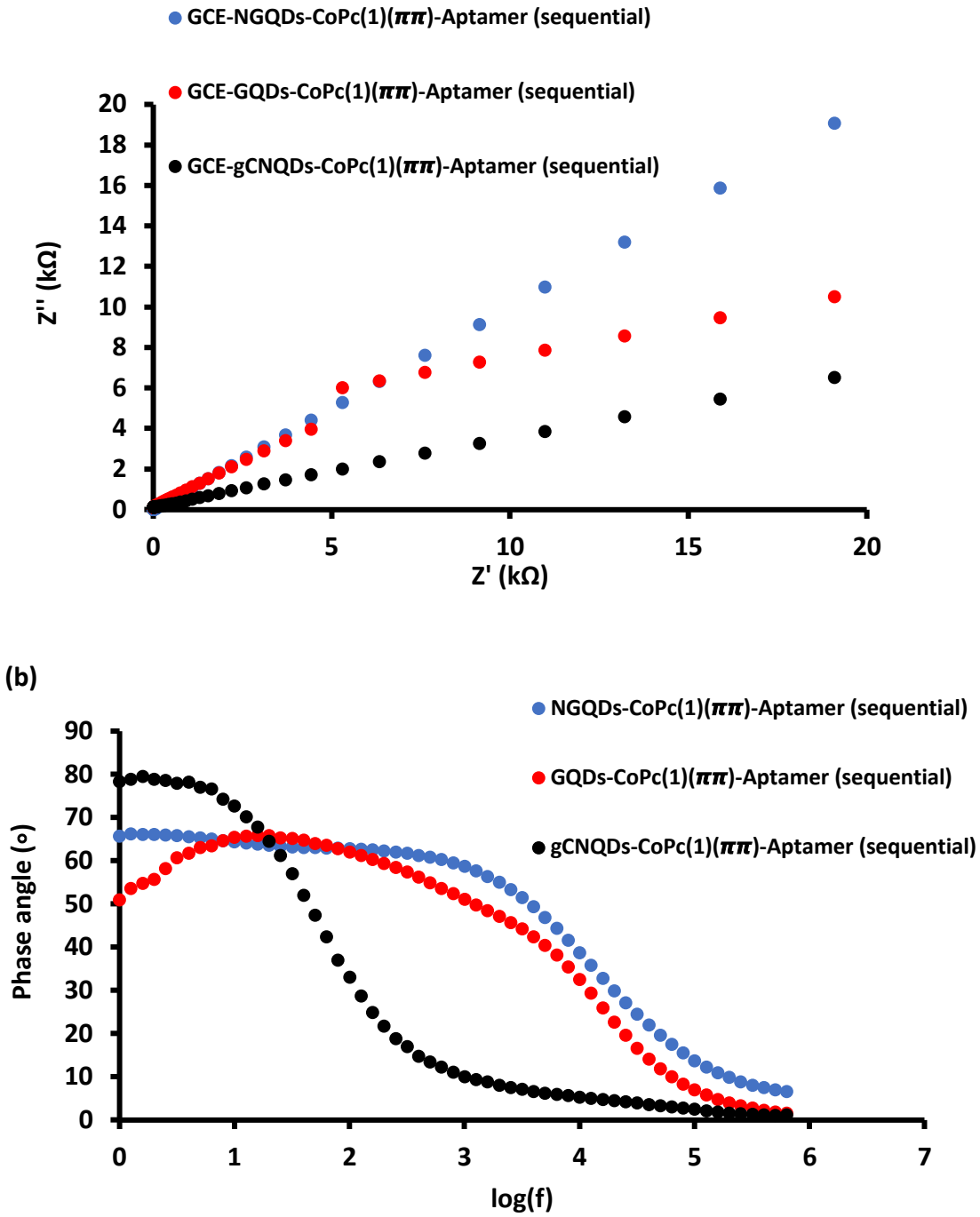

Figure 5.12: (a) Nyquist plots and (b) Bode plots of modified electrodes in a 2μM PSA solution in 30 mM phosphate buffer solution of pH 7.4.

Table 5.6 :EIS parameters for PSA detection.

Electrode	R_{CT}/ kΩ	k_{app} $(cm/s)^2/s)$	-Phase angle (°)
GCE-GQDs-CoPc(1)(ππ) -Aptamer (sequential)	19.13	$8.34x10^{-2}$	58.7
GCE-NGQDs-CoPc(1)(ππ) -Aptamer (sequential)	29.1	$6.72x10^{-2}$	77.1
GCE-gCNQDs-CoPc(1)(ππ) -Aptamer (sequential)	7.53	$1.78x10^{-1}$	65.4

5.2.2.2 Concentration studies using EIS and DPV

For the determination of limits of detection (LoD), the aptamer-containing electrodes were tested in a 30 mM phosphate buffer solution of pH 7.4 with PSA concentrations ranging from 1.2-2.0 pM. The analytical techniques used were and EIS, Fig. 5.13(a) and DPV, Fig.5.13(b). The results shown are for the NGQDs-based electrode as an example. Nyquist plots of the electrodes in PSA solutions of different concentrations are shown in Fig. 5.13(a). The detection limits determined in EIS are also summarized in Table 5.7 alongside other determined characteristics of the aptasensors fabricated. The GQDs, NGQDs and gCNQDs-based electrodes showed detection limits of 0.051, 0.046 and 0.035 ng/mL in EIS, respectively. The gCNQDs shows the highest LoD in EIS with the NGQDs performing the best using this technique. The DPV technique gave LoD values of 0.018, 0.044 and 0.033 ng/mL for the GQDs, NGQDs and gCNQDs-based electrodes respectively, therefore showing that the GQDs-based electrode produced the best results using

DPV. In EIS and DPV, the detection limits obtained for the NGQDs and gCNQDs based electrodes were in similar. The LoD values obtained for the GQDs based electrode suggested that using DPV as the analytical technique produces better results.

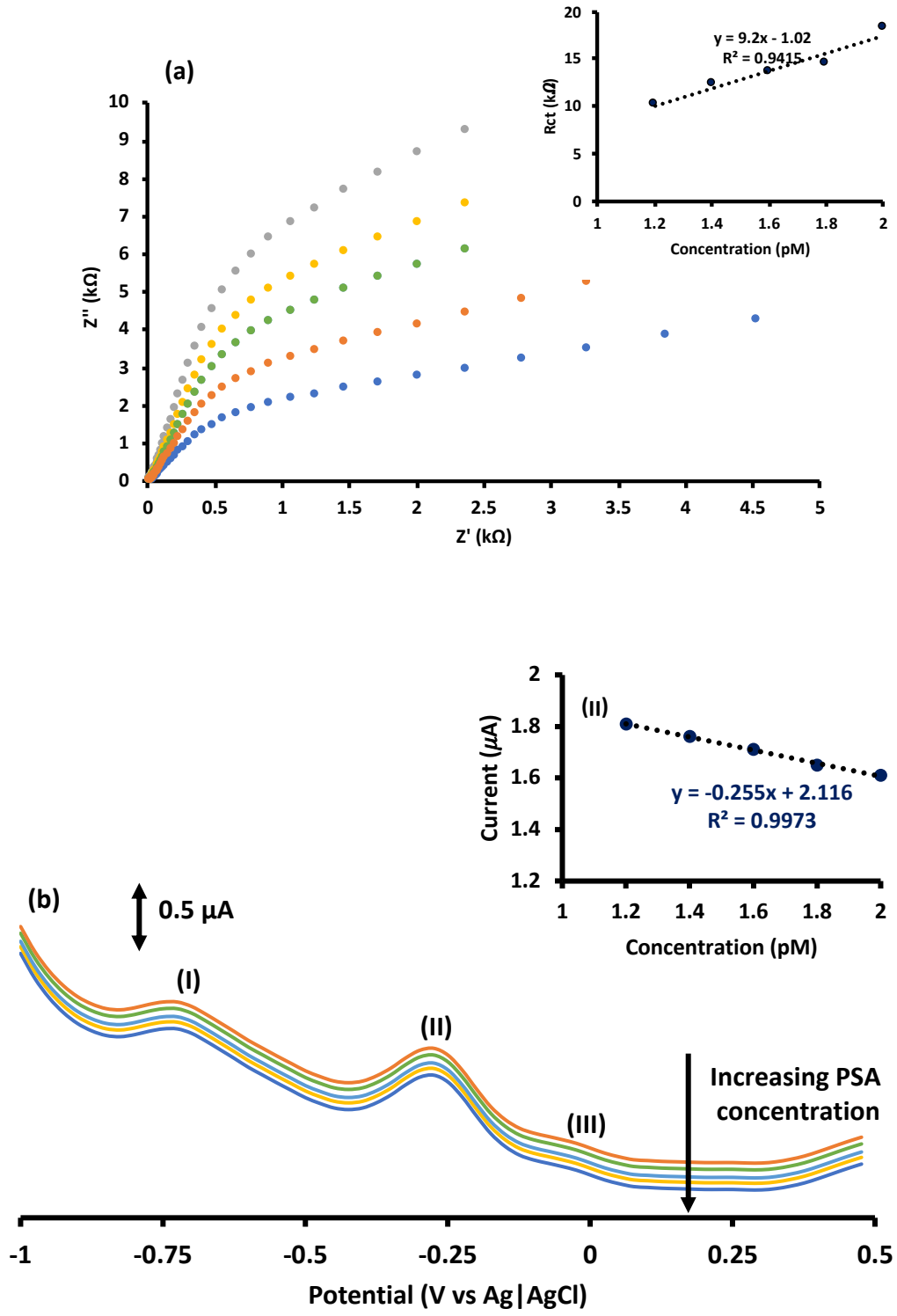

Figure 5.13: (a) Electrochemical impedance (EIS) Nyquist plots and (b) differential pulse voltammograms (DPV) of GCE-NGQDs-CoPc(1)(ππ)-Aptamer in a 30 mM phosphate buffer solution of pH 7.4 with PSA concentrations ranging from 1.2-2.0 pM. Inserts: Linear responses of resistance to changing concentrations.

5.2.2.3 Selectivity, stability, and reproducibility studies

The selectivity, stability and reproducibility of the fabricated electrochemical aptasensors were investigated using DPV. The results shown are for the NGQDs and gCNQDs electrodes since the GQDs based electrode has already been discussed in the previous sub-section. However, for the sake of comparison, the data for the GQDs-based electrode is included in the tables containing the NGQDs and gCNQDs data. The obtained voltammograms for reproducibility and stability studies are similar to those shown in Fig. 5.8- 5.10. The calculated results are summarized in Table 5.7. For reproducibility studies, the same electrode was fabricated on three different occasions (as done in Fig. 5.8) and tested in the PSA solution. The relative standard deviation (RSD (%)) was determined from peaks at 0 V for GQDs and was found to be 3.8 %. For the NGQDs based electrode, the RSD (%) was determined from peaks at -0.25 V and was found to be 6.2 %, Table 5.8. For the gCNQDs based electrode, the RSD (%) was determined from peaks at 0 V and was found to be 6.7 %. When the electrode was not in use, it was stored at 4 ^{o}C. After a week of storage, the aptasensors were used to detect PSA in PBS solution which allowed for the determination of the stability of the aptasensors. By looking at the difference between peak currents, the GQDs, NGQDs and gCNQDs based electrodes maintained approximately 89.0 %, 95.3 % and 92.2 % of their performance ability respectively (Table 5.7), proving to be quite stable in that time frame. Table 5.7 summarizes the LoD, repeatability and reproducibility results obtained in this work, which are further compared to other literature reports related to the detection of PSA [134, 230-234]. The aptasensor reported in this work showed one of the lowest detection limits and one of the lowest reproducibility RSD %. The

values determined were comparable to literature. From this, it can be concluded that these aptasensors have good potential to be used in clinical studies.

Table 5.7: Summary of results obtained in this work for GCE-GQDs-CoPc(1)(ππ)-Aptamer, GCE-NGQDs-CoPc(1)(ππ)-Aptamer and GCE-gCNQDs-CoPc(1)(ππ)-Aptamer (determined from EIS) compared to electrochemical PSA aptasensors reported in literature (units used in this work converted from pM to ng/mL for ease of comparison).

Electrode	Linear range/ ng/mL	LoD in EIS[a]/ ng/mL	Stability (% retention)	Reproducibility (RSD %)	Reference
PGE/AuNP@GMC /aptamer	0.25-200	0.25	92.8	Not reported	[134]
Au/MSF/Aptamer	1-300	0.28	98	2.4	[230]
SPCE-Ag/GO-Aptamer	0.75-100	0.27	77	5.3	[231]
GCE-CNTs-Chitosan-Aptamer	0.85-12.5	0.75	Not reported	3.9	[232]
CdS-Cu_2OTM/NAs-CdS-Cu/Aptamer	0.1-100	0.26	>99	Not reported	[233]
Graphene-PEDOT: PSS modified Whatman paper with aptamer	0.77-14	0.45	Not reported	0.26	[234]
GCE-GQDs-CoPc(1)(ππ)-Aptamer	0.034-0.057	0.051 (0.018)	89.0	3.8	This work
GCE-NGQDs-CoPc(1)(ππ)-Aptamer	0.034-0.057	0.046 (0.044)	95.3	6.2	This work
GCE-gCNQDs-CoPc(1)(ππ)-Aptamer	0.034-0.057	0.035 (0.033)	92.2	6.7	This work

Abbreviations: Au (Gold), MSF (mesoporous silica thin films), SPCE (screen printed carbon electrode), Ag (silver), GO (graphene oxide), CNT (carbon nanotubes), PGE/AuNP@GMC (pyrolytic graphite electrode/gold nanoparticles@graphitized meso- porous carbon), CdS-Cu_2OTM/NAs-CdS-Cu (cadmium selenide cuprous oxide titanium mesh/ nanorod arrays), PEDOT: PSS (poly (3,4-ethylenedioxythiophene):poly(styrenesulfonate)).
[a]LoD values from DPV in brackets

The mixed solution method discussed above, and DPV (Fig. 5.14) were used to test the selectivity of the developed aptasensors in complex mixtures, to prove their selectivity towards PSA. The interferences used and protocols followed were the same as those used for the GQDs-based aptasensor. The fabricated electrodes were incubated in the solutions and calculations carried out to determine the K_{amp} values. The peak potentials employed to calculate the K_{amp} values were -0.25 V (II) (for NGQDs and gCNQDs) and 0 V (III) (for GQDs and gCNQDs) since they were more resolved. The calculated values were summarized in Table 5.8 which indicate low interference and high selectivity of the fabricated sensors towards PSA detection. The gCNQDs-based electrodes also seem to show no interference at the most negative potential which indicates excellent potential as early detection devices towards PSA and thus reliable early diagnosis of prostate cancer.

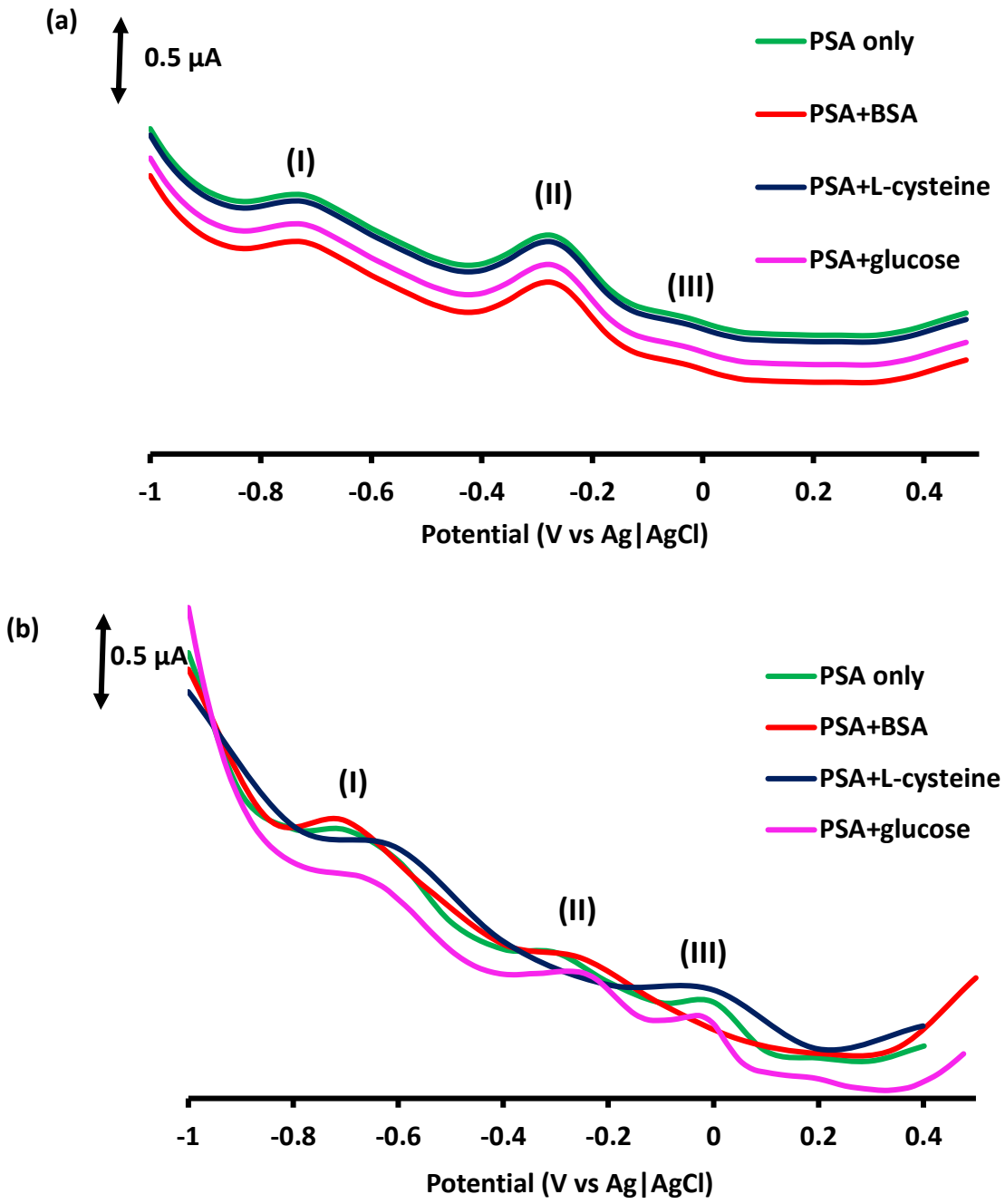

Figure 5.14: Differential pulse voltammograms of (a) GCE-NGQDs-CoPc(1)(ππ)-Aptamer and (b) GCE-gCNQDs-CoPc(1)(ππ)-Aptamer in the absence and presence of interferents in a PSA solution of concentration 2.0 pM.

Table 5.8: Comparative table of selectivity results obtained for the developed aptasensors.

	GQDs-CoPc(1)((ππ) -Aptamer	NGQDs-CoPc(1)((ππ) -Aptamer	gCNQDs-CoPc(1)((ππ) -Aptamer	-
Potential/	0.0	-0.25	-0.25	0.0
$K_{amp\ BSA}$	$-4.60x10^{-4}$	$-1.75x10^{-4}$	$4.14\ x10^{-5}$	$-1.00x10^{-3}$
$K_{amp\ Glucose}$	$-6.40\ x\ 10^{-4}$	$-1.11\ x10^{-4}$	$2.37x10^{-5}$	$-1.27\ x\ 10^{-4}$
$K_{amp\ l\text{-}cysteine}$	$6.80\ x\ 10^{-4}$	$2.96\ x\ 10^{-5}$	$-1.42\ x10^{-4}$	$-1.27\ x\ 10^{-4}$

5.2.3 Influence of MPc substituents

5.2.3.1 EIS

The effects of substituents on the MPc complexes were studied using EIS, by ππ-stacking gCNQDs@Aptamer with complex 1 and complex 2. Sequential modification was not used here as placing MPc complexes first on the electrode surface is not as efficient as placing QDs on the surface first. Moreover, placing the CoPc on top of the QDs-aptamer conjugate may lead to blocking of the binding sites of the aptamer. Therefore, premixing the components, which would lead to ππ conjugation of the modifiers was the best option for the fabrication of these aptasensors. Nyquist plots were obtained from analyzing all modified surfaces in the PSA solution (Fig. 5.15). The R_{ct} values obtained from EIS analyses are summarized in Table 5.9. The highest R_{ct} values were observed for the GCE-gCNQDs@aptamer-CoPc(2)(ππ) (104.3 kΩ) followed by the GCE-gCNQDs@aptamer-CoPc(1)(ππ) (98.6 kΩ) supporting cyclic voltammetry results in terms of ΔE (Table 4.1). The large R_{ct} suggest faster passivation, hence better binding of PSA to

aptamer and better detection. The GCE-gCNQDs@aptamer sensor showed slightly lower resistance to charge transfer compared to the bare electrode, which was not expected. However, this could imply that the gCNQDs enhanced the electron transfer slightly. For this section, the influence of the MPc complexes is the main focus.

Using the R_{ct} values obtained in the impedance studies, the apparent charge transfer rate constant (k_{app}) was calculated using Eqn.5.4 and the results are summarized in Table 5.9. The surface area was obtained as previously described and k_{app} values were high where R_{ct} were low as expected.

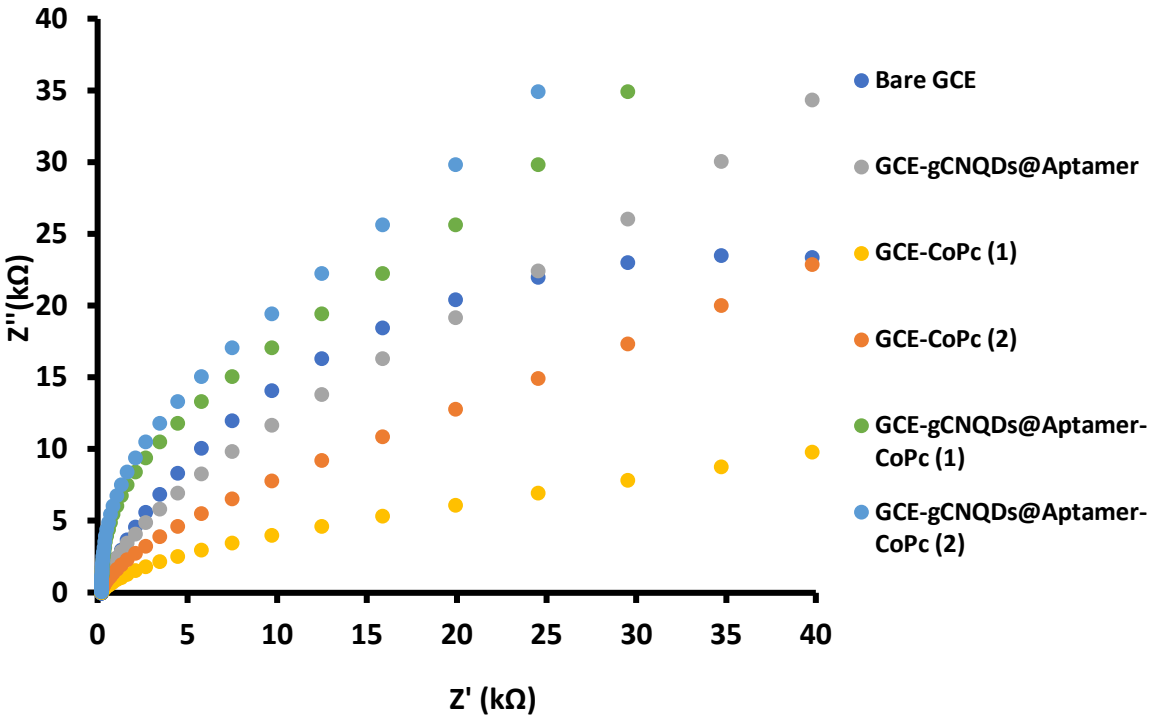

Figure 5.15: Nyquist plots of modified electrodes in a 2 µM PSA solution in 30 mM phosphate buffer solution of pH 7.4.

Table 5.9: Summary of determined R_{ct} and k_{app} values determined from Nyquist plots (in order of increasing R_{ct} values).

Electrode	R_{ct}/ kΩ	k_{app} $(cm/s)^2/s)$	LoD (ng/mL)
Bare GCE	77.6	5.14×10^{-3}	-
GCE-gCNQDs@aptamer	69.5	5.75×10^{-3}	0.042
GCE-CoPc(1)	22.3	3.01×10^{-2}	-
GCE-CoPc(2)	24.1	2.98×10^{-2}	-
GCE-gCNQDs@aptamer-CoPc(1) (ππ)	98.6	6.3×10^{-4}	0.031
GCE-gCNQDs@aptamer-CoPc(2) (ππ)	104.3	6.0×10^{-4}	0.023

5.2.3.2 Concentration studies using EIS

The aptamer-based electrodes were all compared to further show the significance of incorporating the phthalocyanine complexes to the gCNQDs@aptamer. Concentration studies were then carried out in buffer to see if the detection limits of the gCNQDs@Aptamer-based sensor is improved when linked to the phthalocyanine complexes. Detection limits were measured in a 30 mM phosphate buffer solution of pH 7.4 with PSA concentrations ranging from 1.2-2.0 pM. The obtained results are summarized in Fig. 5.16 with the inserts showing a linear relationship where the resistance to charge transfer increases with concentration of PSA. The detection limits obtained for the detection of PSA in buffer solutions using the GCE-gCNQDs@Aptamer, GCE-gCNQDs@Aptamer-CoPc(1)(ππ) and GCE-gCNQDs@Aptamer-CoPc(2)(ππ) were 0.042, 0.031 and 0.023 ng/mL respectively

(Table 5.9), which are all lower than the reported dangerous levels of PSA in males [118]. Although the addition of the asymmetric phthalocyanine complexes improved the detection limit of the gCNQDs@Aptamer conjugate, complex 2 produced better results than complex 1, proving that the nature of the functional groups present in the complexes plays a role in its electrocatalytic activity and influence. The better performance of complex 2 when compared to complex 1 may be explained as follows: Complex 2 has three acetaminophen substituents and an electron donating alkoxy group terminated by an alkyne group. The dominant acetaminophen substituent has a push-pull effect (electron donating-electron withdrawing) through resonance [235] that is independent of the MPc ring. This contributes greatly to the electrocatalytic ability of CoPc(2). Moreover, alkoxy groups lower oxidation potentials which results in a lower potential difference, which implies better electron transfer [236].The substituents of CoPc(2) also possess nitrogen atoms which are known to enhance electrocatalytic ability of composites which was earlier observed for the N-doped GQDs compared to the pristine GQDs.

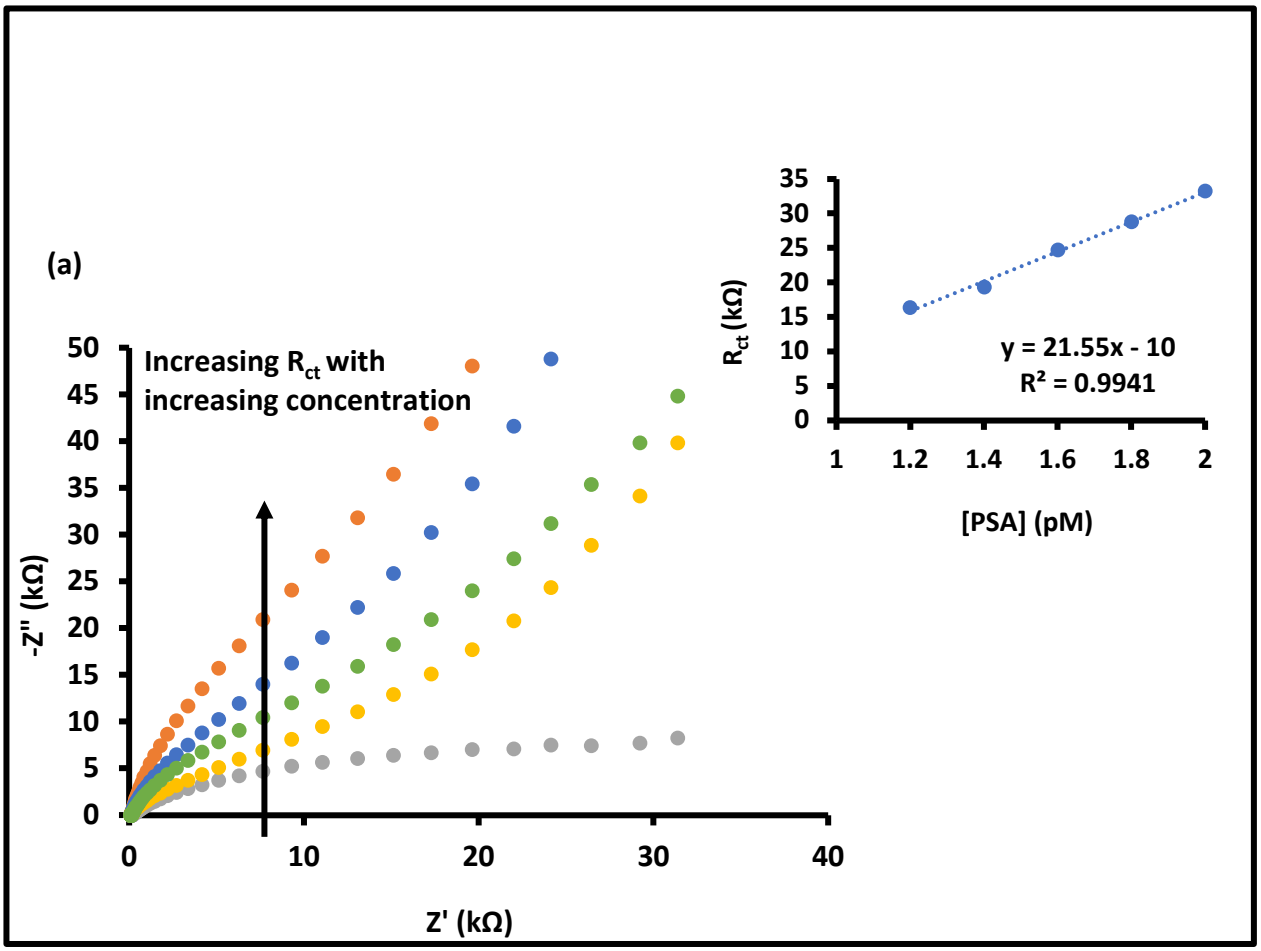
(a)
Increasing R_{ct} with increasing concentration
-Z'' (kΩ)
Z' (kΩ)
R_{ct} (kΩ)
y = 21.55x - 10
R^2 = 0.9941
[PSA] (pM)

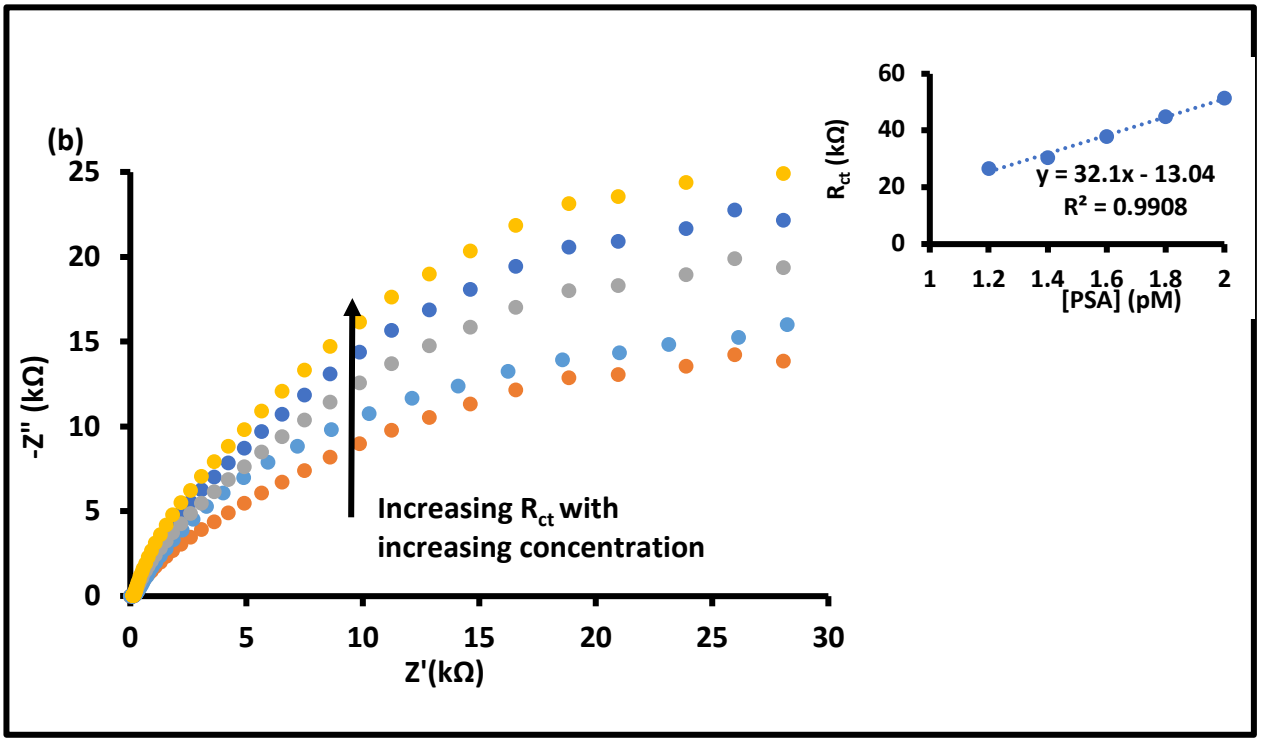
(b)
Increasing R_{ct} with increasing concentration
-Z'' (kΩ)
Z'(kΩ)
R_{ct} (kΩ)
y = 32.1x - 13.04
R^2 = 0.9908
[PSA] (pM)

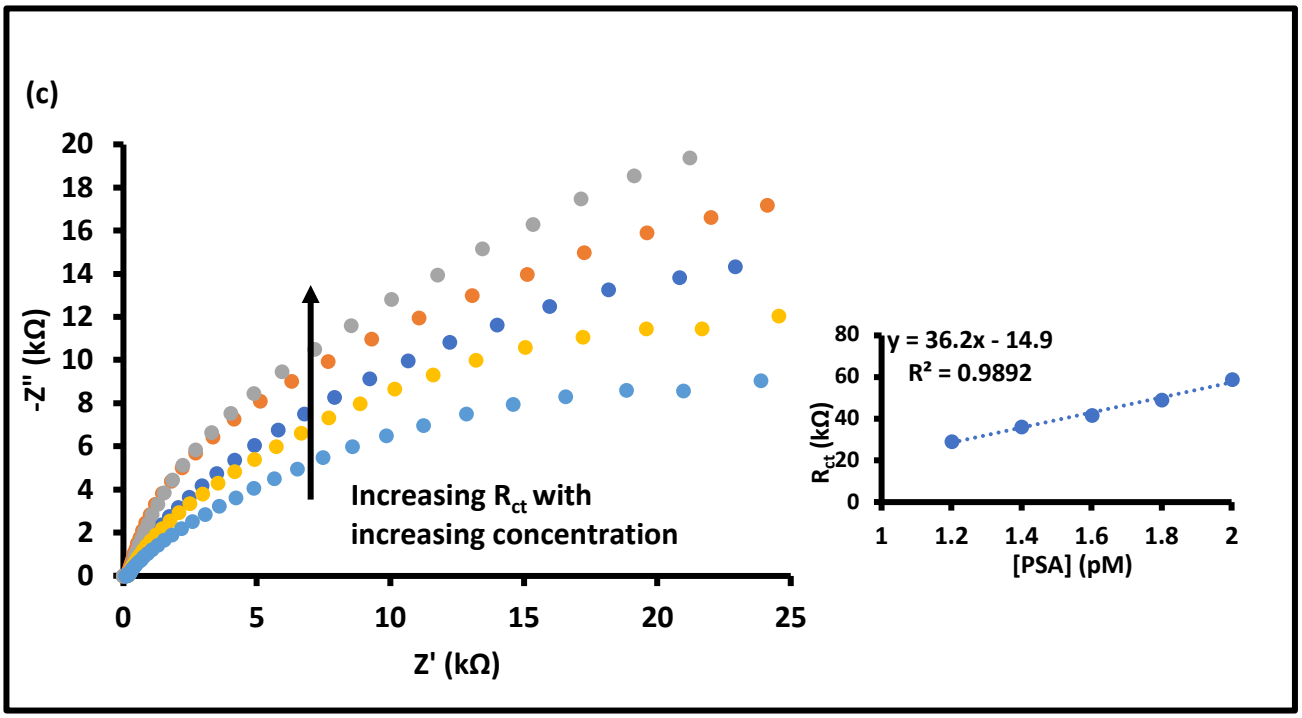

Figure 5.16: Electrochemical impedance (EIS) Nyquist plots of (a) GCE-gCNQDs@Aptamer (b) GCE-gCNQDs@Aptamer-CoPc(1) and (c) GCE-gCNQDs@Aptamer-CoPc(2) in a 30 mM phosphate buffer solution of pH 7.4 with PSA concentrations ranging from 1.2-2.0 pM. Inserts: Linear responses of resistance to changing concentrations.

5.2.3.3 Stability, reproducibility, and repeatability

The best performing aptasensor (GCE-gCNQDs@Aptamer-CoPc (2)) was further used as an example to determine the stability, reproducibility, and repeatability of the fabricated sensor. These tests were run using EIS as this has been the technique used throughout the studies conducted (Table 5.10). For stability, the aptasensor was stored for a week at 4 ^{o}C and then tested again. The sensor managed to retain 96.5 % of its performance. The reproducibility was determined by fabricating the same aptasensor three different times and determining the behavior in the buffer solution containing PSA after incubation. The RSD % was determined as 2.5 % validating the reproducibility of this sensor. The aptasensor was tested 10 times over to determine if the same aptasensor could be used for multiple PSA tests (repeatability). The repeatability RSD % was determined as 4.8 % which is quite low. These studies therefore show that this fabricated aptasensor with low detection limits is reliable and efficient as it is stable, reproducible and can be reused for several tests before a new one is required.

Table 5.10: Raw data recorded for the determination of Stability, reproducibility and repeatability for the GCE-gCNQDs@Aptamer-CoPc(2)(ππ) aptasensor. All measurements were run in triplicate. Repeatability measures were recorded for 10 analyses.

STABILITY			
Rct values in kΩ			
	DAY 0	DAY 7	
	106.2	94.8	
	98.3	100.1	
	99.8	98.6	RETENTION %
AVERAGE	101.4	97.8	96.5

REPRODUCIBILITY			
	Electrode 1	Electrode 2	Electrode 3
Run 1	102.2	104.2	95.4
Run 2	101.3	100.4	89
Run 3	99.4	98.6	105.9
Average	101.0	101.1	96.8
Mean of means	99.6		
SD of means	2.5		
RSD %	2.5		

REPEATABILITY		
Run		
1		103.2
2		101.5
3		97.5
4		90.5
5		99.1
6		101.3
7		102.5
8		91.8
9		103.2
10		104.1
	average	99.5
	SD	4.8
	RSD	4.8

5.2.4 AuNPs-MPc conjugates

5.2.4.1 EIS

A selection of Nyquist plots is shown in Fig. 5.17 and were fitted using a Randles electronic equivalent circuit fitted with a constant phase element (CPE) due to the suppressed semi-circles. As previously stated, using a CPE takes into account the irregularities on the electrode surface that are a result of roughness and inhomogeneities on the modifiers, where the plot starts to appear more linear as opposed to appearing as a semi-circle with a defined linear segment. The apparent charge transfer rate constant (k_{app}) was also calculated using Eqn. 5.4 and summarized in Table 5.11. The R_{ct} value is highest for the GCE-AuNPsØCoPc(2)-Aptamer with the lowest corresponding apparent charge transfer which is expected as R_{ct} and K_{app} are inversely proportional.

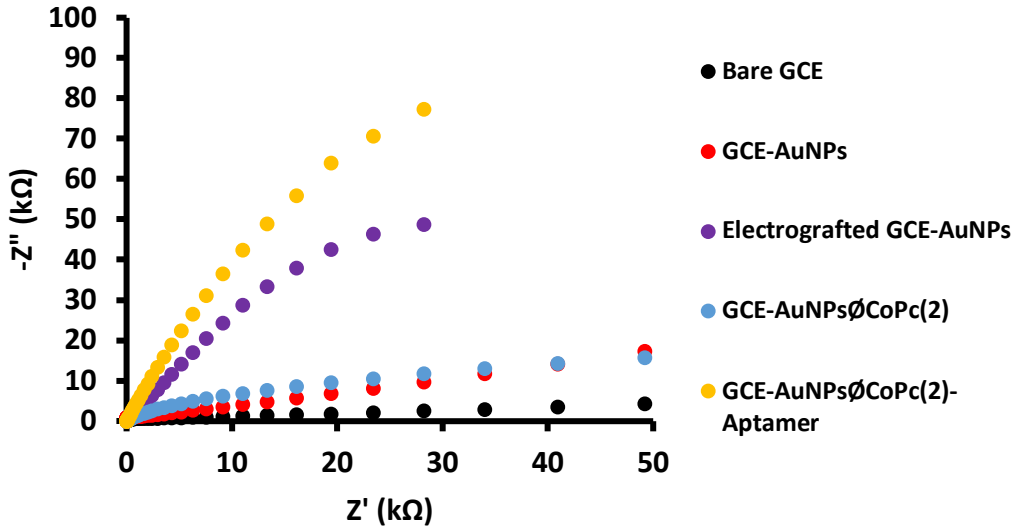

Figure 5.17: Nyquist plots of electrodes in a 2 µM PSA solution in 30 mM PBS solution of pH 7.4.

Table 5.11: Summary of results determined from PSA detection using EIS in 2 µM PSA.

Electrode	R_{CT}/ kΩ	k_{app} $(cm/s)^2/s$
Bare GCE	0.46	$8.42x10^{-4}$
GCE-AuNPs	0.68	$5.80x10^{-4}$
GCE-Aptamer	3.66	$4.8x10^{-5}$
GCE-AuNPs-Aptamer	2.58	$8.8x10^{-5}$
GCEØCoPc (2)	2.46	$9.02\ x10^{-5}$
GCEØCoPc(2)-Aptamer	4.18	$2.09\ x10^{-5}$
GCE-AuNPsØCoPc(2)	1.14	$2.68\ x10^{-4}$
GCE-AuNPsØCoPc(2)-Aptamer	9.62	$1.82\ x10^{-6}$

5.2.4.2 Concentration studies using EIS and DPV

Fig. 5.18, representing GCE-AuNPsØCoPc(2)-Aptamer as an example, shows the Nyquist plots of the electrodes in solutions containing different concentrations of PSA. All electrodes show a linear response to changing PSA concentration after incubation in the PSA solutions. The slopes of each fabricated aptasensor represents the sensitivity of the sensor and the highest sensitivity is observed in the insert of Fig. 5.18, recorded for the GCE-AuNPsØCoPc(2)-Aptamer. The LoDs were also determined (Table 5.12) and the lowest was for the GCE-AuNPsØCoPc(2)-Aptamer as expected, was found to be 0.92 pM (0.026 ng/mL), determined from EIS results and 0.89 pM (0.025 ng/mL) determined from DPV studies.

Table 5.12: Summary of LoD determined from the detection of PSA in buffer and in spiked serum samples.

Electrode	LoD in PBS (pM)	reference
GCE-AuNPs-Aptamer	1.24 (EIS)	This work
	1.09 (DPV)	
GCEØCoPc(2)-Aptamer	1.83 (EIS)	This work
	1.10 (DPV)	
GCE-AuNPsØCoPc(2)-Aptamer	0.92 (EIS)	This work
	0.89 (DPV)	

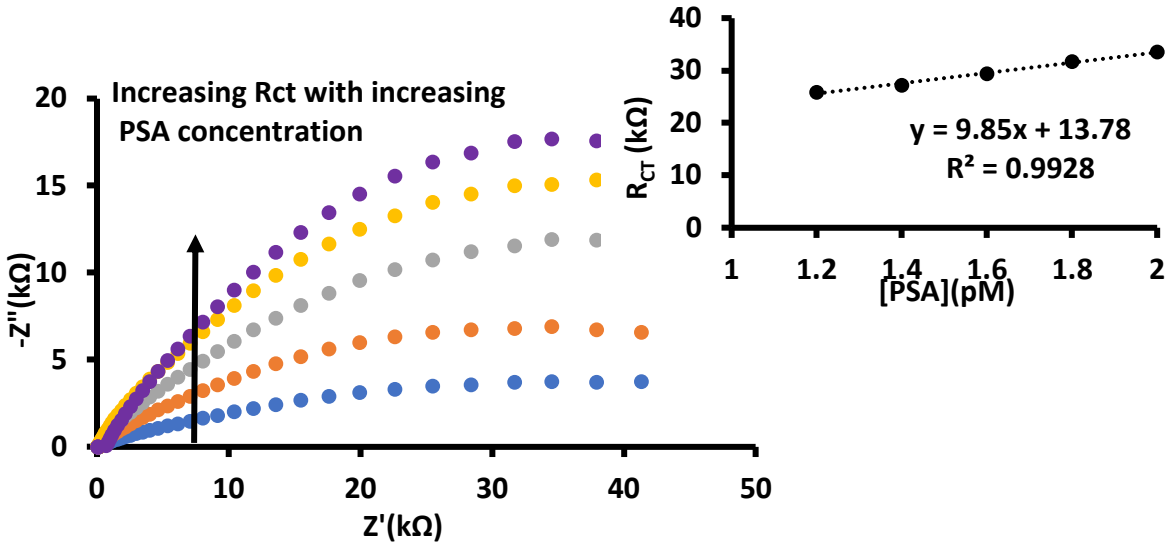

Figure 5.18: Electrochemical impedance (EIS) Nyquist plots of GCE-AuNPsØCoPc(2)-Aptamer in a 30 mM PBS solution of pH 7.4 containing PSA concentrations ranging from 1.2-2.0 pM. I**nsert:** Linear responses of resistance to changing concentrations.

The DPV results are illustrated in Fig. 5.19. Linear responses to change in concentration were also observed where the peak current decreased with increasing PSA concentration due to PSA binding during incubation. The LoD was determined from the peak at 0 V for the GCE-AuNPs-Aptamer aptasensor, 0.0 V for the GCEØCoPc(2)-Aptamer aptasensor and at -0.25 V for the GCE-AuNPsØCoPc(2)-Aptamer aptasensor. In DPV (Fig. 5.19) the GCE-AuNPsØCoPc(2)-Aptamer aptasensor produced a LoD of 0.89 pM. These detection limits will later be compared to those that will be determined in human serum to test the reliability of the studies reported in this work.

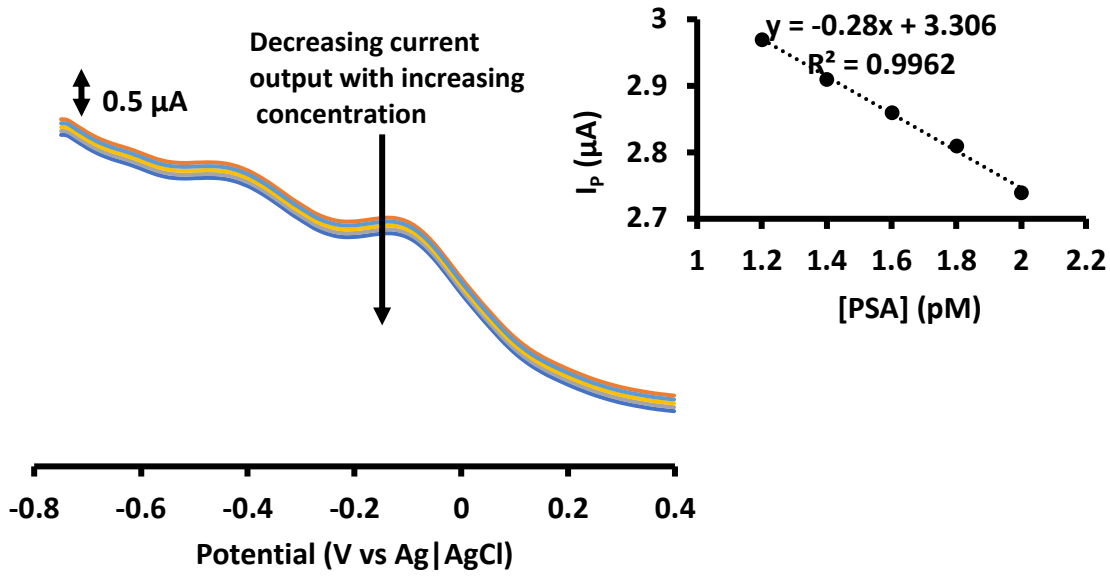

Figure 5.19: Differential pulse voltammograms (DPV) of GCEØCoPc(2)-Aptamer in a 30 mM PBS solution of pH 7.4 containing PSA concentrations ranging from 1.2-2.0 pM. I**nsert:** Linear responses of resistance to changing concentrations.

5.2.4.3 Effects of scan rate

The scan rate studies were conducted using DPV and scan rates of 0.625, 1.25, 2.5, 5, 15 and 20 V/s. The results obtained are summarized in Fig. 5.20 using GCEØCoPc(2)-Aptamer as an example. The general trend observed was an increasing in peak current with increasing scan rate. However, this increase was not linear and did not pass through the origin when scan rate was plotted against peak current as well as peak current vs the square root of scan rate. This has been reported to be characteristic of an electrodic process (i.e., reactions occurring at the electrode surface) preceded by an electrochemical reaction, followed by a

homogenous chemical reaction [196]. Thus, it can be concluded that the process occurring between solution and sensor are mainly adsorption controlled.

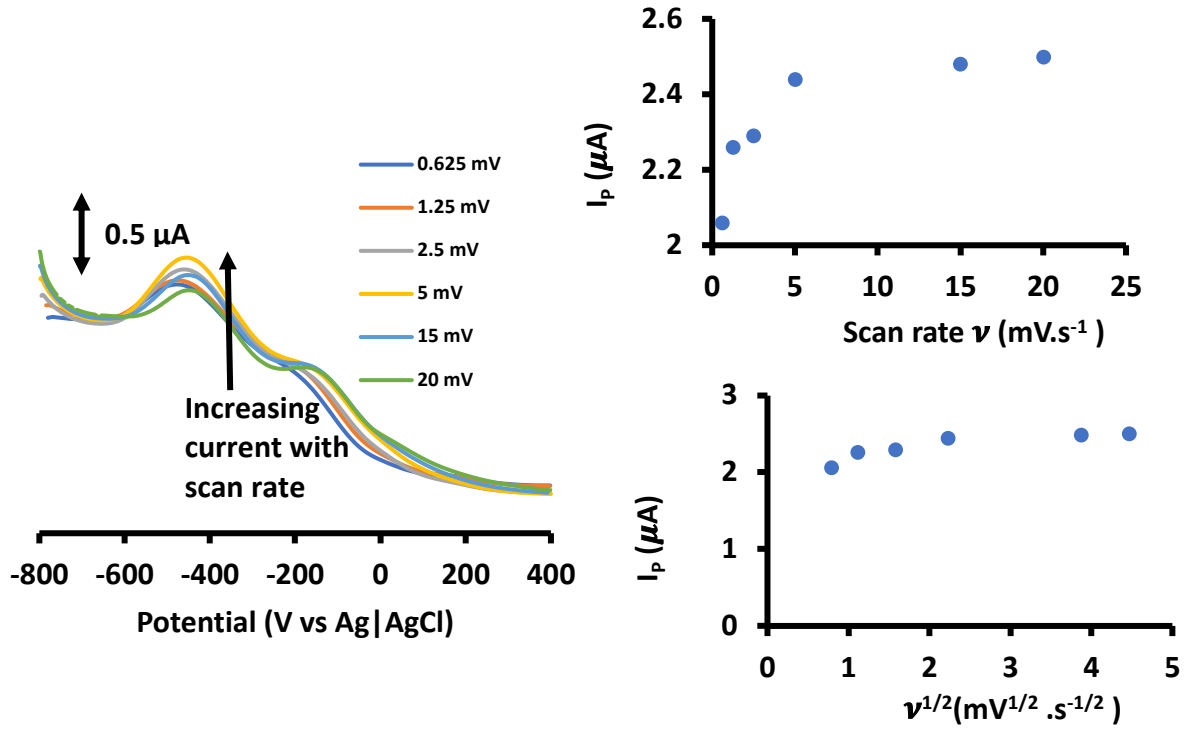

Figure 5.20: Differential pulse voltammograms of scan rate studies of GCEØCoPc(2)-Aptamer in a 30 mM phosphate buffer solution of pH 7.4 with PSA concentration of 2.0 pM. Inserts: Plots of peak current (I_P) vs ν and peak current (I_P) vs $\nu^{1/2}$.

5.2.4.4 Selectivity, stability, repeatability, and reproducibility studies

Selectivity studies were achieved by using the mixed solution method and DPV. The PSA samples were mixed with BSA, L-cysteine and glucose as interferants as done for other fabricated aptasensors already discussed and (K_{amp}) values determined in the same manner as above. The results obtained are summarized in Table 5.13 with the potentials at which the K_{amp} values were calculated. The values determined were very low implying that these sensor platforms could be applied without any pre-separation procedures for the determination of PSA in the presence of the interferents with no need for pre-treatment of sample.

Table 5.13: K_{amp} values determined from the detection of PSA in a complex mixture.

Electrode	K_{AMP} (BSA)	K_{AMP} (Glucose)	K_{AMP} (L-cysteine)
GCE-AuNPs-Aptamer	-4.18×10^{-4}	-1.00×10^{-3}	-4.75×10^{-4}
GCEØCoPc(2)-Aptamer	3.96×10^{-4}	4.57×10^{-4}	4.37×10^{-4}
GCE-AuNPsØCoPc(2)-Aptamer	-2.7×10^{-5}	-5.4×10^{-6}	7.61×10^{-5}

The stability, repeatability, and reproducibility of the proposed aptasensors were also investigated by DPV using a 2 pM PSA in PBS solution of pH 7.4 (30 mM). Table 5.14 summarizes the results obtained. To verify the reproducibility of the aptasensors, each electrode was fabricated three times and tested in the PSA solution of same concentration. The relative standard deviation (% RSD) was determined as 4.89 %, 7.1 % and 0.91 % (Table 5.14) for GCE-AuNPs-Aptamer, GCEØCoPc(2)-Aptamer and GCE-AuNPsØCoPc(2)-Aptamer respectively. The aptasensor with the CoPc(2) and AuNPs combined proved to be the best performing after being refabricated a few times over.

After incubation the PSA solution, the DPV scans were run for 50 cycles and the change in current response was monitored (Figure not shown). The first and the last scan were compared using the marked peaks. The determined % RSD values were 0.81 %, 2.04 %, 0.83 % for GCE-AuNPs-Aptamer, GCEØCoPc(2)-Aptamer and GCE-AuNPsØCoPc(2)-Aptamer, respectively, Table 5.14.

When the electrode was not in use, it was stored in the fridge at 4 ^{o}C. After a week of storage, the final run was compared to an initial run done before storage (Fig. 5.21, point of RSD determination marked with arrows). The % RSD determined for the fabricated aptasensors (Table 5.14) were 4.35 %, 6.97 % and 4.23 % for GCE-AuNPs-Aptamer, GCEØCoPc(2)-Aptamer and GCE-AuNPsØCoPc(2)-Aptamer respectively. The most stable electrodes appear to be the ones with the AuNPs which implies that these nanostructures provide greater stability for the immobilization of the aptamer when coupled with the CoPc(2).

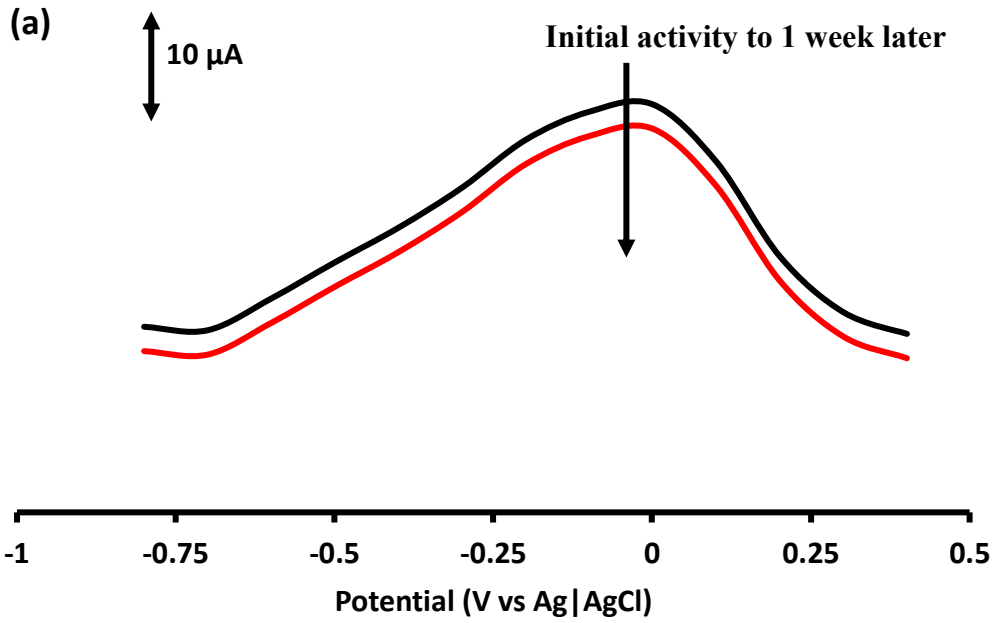
(a)
10 µA
Initial activity to 1 week later
-1
-0.75
-0.5
-0.25
0
0.25
0.5
Potential (V vs Ag|AgCl)

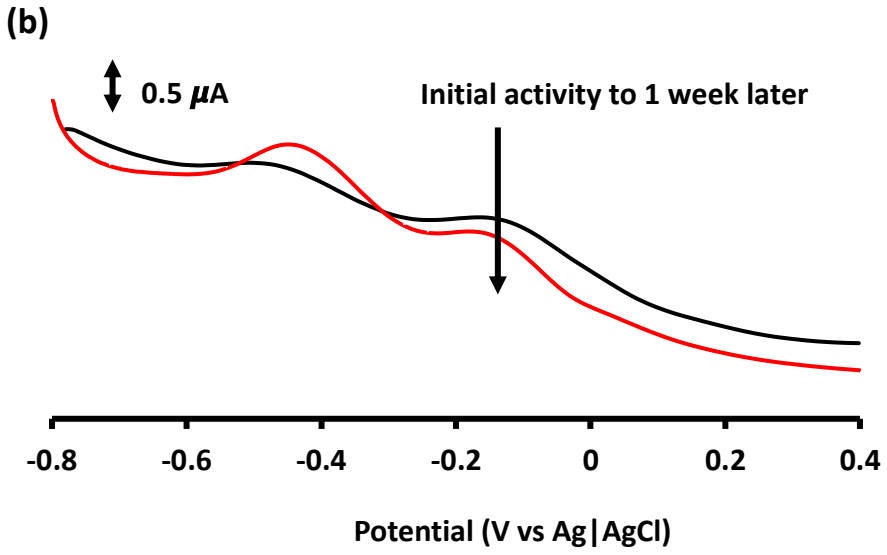
(b)
0.5 µA
Initial activity to 1 week later
-0.8
-0.6
-0.4
-0.2
0
0.2
0.4
Potential (V vs Ag|AgCl)

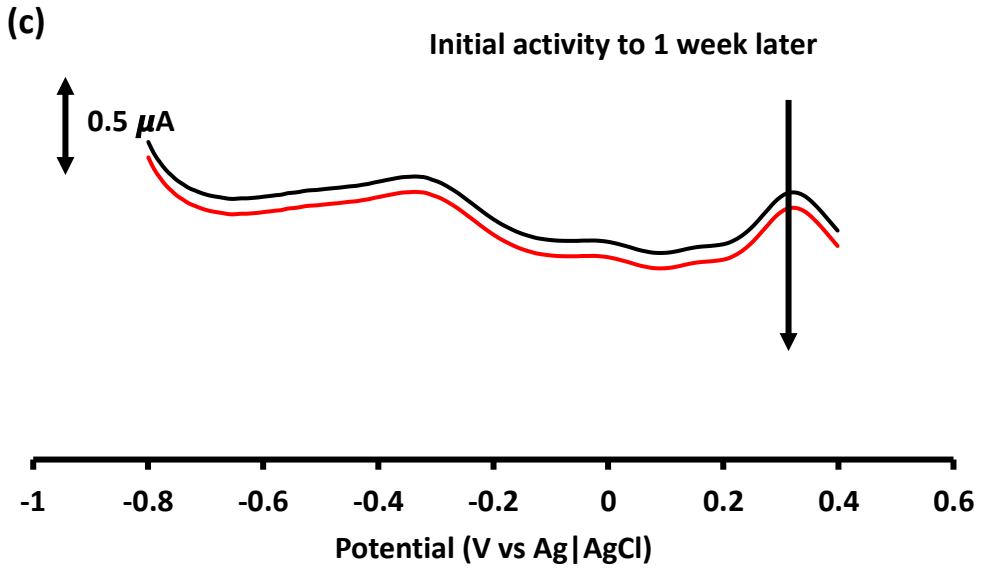

Figure 5.21: Differential pulse voltammograms of (a) GCE-AuNPs-Aptamer, (b) GCEØCoPc(2)-Aptamer and (c) GCE-AuNPsØCoPc(2)-Aptamer in a PSA solution of concentration 2.0 pM measured before and after a week.

Table 5.14: % RSD values determined for stability, repeatability and reproducibility of fabricated aptasensors.

Electrode	Linear range/pM	Stability (RSD%)	Repeatability (RSD%)	Reproducibility (RSD%)
GCE-AuNPs-Aptamer	1.2-2.0	4.35	0.81	4.89
GCEØCoPc(2)-Aptamer	1.2-2.0	6.97	2.04	7.10
GCE-AuNPsØCoPc(2)-Aptamer	1.2-2.0	4.23	0.83	0.91

5.3 Conclusions

This chapter has discussed the electrocatalytic ability of various fabricated sensors. Initially, the electrodes modified with QDs and MPc were used to catalyze L-cysteine to verify their synergistic effects for further use as signal amplifiers and aptamer immobilizers for aptasensing. The synergistic effects of these nanocomposites improved signal output and showed good promise in being applied as signal enhancers and aptamer immobilization platforms towards the fabrication of PSA aptasensors. Thereafter, the GQDs-CoPc(1)($\pi\pi$) conjugate was used as an example, together with aptamer for the detection of PSA in buffer solutions. Various combinations of these composites were immobilized via adsorption on glassy carbon electrodes to determine the best combination that would produce low detection limits and prove superior to other combinations used. It was clearly shown that the sequentially modified electrode, GCE-GQDs-CoPc(1)($\pi\pi$)-Aptamer (sequential), showed the best performance, therefore this modification sequence was used for further study involving the comparison of structure and composition of QDs. The comparative study showed that all electrodes produced low detection limits with good stability, reproducibility, and repeatability as well as selectivity for PSA in complex samples. The NGQDs-based aptasensor however, performed the best in terms of detection limits, especially.

CoPc complexes were also compared, and it was found that the nature of the substituent influenced the performance of the aptasensor towards the detection of PSA. Complex 2 performed the best, owing to the resonance effect of the dominant substituents it possesses, as well as the presence of the nitrogen atoms at the periphery that complex 1 does not possess.

The study was shifted from QDs to AuNPs which are commonly used in PSA aptasensors and the influence of combining these AuNPs with CoPc(2) towards PSA detection was studied. It was proven that incorporating a CoPc complex to the sensor improved its performance. Moreover, using covalent immobilization of the nanocomposites increased the stability of the aptasensor. The aptasensors containing AuNPs also showed good stability, reproducibility, and repeatability. Scan rate studies indicated adsorption-controlled processes occurring between electrode and analyte.

6. Real sample analyses

To validate the reliability and feasibility of the fabricated aptasensors discussed in the previous chapter, they were tested in spiked human serum samples. This was also to prove the trends observed when the PSA was analyzed in buffer. In preparation for this analysis, the serum samples were diluted 100-fold with PBS (pH 7.4) to reduce the matrix effects of the real sample. Thereafter, different concentrations of PSA were added to the diluted serum solutions. The analytical methods as well as concentrations used in this study were the same as the methods used for PSA detection in PBS. The real sample tests were run using DPV and EIS for the sake of comparison of both techniques unless stated otherwise. Table 6.1 summarizes the detection limits obtained in buffer solution and serum samples.

Table 6.1: Summary of determined LoD (ng/mL) values in buffer and spiked serum samples of aptasensors using EIS unless stated otherwise.

Electrode	LoD_{BUFFER}	LoD_{SERUM}
GCE-GQDs-CoPc(1)(ππ)-Aptamer	0.051	0.059 (DPV)
		0.058
GCE -NGQDs-CoPc(1)(ππ)-Aptamer	0.044 (DPV)	0.043
	0.046	
GCE-gCNQDs-CoPc(1) (ππ)-Aptamer	0.033 (DPV)	0.047 (DPV)
	0.035	0.046
GCE-gCNQDs@aptamer	0.042	0.054
GCE-gCNQDs@aptamer-CoPc(1) (ππ)	0.031	0.032
GCE-gCNQDs@aptamer-CoPc(2) (ππ)	0.023	0.027
GCE-AuNPs-Aptamer	0.035	0.037
	0.031 (DPV)	0.040 (DPV)
GCEØCoPc(2)-Aptamer	0.052	0.056
	0.031 (DPV)	0.043 (DPV)
GCE-AuNPsØCoPc(2)-Aptamer	0.026	0.028
	0.025 (DPV)	0.027 (DPV)

6.1 ππ-conjugates

The following conjugates were used as examples to verify the feasibility of the fabricated aptasensors to be used in clinical studies towards the electrochemical detection of PSA: GCE-GQDs-CoPc(1)(ππ)-Aptamer (sequential), GCE-NGQDs-CoPc(1)(ππ)-Aptamer (sequential) and GCE-gCNQDs-CoPc(1)(ππ)-Aptamer (sequential).

Different concentrations of PSA were added to the diluted serum solutions for analysis. The analytical methods as well as concentrations used for analysis of these real samples were the same as the methods used for PSA detection in buffer where the concentration ranged from 1.2 to 2 pM. The verification of the reliability and feasibility of the aptasensors was taken further by determining the % recovery in the concentration range of 1.2-2 pM, using EIS. The recovery was calculated as the ratio of the sensor performance in spiked human serum samples to that obtained in buffer for the same concentrations of PSA as reported in literature [141]. The amount of PSA found in spiked serum was determined by calculating the percentage signal based on PSA detection in the chosen buffer. All experiments were run in triplicate and the recorded values are an average of the values recorded for each run.

For GQDs-CoPc(1)(ππ)-Aptamer both DPV and EIS were employed, DPV is used as an example. The obtained responses in DPV for the GQDs-CoPc(1)(ππ)-Aptamer electrode is shown in Figure 6.1. The LoD for GQDs-CoPc(1)(ππ)-Aptamer was determined from the signal at 0 V as it was the most prominent one. The LoD was determined as 0.059 ng/mL using DPV, which is below the cut-off value of 4 ng/mL in patients suspected to have prostate cancer [118, 237, 238]. The LoD

determined from EIS was 0.058 ng/mL which is close to the value obtained in DPV for GQDs-CoPc(1)(ππ)-Aptamer, Table 6.1. EIS results for the determination of % recoveries are shown in Table 6.2. The percentage recovery calculated was 80.5% at the highest concentration level analyzed and 93.5 % at the lowest concentration level analyzed.

For the NGQDs-based electrode, EIS was used as the analytical tool to detect PSA in the spiked human serum samples for the determination of the LoD and percentage recoveries. DPV was not included as the peaks were too broad for the determination of LoD. The obtained responses in EIS are shown in Figure 6.2. The LoD was determined as 1.52 pM (0.043 ng/mL) which is again below the cut-off value of 4 ng/mL. The recovery results obtained are shown in Table 6.3.The amount of PSA found in spiked serum was also determined. The percentage recovery calculated was 85.9 % at the lowest concentration level of 1.2 pM and 93.7 % at the highest concentration level of 2 pM.

The obtained responses in DPV for the gCNQDs-based electrode are shown in Figure 6.3. The LoD was determined from the signal at 0 V as it was the most prominent one. The LoD was determined as 0.936 pM (0.027 ng/mL) in DPV and 0.929 pM (0.026 ng/mL), (Table 6.1), in EIS which is also below the cut-off value of 4 ng/mL. The verification of the reliability and feasibility were performed as explained above. The results obtained are shown in Table 6.4. The percentage recovery calculated was 86 % at the lowest concentration level analyzed and 94.9 % at the highest concentration level analyzed.

In summary, it has been shown that the results obtained from detecting PSA in buffer are feasible as they are comparable to the values determined in serum samples, Table 6.1. The R_{ct} values were lower in serum compared to PBS. The

decrease could indicate some protein-protein interaction which results in a decrease in sensitivity hence the reduced R_{ct} values obtained in serum analyses compared to those done in PBS. The interferences, however, are not strong enough to affect the ability of the aptasensor to detect PSA in real samples. Some literature reports have shown detection limits determined from electrochemically detecting PSA in spiked serum samples [226, 230, 231, 239-241] for PSA electrochemical detection. When compared to the data obtained herein, the fabricated sensors in this work showed better performance.

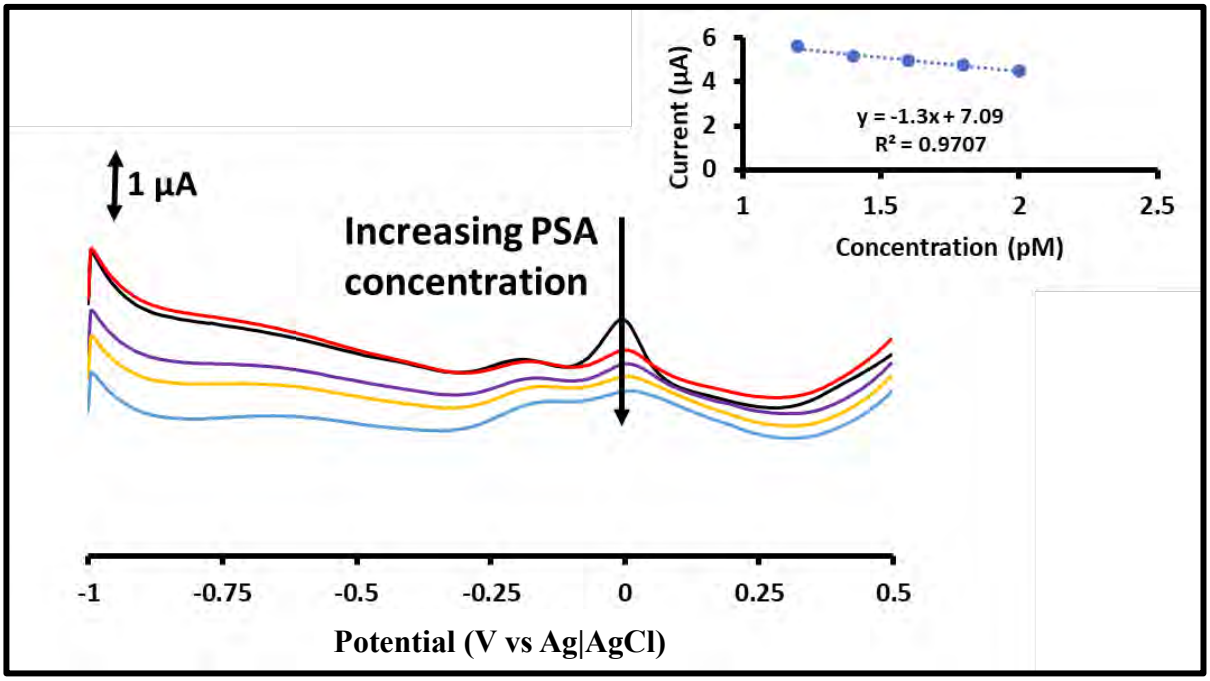

Figure 6.1: Differential pulse voltammograms of GCE-GQDs-CoPc(1)(ππ)-Aptamer in spiked human serum with PSA concentrations ranging from 1.2-2.0 pM. Insert: Linear responses of currents to changing concentration.

Table 6.2: Summary of recovery measurements of PSA in spiked human serum samples for the GCE-GQDs-CoPc(1)(ππ)-Aptamer aptasensor. % RSD = relative standard deviation (standard deviation/mean × 100; n = 3).

[PSA] added/ pM In buffer	R_{ct} (kΩ) In buffer	[PSA] found/ pM In serum	R_{ct} (kΩ) In serum	% RSD	% Recovery
1.2	3.1	1.12	2.9	4.2	93.5
1.4	4.2	1.30	3.9	6.1	92.8
1.6	5.8	1.46	4.7	5.4	81.0
1.8	7.9	1.20	6.8	4.5	86.1
2.0	10.3	0.97	8.3	7.4	80.5

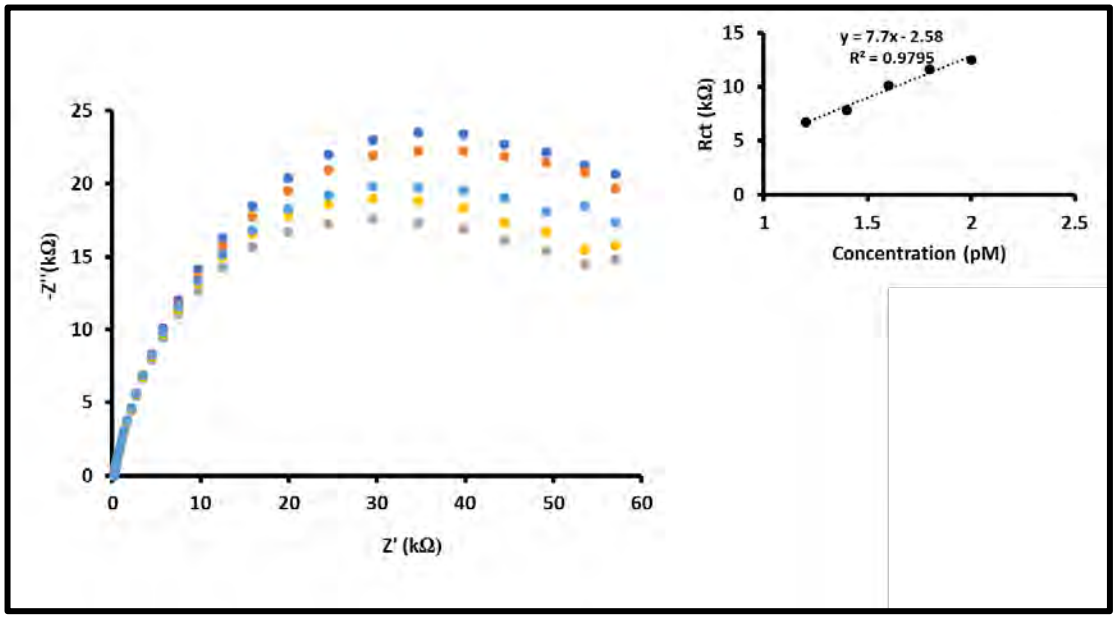

Figure 6.2: Nyquist plots of GCE-NGQDs-CoPc(1)(ππ)-Aptamer in spiked human serum with PSA concentrations ranging from 1.2-2.0 pM. Insert: Linear responses of currents and resistance to changing concentration.

Table 6.3: Summary of recovery measurements of PSA in spiked human serum samples for the GCE-NGQDs-CoPc(1)(ππ)-Aptamer aptasensor. % RSD = relative standard deviation (standard deviation/mean × 100; n = 3).

[PSA] added/ pM In buffer	R_{ct} (kΩ) In buffer	[PSA] found/ pM In serum	R_{ct} (kΩ) In serum	% RSD	% Recovery
1.2	7.80	1.03	6.7	5.9	85.9
1.4	8.59	1.16	7.1	5.4	82.6
1.6	10.9	1.48	10.1	6.2	92.7
1.8	11.8	1.77	11.6	4.9	98.3
2.0	12.8	1.87	12.0	8.6	93.7

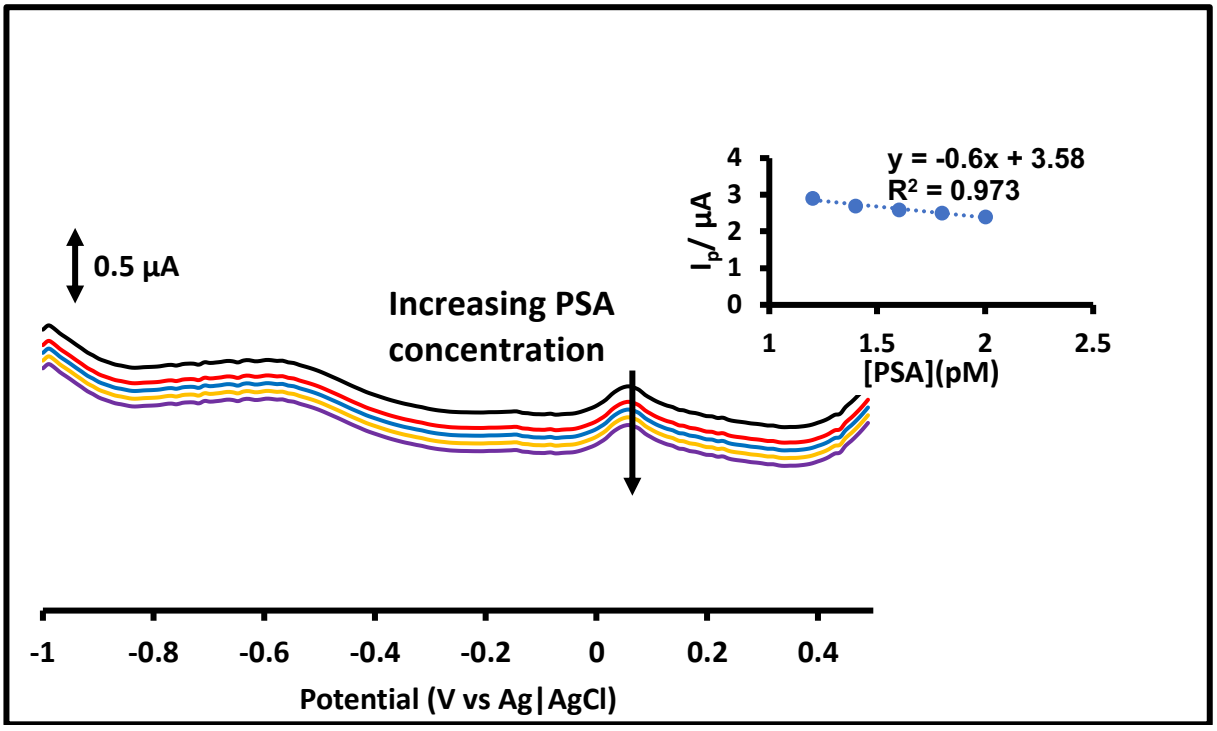

Figure 6.3: Differential pulse voltammograms of GCE-gCNQDs-CoPc(1)(ππ)-Aptamer in spiked human serum with PSA concentrations ranging from 1.2-2.0 pM. Insert: Linear responses of current to changing concentration.

Table 6.4: Summary of recovery measurements of PSA in spiked human serum samples for the GCE-gCNQDs-CoPc(1)(ππ)-Aptamer aptasensor. % RSD = relative standard deviation (standard deviation/mean × 100; n = 3).

[PSA] added/ pM In buffer	R_{ct} (kΩ) In buffer	[PSA] found/ pM In serum	R_{ct} (kΩ) In serum	% RSD	% Recovery
1.2	4.66	1.03	4.01	6.2	86.0
1.4	6.47	1.38	6.39	5.9	98.7
1.6	7.46	1.56	7.28	2.3	97.6
1.8	8.46	1.77	8.33	8.1	98.5
2.0	11.7	1.89	11.1	8.3	94.9

6.2 Covalently linked conjugates followed by ππ conjugation

The following conjugates were used as examples to verify the feasibility of the fabricated aptasensors to be used in clinical studies towards the electrochemical detection of PSA: GCE-gCNQDs@Aptamer, GCE-gCNQDs@Aptamer-CoPc(1) (ππ) and GCE-gCNQDs@Aptamer-CoPc(2) (ππ).

The obtained responses of the gCNQDs@Aptamer based sensors are shown in Fig. 6.4. The detection limits were determined as 0.054, 0.032 and 0.027 ng/mL, which are as those obtained for PSA in buffer and are still below the cut-off value of 4 ng/mL of patients suspected to have prostate cancer. When CoPc complexes were immobilized on the electrode surface and tested in a ferricyanide solution, complex 2 compared to complex 1 showed better electrocatalytic ability. In addition, a higher surface coverage was calculated for complex 2 (Table 4.1) which would indicate a larger surface area for aptamer immobilization. With a higher aptamer concentration at the surface as well as better current output due to the substituents complex 2 possesses, the aptasensor with complex 2 is expected to perform better. The verification of the reliability and feasibility of these aptasensor was also done by calculating the % recovery in the concentration range of 1.2-2 pM, using EIS. The recovery was calculated as was done for previously discussed aptasensors. The results obtained are shown in Table 6.5 corresponding to the aptamer-based electrodes. The percentage recoveries calculated ranged within an 85 and 98 % window in general for all sensors fabricated. Although the results obtained from EIS indicate some interference due to the complexity of the serum which resulted in a decrease in sensitivity (i.e., reduced R_{ct} values obtained in serum analyses compared to those done in the

buffer solution), the differences in recorded values are minimal, making these aptasensors feasible for further use in clinical studies. Moreover, the good recoveries also prove their reliability.

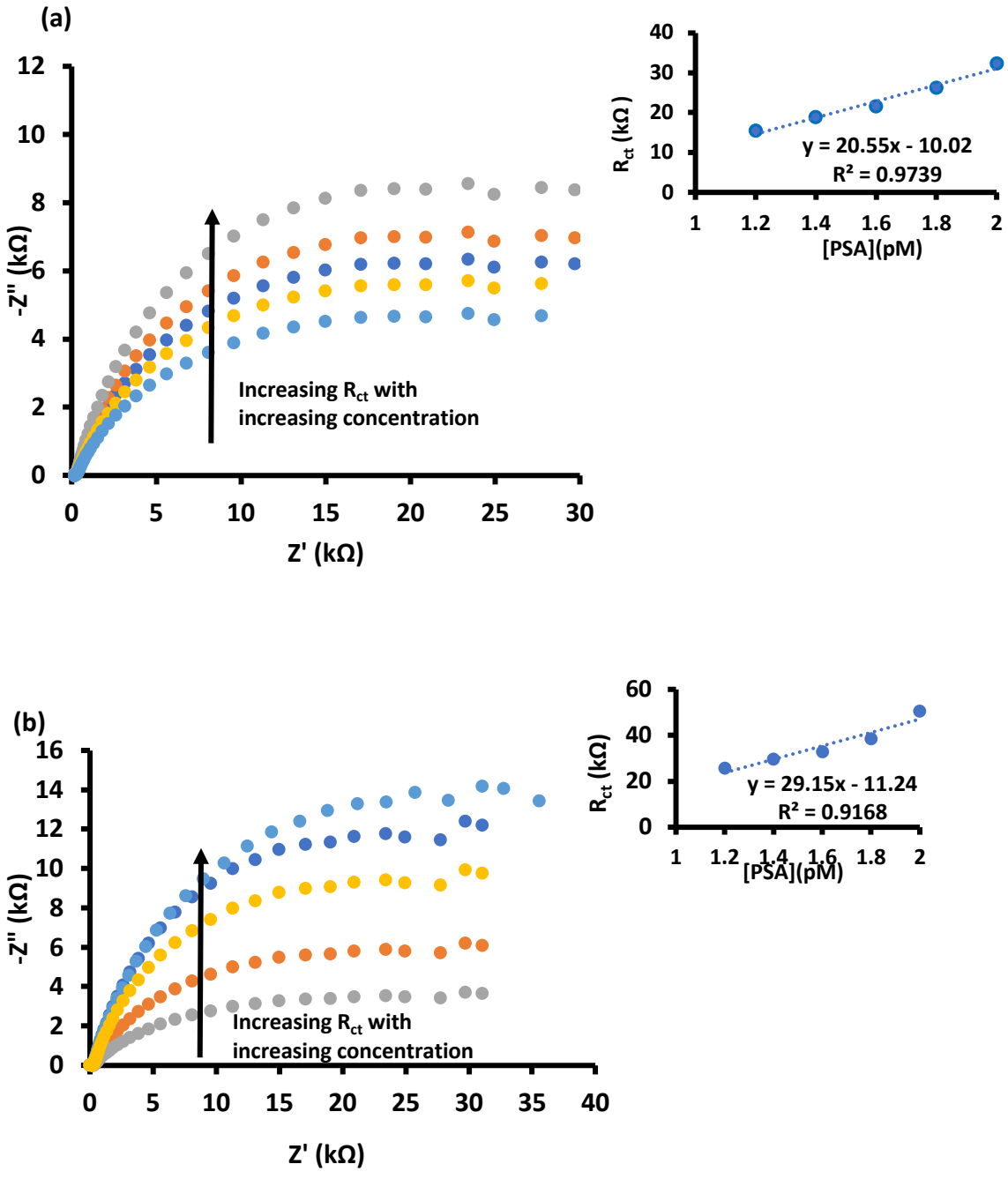

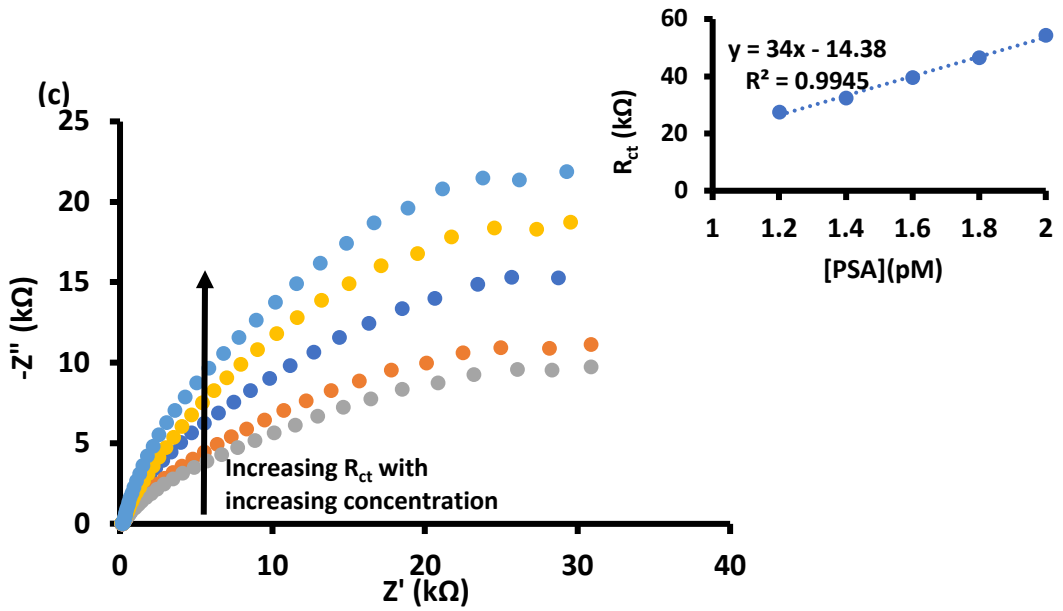

Figure 6.4: Electrochemical impedance (EIS) Nyquist plots of (a) GCE-gCNQDs@Aptamer, (b) GCE-gCNQDs@Aptamer-CoPc(1)(ππ) and (c) GCE-gCNQDs@Aptamer-CoPc(2)(ππ) in spiked human serum with PSA concentrations ranging from 1.2-2.0 pM. Insert: Linear responses of currents and resistance to changing concentration.

Table 6.5: Summary of recovery measurements of PSA in spiked human serum samples for the aptasensors. % RSD. (relative standard deviation) = standard deviation/mean × 100; n = 3.

[PSA] added/ pM in buffer	R_{ct} (k**Ω**) in buffer	[PSA] found/ pM In serum	R_{ct} (k**Ω**) In serum	% RSD	% Recovery
GCE-gCNQDs@Aptamer					
1.2	16.4	1.13	15.4	1.8	93.9
1.4	19.3	1.37	18.9	2.1	97.9
1.6	24.7	1.39	21.5	1.2	87.0
1.8	28.8	1.64	26.2	3.3	90.9
2.0	33.2	1.94	32.3	7.2	97.3
GCE-gCNQDs@AptamerCoPc(1)(ππ)					
1.2	26.7	1.16	25.8	1.4	96.6
1.4	30.5	1.35	29.5	2.6	96.7
1.6	37.9	1.38	32.8	1.8	86.5
1.8	44.9	1.54	38.4	3.8	85.5
2.0	51.6	1.96	50.5	6.2	97.9
GCE-gCNQDs@Aptamer-CoPc(2)(ππ)					
1.2	29.2	1.13	27.4	5.4	93.8
1.4	36.2	1.25	32.3	3.1	89.2
1.6	41.6	1.52	39.6	2.8	95.2
1.8	49.2	1.70	46.5	1.2	94.5
2.0	58.9	1.84	54.3	1.7	92.2

6.3 Self-assembly, electrografting and click chemistry

The following electrodes were used after modification by self-assembly and covalent linking, to show the synergistic effects of AuNPs combined with complex 2: GCE-AuNPs-Aptamer, GCEØCoPc(2)-Aptamer and GCE-AuNPsØCoPc(2)-Aptamer.

The aptasensors based on AuNPs and complex 2 were also verified in spiked serum samples. The real sample tests were run using DPV and EIS. The obtained responses are shown in Fig. 6.5(a) (DPV) and Fig. 6.5(b) (EIS) as examples of the plots used to extract the validating data from. The best performing aptasensor was the one where the AuNPs and CoPc(2) were coupled, as expected with detection limits determined as 0.028 ng/mL (EIS) and 0.027 ng/mL (DPV), Table 6.1. These values are similar to those determined from analyses done in PBS and are still well below the cut-off value of 4 ng/mL (13.3 nM) of patients suspected to have prostate cancer. The % recovery in the concentration range of 1.2-2 pM, using EIS was also determined. The results obtained are shown in Table 6.6, 6.7 and 6.8 for GCE-AuNPs-Aptamer, GCEØCoPc(2)-Aptamer and GCE-AuNPsØCoPc(2)-Aptamer, respectively. All experiments were run in triplicate and the recorded values are an average of the values recorded for each run. The percentage recoveries were higher and more reliable for the aptasensor in which the AuNPs and CoPc(2) are coupled. This shows that the results obtained from detecting PSA in buffer are feasible. Moreover, these results obtained from EIS also indicate some protein-protein interactions which results in a decrease in sensitivity hence the reduced R_{ct} values obtained in serum analyses compared to those done in PBS.

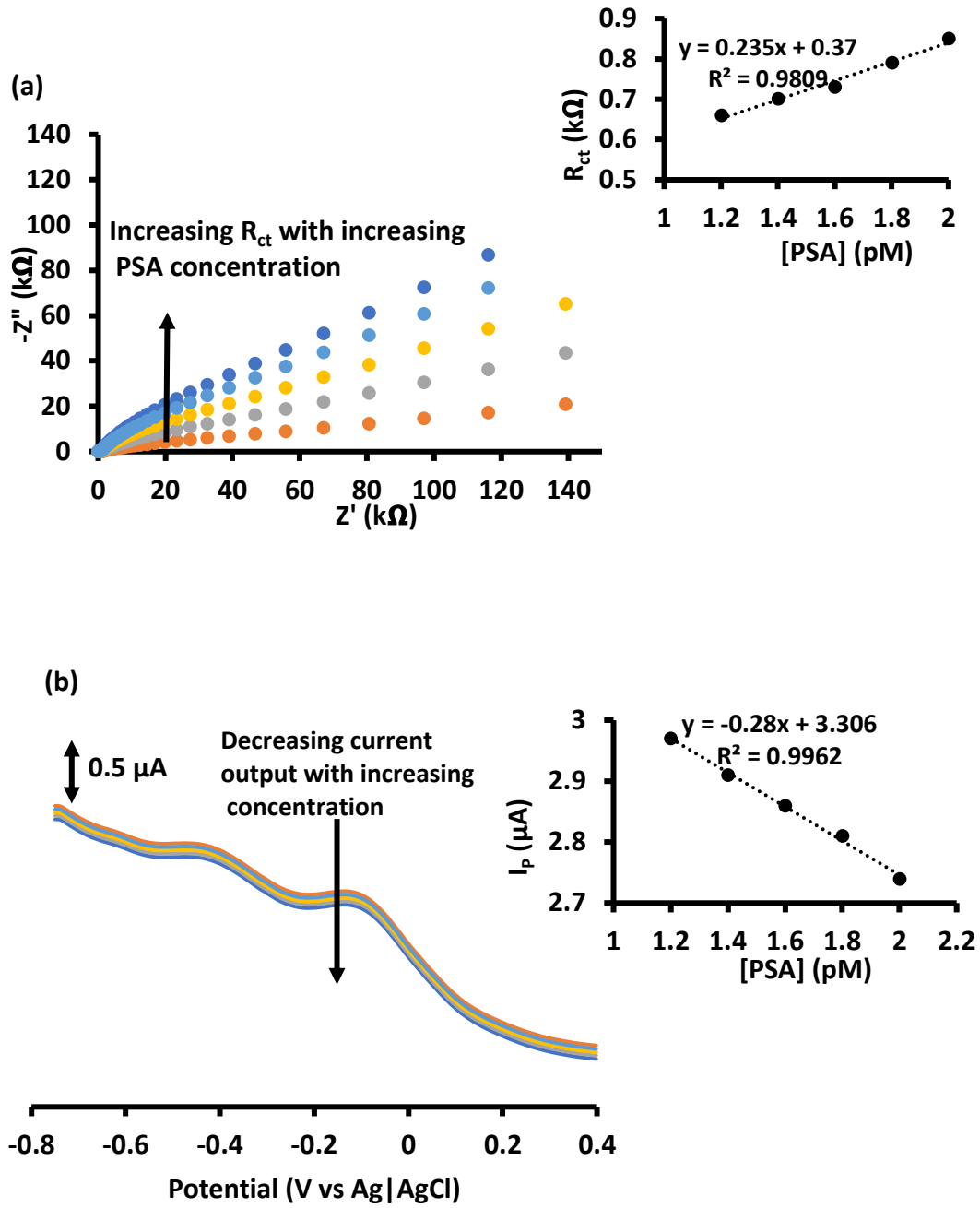

Figure 6.5: (a) EIS Nyquist plots and (b) differential pulse voltammograms (DPV) of GCEØCoPc(2)-Aptamer in a 30 mM PBS solution of pH 7.4 containing PSA concentrations ranging from 1.2-2.0 pM. **Inserts:** Linear responses of resistance to changing concentrations.

Table 6.6: Summary of recovery measurements of PSA in spiked human serum samples for the GCE-AuNPs-Aptamer aptasensor. % RSD (relative standard deviation) = standard deviation/mean × 100; n = 3.

[PSA] added/ pM In buffer	R_{ct} (kΩ) In buffer	[PSA] found/ pM In serum	R_{ct} (kΩ) In serum	% RSD	% Recovery
1.2	0.586	0.26	0.127	2.79	21.7
1.4	0.602	0.30	0.131	1.53	21.8
1.6	0.776	0.31	0.145	3.62	18.7
1.8	0.877	0.31	0.153	1.43	17.4
2.0	1.25	0.25	0.155	2.67	12.4

Table 6.7: Summary of recovery measurements of PSA in spiked human serum samples for the GCEØCoPc(2)-Aptamer aptasensor. % RSD (relative standard deviation) = standard deviation/mean × 100; n = 3.

[PSA] added/ pM In buffer	R_{ct} (kΩ) In buffer	[PSA] found/ pM In serum	R_{ct} (kΩ) In serum	% RSD	% Recovery
1.2	0.854	0.82	0.587	2.73	68.7
1.4	0.861	0.95	0.600	1.63	67.7
1.6	0.868	1.12	0.617	2.36	71.1
1.8	0.877	1.31	0.637	3.35	72.6
2.0	0.892	1.45	0.647	2.35	72.5

Table 6.8: Summary of recovery measurements of PSA In spiked human serum samples for the GCE-AuNPsØCoPc(2)-Aptamer aptasensor. % RSD. (relative standard deviation) = standard deviation/mean × 100; n = 3.

[PSA] added/ pM In buffer	**R_{ct} (kΩ) In buffer**	**[PSA] found/ pM In serum**	**R_{ct} (kΩ) In serum**	**% RSD**	**% Recovery**
1.2	24.9	1.18	24.6	5.46	98.7
1.4	27.2	1.39	27.0	6.80	99.3
1.6	29.4	1.57	28.9	6.68	98.3
1.8	31.7	1.73	30.5	2.94	96.2
2.0	33.5	1.98	33.2	1.62	99.1

6.4 Conclusions

The aptasensors fabricated in this work showed good performance in spiked serum samples with low detection limits. Moreover, they showed good recoveries and the results verified their feasibility to be used in clinical studies. Comparing the performances of these fabricated aptasensors, the GCE-NGQDs-CoPc(1)(ππ)-Aptamer showed the lowest detection limits in serum and buffer where the QDs were concerned using where EIS was used. The GCE-AuNPsØCoPc(2)-Aptamer fabricated sensor showed improved performance when AuNPs and CoPc(2) were combined and the best performance when compared to all the sensors fabricated in this work. This proves the combination of MPc with other nanostructures is ideal for the fabrication and development of stable, efficient, low cost aptasensor.

7. Summary, conclusions, and prospects

This chapter summarizes all the work discussed in this thesis and highlights again the novelty of the work and the new perspective it has brought to the fabrication and the development of PCa early diagnostic tools.

7.1 Overview of the thesis.

This thesis reported for the first time, the combination of graphene-based quantum dots, AuNPs, MPcs and an aptamer for the fabrication of electrochemical aptasensors, towards the detection of PSA. The nanostructures were synthesized and fully characterized prior to being used as electrode modifiers. Moreover, the synergistic effects of the quantum dots, AuNPs and CoPcs were proven using electrochemical methods. Glassy carbon electrodes or plates were modified and characterized at each modification step. Where covalent linkage was employed, XPS analyses verified the success of the formation of new bonds. Using adsorption and click chemistry as surface modification techniques yielded stable electrochemical sensors. The aptasensors were used to detect PSA in buffer solution and proved to be efficient, selective, and specific and showed low detection limits which were compared to reported literature values. The best performing aptasensors that were fabricated herein were then used to detect PSA in spiked serum samples to verify their feasibility and potential use in clinical studies. The results agreed with those obtained in buffer analyses and some performed slightly better in serum analyses. In addition, the sensors were stable, reproducible, and proved to be reusable for several experiments before having to refabricate them. It is important to note that the combination of MPcs with other nanomaterials contributed greatly to the enhancement of the signal output of the fabricated aptasensors, thus obtaining low detection limits. Moreover, the characteristics of these nanostructures, also contributed to the increased sensitivity, stability, and reproducibility of the sensors.

7.2 Future prospects and final remarks.

If more work and optimization is invested in advancing this study, where MPcs are conjugated to graphene-based quantum dots and AuNPs for the development of aptasensors, this work has the potential to contribute greatly to the accessibility of medical care, especially early cancer diagnostics of various diseases. The materials used have a high shelf life, are stable and cost less than current systems in place; therefore, further exploration in this area of study would be greatly beneficial.

References

[1] C.G. Claessens, U.W.E. Hahn, T. Torres, Phthalocyanines: From outstanding electronic properties to emerging applications, Chem. Rec. 8 (2008) 75–97.

[2] D. Klyamer, A. Sukhikh, S. Gromilov, P. Krasnov, T. Basova, Fluorinated metal phthalocyanines: interplay between fluorination degree, films orientation, and ammonia sensing properties, Sensors 18 (2018) 2141-2154.

[3] Y. Wang, X. Zheng, X. Liu, Y. Feng, H. Shan, L. Dong, G. Fang, Z.-X. Xu, A study of different central metals in octamethyl-substituted phthalocyanines as dopant-free hole-transport layers for planar perovskite solar cells, Org. Electron. 56 (2018) 276–283.

[4] V.N. Nemykin, E.A. Lukyanets, Synthesis of substituted phthalocyanines, Arkivoc. (2010) 136-208.

[5] G. Dilber, H. Altunparmak, A. Nas, H. Kantekin, M. Durmuş, The peripheral and non-peripheral 2H-benzotriazole substituted phthalocyanines: Synthesis, characterization, photophysical and photochemical studies of zinc derivatives, Spectrochim. Acta Part A Mol. Biomol. Spectrosc. 217 (2019) 128–140.

[6] E.N. Kaya, S. Tuncel, T. V Basova, H. Banimuslem, A. Hassan, A.G. Gürek, V. Ahsen, M. Durmuş, Effect of pyrene substitution on the formation and sensor properties of phthalocyanine-single walled carbon nanotube hybrids, Sens. Actuators B Chem. 199 (2014) 277–283.

[7] B.N. Şen, H. Mert, H. Dinçer, A. Koca, Synthesis and characterization of terminalalkynyl-substituted unsymmetrical zinc phthalocyanine conjugated with well-defined polymers, Dye. Pigment. 100 (2014) 1–10.

[8] G. de la Torre, C.G. Claessens, T. Torres, Phthalocyanines: The need for selective synthetic approaches, European J. Org. Chem. 2000 (2000) 2821–2830.

[9] J. Rak, P. Pouckova, J. Benes, D. Vetvicka, Drug delivery systems for phthalocyanines for photodynamic therapy, Anticancer Res. 39 (2019) 3323–3339.

[10] Y. Baygu, Y. Gök, A highly water-soluble zinc (II) phthalocyanines as potential for PDT studies: Synthesis and characterization, Inorg. Chem. Commun. 96 (2018) 133–138.

[11] F. Yurt, M. Ince, S.G. Colak, K. Ocakoglu, O. Er, H.M. Soylu, C. Gunduz, C.B. Avci, C.C. Kurt, Investigation of in vitro PDT activities of zinc phthalocyanine immobilised TiO2 nanoparticles, Int. J. Pharm. 524 (2017) 467–474.

[12] A.Y. Tolbin, M.S. Savelyev, A.Y. Gerasimenko, L.G. Tomilova, N.S. Zefirov, Thermally stable J-type phthalocyanine dimers as new non-linear absorbers for low-threshold optical limiters, Phys. Chem. Chem. Phys. 18 (2016) 15964–15971.

[13] O.M. Bankole, J. Britton, T. Nyokong, Photophysical and non-linear optical behavior of novel tetra alkynyl terminated indium phthalocyanines: Effects of the carbon chain length, Polyhedron 88 (2015) 73–80.

[14] A.C.S. Lobo, A.D. Silva, V.A. Tomé, S.M.A. Pinto, E.F.F. Silva, M.J.F. Calvete, C.M.F. Gomes, M.M. Pereira, L.G. Arnaut, Phthalocyanine labels for near-

infrared fluorescence imaging of solid tumors, J. Med. Chem. 59 (2016) 4688–4696.

[15] F. Lv, X. He, L. Wu, T. Liu, Lactose substituted zinc phthalocyanine: A near infrared fluorescence imaging probe for liver cancer targeting, Bioorg. Med. Chem. Lett. 23 (2013) 1878–1882.

[16] G. Avşar, F.A. Sari, A.C. Yuzer, H.M. Soylu, O. Er, M. Ince, F.Y. Lambrecht, Intracellular uptake and fluorescence imaging potential in tumor cell of zinc phthalocyanine, Int. J. Pharm. 505 (2016) 369–375.

[17] W. Vallejo, C. Diaz-Uribe, A. Cantillo, Methylene blue photocatalytic degradation under visible irradiation on TiO2 thin films sensitized with Cu and Zn tetracarboxy-phthalocyanines, J. Photochem. Photobiol. A Chem. 299 (2015) 80–86.

[18] Q. Liang, M. Zhang, C. Liu, S. Xu, Z. Li, Sulfur-doped graphitic carbon nitride decorated with zinc phthalocyanines towards highly stable and efficient photocatalysis, Appl. Catal. A Gen. 519 (2016) 107–115.

[19] W.-L. He, C.-D. Wu, Incorporation of Fe-phthalocyanines into a porous organic framework for highly efficient photocatalytic oxidation of arylalkanes, Appl. Catal. B Environ. 234 (2018) 290–295.

[20] Z. Jiang, Y. Wang, X. Zhang, H. Zheng, X. Wang, Y. Liang, Revealing the hidden performance of metal phthalocyanines for CO2 reduction electrocatalysis by hybridization with carbon nanotubes, Nano Res. 12 (2019) 2330–2334.

[21] T.T. Tasso, T. Furuyama, N. Kobayashi, Absorption and electrochemical properties of cobalt and iron phthalocyanines and their quaternized derivatives: aggregation equilibrium and oxygen reduction electrocatalysis, Inorg. Chem. 52 (2013) 9206–9215.

[22] A. Pizarro, G. Abarca, C. Gutiérrez-Cerón, D. Cortés-Arriagada, F. Bernardi, C. Berrios, J.F. Silva, M.C. Rezende, J.H. Zagal, R. Oñate, Building pyridinium molecular wires as axial ligands for tuning the electrocatalytic activity of iron phthalocyanines for the oxygen reduction reaction, ACS Catal. 8 (2018) 8406–8419.

[23] D.-D. Ma, S.-G.Han, C. Cao, X. Li, X.-T.Wu, Q.-L. Zhu, Remarkable electrocatalytic CO2 reduction with ultrahigh CO/H2 ratio over single-molecularly immobilized pyrrolidinonyl nickel phthalocyanine, Appl. Catal. B Environ. 264 (2020) 118530.

[24] K.I. Ozoemena, T. Nyokong, Comparative electrochemistry and electrocatalytic activities of cobalt, iron and manganese phthalocyanine complexes axially co-ordinated to mercaptopyridine self-assembled monolayer at gold electrodes, Electrochim. Acta 51 (2006) 2669–2677.

[25] J.H. Zagal, M.A. Gulppi, G. Cárdenas-Jirón, Metal-centered redox chemistry of substituted cobalt phthalocyanines adsorbed on graphite and correlations with MO calculations and Hammett parameters. Electrocatalytic reduction of a disulfide, Polyhedron 19 (2000) 2255–2260.

[26] L.S. Mpeta, P. Sen, T. Nyokong, The effects of asymmetry in combination with reduced graphene oxide nanosheets on hydrazine electrocatalytic detection on cobalt phthalocyanines, Electroanalysis 32 (2020) 2723–2732.

[27] E. Güzel, M.N. Yarasir, A.R. Özkaya, Low symmetry solitaire- and trans-functional porphyrazine/phthalocyanine hybrid complexes: Synthesis, isolation, characterization, and electrochemical and in-situ spectroelectrochemical properties, Synth. Met.262 (2020) 116331.

[28] C. Zúñiga, F. Tasca, S. Calderon, D. Farías, F.J. Recio, J.H. Zagal, Reactivity indexes for the electrocatalytic oxidation of hydrogen peroxide promoted by several ligand-substituted and unsubstituted Co phthalocyanines adsorbed on graphite, J. Electroanal. Chem. 765 (2016) 22–29.

[29] E.T. Acar, T.A. Tabakoglu, D. Atilla, F. Yuksel, G. Atun, Synthesis, electrochemistry and electrocatalytic activity of cobalt phthalocyanine complexes – Effects of substituents for oxygen reduction reaction, Polyhedron 152 (2018) 114–124.

[30] R. Nkhahle, T. Nyokong, Creating the ideal push-pull system for electrocatalysis: A comparative study on symmetrical and asymmetrical cardanol-based cobalt phthalocyanines, Electroanalysis 33 (2021) 11–22.

[31] J. Mack, N. Kobayashi, Low symmetry phthalocyanines and their analogues, Chem. Rev. 111 (2011) 281–321.

[32] S.S. Erdem, I. V Nesterova, S.A. Soper, R.P. Hammer, Solid-phase synthesis of asymmetrically substituted “AB3-Type” phthalocyanines, J. Org. Chem. 73 (2008) 5003–5007.

[33] D.R. Cooper, B. D’Anjou, N. Ghattamaneni, B. Harack, M. Hilke, A. Horth, N. Majlis, M. Massicotte, L. Vandsburger, E. Whiteway, Experimental review of graphene, Int. Sch. Res. Not. 2012 (2012) 1-56.

[34] H. Nakano, H. Tetsuka, M.J.S. Spencer, T. Morishita, Chemical modification of group IV graphene analogues, Sci. Technol. Adv. Mater. 19 (2018) 76-100.

[35] M.H. Kang, L.O. Prieto López, B. Chen, K. Teo, J.A. Williams, W.I. Milne, M.T. Cole, Mechanical robustness of graphene on flexible transparent substrates, ACS Appl. Mater. Interf. 8 (2016) 22506–22515.

[36] S. Saxena, T.A. Tyson, S. Shukla, E. Negusse, H. Chen, J. Bai, Investigation of structural and electronic properties of graphene oxide, Appl. Phys. Lett. 99 (2011) 13104.

[37] Y. Chong, Y. Ma, H. Shen, X. Tu, X. Zhou, J. Xu, J. Dai, S. Fan, Z. Zhang, The in vitro and in vivo toxicity of graphene quantum dots, Biomat. 35 (2014) 5041–5048.

[38] M. Bacon, S.J. Bradley, T. Nann, Graphene quantum dots, Part. Part. Syst. Charact. 31 (2014) 415–428.

[39] Y. Zhan, Z. Liu, Q. Liu, D. Huang, Y. Wei, Y. Hu, X. Lian, C. Hu, A facile and one-pot synthesis of fluorescent graphitic carbon nitride quantum dots for bio-imaging applications, New J. Chem. 41 (2017) 3930–3938.

[40] A. Kalluri, D. Debnath, B. Dharmadhikari, P. Patra, Graphene quantum dots: Synthesis and applications, Methods Enzymol. 609 (2018) 335–354.

[41] S. Gu, C.-T. Hsieh, Y.-M.Chiang, D.-Y.Tzou, Y.-F. Chen, Y.A. Gandomi, Optimization of graphene quantum dots by chemical exfoliation from graphite powders and carbon nanotubes, Mater. Chem. Phys. 215 (2018) 104–111.

[42] H. Sun, H. Ji, E. Ju, Y. Guan, J. Ren, X. Qu, Synthesis of fluorinated and nonfluorinated graphene quantum dots through a new top-down strategy for long-time cellular imaging, Chem. Eur. J. 21 (2015) 3791–3797.

[43] R. Tian, S. Zhong, J. Wu, W. Jiang, Y. Shen, T. Wang, Solvothermal method to prepare graphene quantum dots by hydrogen peroxide, Opt. Mater. 60 (2016) 204–208.

[44] G. Wang, Q. Guo, D. Chen, Z. Liu, X. Zheng, A. Xu, S. Yang, G. Ding, Facile and highly effective synthesis of controllable lattice sulfur-doped graphene quantum dots via hydrothermal treatment of durian, ACS Appl. Mater. Interf. 10 (2018) 5750–5759.

[45] C. Zhang, Y. Cui, L. Song, X. Liu, Z. Hu, Microwave assisted one-pot synthesis of graphene quantum dots as highly sensitive fluorescent probes for detection of iron ions and pH value, Talanta 150 (2016) 54–60.

[46] P. Atienzar, A. Primo, C. Lavorato, R. Molinari, H. García, Preparation of graphene quantum dots from pyrolyzed alginate, Langmuir 29 (2013) 6141–6146.

[47] K. Habiba, V. Makarov, B. Weiner, G. Morell, Fabrication of Nanomaterials by Pulsed Laser Synthesis. In: A. Waqar, N. Ali (editors). Manufacturing Nanostructures. Altrincham: One Central Press (OCN); 2014. 263-292.

[48] B.P. Kafle, Chapter 6 - Introduction to nanomaterials and application of UV–Visible spectroscopy for their characterization, in: B.P. Kafle (editors), Chemical analysis and material characterization by spectrophotometry, Amsterdam. Elsevier, 2020: pp. 147–198.

[49] H.-H. Cho, H. Yang, D.J. Kang, B.J. Kim, Surface engineering of graphene quantum dots and their applications as efficient surfactants, ACS Appl. Mater. Interf. 7 (2015) 8615–8621.

[50] S. Wang, Z.-G. Chen, I. Cole, Q. Li, Structural evolution of graphene quantum dots during thermal decomposition of citric acid and the corresponding photoluminescence, Carbon 82 (2015) 304–313.

[51] R. Adel, S. Ebrahim, A. Shokry, M. Soliman, M. Khalil, Nanocomposite of CuInS/ZnS and nitrogen-doped graphene quantum dots for cholesterol sensing, ACS Omega 6 (2021) 2167–2175.

[52] M. Mokaddem, P. Gareil, J. Belgaied, A. Varenne, A new insight into suction and dilution effects in capillary electrophoresis coupled to mass spectrometry via an electrospray ionization interface. Part I-Suction effect, Electrophoresis 29 (2008) 1957–1964.

[53] J.S. Toraño, R. Ramautar, G. de Jong, Advances in capillary electrophoresis for the life sciences, J. Chromatogr. B. 1118 (2019) 116–136.

[54] L. Trapiella-Alfonso, F. d'Orlyé, A. Varenne, Recent advances in the development of capillary electrophoresis methodologies for optimizing, controlling, and characterizing the synthesis, functionalization, and physicochemical, properties of nanoparticles, Anal. Bioanal. Chem. 408 (2016) 2669–2675.

[55] S. Fermas, F. Gonnet, A. Varenne, P. Gareil, R. Daniel, Frontal analysis capillary electrophoresis hyphenated to electrospray ionization mass spectrometry for the characterization of the antithrombin/heparin pentasaccharide complex, Anal. Chem. 79 (2007) 4987–4993.

[56] N.B. Cech, C.G. Enke, Practical implications of some recent studies in electrospray ionization fundamentals, Mass Spectrom. Rev. 20 (2001) 362–387.

[57] G. Bonvin, J. Schappler, S. Rudaz, Capillary electrophoresis–electrospray ionization-mass spectrometry interfaces: Fundamental concepts and technical developments, J. Chromatogr. A. 1267 (2012) 17–31.

[58] Z. Qian, J. Ma, X. Shan, L. Shao, J. Zhou, J. Chen, H. Feng, Surface functionalization of graphene quantum dots with small organic molecules from photoluminescence modulation to bioimaging applications: an experimental and theoretical investigation, RSC Adv. 3 (2013) 14571–14579.

[59] J.-P. Zou, L.-C.Wang, J. Luo, Y.-C.Nie, Q.-J.Xing, X.-B.Luo, H.-M.Du, S.-L. Luo, S.L. Suib, Synthesis and efficient visible light photocatalytic H2 evolution of a metal-free g-C3N4/graphene quantum dots hybrid photocatalyst, Appl. Catal. B Environ. 193 (2016) 103–109.

[60] D.A. Nguyen, H.M. Oh, N.T. Duong, S. Bang, S.J. Yoon, M.S. Jeong, Highly enhanced photoresponsivity of a monolayer WSe2 photodetector with nitrogen-doped graphene quantum dots, ACS Appl. Mater. Interf. 10 (2018) 10322–10329.

[61] J. Lu, M. Yan, L. Ge, S. Ge, S. Wang, J. Yan, J. Yu, Electrochemiluminescence of blue-luminescent graphene quantum dots and its application in ultrasensitive aptasensor for adenosine triphosphate detection, Biosens. Bioelectron. 47 (2013) 271–277.

[62] E. Sharma, D. Vashisht, A. Vashisht, V.K. Vats, S.K. Mehta, K. Singh, Facile synthesis of sulfur and nitrogen codoped graphene quantum dots for optical sensing of Hg and Ag ions, Chem. Phys. Lett. 730 (2019) 436–444.

[63] Y. Zhou, S. Yang, X. Yin, J. Han, M. Tai, X. Zhao, H. Chen, Y. Gu, N. Wang, H. Lin, Enhancing electron transport via graphene quantum dot/SnO2 composites for efficient and durable flexible perovskite photovoltaics, J. Mater. Chem. A. 7 (2019) 1878–1888.

[64] S. Campuzano, P. Yáñez-Sedeño, J.M. Pingarrón, Carbon dots and graphene quantum dots in electrochemical biosensing, Nanomat. 9 (2019) 634-651.

[65] H. Zhao, Y. Chang, M. Liu, S. Gao, H. Yu, X. Quan, A universal immunosensing strategy based on regulation of the interaction between graphene and graphene quantum dots, Chem. Commun. 49 (2013) 234–236.

[66] S. Chaiyo, E. Mehmeti, W. Siangproh, T.L. Hoang, H.P. Nguyen, O. Chailapakul, K. Kalcher, Non-enzymatic electrochemical detection of glucose

with a disposable paper-based sensor using a cobalt phthalocyanine–ionic liquid–graphene composite, Biosens. Bioelectron. 102 (2018) 113–120.

[67] X. Chen, T. Wang, B. Li, M. Zeng, J. Yang, N. Hu, Y. Su, Z. Zhou, Z. Yang, Enhancing room-temperature NO2 gas sensing performance based on a metal phthalocyanine/graphene quantum dot hybrid material, RSC Adv. 11 (2021) 5618–5628.

[68] O.J. Achadu, T. Nyokong, Application of graphene quantum dots decorated with TEMPO-derivatized zinc phthalocyanine as novel nanoprobes: probing the sensitive detection of ascorbic acid, New J. Chem. 40 (2016) 8727–8736.

[69] O.J. Achadu, T. Nyokong, Fluorescence "turn-ON" nanosensor for cyanide ion using supramolecular hybrid of graphene quantum dots and cobalt pyrene-derivatized phthalocyanine, Dye. Pigment. 160 (2019) 328–335.

[70] O.J. Achadu, T. Nyokong, Graphene quantum dots decorated with maleimide and zinc tetramaleimido-phthalocyanine: Application in the design of "OFF-ON" fluorescence sensors for biothiols, Talanta 166 (2017) 15–26.

[71] S. Guo, E. Wang, Synthesis and electrochemical applications of gold nanoparticles, Anal. Chim. Acta 598 (2007) 181–192.

[72] Y. Hu, Y. Song, Y. Wang, J. Di, Electrochemical synthesis of gold nanoparticles onto indium tin oxide glass and application in biosensors, Thin Solid Films 519 (2011) 6605–6609.

[73] C. Zou, B. Yang, D. Bin, J. Wang, S. Li, P. Yang, C. Wang, Y. Shiraishi, Y. Du, Electrochemical synthesis of gold nanoparticles decorated flower-like

graphene for high sensitivity detection of nitrite, J. Colloid Interface Sci. 488 (2017) 135–141.

[74] S. Singh, D.V.S. Jain, M.L. Singla, One step electrochemical synthesis of gold-nanoparticles–polypyrrole composite for application in catechin electrochemical biosensor, Anal. Methods 5 (2013) 1024–1032.

[75] H. Ma, B. Yin, S. Wang, Y. Jiao, W. Pan, S. Huang, S. Chen, F. Meng, Synthesis of silver and gold nanoparticles by a novel electrochemical method, Chem. Phys. Chem. 5 (2004) 68–75.

[76] E.C. Dreaden, A.M. Alkilany, X. Huang, C.J. Murphy, M.A. El-Sayed, The golden age: gold nanoparticles for biomedicine, Chem. Soc. Rev. 41 (2012) 2740–2779.

[77] K. Saha, S.S. Agasti, C. Kim, X. Li, V.M. Rotello, Gold nanoparticles in chemical and biological sensing, Chem. Rev. 112 (2012) 2739–2779.

[78] A.S. Matias, F.F. Carlos, P. Pedrosa, A.R. Fernandes, P. V Baptista., Gold nanoparticles in molecular diagnostics and molecular therapeutics, In: Rai, Ph.D M., Shegokar, Ph.D R. (editors) Metal Nanoparticles in Pharma, Springer Heidelburg. (2017) 365–387.

[79] T.T-T. Ho, C.-H. Dang, T.K-C.Huynh, T.K-D.Hoang, T-D. Nguyen, In situ synthesis of gold nanoparticles on novel nanocomposite lactose/alginate: Recyclable catalysis and colorimetric detection of Fe (III), Carbohydr. Polym.251 (2021) 116998.

[80] G. Han, P. Ghosh, V.M. Rotello, Functionalized gold nanoparticles for drug delivery, Nanomed. 2 (2007) 113-123.

[81] A. Ananthi, K.L. Phani, Self-assembly of gold nanoparticles on sulphide functionalized polydopamine in application to electrocatalytic oxidation of nitric oxide, J. Electroanal. Chem. 764 (2016) 7–14.

[82] D.J. Siegwart, A. Srinivasan, S.A. Bencherif, A. Karunanidhi, J.K. Oh, S. Vaidya, R. Jin, J.O. Hollinger, K. Matyjaszewski, Cellular uptake of functional nanogels prepared by inverse mini-emulsion ATRP with encapsulated proteins, carbohydrates, and gold nanoparticles, Biomacromolecules 10 (2009) 2300–2309.

[83] X. Chen, X. Zhao, G. Wang, Review on marine carbohydrate-based gold nanoparticles represented by alginate and chitosan for biomedical application, Carbohydr. Polym.(2020) 116311.

[84] D. Shahdeo, V. Kesarwani, D. Suhag, J. Ahmed, S.M. Alshehri, S. Gandhi, Self-assembled chitosan polymer intercalating peptide functionalized gold nanoparticles as nanoprobe for efficient imaging of urokinase plasminogen activator receptor in cancer diagnostics, Carbohydr. Polym.(2021) 118138.

[85] A.A. Saeed, B. Singh, M.N. Abbas, Y.M. Issa, E. Dempsey, Electrocatalytic nitrite determination using iron phthalocyanine modified gold nanoparticles. Electroanalysis 27 (2015) 1086–1096.

[86] V.P. Chauke, E. Antunes, T. Nyokong, Comparative behavior of conjugates of tantalum phthalocyanines with gold nanoparticles or single walled carbon

nanotubes towards bisphenol A electrocatalysis, J. Electroanal. Chem. 661 (2011) 1–7.

[87] A.J. Jeevagan, S.A. John, Synthesis of non-peripheral amine substituted nickel(ii) phthalocyanine capped gold nanoparticles and their immobilization on electrode for the electrocatalytic oxidation of hydrazine, RSC Adv. 3 (2013) 2256–2264.

[88] Q. Xu, H. Yuan, X. Dong, Y. Zhang, M. Asif, Z. Dong, W. He, J. Ren, Y. Sun, F. Xiao, Dual nanoenzyme modified microelectrode based on carbon fiber coated with AuPd alloy nanoparticles decorated graphene quantum dots assembly for electrochemical detection in clinic cancer samples, Biosens. Bioelectron. 107 (2018) 153–162.

[89] M. Lakshmanakumar, N. Nesakumar, S. SethuRaman, K.S. Rajan, U.M. Krishnan, J.B.B. Rayappan, Functionalized graphene quantum dot interfaced electrochemical detection of cardiac Troponin I: An antibody free approach, Sci. Rep. 9 (2019) 17348.

[90] B.D. Mansuriya, Z. Altintas, Enzyme-Free Electrochemical nano-immunosensor based on graphene quantum dots and gold nanoparticles for cardiac biomarker determination, Nanomaterials 11 (2021) 578-595.

[91] Z. Shekari, H.R. Zare, A. Falahati, Electrochemical sandwich aptasensor for the carcinoembryonic antigen using graphene quantum dots, gold nanoparticles and nitrogen doped graphene modified electrode and exploiting the peroxidase-mimicking activity of a G-quadruplex DNAzyme, Microchim. Acta 186 (2019) 530.

[92] Z. Fredj, M. Ben Ali, M.N. Abbas, E. Dempsey, Determination of prostate cancer biomarker acid phosphatase at a copper phthalocyanine-modified screen printed gold transducer, Anal. Chim. Acta 1057 (2019) 98-105.

[93] F. Duan, C. Guo, M. Hu, Y. Song, M. Wang, L. He, Z. Zhang, R. Pettinari, L. Zhou, Construction of the 0D/2D heterojunction of Ti3C2Tx MXene nanosheets and iron phthalocyanine quantum dots for the impedimetric aptasensing of microRNA-155, Sensors Actuators B Chem. 310 (2020) 127844.

[94] E.B. Aydın, M. Aydın, A. Yuzer, M. Ince, K. Ocakoğlu, M.K. Sezgintürk, Detection of kallikrein-related peptidase 4 with a label-free electrochemical impedance biosensor based on a Zinc(II) phthalocyanine tetracarboxylic acid-functionalized disposable Indium Tin Oxide electrode, ACS Biomater. Sci. Eng. 7 (2021) 1192–1201.

[95] H. Xu, C. Liao, Y. Liu, B.-C. Ye, B. Liu, Iron phthalocyanine decorated nitrogen-doped graphene biosensing platform for real-time detection of nitric oxide released from living cells, Anal. Chem. 90 (2018) 4438–4444.

[96] F. Duan, M. Hu, C. Guo, Y. Song, M. Wang, L. He, Z. Zhang, R. Pettinari, L. Zhou, Chromium-based metal-organic framework embedded with cobalt phthalocyanine for the sensitively impedimetric cytosensing of colorectal cancer (CT26) cells and cell imaging, Chem. Eng. J. 398 (2020) 125452.

[97] J. Kang, Z. Li, G. Wang, A novel signal amplification strategy electrochemical immunosensor for ultra-sensitive determination of p53 protein, Bioelectrochem.137 (2021) 107647.

[98] M. Hu, K. Zhang. The application of aptamers in cancer research: an up-to-date review. Future Oncol. 9 (2013) 369–376.

[99] J. Zhou, J. Rossi, Aptamers as targeted therapeutics: current potential and challenges. Nat. Rev Drug Discov.16 (2017) 181–202.

[100] A.D. Keefe, S.T. Cload.SELEX with modified nucleotides.Current Opinion in Chem. Bio. 12 (2008) 448-456.

[101] R. Stoltenburg, C. Reinemann, B. Strehlitz. SELEX—A (r)evolutionary method to generate high-affinity nucleic acid ligands. Biomol. Eng. 24 (2007) 381-403.

[102] K-N.Kang, Y-S. Lee. RNA aptamers: A review of recent trends and applications. Future Trends in Biotech. 131 (2012) 153-169.

[103] K-T. Guo, A. Paul, C. Schichor, G. Ziemer, H.P. Wendel. CELL-SELEX: Novel perspectives of aptamer-based therapeutics. Int. J. Mol. Sci. 9 (2008) 668-678.

[104] J.K. Herr, J.E. Smith, C.D. Medley, D. Shangguan, W. Tan.Aptamer-conjugated nanoparticles for selective collection and detection of cancer cells.Anal. Chem. 78 (2006) 2918–2924.

[105] Y-F.Huang, K. Sefah, S. Bamrungsap, H-T. Chang, W. Tan. Selective photothermal therapy for mixed cancer cells using aptamer-conjugated nanorods. Langmuir 24 (2008) 11860–11865.

[106] X. Chen, M.-C.Estévez, Z. Zhu, Y-F. Huang, Y. Chen, L. Wang, W. Tan. Using aptamer-conjugated fluorescence resonance energy transfer nanoparticles for multiplexed cancer cell monitoring.Anal. Chem. 81 (2009) 7009–7014.

[107] R. Savla, O. Taratula, O. Garbuzenko, T. Minko. Tumor targeted quantum dot-mucin 1 aptamer-doxorubicin conjugate for imaging and treatment of cancer. J. Controlled Release 153 (2011) 16-22.

[108] J.A. Hanson, , J. Wang, A-N. Kawde, Y. Xiang, K.V. Gothelf, G. Collins. Quantum-dot/aptamer-based ultrasensitive multi-analyte electrochemical biosensor. J. Am. Chem. Soc.128 (2006) 2228–2229.

[109] F-B.Wang, Y. Rong, M. Fang, J-P.Yuan, C-W.Peng, S-P. Liu, Y. Li. Recognition and capture of metastatic hepatocellular carcinoma cells using aptamer-conjugated quantum dots and magnetic particles. Biomat. 34 (2013) 3816-3827.

[110] Y. Cao, H. Dong, Z. Yang, X. Zhong, Y. Chen, W. Dai, X. Zhang. Aptamer-conjugated graphene quantum dots/porphyrin derivative theranostic agent for intracellular cancer-related microRNA detection and fluorescence-guided photothermal/photodynamic synergetic therapy. Appl. Mater. Interf.9 (2017) 159−166.

[111] Z. S. Qian, X.Y. Shan, L.J. Chai, J.R. Chen, H. Feng. A fluorescent nanosensor based on graphene quantum dots–aptamer Probe and graphene oxide platform for detection of lead(II)ion. Biosens.Bioelectron. 68 (2015) 225–231.

[112] Y. Liu, K. Yan, J. Zhang. Graphitic carbon nitride sensitized with CdS quantum dots for visible-light-driven photoelectrochemical aptasensing of tetracycline. Appl. Mater. Interf.8 (2016) 28255−28264.

[113] C-Y. Zhang, La.W. Johnson. Single quantum-dot-based aptameric nanosensor for cocaine.Anal. Chem. 81 (2009) 3051–3055.

[114] V. Bagalkot, L. Zhang, E. Levy-Nissenbaum, S. Jon, P.W. Kantoff, R. Langer, O.C. Farokhzad. Quantum dot–aptamer conjugates for synchronous cancer imaging, therapy, and sensing of drug delivery based on bi-fluorescence resonance energy transfer. Nano Lett. 7 (2007) 3065-3070.

[115] Y. Shibui, R. Sakai, Y. Manabe, T. Masuyama.Comparisons of L-cysteine and D-cysteine toxicity in 4-week repeated dose toxicity studies of rats receiving daily oral administration, J. Toxicol.Pathol. 3 (2017) 217-229.

[116] H. Lilja, D. Ulmert, A.J. Vickers, -Prostate-specific antigen and prostate cancer: prediction, detection and monitoring, Nat. Rev. Cancer 8 (2008) 268-278.

[117] U-H.Stenman, J. Leinonen, W-M.Zhang, P. Finne, Prostate-specific antigen, Seminars in Cancer Biol. 9 (1999) 83-93.

[118] D. Ilic, M. Djulbegovic, J. H. Jung, E. C. Hwang, Q. Zhou, A. Cleves, T. Agoritsas,P. Dahm, Prostate cancer screening with prostate-specific antigen (PSA) test: a systematic review and meta-analysis, British Med. J. 362 (2018) k3519-k3531.

[119] K. Matsumoto, N. Konishi, Y. Hiasa, E. Kimura, Y. Takahashi, K. Shinohara, T. Samori, A highly sensitive enzyme-linked immunoassay for serum free prostate specific antigen (f-PSA), Clin. Chim. Acta 281 (1999) 57–69.

[120] H.H. Lee, M.A. Dineva, Y.L. Chua, A. Ritchie, I. Ushiro-Lumb, C.A. Wisniewski, Simple amplification-based assay: A nucleic acid-based point-of-care platform for HIV-1 testing, J. Infect. Dis. 201 (2010) S65–S71.

[121] T. Yang, P. Hou, L.L. Zheng, L. Zhan, P.F. Gao, Y.F. Li, C.Z. Huang, Surface-engineered quantum dots/electrospun nanofibers as a networked fluorescence aptasensing platform toward biomarkers, Nanoscale 9 (2017) 17020–17028.

[122] R.-M.Kong, X. Zhang, L. Ding, D. Yang, F. Qu, Label-free fluorescence turn-on aptasensor for prostate-specific antigen sensing based on aggregation-induced emission–silica nanospheres, Anal.Bioanal. Chem. 409 (2017) 5757–5765.

[123] Y.-B.Choi, N.-H.Kim, S.-H.Kim, G.-S.Tae, H.-H. Kim, Heterogeneous Electrochemical Immunoassay of Hippuric Acid on the Electrodeposited Organic Films, Sensors 14 (2014) 18886–18897.

[124] S.B. Nimse, M.D. Sonawane, K.-S.Song, T. Kim, Biomarker detection technologies and future directions, Analyst 141 (2016) 740–755.

[125] S. Gutkin, O. Green, G. Raviv, D. Shabat, O. Portnoy, Powerful Chemiluminescence Probe for Rapid Detection of Prostate Specific Antigen Proteolytic Activity: Forensic Identification of Human Semen, Bioconj. Chem. 31 (2020) 2488–2493.

[126] G. Ertürk, H. Özen, M.A. Tümer, B. Mattiasson, A. Denizli, Microcontact imprinting based surface plasmon resonance (SPR) biosensor for real-time and

ultrasensitive detection of prostate specific antigen (PSA) from clinical samples, Sens. Actuators B Chem. 224 (2016) 823–832.

[127] P. Singh, SPR Biosensors: Historical perspectives and current challenges, Sens. Actuators B Chem. 229 (2016) 110–130.

[128] Y.Z. Grasso, M.K. Gupta, H.S. Levin, C.D. Zippe, E.A. Klein, Combined nested RT-PCR Assay for prostate-specific antigen and prostate-specific membrane antigen in prostate cancer patients: correlation with pathological stage, Cancer Res. 58 (1998) 1456–1459.

[129] L. Xie, X. Yang, Y. He, R. Yuan, Y. Chai, Polyacrylamide gel-contained Zinc finger peptide as the “lock” and zinc ions as the “key” for construction of ultrasensitive prostate-specific antigen SERS immunosensor, ACS Appl. Mater. Interf. 10 (2018) 15200–15206.

[130] Y.C. Cao, R. Jin, C.A. Mirkin, Nanoparticles with Raman spectroscopic fingerprints for DNA and RNA detection, Science 297 (2002) 1536–1540.

[131] M. Souada, B. Piro, S. Reisberg, G. Anquetin, V. Noël, M.C. Pham, Label-free electrochemical detection of prostate-specific antigen based on nucleic acid aptamer, Biosens. Bioelectron. 68 (2015) 49–54.

[132] J.S. Wysock, Genetic mutations associated with prostate cancer and normal serum PSA and DRE—implications for prostate cancer screening and management: NYU case of the month November 2020, Rev. Urol. 22 (2020) 177-181.

[133] S. Saini, PSA and beyond: alternative prostate cancer biomarkers, Cell. Oncol. 39 (2016) 97–106.

[134] B. Liu, L. Lu, E. Hua, S. Jiang, G. Xie, Detection of the human prostate-specific antigen using an aptasensor with gold nanoparticles encapsulated by graphitized mesoporous carbon, Microchim. Acta 178 (2012) 163–170.

[135] Q. Hu, S. Gan, Y. Bao, Y. Zhang, D. Han, L. Niu. Electrochemically controlled ATRP for cleavage-based electrochemical detection of the prostate-specific antigen at femtomolar level concentrations. Anal Chem. 92 (2020) 15982-15988.

[136] Y.J. Li, M.J. Ma, G. Yin, Y. Kong, J.J. Zhu, Phthalocyanine-sensitized graphene-CdS nanocomposites: an enhanced photoelectrochemical immunosensing platform, Chemistry 19 (2013) 4496-505.

[137] D. Wu, Y. Liu, Y. Wang, L. Hu, H. Ma, G. Wang, Q. Wei, Label-free electrochemiluminescent immunosensor for detection of prostate specific antigen based on aminated graphene quantum dots and carboxyl graphene quantum dots, Sci. Rep. 6 (2016) 20511.

[138] H. Wang, X. Huang, A. Wang, X. Luo, W. Liu, P. Yuan, J. Feng, Construction of efficient “on-off-on” fluorescence aptasensor for ultrasensitive detection of prostate specific antigen via covalent energy transfer between g-C3N4 quantum dots and palladium triangular plates, Anal. Chim. Acta 1104 (2020) 53-59.

[139] Q. Zhou, Y. Lin, K. Zhang, M. Li, D. Tang, Reduced graphene oxide/BiFeO3 nanohybrids-based signal-on photoelectrochemical sensing system for prostate-specific antigen detection coupling with magnetic microfluidic device, Biosens. Bioelectron. 101 (2018) 146–152.

[140] Y. Wei, X. Li, X. Sun, H. Ma, Y. Zhang, Q. Wei, Dual-responsive electrochemical immunosensor for prostate specific antigen detection based on Au-CoS/graphene and CeO2/ionic liquids doped with carboxymethyl chitosan complex, Biosens. Bioelectron. 94 (2017) 141–147.

[141] P. Jolly, P. Zhurauski, J.L. Hammond, A. Miodek, S. Liébana, T. Bertok, Jan Tkáč, P. Estrela, Self-assembled gold nanoparticles for impedimetric and amperometric detection of a prostate cancer biomarker, Sens. Actuators B Chem. 251 (2017) 637-643.

[142] A.R. Jalalvand, Fabrication of a novel and ultrasensitive label-free electrochemical aptasensor for detection of biomarker prostate specific antigen, Int. J. Biol. Macromol. 126 (2019) 1065-1073.

[143] F. Duan, S. Zhang, L. Yang, Z. Zhang, L. He, M. Wang, Bifunctional aptasensor based on novel two-dimensional nanocomposite of MoS2 quantum dots and g-C3N4 nanosheets decorated with chitosan-stabilized Au nanoparticles for selectively detecting prostate specific antigen, Anal. Chim. Acta 1036 (2018) 121-132.

[144] A. Rahi, N. Sattarahmady, H. Heli, Label-free electrochemical aptasensing of the human prostate-specific antigen using gold nanospears, Talanta 156–157 (2016) 218-224.

[145] E. Heydari-Bafrooei, N.S. Shamszadeh, Electrochemical bioassay development for ultrasensitive aptasensing of prostate specific antigen, Biosens.Bioelectron. 91 (2017) 284–292.

[146] G. Zhang, Z. Liu, L. Fan, Y. Guo, Electrochemical prostate specific antigen aptasensor based on hemin functionalized graphene-conjugated palladium nanocomposites, Microchim. Acta 185 (2018) 1-8.

[147] G.J. Ashwell, A.T. Williams, S.A. Barnes, S.L. Chappell, L.J. Phillips, B.J. Robinson, B. Urasinska-Wojcik, P. Wierzchowiec, I.R. Gentle, B.J. Wood, Self-Assembly of amino– thiols via gold– nitrogen links and consequence for in situ elongation of molecular wires on surface-modified electrodes, J. Phys. Chem. C. 115 (2011) 4200–4208.

[148] M. Cesbron, E. Levillain, T. Breton, C. Gautier, Click chemistry: A versatile method for tuning the composition of mixed organic layers obtained by reduction of diazonium cations, ACS Appl. Mater. Interf. 10 (2018) 37779–37782.

[149] Y. Liu, D.D. Díaz, A.A. Accurso, K.B. Sharpless, V. V Fokin, M.G. Finn, Click chemistry in materials synthesis. III. Metal-adhesive polymers from Cu (I)-catalyzedazide–alkyne cycloaddition, J. Polym. Sci. Part A Polym. Chem. 45 (2007) 5182–5189.

[150] G. Fomo, N. Nwaji, T. Nyokong, Low symmetric metallophthalocyanine modified electrode via click chemistry for simultaneous detection of heavy metals, J. Electroanal. Chem. 813 (2018) 58–66.

[151] D. Akyüz, A. Koca, An electrochemical sensor for the detection of pesticides based on the hybrid of manganese phthalocyanine and polyaniline, Sens. Actuators B Chem. 283 (2019) 848–856.

[152] B. Öztaş, D. Akyüz, A. Koca, Immobilization of alkynyl functionalized manganese phthalocyanine via click electrochemistry for electrocatalytic oxygen evolution reaction, Phys. Chem. Chem. Phys. 19 (2017) 26121–26131.

[153] Y. İpek, H. Dinçer, A. Koca, Electrode modification based on "click electrochemistry" between terminal-alkynyl substituted cobalt phthalocyanine and 4-azidoaniline, Sens. Actuators B Chem. 193 (2014) 830–837.

[154] C.S.J.N. O'Donoghue, G. Fomo, T. Nyokong, Electrode modification using alkyne manganese phthalocyanine and click chemistry for electrocatalysis, Electroanal. 28 (2016) 3019–3027.

[155] D. Evrard, F. Lambert, C. Policar, V. Balland, B. Limoges, Electrochemical functionalization of carbon surfaces by aromatic azide or alkyne molecules: a versatile platform for click chemistry, Chem. Eur. J. 14 (2008) 9286–9291.

[156] H.R. Phillip, E.A. Taft, Kramers-Kronig Analysis of Reflectance Data for Diamond, Phys. Rev. 136 (1964) A1445-A1448.

[157] G. C. Eastmond, P. C. B. Page, J. Paprotny, R. E. Richards and R. Shaunak, Poly (ether imide)s with hindering substituents in the anhydride moiety: synthesis, properties and gas permeabilities, Polymer 35 (1994) 4215–4227.

[158] X. Zhang, L. Mao, D. Zhang, L. Zhang. Synthesis, characterization and electrochemistry of novel unsymmetrical zinc phthalocyanines sensitizer with extended conjugation. J. Mol. Struc. 1022 (2012) 153-158.

[159] D. Quinton, E. Antunes, S. Griveau, T. Nyokong, F. Bedioui, Cyclic Voltammetry and Spectroelectrochemistry of a Novel Manganese Phthalocyanine Substituted with Hexynyl Groups. Inorg. Chem. Comm. 14 (2011) 330–332.

[160] M.S. Ağirtas, M.S. Izgi, Synthesis and Characterization of New Metallophthalocyanines with Four Phenoxyacetamide Units. J. Mol. Structure 927 (2009) 126–128.

[161] O.J. Achadu, T. Nyokong, In situ one-pot synthesis of graphitic carbon nitride quantum dots and its 2,2,6,6-tetramethyl(piperidin-1-yl)oxyl derivatives as fluorescent nanosensors for ascorbic acid, Anal. Chim. Acta 991 (2017) 113-126.

[162] O.J. Achadu, T. Nyokong, Interaction of Graphene Quantum Dots with 4-Acetamido-2,2,6,6-Tetramethylpiperidine-Oxyl Free Radicals: A Spectroscopic and Fluorimetric Study. J. Fluoresc. 26 (2016) 283–295.

[163] J. Cheng, B.A. Teply, I. Sherifi, J. Sung, G. Luther, F.X. Gu, E. Levy-Nissenbaum, A.F. Radovic-Moreno, R. Langer, O.C. Farokhzad, Formulation of functionalized PLGA-PEG nanoparticles for in vivo targeted drug delivery, Biomaterials 28 (2007) 869-876.

[164] P. Jolly, N. Formisano, J. Tkáč, P. Kasák, C.G. Frost, P. Estrela, Label-free impedimetric aptasensor with antifouling surface chemistry: A prostate specific antigen case study, Sens. Actuators B Chem. 209 (2015) 306-312.

[165] T. Hezard, K. Fajerwerg, D. Evrard, V. Colliere, P. Behra, P. Gros, Gold nanoparticles electrodeposited on glassy carbon electrode using cyclic voltammetry: Application to Hg(II) trace analysis. J. Electroanal. Chem. 664 (2012) 46-52.

[166] A.B. Shivanandareddy, M. Kumar, V. Lakshminarayanan, RSC Advances Self-assembly of thiolated graphene oxide onto a gold surface and in the supramolecular order of discotic liquid crystals y, RSC Adv. 5 (2015) 47692–47700.

[167] S. Griveau, D. Mercier, C. Vautrin-Ul, A. Chaussé, Electrochemical grafting by reduction of 4-aminoethylbenzenediazonium salt: Application to the immobilization of (bio)molecules, Electrochem. Commun. 9 (2007) 2768–2773.

[168] D. Bélanger, J. Pinson. Electrografting: a powerful method for surface modification. Chem. Soc. Rev. 40 (2011) 3995-4048.

[169] J. C. Lacroix, G. Trippe-Allard, J. Ghilane, P. Martin, Optical nanoparticles: synthesis and biomedical application. Adv. Nat. Sci.: Nanosci. Nanotech.5 (2014) 015001.

[170] L.S. Mpeta, G. Fomo, T. Nyokong, Click chemistry electrode modification using 4-ethynylbenzyl substituted cobalt phthalocyanine for applications in electrocatalysis, J. Coord. Chem. 71 (2018) 1623-1638.

[171] F. Zhang, F. Liu, C. Wang, X. Xin, J. Liu, S. Guo, J. Zhang, Effect of Lateral Size of Graphene Quantum Dots on Their Properties and Application. ACS Appl. Mater. Interf. 8 (2016) 2104–2110.

[172] L. Trapiella-Alfonso, G. Ramírez-García, F. d'Orlyé, A. Varenne, Electromigration separation methodologies for the characterization of nanoparticles and the evaluation of their behavior in biological systems, Trends Anal. Chem. 84 (2016) 121-130.

[173] E. Dervishi, Z. Ji, H. Htoon, M. Sykora, S.K. Doorn, Raman spectroscopy of bottom-up synthesized graphene quantum dots: Size and structure dependence, Nanoscale 11 (2019) 16571-16581.

[174] T. Fan, W. Zeng, W. Tang, C. Yuan, S. Tong, K. Cai, Y. Liu, W. Huang, Y. Min, A.J. Epstein, Controllable size-selective method to prepare graphene quantum dots from graphene oxide, Nanoscale Res. Lett. 10 (2015) 1-8.

[175] S. Bansal, J. Singh, U.Kumari, I.P. Kaur, R.P. Barnwal, R. Kumar, S. Singh, G. Singh, M. Chatterjee, Development of biosurfactant-based graphene quantum dot conjugate as a novel and fluorescent theranostic tool for cancer, Int. J. Nanomedicine 14 (2019) 809-818.

[176] H. Shah, W. Xie, Y. Wang, X. Jia, A. Nawaz, Q. Xin, M. Song, J.R. Gong, Preparation of blue- and green-emissive nitrogen-doped graphene quantum dots from graphite and their application in bioimaging, Mater. Sci. Eng. C. 119 (2021) 111642.

[177] S. Barman, M. Sadhukhan, Facile bulk production of highly blue fluorescent graphitic carbon nitride quantum dots and their application as highly selective and sensitive sensors for the detection of mercuric and iodide ions in aqueous media, J. Mater. Chem. 22 (2012) 21832-21837.

[178] S. Thaweesak, S. Wang, M. Lyu, M. Xiao, P. Peerakiatkhajohna, L. Wang. Boron-doped graphitic carbon nitride nanosheets for enhanced visible light photocatalytic water splitting, Dalton Trans. 46 (2017) 10714-10720.

[179] C.J. Chirayil, J. Abraham, R. Kumar Mishra, S.C. George, S. Thomas, Chapter 1- Instrumental Techniques for the Characterization of Nanoparticles, in: S. Thomas, R. Thomas, A.K. Zachariah, R.K. Mishra (editors), Thermal and Rheological Measurement Techniques for Nanomaterials Characterization., Elsevier, Boston (2017) 1–36.

[180] K. Syamantak, C.V. Navneet, G. Prashant, J. Sanjhal, G. Souvik G, K.N. Chayan, Mechanistic Insight into the Carbon Dots: Protonation induced Photoluminescence, J. Mat. Sci. Eng. 7 (2018) 1-6.

[181] D. Bhattacharya, M.K. Mishra, G. De, Carbon Dots from a Single Source Exhibiting Tuneable Luminescent Colors through the Modification of Surface Functional Groups in ORMOSIL Films, J. Phys. Chem. C. 121 (2017) 28106−28116.

[182] F. d'Orlye, A. Varenne, T. Georgelin, J-M. Siaugue, B. Teste, S. Descroix, P. Gareil, Charge-based characterization of nanometric cationic bifunctional maghemite/silica core/shell particles by capillary zone electrophoresis, Electrophoresis 30 (2009) 2572-2582.

[183] G. Ramírez-García, D.O. Oluwole, S.R. Nxele, F. d'Orlyé, T. Nyokong, F. Bedioui, A. Varenne, Characterization of phthalocyanine functionalized quantum dots by dynamic light scattering, laser Doppler, and capillary electrophoresis, Anal. Bioanal. Chem. 409 (2017) 1707–1715.

[184] N. Surugau, P.L. Urban, Electrophoretic methods for separation of nanoparticles, J. Sep. Sci. 32 (2009) 1889 – 1906.

[185] M.J. Stillman, T. Nyokong In: Eds. Phthalocyanines: Properties and applications, edited by Leznoff CC, Lever ABP VCH, New York, Vol.1, (1989) Chapt 3.

[186] S. Roy, E. Reisner, Visible-Light-Driven CO2 Reduction by Mesoporous Carbon Nitride Modified with Polymeric Cobalt Phthalocyanine, Angew. Chemie - Int. Ed. 58 (2019) 12180-12184.

[187] A. Aravind, P. Jeyamohan, R. Nair, S. Veeranarayanan, Y. Nagaoka, Y. Yoshida, T. Maekawa, D.S. Kumar, AS1411 aptamer tagged PLGA-lecithin-PEG nanoparticles for tumor cell targeting and drug delivery, Biotechnol. Bioeng. 109 (2012) 2920-2931.

[188] Z. Zhang, S. Liu, Y. Shi, Y. Zhang, D. Peacock, F. Yan, P. Wang, L. He, X. Feng, S. Fang, Label-free aptamer biosensor for thrombin detection on a nanocomposite of graphene and plasma polymerized allylmine, J. Mat. Chem. B. 2 (2014) 1530-1538.

[189] S. Ni, Z. Shen, P. Zhang, G. Liu, Enhanced performance of an electrochemical aptasensor for real-time detection of vascular endothelial

growth factor (VEGF) by nanofabrication and ratiometric measurement, Anal. Chim. Acta 1121 (2020) 74-82.

[190] S. Chung, J.M. Moon, J. Choi, H. Hwang, Y.B. Shim, Magnetic force assisted electrochemical sensor for the detection of thrombin with aptamer-antibody sandwich formation, Biosens. Bioelectron. 117 (2018) 480-486.

[191] G.G. Matlou, N. Kobayashi, M. Kimura, T. Nyokong, Physicochemical properties of water soluble unsymmetrical phthalocyanine-folic acid conjugates, Dye.Pigment. 149 (2018) 393-398.

[192] S. Pang, T.P. Labuza, L. He, Development of a single aptamer-based surface enhanced Raman scattering method for rapid detection of multiple pesticides. Analyst 139 (2014)1895-1901.

[193] S. Liu, Y. Huo, J. Bai, B. Ning, Y. Peng, S. Li, D. Han, W. Kang, Z. Gao, Rapid and sensitive detection of prostate-specific antigen via label-free frequency shift Raman of sensing graphene, Biosens. Bioelectron.158 (2020) 112184.

[194] A. Zasedatelev, T. Dubinina, D. Krichevsky, V. Krasovskii, V. Gak, V. Pushkarev, L. Tomilova, A. Chistyakov, Plasmon-induced light absorption of phthalocyanine layer in hybrid nanoparticles: Enhancement factor and effective spectra. J. Phys. Chem. 120 (2016) 1816–1823.

[195] S. Nyoni, T. Mugadza, and T. Nyokong, Improved l-cysteine electrocatalysis through a sequential drop dry technique using multi-walled carbon nanotubes and cobalt tetraaminophthalocyanine conjugates. Electrochim. Acta 128 (2014) 32-40.

[196] N. Hashemzadeh, M. Hasanzadeh, N. Shadjou, J. Eivazi-Ziaei, M. Khoubnasabjafari, A. Jouyban, Graphene quantum dot modified glassy carbon electrode for the determination of doxorubicin hydrochloride in human plasma, J. Pharma. Anal. 6 (2016) 235–241.

[197] C.A. Caro, F. Bedioui, J.H. Zagal. Electrocatalytic oxidation of nitrite on a vitreous carbon electrode modified with cobalt phthalocyanine, Electrochim. Acta 47 (2002) 1489-1494.

[198] L. Trnková, Electrochemical behavior of DNA at a silver electrode studied by cyclic and elimination voltammetry, Talanta 56 (2002) 887–894.

[199] J. Jankowska-Śliwińska, M. Dawgul, J. Kruk, D. G. Pijanowska, Comparison of electrochemical determination of purines and pyrimidines by means of carbon, graphite and gold paste electrodes, Int. J. Electrochem. Sci. 12 (2017) 2329 – 2343.

[200] J. Gooding, V. Praig, E. Hall.Platinum-Catalyzed Enzyme Electrodes Immobilized on Gold Using Self-Assembled Layers, Anal. Chem. 70 (1998) 2396-2402.

[201] Z. Li, M. Lieberman, W. Hill. XPS and SERS Study of Silicon Phthalocyanine Monolayers: Umbrella vs Octopus Design Strategies for Formation of Oriented SAMs, Langmuir 17 (2001) 4887-4894.

[202] M.B. Jensen, D.E. Tallman, A LabVIEW-based virtual instrument for simulation and analysis of SECM approach curves, J. Solid State Electrochem. 17 (2013) 2999–3003.

[203] G. Cai, Z. Yu, R. Ren, D. Tang, Exciton–Plasmon Interaction between AuNPs/Graphene Nanohybrids and CdS Quantum Dots/TiO_2 for Photoelectrochemical aptasensing of prostate-specific antigen, ACS Sens. 3 (2018) 632–639.

[204] A. Maringa, E. Antunes, T. Nyokong, Electrochemical behavior of gold nanoparticles and Co tetraaminophthalocyanine on glassy carbon electrode, Electrochim. Acta 121 (2014) 93-101.

[205] M. Delamar, R. Hitmi, J. Pinson, J.M. Saveant. Covalent Modification of Carbon Surfaces by Grafting of Functionalized Aryl Radicals Produced from Electrochemical Reduction of Diazonium Salts. J. Am. Chem. Soc. 12 (1992) 5883-5884.

[206] L. Gonzalez-Macia, S. Griveau, F. d'Orlyé, A. Varenne, C. Sella, L. Thouin, F. Bedioui, Electrografting of aryl diazonium on thin layer platinum microbands: Towards customized surface functionalization within microsystems, Electrochem. Commun. 70 (2016) 78–81.

[207] D. Mwanza, S. Mvango, S. Khene, T. Nyokong, P. Mashazi, Exploiting Click Chemistry for the Covalent Immobilization of Tetra (4-Propargyloxyphenoxy) Metallophthalocyanines onto phenylazide-grafted gold surfaces, Electrochim. Acta 254 (2017) 89–100.

[208] A. Devia, H. Castillo, V. Benavides, Y. Arango, J. Quintero, Growth and characterization of AuN films through the pulsed arc technique, Mater. Mater.Charact. – Material Characterization 59 (2008) 105–107.

[209] S. Prakash, T.M. Long, J.C. Selby, J.S. Moore, M.A. Shannon, “Click” modification of silica surfaces and glass microfluidic channels, Anal. Chem. 79 (2007) 1661-1667.

[210] X. Yan, T. Xu, G. Chen, S. Yang, H. Liu, Q. Xue, Preparation and characterization of electrochemically deposited carbon nitride films on silicon substrate, J. Phys. D: Appl. Phys. 37 (2004) 1–7.

[211] S. Krishnan, Y. Chipatecua, Deep Eutectic Solvent-Assisted Synthesis of Au Nanostars Supported on Graphene Oxide as an Efficient Substrate for SERS-Based Molecular Sensing, ACS Omega. 5 (2020) 1384-1393.

[212] I.G. Casella, M. Contursi, Electrocatalytic oxidation of some hydrazine compounds at glassy carbon electrode modified with co-gluconate complex, Electroanalysis 24 (2012) 752-758.

[213] S. Maree, T. Nyokong.Electrocatalytic behavior of substituted cobalt phthalocyanines towards the oxidation of cysteine, J.Electroanal. Chem. 492 (2000) 120–127.

[214] C.E. Banks, R.G. Compton. New electrodes for old: from carbon nanotubes to edge plane pyrolytic graphite, Analyst 131 (2006)15-21.

[215] Z. Galus, Fundamentals of Electrochemical Analysis, Ellis Horwood Press, New York, 1976, p. 313, Ch. 10.

[216] R. Devasenathipathy, V. Mani, S-M. Chen, K. Kohilarani, S. Ramaraj.Determination of L-cysteine at Iron Tetrasulfonated Phthalocyanine

Decorated Multiwalled Carbon Nanotubes Film Modified Electrode, Int. J. Electrochem. Sci. 10 (2015) 682 – 690.

[217] A.P Gutierrez, M.R. Argote, S.E Griveau, J.H. Zagal, S.G. Granados, A.A. Ordas, F. Bedioui. Catalytic activity of electrode materials based on polypyrrole, multi-walled carbon nanotubes and cobalt phthalocyanine for the electrooxidation of glutathione and l-cysteine, J. Chil. Chem. Soc. 57 (2012) 1244-1247.

[218] N. Hernández-Ibáñez, I. Sanjuán, M.Á. Montiel, C.W. Foster, C.E. Banks, J. Iniesta, L-cysteine determination in embryo cell culture media using Co (II)-phthalocyanine modified disposable screen-printed electrodes, J. Electroanal.Chem. 780 (2016) 303–310.

[219] J. Bisquert, A. Compte, Theory of the electrochemical impedance of anomalous diffusion, J. Electroanal. Chem. 499 (2001) 112–120.

[220] P. Salazar, M. Martín, J.L. González-Mora In situ electrodeposition of cholesterol oxidase-modified polydopamine thin film on nanostructured screen printed electrodes for free cholesterol determination, J. Electroanal. Chem. 837 (2019) 191–199

[221] E. Sabatani, I. Rubinstein, Organized self-assembling monolayers on electrodes. 2. Monolayer-based ultramicroelectrodes for the study of very rapid electrode kinetics, J. Phys. Chem. 91 (1987) 6663–6669.

[222] R.I. Stefan, J.F. van Staden, H.Y. Aboul-Enein, Electrochemical Sensors in Bioanalysis, Marcel Dekker, New York, 2001.

[223] R. Jannatifar, K. Parivar , Na. HayatiRoodbari, M.H. Nasr-Esfahani, Effects of N-acetyl-cysteine supplementation on sperm quality, chromatin integrity and level of oxidative stress in infertile men, Reprod. Biol. Endocrinol.17 (2019) 24-32.

[224] M. Mazloum-Ardakani, P. Pourhakkak, M. Salavati-Niasari, M. A. Karimid, M. H. Mashhadizadehe, Highly Selective and Sensitive Membrane Salicylate Electrode Based on Complex of (1,8-Diamino-3,6-dioxaoctane) Nickel(II), J. Braz. Chem. Soc. 22 (2011) 30-37.

[225] K. Mao, D. Wu, Y. Li, H. Ma, Z. Ni, H. Yu, C. Luo, Q. Wei, B. Du, Label-free electrochemical immunosensor based on graphene/methylene blue nanocomposite, Anal. Biochem. 422 (2012) 22–27.

[226] C. Ibau, M.K. Md Arshad, S.C.B. Gopinath, M. Nuzaihan, M.F.M. Fathil, P. Estrela.Gold interdigitated triple-microelectrodes for label-free prognosticative aptasensing of prostate cancer biomarker in serum, Biosens.Bioelectron. 136 (2019) 118–127.

[227] F.-M. Wang, J. Rick, Synergy of Nyquist and Bode electrochemical impedance spectroscopy studies to commercial type lithium ion batteries, Solid State Ion. 268 (2014) 31–34.

[228] A.A. Shah, N. Yasmeen, G. Rahman, S. Bilal, High Electrocatalytic Behaviour of Ni Impregnated Conducting Polymer Coated Platinum and Graphite Electrodes for Electrooxidation of Methanol, Electrochim. Acta 224 (2017) 468–474.

[229] G. Bouvet, D.D. Nguyen, S. Mallarino, S. Touzain, Analysis of the non-ideal capacitive behaviour for high impedance organic coatings, Prog. Org. Coat. 77 (2014) 2045–2053.

[230] W. Argoubi, A. Sánchez, C. Parrado, N. Raouafi, R. Villalonga, Label-free electrochemical aptasensing platform based on mesoporous silica thin film for the detection of prostate specific antigen, Sens. Actuators B Chem. 255 (2018) 309–315.

[231] C. Thunkhamrak, P. Chuntib, K. Ounnunkad, P. Banet, P.-H.Aubert, G. Saianand, A.-I. Gopalan, J. Jakmunee, Highly sensitive voltametric immunosensor for the detection of prostate specific antigen based on silver nanoprobe assisted graphene oxide modified screen printed carbon electrode, Talanta 208 (2020) 120389.

[232] F. Tahmasebi, A. Noorbakhsh, Sensitive electrochemical prostate specific antigen aptasensor: Effect of carboxylic acid functionalized carbon nanotube and glutaraldehyde linker, Electroanalysis 28 (2016) 1134–1145.

[233] W. Kong, F. Qu, L. Lu, A photoelectrochemical aptasensor based on p-n heterojunction CdS-Cu2O nanorod arrays with enhanced photocurrent for the detection of prostate-specific antigen, Anal. Bioanal. Chem. 412 (2020) 841-848.

[234] Y.-K.Yen, C.-H.Chao, Y.-S. Yeh, A Graphene-PEDOT:PSS Modified Paper-Based Aptasensor for Electrochemical Impedance Spectroscopy Detection of TumorMarker, Sensors 20 (2020) 1372-1382.

[235] V. Bernal, A. Erto, L. Giraldo, J.C. Moreno-Piraján, Effect of Solution pH on the Adsorption of Paracetamol on Chemically Modified Activated Carbons, Molecules 22 (2017) 1032-1045.

[236] J.H. Zagal, M.A. Gulppi, C. Depretz, D. Lelièvre, Synthesis and electrocatalytic properties of octaalkoxycobalt phthalocyanine for the oxidation of 2-mercaptoethanol, J. Porphyr. Phthalocyanines. 3 (1999) 355–363.

[237] W.J. Catalona, D.S. Smith, T.L. Ratliff, K.M. Dodds, D.E. Coplen, J.J. Yuan, J.A. Petros, G.L. Andriole, Measurements of Prostate-Specific Antigen in Serum as Screening Test for Prostate Cancer. New Engl. J. Med. 324 (1991) 1156-1161.

[238] H. Liu, Z. Tian, Z. Lu, Z. Zhang, M. Zhang, D. Pang, Direct electrochemistry and electrocatalysis of heme-proteins entrapped in agarose hydrogel films, Biosens. Bioelectron. 20 (2004) 294–304.

[239] M. Srivastava, N.R. Nirala, S.K. Srivastava, R. Prakash, A comparative Study of Aptasensor Vs Immunosensor for Label-Free PSA Cancer Detection on GQDs-AuNRs Modified Screen-Printed Electrodes, Sci. Rep. 8 (2018) 1923-1933.

[240] A. Díaz-Fernández, R. Miranda-Castro, P. Estrela, N. de-los-Santos-Álvarez, M.J. Lobo-Castañón, Catching the Sugars: Electrochemical Aptasensors for the Detection of Cancer-Related Glycosylation Changes in Prostate-Specific Antigen, Proceedings 60 (2020) 47-51.

[241] B.P. Crulhas, A.E. Karpik, F.K. Delella, G.R. Castro, V.A. Pedrosa, Electrochemical aptamer-based biosensor developed to monitor PSA and VEGF released by prostate cancer cells, Anal. Bioanal.Chem. 409 (2017) 6771–678.